Studies on Development of a Solar-Powered, Colour-Tunable and Smart Outdoor LED Lighting System with Wireless Control

Thesis Submitted by

Rajib Malik

Doctor of Philosophy (Engineering)

Department of Electrical Engineering
Faculty Council of Engineering & Technology
Jadavpur University
Kolkata, India

2019

JADAVPUR UNIVERSITY
KOLKATA-700032, INDIA

INDEX NO. 57/15/E

1. Title of the thesis:

Studies on Development of a Solar-Powered, Colour-Tunable and Smart Outdoor LED Lighting System with Wireless Control

2. Name, Designation and Institution of the Supervisors:

Dr. Saswati Mazumdar

Professor,
Electrical Engineering Department
Jadavpur University
Kolkata 700032

Dr. Kalyan Kumar Ray

Former Professor,
Instrumentation and Electronics Engineering Department
Jadavpur University
Kolkata 700032

3. List of Journal Publications:

- **R. Malik**, K. K. Ray, and S. Mazumdar, "Wide-Range, Open-Loop, CCT and Illuminance Control of an LED Lamp Using Two-Component Color Blending," ***IEEE Transactions on Power Electronics***, vol. 33, no. 11, pp.9830-9818, 2018.

- **R. Malik**, K. K. Ray, and S. Mazumdar, "A Low-Cost, Wide-Range, CCT-Tunable, Variable-Illuminance LED Lighting System", ***LEUKOS***, pp. 1–20, 2019 (in press) DOI: 10.1080/15502724.2018.1541747.

- **R. Malik**, and S. Mazumdar , "DEVELOPMENT OF CCT TUNABLE LED LIGHTING SYSTEM USING RED-BLUE-WHITE LED", ***Light & Engineering,*** vol- 25, no-4, pp. 99-108, 2017.

4. List of Presentations in International/National Conferences:

- **R. Malik**, S. Mazumdar, "Development of an intelligent hybrid (solar & conventional AC) controller for solar street or home lighting system", presented in International Conference on Emerging Trends in Lighting Concepts for a Greener World, **Light India International** , Chennai, India, 16th September 2013.
- **R. Malik**, S. Saha, S. Mazumdar, "Development of Discrete Component based LED Driver with RGB PWM dimming", presented in International Conference of **LUX Pacifica 2015**, Kolkata, pp-635-641, 27-29 November 2015.

- **R. Malik,** K. K. Ray, and S. Mazumdar, "A Maximum Power Point Tracking VRLA Battery Charger Based on Modified Perturb and Observe Technique", **2019 IEEE Region Ten Symposium (TENSYMP)**, Kolkata, India, 2019. (Accepted for presentation and publication, Paper ID-143)

Certificate from the supervisors

This is to certify that the thesis entitled "***Studies on Development of a Solar-Powered, Colour-Tunable and Smart Outdoor LED Lighting System with Wireless Control***" submitted by **Shri Rajib Malik**, who got his name registered on 02/01/2015 for the award of Ph.D (Engg.) degree of Jadavpur University is absolutely based upon his own work under the joint supervision of the under signed and that neither his thesis nor any part of the thesis has been submitted for any degree/diploma or any other academic award anywhere before.

1._____

Signature of the Supervisor and Date
with Official Seal

2. _____

Signature of the Supervisor and Date
with Official Seal

Acknowledgments

The author would like to express his sincere gratitude and deep appreciation to his supervisors *Prof. Saswati Mazumdar* of Electrical Engineering Department and Former-Professor *Dr. Kalyan Kumar Ray* of Instrumentation and Electronics Engineering Department, Jadavpur University for their invaluable guidance in carrying out the thesis work. The author has been provided with necessary freedom during the course of the research work and at the same time the intense supervision by the supervisors has helped to enhance the quality of the research. Their moral support, amiable and amicable personality, encouragement and profound knowledge about the subject have made the research work possible. Besides, the author is also grateful to the supervisors for providing necessary mental support during difficult times helping him to become a better individual which led to his overall professional development.

The author would like to acknowledge his respected teachers Prof. Biswanath Roy, Mr. Suddhasatwa Chakraborty and Mrs. Sangeeta Sahana of Illumination Engineering Section, Jadavpur University, for providing necessary advice and support to the research work.

The author is grateful to the Head of the Department of Electrical Engineering, Jadavpur University for providing necessary departmental facilities needed to carry out the research work.

The author would like to acknowledge Dr. Kamalika Ghosh, Assistant Professor and Mr. Parthasarathi Satvaya, Assistant Professor of School of Illumination Science Engineering and Design (SISED), Jadavpur University for providing some necessary instruments to carry out this research work.

The author would like to acknowledge my sincere thanks and respect to Mr. Asit Kumar Sur, Visiting Demonstrator of Illumination Engineering Section for his enormous support.

The author would like to acknowledge Visvesvaraya Ph.D. scheme from Govt. of India and TEQIP-II for awarding the fellowship under the schemes to carry out this research work.

The author would like to thank his colleagues Ms. Moutusi Bag, Mr. Dipayan Nath, Mr. Saptarshi Chatterjee, Dr. Nasirul Haque, Mr. Pradip Kumar Maiti, Mrs. Purnima Mandal, Mr. Basudeb Das, Mr. Bappaditya Sinha, Mr. Shibabrata Mukherjee, Ms. Tishya Sarma Sarkar, and Mr. Vishwanath Gupata for providing support in various ways and making the laboratory an interesting place in carrying out the research work.

I would also like to thank all the staff members Mr. Pradip Pal, Mr. Santosh Sahoo, Mr. Chandan Bikash Dey, Mr. Samir Mandi, of Illumination Engineering Laboratory of Jadavpur University for their cooperation and assistance towards completion of this work.

The author would also like to extend thanks to all the existing and past graduate students of the Illumination Engineering Laboratory of Electrical Engineering Department, Jadavpur University for making it possible to work in a homely atmosphere.

The author would like to convey his deep love and respect towards his parents Mr. Arjun Malik and Mrs. Bijali Malik for their never ending support and encouragement during difficult times. Without their support, this work could never have been completed.

Finally, as it is impossible to mention everybody by name, the author would like to convey his gratitude to all who have contributed in one way or another, in making this work possible.

Abstract

Nowadays, outdoor lighting is an important aspect in the life of people in urban as well as rural areas mainly for security, safety and aesthetic purposes. Over the past few decades, researchers in outdoor lighting technologies are trying to increase energy efficiency, use renewable energy, reduce maintenance costs, improve safety measure, enhance visual environment and reduce light pollution. The use of solar-powered LED lighting system with remote control is a very appropriate and decisive step in achieving the goals. Therefore, the overall objective is to develop and integrate the several technological possibilities in outdoor lighting system so that it can efficiently harvest solar energy and maximize the battery life, while provides the much-needed system reliability.

In this study, two remote control and monitoring based, 'smart', energy-efficient, long-life, low-cost and low-maintenance solar-powered outdoor lighting systems (OLSs) have been developed, implemented and successfully tested. These systems run automatically with minimal manual intervention. Moreover, they can send information related to the management and maintenance of the system to the central monitoring station through a GSM-SMS technology. Such information can be sent on a periodic, say hourly, daily or weekly basis. After analyzing the received information, the central station can also control some parameters of the remote lighting system through the same network. Additionally, on receiving the information, the state-of-health and nature of the fault of the system can be predicted from the remote monitoring station. Necessary maintenance strategy and the procedure can then be decided centrally.

In this study, two types of LED lighting systems have been developed, each suitable for a specific application area. The first one is a tunable-CCT, variable-illuminance LED lighting system for colour-tunable outdoor lighting applications (e.g., residential non-living areas, public buildings and structures, gardens, parks, etc.). The second one is a fixed-CCT, three-step dimmable LED lighting system for single colour outdoor lighting applications (e.g., streets, pathways, parking lots, industrial yards, security areas etc.).

The work also involves development of an improved maximum power point tracking (MPPT) algorithm derived from the Perturb and Observe (P&O) technique. This ensures the efficient operation of the PV power plant by rapidly and accurately tracking the maximum power point (MPP) of the PV array regardless of changes in environmental conditions.

The methodology and implementation approaches used in this work is quite simple, straightforward, and do not require any complicated algorithm or costly component or costly tools. The hardware of the whole outdoor lighting system has been implemented by using readily available components including a low-cost microcontroller. The developed algorithm is experimentally validated by this hardware. The control algorithm is developed using C programming language. The necessary compiler and the associated tools are available as freeware. This has reduced the software development cost to a large extent.

Dedicated to-

My parents

Contents

Table of contents

List of Figures

List of Tables

List of Abbreviations

AC	Alternating Current
ADC	Analog to Digital Converter
AGM	Absorbent Glass Mat
ANN	Artificial Neural Network
ANSI	American National Standard Institute
BCM	Boundary Conduction Mode
CC	Constant Current
CCM	Continuous Conduction Mode
CCT	Correlated Colour Temperature
CFL	Compact Fluorescent Lamp
CICU	CCT and Illuminance Control Unit
CIE	Commision Internationale de l'Eclairage
CMOS	Complementary Metal-Oxide-Semiconductor
CRI	Colour Rendering Index
CTLED	Colour Tunable Light Emitting Diode
CV	Constant Voltage
CW	Cool White
CWLED	Cool-White Light Emitting Diode
DC	Direct Current
DCM	Discontinuous Conduction Mode
DEMUX	De-multiplexer
DOD	Depth-of-Discharge
ESR	Equivalent Series Resistance
FCOLS	Fixed-CCT Outdoor Lighting System
FLC	Fuzzy Logic Controller
FOCV	Fractional Open Circuit Voltage
FSCI	Fractional Short Circuit Current Technique
GPRS	General Packet Radio Service
GSM	Global System for Mobile Communication
GUI	Graphical User Interface
HB-LED	High-Brightness Light Emitting Diode
ICC	Interrupted Charge Control
IC	Integrated Circuit
IEEE	Institute of Electrical and Electronics Engineers
I-V	Current-Voltage
LCD	Liquid Crystal Display
LED	Light Emitting Diode
LPF	Low Pass Filter
MCU	Microcontroller Unit
MOSFET	Metal-Oxide-Semiconductor Field-Effect Transistor
MPP	Maximum Power Point

MPPT	Maximum Power Point Tracking
NIST	National Institute Standards and Technology
NPT	Non-Power Tracking
NV RAM	Non-Volatile Random Access Memory
OLS	Outdoor Lighting System
P & O	Perturb and Observe
PCB	Printed Circuit Board
PC-LED	Phosphor-Coated Light Emitting Diode
PGA	Programmable Gain Amplifier
PI	Proportional-plus-Integral
POC	Proof-of-Concept
PSH	Peak Sun Hours
PV	Photovoltaic
P-V	Power-Voltage
PWM	Pulse Width Modulation
RAM	Random Access Memory
RBW	Red-Blue-White
RCC	Ripple Correlation Control
RF	Radio Frequency
RGB	Red-Green-Blue
RMS	Root Mean Square
RTC	Real Time Clock
SIM	Subscriber Identity Module
SMS	Short Message Service
SOC	State-of-Charge
SOH	State-of-Health
SPD	Spectral Power Distribution
STC	Standard Test Conditions
TCOLS	Tunable-CCT Outdoor Lighting System
TSC	Three Stage Charging
TTL	Transistor Transistor Logic
USART	Universal Synchronous-Asynchronous Receiver-Transmitter
VRLA	Valve-Regulated Lead-Acid
WB	White-Blue
WR	White-Red
WW	Warm White

List of Symbols

ε	Electrical energy
ε_s	Solar energy
η	Efficiency
D	Duty cycle
D [k]	Duty cycle at k-th sample
D_{uv}	Deviation of the operating point from Planckian locus in CIE 1976 chromaticity diagram
E	Illuminance
e_{fb}	Voltage feedback for fixed CCT LED driver
F_{clk}	System clock frequency
f_S	Converter switching frequency
I_B	Battery current
i_g	Gassing current of the battery
i_L	Inductor current
$I_{L,avg}$	Average inductor current
$I_{L,max}$	Maximum inductor current
$I_{L,min}$	Minimum inductor current
I_{LED}	LED current
I_O	Output current
I_{OTH}	Higher threshold current
I_{OTHL}	Lower threshold current
I_{SC}	Short circuit current
i_T	Battery terminal current
K_{FF}	Fill factor
n_{ad}	Positive integer as output of the ADC
P_i	Input power to the converter
P_L	Power loss in converter
P_{max}	Power at maximum power point
P_O	Output power of the converter
P_{PV}	Photovoltaic power
q	Resolution of the AD converter
R_{CS}	Current sensing resistor
S_c	State-of-charge

T	Sampling period of controller, Switching period of the converter,
T_b	Case temperature of the battery
T_{cr}	Correlated colour temperature
T_{PS}	Peak sun hours
$u_{i,AD}$	Input analog voltage to the ADC
U_R	Reference voltage of the ADC
V_B	Battery Voltage
V_{BREFH}	Higher threshold voltage
V_{BREFL}	Lower threshold voltage
V_F	Forward voltage of diode
V_i	Input voltage to converter
V_{mpp}	Voltage at maximum power point
V_O	Output voltage
V_{OC}	Open circuit voltage
V_{PV}	Photovoltaic voltage
V_R	Reference voltage
V_γ	Forward voltage of LED
W_p	Watt-Peak
x_b	x coordinate of CIE 1931 for bended source
x_e	x coordinate of an epicentre on CIE1931 diagram
x_k	x coordinate of CIE 1931 for k-th source
y_b	y coordinate of CIE 1931 for bended source
y_e	y coordinate of an epicentre on CIE1931 diagram
y_k	y coordinate of CIE 1931 for k-th source
ΔD	Incremental duty cycle
Δi_L	Incremental inductor current
ΔP_i	Incremental input power to the converter
ΔP_O	Incremental output power
ΔV_i	Incremental input voltage to converter
ΔV_o	Incremental output voltage
ΔV_{PV}	Incremental photovoltaic voltage
ΔV_R	Incremental reference voltage

Chapter 1
Introduction

1.1 Background

It is possible that our prehistoric ancestors kept the blazing embers of a forest fire in their caves to provide warmth and light necessary for their lives. Wood with high natural oil content was used for lighting. The first likely portable lamps were flaming torches using pine knots. Wood did not turn out to be very satisfactory as a source of light. Down through recorded history, three other basic pre-electric light sources have emerged in chronological order; oil lamps, candles and gas lighting. The ancient Babylonian and Egyptian civilizations had crude oil lamps. These were in the form of small bowls containing fish or animal fat or vegetable oil. The discovery of coal oil in the mid-19th century provided a new liquid fuel for lighting [1]. People turned next to the development of the candle, which was made of beeswax and was quite expensive. Most inexpensive candles today are made of moulded paraffin. Historically, natural gas was used for lighting after this. Throughout most of the nineteenth century, gas lighting was provided by the light from an open gas flame, rather than the alternative of heating an object to incandescence by burning gas. The gas lighting devices had several disadvantages like they had to be burned upright, they were difficult to start, and above all, they generated dirty soot. To overcome the disadvantages of pre-electric lights, the electric lights were developed.

A commercially practical incandescent lamp was invented by Thomas Edison in 1879 [1]. Edison used a fine hairlike filament which had high resistance and thus required to cause it to emit light. The second electric light source was the arc lamp by Humphrey Davy, in concurrent with early incandescent lamp development. The carbon arc lamp produced an arc between two carbon electrodes in the air. The third light source in the 1800s was that of enclosed gaseous discharge lamps. In this type of lamp, the light was produced by an electric discharge through creating an ionized gas. In 1930 Fluorescent lamp (a low-pressure mercury vapor gas discharge lamp) was developed. It was based on fluorescence, phenomena which convert ultraviolet light to visible light. The high-pressure mercury lamp was developed also in 1930 followed by Metal halide and Sodium lamps in 1950 and 1960, respectively [1].

The first revolutionary change in the field of efficient lighting came with fluorescent lamps, which used 75 percent less electricity than incandescent lamps. The second major breakthrough in lighting technology is the solid-state lighting, which uses up to 85 percent less electricity than incandescent lamp. During the last four decades, technical progress in the field of solid-state lighting has been breathtaking, in terms of cost reduction and an increase of efficacy. In recent years, solid-state light employing Light Emitting Diodes (LEDs), which use the electroluminescence phenomena in a semiconductor junction to produce light, has become more popular for the general lighting applications. As it has great advantages like high-efficiency, long operating life, small size and environment friendliness, its potential to replace incandescent, fluorescent and gas discharge lamps is apparent.

An estimate made in 2005 [2] states that the total consumption of electricity was about 18 PWh (18,000Twh), 19% of which or about 3420 TWh was consumed for lighting. If the consumption in lighting can be reduced to 35% of the above value by use of energy efficient lighting systems, 2223TWh of energy is saved. This would mean a total energy consumption of 15777 TWh, which is 87.6% of the current value. The resulting electrical energy savings is equivalent to shutdown of 440 coal-fired power plants of 800 MW each (Compiled by Earth Policy Institute from International Energy Agency). It thus reduces the emission of greenhouse gases, most importantly carbon dioxide (CO_2), into the atmosphere. The increase of energy efficiency is, therefore, a crucial requirement for all future lighting system designs.

A considerable amount of electrical energy can be saved by various means of lighting control. The different types of lighting control based on energy saving scheme can be broadly classified into two types, on-off control and lighting level control. The latest breakthrough in lighting control is a combination of pre-programmed on-off control, dimming control, space lighting levels control etc. Modern, wireless lighting control systems have additional benefits including reduction of installation cost and increase of flexibility where switches and sensors can be placed easily in the lighting system. This control allows the users to remotely switch on/off and dimming control to individual or groups of light. According to the recent finding, the automatic light control can reduce light energy consumption by 50% in existing building and at least 35% in new construction. Besides energy management, color control is also an important issue for mood lighting, which affects the emotional feeling of human being.

As the requirement of electrical energy is essential to power up the artificial lights, its energy supply should be secured and sustainable. The energy requirement of the world is ever

growing. It is expected to grow further in the future. There are two main reasons for the increase in energy demand, the first one is growth in the world's population and the second one is the techno-economic growth of the countries, particularly in developing countries. The increasing energy demand puts a lot of pressure on the non-renewable energy sources (coal, oil and natural gas). The fossil fuel-based energy sources are limited in quantity and also cause environmental pollution. So, there is a pressing need to accelerate the development of renewable energy based technologies in order to address the global challenges of energy security, climate change and sustainable development. Among the renewable energy sources (wind, solar, biomass), solar energy has some advantages like its easy availability and lack of rotational parts in the energy conversion process are well known, so, solar energy has a vital role in the rural as well as in urban area.

Recently, a large emphasis is being given on sustainable energy and energy efficient lighting to reduce carbon emission. Solar-Powered LED lighting system is a perfect combination to meet the requirements. As high starting voltage pulse required for discharge lamp is not necessary, LEDs can be more conveniently driven from solar cell fed battery compared to the former. Although switching to solar power and LED lighting definitely requires a high amount of capital investment, it can be justified to reduce carbon footprint.

1.2 Benefits of solar energy

Benefits of solar energy over the other renewable energy are given below.

- The solar photovoltaic module can be installed over the top or very near to the consumption area. Hence, most of the time no distribution network is required as compared to other renewable energy sources like wind, hydro, geothermal, biomass etc.
- Solar power is customizable compared to other renewable sources, as it can be used for the small electronic devices (like a watch, calculator, toy, etc.) to large power plants.
- Solar cells convert the solar radiation directly into electricity based on the photovoltaic effect without going through any thermal process as in the case of solar thermal energy.
- Solar modules, once installed, require minimum or no maintenance as they have no rotational parts in the conversion process. Hence, it is very much suitable for isolated or remote areas. The maintenance cost is also very low as compared to other renewable sources.

- Solar energy is an everlasting consistent source of supply as compared to the seasonal wind energy.
- Less capital investment is required for solar power as compared to the wind and hydropower.
- Solar energy can play a vital role in very remote areas where it is too expensive for extension of the grid.
- The installation process of solar array is very easy, cost-effective and can be built within a short time duration.

1.3 Global and national status of solar energy

Throughout the globe, tremendous growth in solar PV technology is clearly visible, specifically for the last two decades. As of 2016, renewable electricity provides an estimated 24.5% of total global electricity production [3]. Among other renewable energy sources, solar photovoltaic energy provides 6.1% of total renewable electricity [3]. In 2016, solar PV energy added an amount of 75GW$_p$, which is 48% addition over the previous year 2015 [3]. Total global capacity and annual additions for solar PV technology are shown in Fig. 1.1 from the 2006 to 2016.

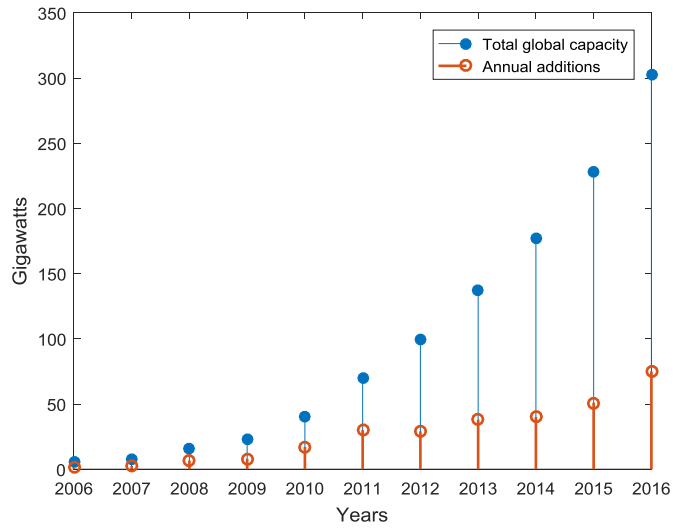

Fig. 1.1. Solar PV total global capacity and annual additions (2006-2016)

The worldwide annual production of PV module in terms of megawatt-peak (MW$_p$) and the PV module cost in terms of US$/W$_p$ are given in Fig. 1.2 [4], [5]. In 1975 the PV module price was about 100$/W$_p$, which has become 0.3 $/W$_p$ in 2016. On the other hand, in 1975,

the worldwide annual production of PV module was about $2MW_p$, which has become 78060 MW_p in 2016. Due to the tremendous growth in the production of PV module, there is a significant amount of price drop as shown in Fig. 1.2. It can be easily predicted, that the price will be further reduced in the upcoming years, as annual production of the solar module is snowballing, depends on the worldwide PV module demand.

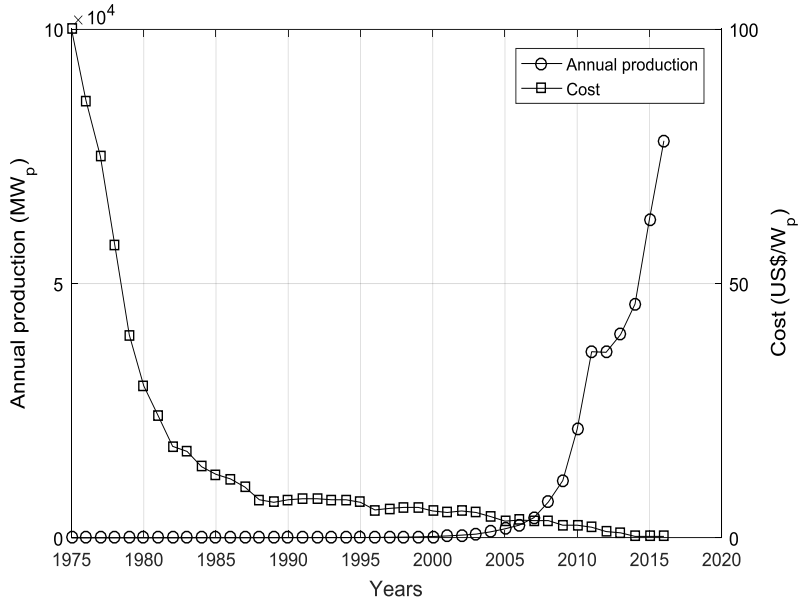

Fig. 1.2. Worldwide annual production of PV modules and annual average cost

PV module installed capacity in India during 2016 was $4.1GW_p$, which is 5.5% of total global capacity addition compared to 20% in the United States. In 2017, India is globally placed at 6^{th} position in terms of solar power installed capacity. The Government of India has set a target to install 175GW renewable power by the end of 2022. This includes 100GW from solar power, 60GW from wind power, 10GW from biomass power and 5GW from small hydropower. As of 2017, grid-connected and off-grid solar electricity capacity is of 16611.73MW and 551.56MW, respectively [6]. From the available data, it can be easily concluded that the Government of India is giving a considerable emphasis to solar power compared to other renewable power sources.

1.4 LED-based outdoor lighting

Nowadays, outdoor lighting is an important aspect in the life of people in urban as well as rural areas mainly for security, safety and aesthetic purposes. In general, outdoor lighting is provided in residential areas, streets, parking lots, buildings and structures, security area,

gardens, parks, pathways etc. Traditionally, the lamp types used for outdoor lighting were the incandescent lamps and gas-discharge lamps, e.g.: low and high-pressure mercury vapour lamps, high-pressure sodium vapour lamps, metal halide lamps, etc. These are now being replaced by LEDs, CFLs etc. Different types of lamps for outdoor lighting being used for the last decade with their parameters like efficacy, correlated colour temperature (CCT), colour rendering index (CRI), lifetime and available wattage are given in Table 1.1 [7]. The values in this table may change as the technology improves.

Table 1.1. Different lamps for outdoor lighting with their photometric parameters, life and available power.

Sl. no.	Lamp type	Source efficacy (lm/w)	CCT(K)	CRI, R_a	Lifetime (Hours)	Available power(W)
1	High-pressure sodium (HPS)	80–120	1,900–2,200	22–70	15,000–40,000	70–400
2	Low Pressure Sodium (LPS)	130–170	1,700–1,800	-	16,000–18,000	55 – 180
3	Metal halide	40–70	3,000–4,200	60–80	10,000–20,000	70–400
4	Ceramic Metal Halide	75–110	3,000–4,200	80–94	10,000–24,000	70–400
5	Mercury vapor	20–40	3,200–6,700	15–50	16,000–24,000	75–1,000
6	Induction	50–85	3,500–5,000	80–85	100,000	70–250
7	CFL	80–85	2,700–5,000	80–85	6,000–20,000	20–70
8	LED	up to 130	2,700–10,000	50–80	35,000–50,000	40–250

From this table, it is clearly visible that LED lamp is the prime candidate for exterior lighting in terms of efficacy, lifetime and availability of wide range CCT. So, in recent years, LED-based outdoor light is gaining more popularity throughout the world, mainly due to energy saving potential and versatility in spectral power distribution [8]–[11].

Researchers in outdoor lighting technologies are trying to increase energy efficiency, reduce maintenance costs, improve safety measures, enhance visual environments and reduce light pollution or sky glow [12], [13] [14]. Recently in 2017, the U.S. Department of Energy (DOE), together with experts in astronomy and atmospheric scattering conducted a comparative study for street lighting to evaluate the contribution of sky glow from conventional high-pressure sodium (HPS) lamp and new LED lamp [14]. This study concluded that all of the tested LED product with different CCT reduced sky glow relative to

an HPS lamp, for both near and distant observers, when the results are expressed as unweighted radiant power.

1.5 Effect of light on human psychology and biology

Recent research findings indicate that biological and psychological system of human body can be controlled by appropriate light exposure [15]–[17]. Exposure to light should be in terms of spectral composition (quality), illuminance level (quantity) as well as timing. Light incident on the subject sends signals via the photoreceptor cells and a separate nerve system to her/his biological clock, which in turn regulates the circadian (daily) and circannual (seasonal) rhythms of a large variety of bodily processes. Previous studies showed that the light can influence the secretion of cortisol and melatonin hormones [16], [17]. Melatonin and cortisol levels play important roles in terms of sleep and alertness, respectively. Cortisol levels increase in the morning and prepare the body for the coming day's activity. It then decreases gradually but remain at a sufficiently high level to give sufficient blood sugar (and thus energy) over the course of the day, falling finally to a minimum at midnight. The level of melatonin is lowest in the morning and remains fairly flat till early evening. It then starts to increase, eventually reaching a maximum at midnight. It then falls to a minimum level in the next morning. Good health demands that these two rhythms are not disturbed too much. In the event of a disruption of the rhythm, bright light in the morning helps restore the normal rhythm. Colour tunable light sources also may be used for mood lighting, which affects the emotional feeling of humans [18], [19].

1.6 Problem statement and objective of the thesis

The shortcomings of the existing outdoor lighting system motivated to develop and integrate the several technological possibilities in this developed smart outdoor lighting system. Most of the existing outdoor lighting systems suffer from the following shortcomings.

- Renewable energy is not usually used as a power source.
- Maintenance of outdoor lighting system is often difficult due to the accessibility of the luminaire specifically in rural or isolated areas.
- Often light output falls due to lack of preventive maintenance like dust accumulation, insect accumulation, etc.

- Lack of information about the precise location and nature of the fault in the system.
- Remote control and monitoring facilities are not usually incorporated.
- Dimming facility is not commonly available to optimize the power requirement and to maintain natural nocturnal atmosphere, simultaneously.
- Colour changeable lights are not being used, so outdoor lighting system becomes monotonous and sometimes special attraction of a place is lost at night due to improper choice of light colour.

The primary objective of this thesis work is to integrate the several possibilities in outdoor lighting systems, as no such work has been done on integrating the existing technology. The main objectives are given as follows

I. To maximize the solar power available at a location under variable irradiance and temperature.
II. To maximize the battery life and minimize the charging time.
III. To estimate the state-of-charge of the battery
IV. To produce the desired CCT and illuminance independently at the outdoor if necessary.
V. To optimize power consumption by proper switching and dimming.
VI. To make maintenance of outdoor lighting system easy.
VII. To monitor and control the outdoor lights from remote places using wireless communication.

In order to develop the solar-powered outdoor lighting system, the following contributions have been made in this thesis work.

To fulfill objectives I, II and III the following work have been done.

- Development of hardware and software for a solar-powered multi-stage battery charging system.
- Development of a maximum power point tracking (MPPT) algorithm for efficient harvesting of solar energy.
- Development of a discrete component based high-side MOSFET driver.
- Implementation of a digital PI controller to maintain a constant output voltage at the output of the converter.

- Implementation of state-of-charge estimation of a rechargeable battery.

To fulfill objectives IV and V, the following developments have been made.

- Development of necessary hardware and software for tunable-CCT and variable-illuminance LED lighting system.
- Development of a PWM dimmable high-side LED driver for tunable-CCT outdoor lighting system (OLS).
- Development of a three-step dimmable LED driver for fixed-CCT OLS.
- Development of a model to estimate the luminous parameters (viz. xy chromaticity coordinates and peak illuminance) with respect to junction temperature of the LED.

To fulfill objectives VI and VII, the following have been made.

- Implementation of remote health monitoring and control of the outdoor lighting system by using GSM technology.
- Implementation of different health monitoring schemes (such as battery internal resistance, battery voltage, light output, etc.).
- Some of the parameters (like battery voltage, battery current, status, duty cycle etc.) are also displayed on the LCD screen to help the maintenance personnel.

The developed OLS with the above mentioned innovative features make the system smart and useful.

1.7 Literature survey

The proposed research work can be broadly classified into four categories. The literature surveys of these categories are discussed in this section.

1.7.1 Solar charge controller

Solar radiation, although available free, is an unpredictable source of energy. It varies as a function of time through the day and not available during the night. It also depends on the atmospheric conditions like cloud, fog etc. Therefore, when a solar photovoltaic system is used for off-grid application, a backup source of energy is necessary to provide

uninterruptible power to the load. Commonly, batteries are used as a backup source in such applications. The battery is used to store the extra energy generated by the solar photovoltaic (PV) module throughout the day. In turn, this stored energy can be used by the load during non-sunshine hours. In such an off-grid system, an electronic circuit known as a charge controller is an essential subsystem to protect the battery from over-charging and deep-discharging. This consequently extents the performance and life-span of the battery. Block diagram of a typical off-grid PV system with charge controller and battery is shown in Fig. 1.3.

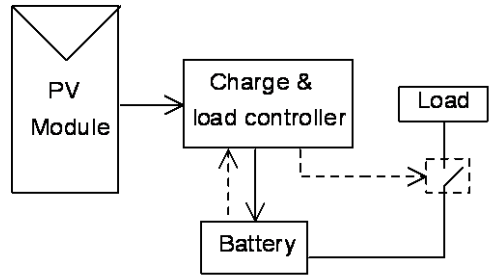

Fig. 1.3. Block diagram of a typical off-grid PV system

Other requirements of the charge controller are given below.

- Provide load control function: This function automatically connects or disconnects the load depending on various situations like occupancy, daylight availability, traffic density, preset time, etc.
- Blocking of reverse current: This function restricts the reverse flow of current from the battery to the solar module during the night low insolation periods. It thus prevents the battery from excessive discharge consequently increases the battery uptime.
- Configure control set points: Charging and discharging voltage and/or current of the battery can be pre-programmed. This is required for fine tuning of battery charging and discharging rate.
- Temperature compensated control: The battery charging voltage/current need to be temperature compensated to maximize battery life-span and minimize the charging time.
- Display and monitoring: Some charge controller systems can display various parameters like charging status, remaining battery life, battery health, etc. A modern high-end controller also has some facilities like inbuilt memory for data logging, data

communication to the remote places for system monitoring, remote controlling of the system, etc.

Solar charge controller can be broadly divided into two types: traditional and modern. The traditional series and shunt types of linear charge controllers prevent the battery from overcharging and deep discharging, but they are not efficient and cannot produce the desired voltage or current incompatible with the load[5]. Moreover, advanced power control algorithms cannot be implemented in these controllers. As a result, nowadays, these types of traditional charge controllers have become obsolete. On the other hand, the modern DC-DC converter based charge controllers are gaining popularity as these use the PV modules in a more energy efficient manner. In these configurations voltage of the PV module is raised or lowered in accordance with the load or battery voltage. The modern charge controller can be further divided into non-power tracking (NPT) and maximum power point tracking (MPPT) controllers. In the NPT version, the voltage and the current of the PV module and or the load are measured and controlled to keep them within safe values, while in the MPPT version, the controller extracts the maximum possible power from the PV module. The MPPT-based charge controller charges the battery or feeds the load more efficiently than non-power tracking controller. The NPT and MPPT charge controllers use DC-DC converters in between the PV module and the load. The duty cycle of a NPT converter is controlled to maintain the load current or voltage within a certain value, while the MPPT-based controller uses a suitable control algorithm to compute the output power of a PV module and maximize it by manipulating the duty cycle of the converter. The block diagram of an MPPT system is shown in Fig. 1.4. Detailed descriptions of common MPPT algorithms are given below.

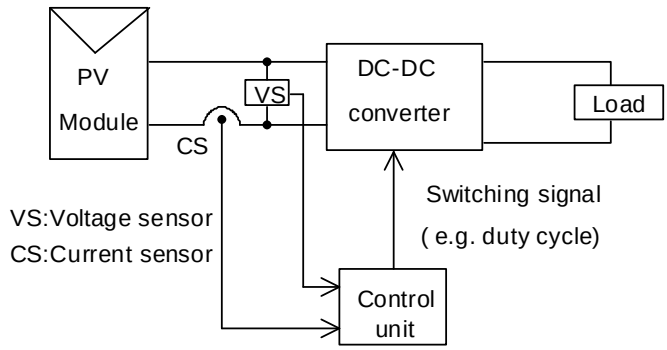

Fig. 1.4. Block diagram of a typical MPPT system

Current-voltage (I-V) and power-voltage (P-V) characteristic curves of a 60 watt-peak (W_p) PV module under a fixed irradiance and temperature are given in Fig. 1.5. The non-linear I-V characteristic of a PV panel has a unique maximum power point (MPP) at the knee of the curve corresponding to a specific current (I_{mpp}) and voltage (V_{mpp}). The maximum power (P_{max}) is the area of the inscribed rectangle under the I-V curve which has a maximum value. The PV module should be operated at the point Q (corresponding to P_{max} as shown in Fig. 1.5) to extract the maximum possible power. The ratio of the maximum power to product of the open circuit voltage and the short circuit current is often termed as the fill-factor.

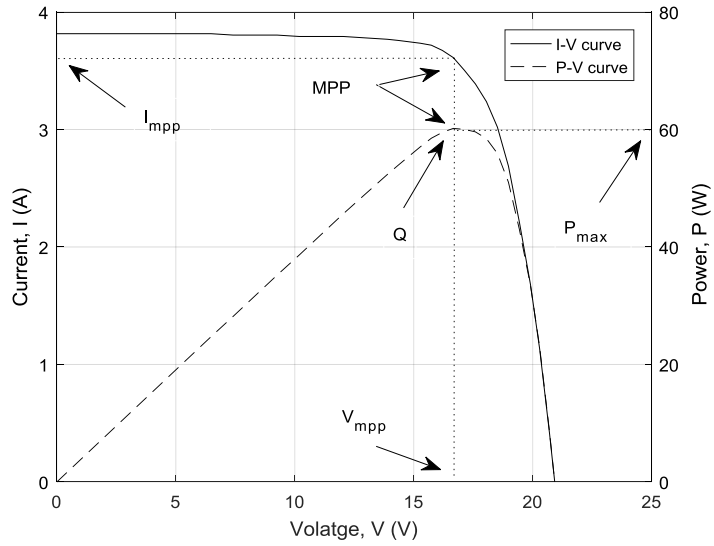

Fig. 1.5. I-V and P-V characteristic curves of a PV module rated at $60W_p$

Review of MPPT techniques

Various MPPT methods have been implemented by factors like tracking accuracy, complexity, convergence speed, steady state and transient response, digital or analog implementation, cost, sensor requirement, ease of implementation and in other respects. For the last two decade, so many MPPT algorithms have been developed that it is very difficult to determine which algorithm is most appropriate for a given PV system. Some popular MPPT techniques have been discussed below and based on these we developed a novel technique for battery charging for the stand-alone PV system.

a) Perturb and observe (P&O) and Hill-climbing techniques

Perturb and observe (P&O) [20]–[26] and Hill-climbing [25]–[33] techniques are the most popular algorithms used for MPPT tracking because of their ease of implementation. P&O

technique gives a perturbation in the operating voltage or current of the PV module while Hill-climbing technique gives a perturbation in the duty cycle of the power converter [25]. P&O and Hill-climbing techniques employ different strategies to reach and track the MPP. It can be seen from the P-V characteristic of Fig. 1.5 that when the operating point on the power graph is to the left of the point Q an increase of voltage is followed by an increase of power. On the other hand, when operating point is to the right of Q, increase of voltage is followed by a decrease of power.

To explain the P & O algorithm where the perturbation in voltage is given we can consider a simple system whose block diagram is shown in Fig. 1.6. The MPPT algorithm is usually implemented as a sampled-data system. In the discussions to follow x [k] will indicate the k^{th} sample of a variable x. As a first step, the increments in the PV array power and voltage resulting from a perturbation in the reference voltage $V_{PV,\,r}$ [k − 1] in the k^{th} sample are computed as follows

$$\Delta P_{PV}[k] = P_{PV}[k] - P_{PV}[k-1] \tag{1.1}$$

$$\Delta V_{PV}[k] = V_{PV}[k] - V_{PV}[k-1] \tag{1.2}$$

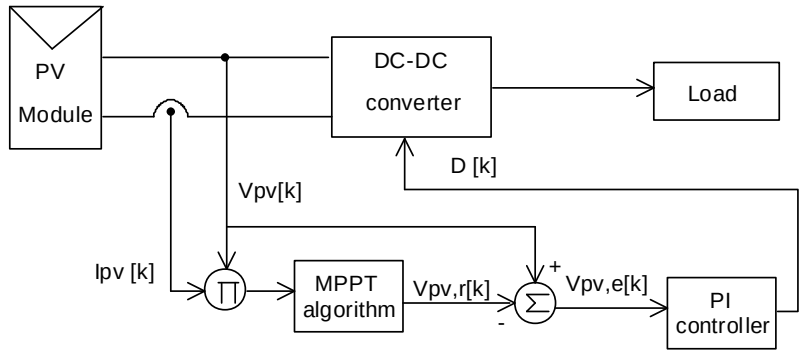

Fig. 1.6. Simplified block diagram for the implementation of P & O algorithm

Following this, a number m whose value is either +1 or -1 is determined depending on the relative sign of $\Delta V_{PV}[k]$ and $\Delta P_{PV}[k]$, provided $|\Delta V_{PV}[k]|$ is greater than a small positive value ε_1 and $|\Delta P_{PV}[k]|$ is greater than small positive value ε_2. Symbolically, m is given by

$$m = \text{sgn}\,\frac{\Delta P_{PV}[k]}{\Delta V_{PV}[k]} \tag{1.3}$$

Equation (1.3) can be further explained by stating that m has a value of +1 if both the numerator and denominator of equation (1.3) has the same sign and has a value of -1 if their sign is different. As special cases if the modulus of the incremental power is less than a

preassigned power, ε_2 or V, m is given a value of zero. The current value of $\Delta V_{PV,r}$ is then decided by the following equation

$$\Delta V_{PV,\,r}\,[k] = m\, V_{PV,\,st} \tag{1.4}$$

where, $V_{PV,\,st}$ is a preselected step increment in the reference value of V_{PV}.

Ultimately, the value of $V_{pv,r}$ is computed from the expression

$$V_{pv,\,r}\,[k] = V_{PV,\,r}\,[k\text{-}1] + \Delta V_{PV,\,r}\,[k] \tag{1.5}$$

In order to ensure that the reference and the actual values of V_{pv} are equal in the steady state, the error $V_{pv,\,e}[k]$ is computed as

$$V_{pv,\,e}[k] = V_{pv}\,[k] - V_{pv,\,r}\,[k] \tag{1.6}$$

The error is then fed to a direct-acting PI controller which produces the output duty cycle D[k] of the converter. If the overall system is stable the presence of the integral term in the controller will ensure that the reference and actual values of V_{pv} are equal. So, if the given perturbation increases (decreases) the power, the subsequent perturbation should be in the same (opposite) direction to reach the MPP. This process is repeated until the MPP is reached. The flow chart of the algorithm is illustrated in Fig. 1.7. For brevity, the subscript 'PV' is dropped from the symbols for V, I and P in this figure. V_o, P_o and V_{ro} represent, respectively, values of V, P and V_r in the previous sampling instant. The symbol V_{st} indicates the step size of reference voltage perturbation. To start the algorithm, the values of V_o, P_o, V_{ro} and V_{st} need initialization.

In the conventional P & O method, a fixed perturbation is used to generate the reference signal. Once the controller reaches the MPP, it might enter an oscillatory state especially if a large perturbation is used to achieve fast convergence. This oscillation can be minimized by reducing the fixed step size. However, a small perturbation step leads to a slowdown of the MPPT algorithm. Hence, a trade-off between the system speed and oscillation is needed. Many researchers propose a solution by providing a variable perturbation size that gets smaller towards the maximum power point [21], [22], [24], [30], [34]–[36]. Despite the fair performance, they suffer from several demerits like high computational load and the use of system dependent constants.

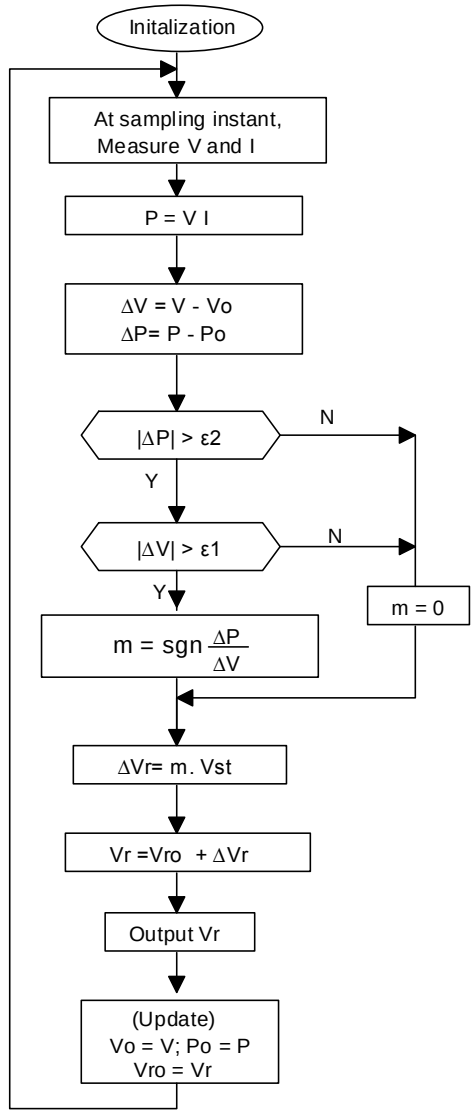

Fig. 1.7. Flowchart of the perturb and observe algorithm

The hill-climbing technique of MPP tracking [25]–[33] is a one-dimensional search method that uses the converter duty cycle D as the manipulated variable. In simple terms, it perturbs the value of D by an amount ΔD at a particular sampling instant and observes its effects e.g. ΔP, ΔV etc. at the next sampling instant. The value of ΔD at this instant is decided in a way similar to that in the P&O method. The use of fixed step size in D again gives rise to problems of stability and speed of convergence, unless an adaptive step size algorithm is used.

Some P&O and hill-climbing methods are not capable of tracking the MPP under rapidly changing atmospheric conditions. To solve the problem, a three-point weight comparison

method has been proposed [37]. In this method, the algorithm compares the actual operating point power with two preceding ones before a decision is made.

b) Incremental conductance (IncCond) method:

Referring to the P-V curve in Fig. 1.5, it can be seen that the derivative of the array output power P_{pv} with respect to PV module voltage V_{pv} is equal to zero at the MPP, positive at the left of MPP and negative at the right of MPP. The incremental conductance method is based on this fact [38]–[43]. For brevity, the subscript 'PV' is dropped from the symbols for V, I and P in this section.

The term dP/dV can be expressed as follows

$$\frac{dP}{dV} = \frac{d(IV)}{dV} = I + V\frac{dI}{dV} \cong I + V\frac{\Delta I}{\Delta V} \tag{1.7}$$

In terms of the sampled quantities equation (1.7) can be rewritten as

$$\frac{dP}{dV}[k] = I[k] + V[k]\frac{I\,[k]-I\,[k-1]}{V[k]-V\,[k-1]} \tag{1.8}$$

In view of the observations made above regarding dP/dV and equation (1.7), we get

$$\frac{\Delta I}{\Delta V} = -\frac{I}{V} \text{ , At MPP} \tag{1.9}$$

$$\frac{\Delta I}{\Delta V} > -\frac{I}{V} \text{, at the left of MPP} \tag{1.10}$$

$$\frac{\Delta I}{\Delta V} < -\frac{I}{V} \text{, at the right of MPP} \tag{1.11}$$

Thus, the maximum power point is tracked by comparing the values of the dynamic or incremental conductance ΔI/ΔV and static conductance I/V as shown in Fig. 1.8. In practice, due to noise and measurement error, it is very difficult to satisfy equation (1.9). As a remedy, this condition is modified in [41], [44] by

$$\left|\frac{\Delta I}{\Delta V} + \frac{I}{V}\right| < \varepsilon \tag{1.10}$$

where ε is a positive small value. For convenience, the quantity ΔI/ΔV + I/V is denoted by a symbol G_r in the flowchart of Fig. 1.8 where V_o, I_o and V_{ro} represent, respectively, values of V, I and V_r in the previous sampling instant. The symbol ΔV_r indicates the constant increment that is given to the reference voltage V_r. To start the algorithm, the values of V_o, P_o, V_{ro}, and ΔV_r need initialization.

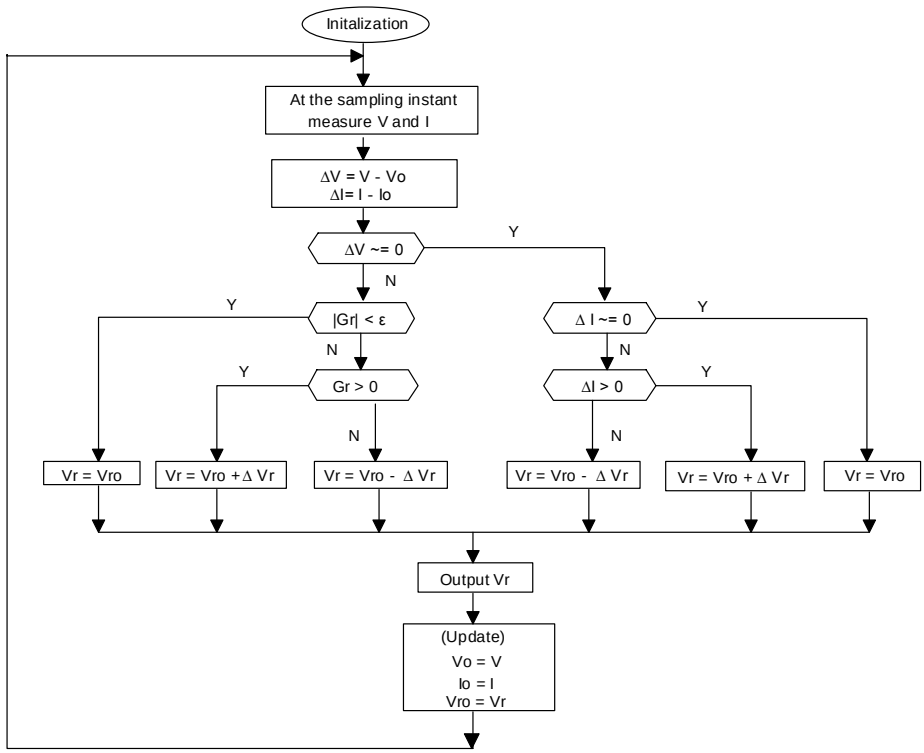

Fig. 1.8. Flowchart of conventional incremental conductance algorithm

Like P & O algorithm, IncCond also suffers from a fixed perturbation step size problem as discussed above. This problem has been solved by taking a variable step size as discussed in [45], [46].

c) Fractional open-circuit voltage (FOCV) technique

FOCV technique is based on the fact that the existence of an empirical relationship in between the maximum power point voltage, V_{mp} and open circuit voltage V_{oc} as given below [25], [26], [47]–[49].

$$V_{mp} \approx K_{oc}\, V_{oc} \tag{1.11}$$

where K_{oc} is a proportionality constant. Generally, K_{oc} can be determined by the empirical relationship in between V_{mpp} and V_{oc} under a wide range of solar radiations and temperatures. As reported in [25] the value of constant K_{oc} is in between 0.71 and 0.78. After determination of $K_{oc,}$ V_{mp} can be evaluated by using equation (1.11). In this technique, the $V_{oc\ is}$ measured periodically by disconnecting the load for a fraction of second. So, during disconnection of the load, a small amount of power is lost. To overcome this situation a pilot cell may be used to determine V_{oc}, as discussed in [50]. The characteristic of the pilot cell

should be identical as PV module. Moreover, the atmospheric condition of operation for both the PV cell and module should be alike. Implementation FOVC technique is very easy as it has no requirements of the complex control system and implementation cost also very low. The disadvantages of this technique are a loss of power during disconnection of the load, the requirement of the pilot cell and unreliability under partial shading condition.

d) Fractional short-circuit current (FSCI) technique

FSCI is based on the fact that the current at the maximum power point, I_{mpp} is proportional to the short circuit current, I_{sc} of the PV array at the given atmospheric condition [47], [51], [52], which is given as follows:

$$I_{mp} \approx K_{sc} I_{sc} \tag{1.12}$$

where K_{sc} is a proportionality constant. The value of K_{oc} is in between 0.78 and 0.92 as reported in [25]. I_{sc} is measured periodically by short-circuiting the PV array, then, I_{mp} is evaluated based on equation (1.12). In this scheme, an additional switch is required to make a short circuit of PV terminals for a moment. So, the component count increases and consequently the system cost also increases.

e) Curve-fitting technique

In this technique, the P-V characteristic of a PV module is modeled by using a polynomial function[53]–[55]. In the following example, the function has been represented by a third order polynomial as given below in equation (1.13). Higher order polynomials may be considered for better accuracy.

$$P = qV^3 + rV^2 + sV + t \tag{1.13}$$

where, q, r, s, t, are the coefficients of the polynomial and evaluated by sampling the PV power and voltage.

Differentiation of equation (1.13) yields

$$\frac{dP}{dV} = 3qv^2 + 2rv + s \tag{1.14}$$

Since, at maximum power point dP/dV = 0, the voltage at maximum power point can be evaluated from a solution of equation (1.14) as

$$V_{mp} = \frac{-r \pm \sqrt{r^2 - 3qs}}{3q} \quad (1.15)$$

Therefore, the voltage at MPP is calculated based on the coefficient values of each sample and a suitable controller can be used to force the difference between reference values of voltage as given by equation (1.15) and the actual voltage.

f) Ripple Correlation Control (RCC) Technique

When a PV module is connected to a power converter, the switching action of the converter introduces ripples of voltage and current into the PV array line. As a result, this produces ripple in the generated power of the PV system. The RCC technique utilizes these ripples to perform the MPPT algorithm [56]–[61]. RCC correlates dp/dt (i.e. time derivative of the time-varying PV power) with dv/dt or di/dt (i.e. time derivative of the time-varying PV voltage or current), to eventually force the power gradient to zero, thus ensuring operation at MPP. Although a boost topology based power converter is used in [56] to implement the RCC technique, any other topology can also be used. A simplified circuit diagram of a boost converter for RCC implementation is shown in Fig. 1.9. The voltage drop across the current sense resistor R_{CS} is used as a replica of the current I_{pv} in the control scheme.

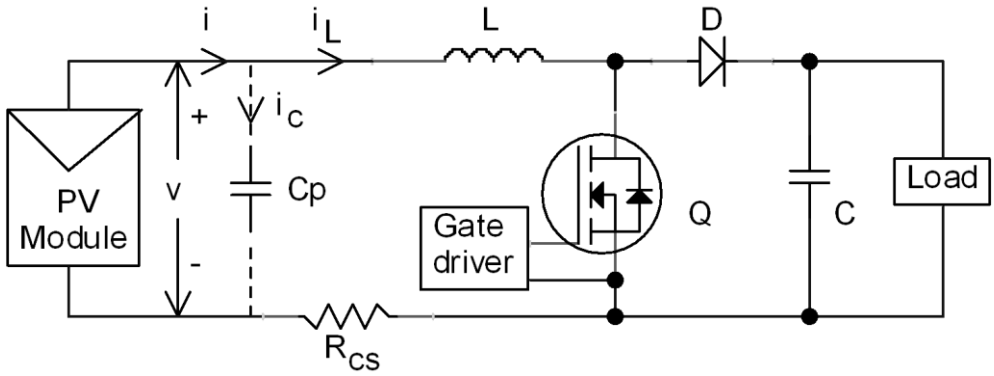

Fig. 1.9. Power circuit for realization of RCC technique in a boost converter

A PV cell has a parasitic capacitance which is formed due to the storage of charge across the junction of the cell. For a PV module, this capacitance can be modeled by placing an equivalent capacitance $C_{p,}$ across the module as shown in Fig. 1.9. In practice, along with $C_{p,}$ a capacitance is added to the input of the power converter. This capacitance causes a phase shift of power and current or voltage ripple which may adversely affect the RCC technique. For simplified analysis, we assume C_p of the module to be zero. This results in $i_L = i$.

In the discussions below, we use a symbol x′ to indicate the time derivative of a variable x. Referring to Fig. 1.10, when the PV voltage v is less than, more than or equal to the maximum power point voltage V_{mp}, a voltage ripple imposed along the curve leads to, respectively, an in-phase, out-of-phase or zero power ripple implying that the product p′v′ satisfies the following conditions

$$p'v' = 0 \text{ at the MPP } (V = V_{mp}) \tag{1.16}$$

$$p'v' > 0 \text{ at the left of MPP } (V < V_{mp}) \tag{1.17}$$

$$p'v' < 0 \text{ at the right of MPP } (V > V_{mp}) \tag{1.18}$$

Similar, but not identical, observations can be made and conditions can be obtained for the product p′i′. The conditions that replace equation (1.16) to equation (1.18) will lead to a slightly different circuit realization from the one that follows in Fig. 1.9.

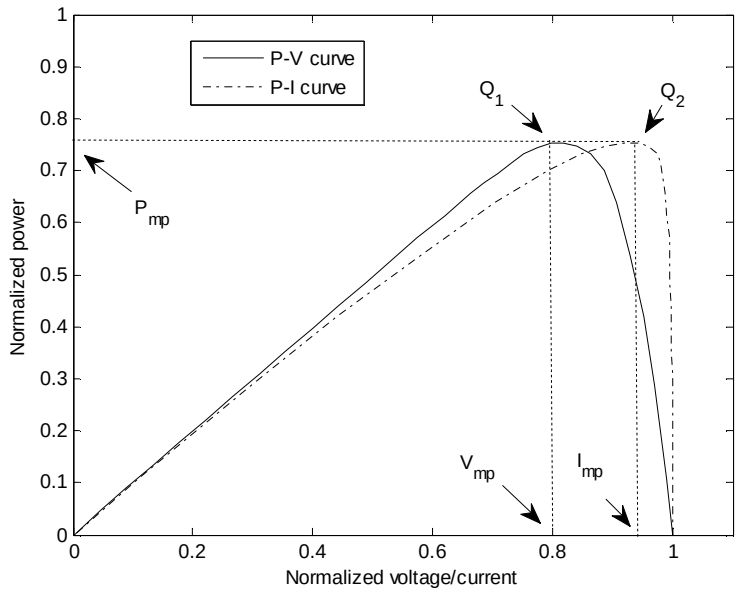

Fig. 1.10. Normalized P-I and P-V characteristics of a PV module

If the power converter uses the buck, boost or buck-boost topology, increasing the duty cycle increases the PV current, but decreases the PV voltage. It is assumed here that the PWM drive signal of the converter switch is generated by modulating a sawtooth carrier signal at the converter switching frequency by a modulating signal D(t). The signal D(t) can be produced in a simple way by observing the time integral of the product p′v′. If this integral is positive, the earlier argument dictates that the value of the converter duty cycle has to be

decreased so that the voltage V increases. On the other hand, if the integral is negative, the duty cycle has to be increased so that V decreases. In both of these cases the power peak point voltage V_{mp} corresponding to the point Q_1 is automatically reached in the steady-state. At this point, the value of the integrand p′v′ being zero, no further change of duty cycle occurs. The aforesaid arguments will lead to a very simple control strategy

$$D(t) = - k \int p'v'dt \qquad (1.19)$$

where k is a positive constant. A judicious choice of k gives rise to a fast converging yet stable system performance. An analog realization of equation (1.19), adapted from [56], is shown in Fig. 1.11.

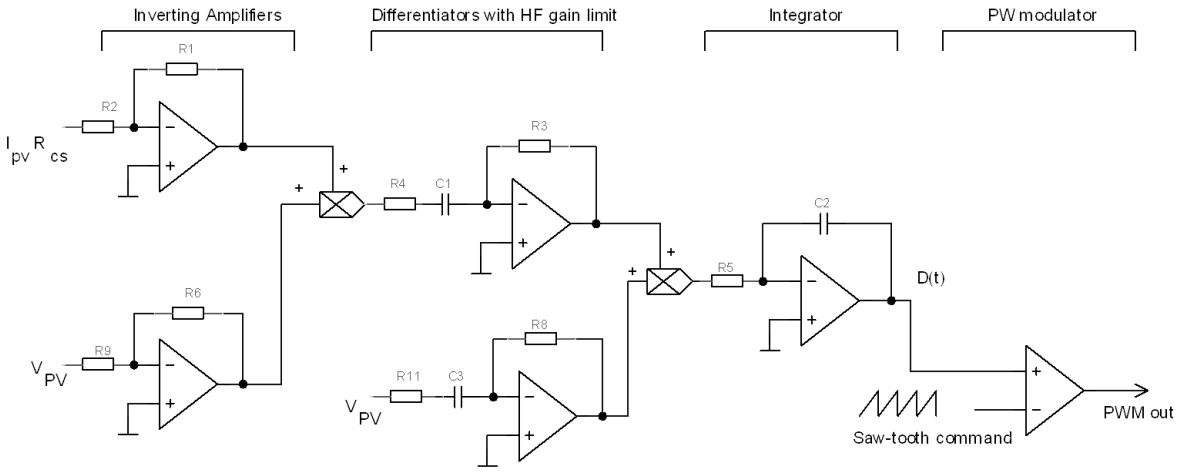

Fig. 1.11.Typical realization of the switch drive signal in an RCC circuit

As the ripple is inherently available in a switching converter, the artificial perturbation, necessary for the other methods, is not required in the RCC method. This method does not require any prior information about the PV array characteristic, thereby increasing its acceptability in any PV system. It also quickly tracks the MPP even under rapidly varying irradiance condition. Most of the RCC methods are implemented by using low-cost and simple analog circuits as given in [56], [59], [62]. In recent years, keeping in mind the advantages of the digital control systems, the RCC methods have also been implemented digitally as mentioned in [57], [58], [60], [61]. The disadvantages of RCC technique are low accuracy and instability at the high converter switching frequencies.

g) Fuzzy Logic Technique

Over the last three decades, fuzzy logic controllers (FLCs) have been widely used for the industrial applications due to their heuristic nature for both linear and non-linear systems[63]. The advantages of the FLCs over the conventional controllers as mentioned in [64], are 1) they are able to work with imprecise input, 2) they do not require accurate mathematical model 3) they have the ability to work with non-linear systems, 4) they are more robust than the conventional controllers. In recent years, fuzzy logic control has also been used to implement the MPPT algorithms [65]–[68]. Generally, three stages are used in the fuzzy logic control technique, namely, fuzzification, rule based table look up and defuzzification. In the fuzzification stage, the numerical input variables convert into the linguistic variables based on some membership functions that may be of symmetrical type as in [68] or of asymmetrical type as in [64], [69]. An asymmetric membership function as in [64] has been shown in Fig. 1.12. The membership functions are more compact around the center to give more impact to a specific fuzzy level. In Fig. 1.12 five fuzzy levels are chosen, viz., negative big (NB), negative small (NS), zero (ZE), positive small (PS) and positive big (PB). More than five fuzzy level may be used to increase the accuracy as seven fuzzy levels have been used in [70] and [71].

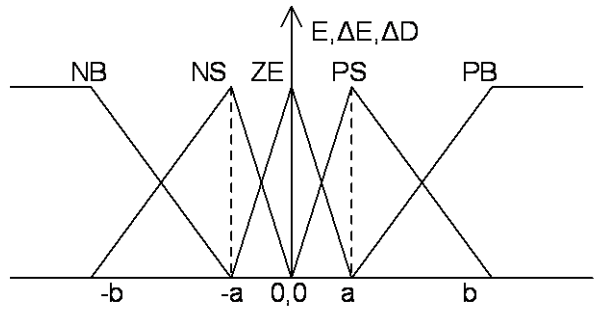

Fig. 1.12. Membership function for input and output of fuzzy logic controller

Generally, two inputs to the FLC for MPPT are an error E and a change in error ΔE (as shown in Fig. 1.12.). There are several techniques for calculating E and ΔE.

In [25], [72] authors used equations (1.20) and (1.21) to evaluate E and ΔE.

$$E[k] = \frac{p[k]-p[k-1]}{v[k]-v[k-1]} \quad (1.20)$$

and

$$\Delta E\,[k] = E\,[k] - E\,[k\text{-}1] \tag{1.21}$$

In the second stage, the fuzzy output is derived by using some rule base table as described in [29]. For an example, Table 1.2 can be used in any fuzzy logic based MPPT algorithm irrespective of the size and type of the converter.

Table 1.2. Rule base table for the fuzzy controller

E→ / ΔE↓	NB	NS	ZE	PS	PB
NB	NB	NS	NS	NS	ZE
NS	NS	NS	NS	ZE	PS
ZE	NS	NS	ZE	PS	PS
PS	PS	ZE	PS	PS	PS
PB	ZE	PS	PS	PS	PB

In the final stage called defuzzification, the output of the fuzzy logic controller is transformed from a linguistic variable using a similar membership function. The value of the numerical variable can be used to generate the change in duty cycle ΔD. Now, the output duty cycle can be evaluated by using equation (1.22). Block diagram of an FLC for the MPPT implementation is shown in Fig. 1.13.

$$D\,[k] = D\,[k\text{-}1] + \Delta D\,[k] \tag{1.22}$$

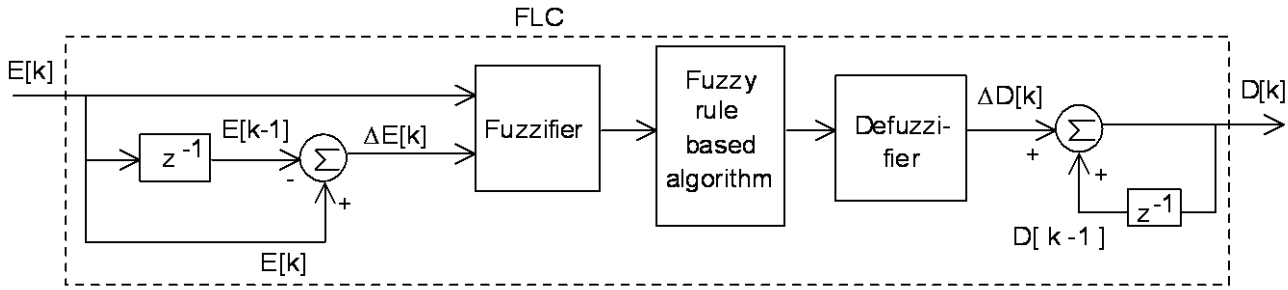

Fig. 1.13. Block diagram of FLC for the MPPT implementation

An adaptive fuzzy logic controller has been proposed in [71], where the membership functions and rule base tables are tuned in each sample interval. Fuzzy logic based MPPT technique has higher flexibility over conventional MPPT technique and also performs well under variable atmospheric condition. However, the accuracy of this technique depends on the prior knowledge and experience of the system designers. The disadvantage of this

technique is the requirement of more memory space for implementation in comparison to other MPPT techniques.

h) Artificial neural network technique:

In recent years, artificial neural networks (ANNs) have been used in the field of identification and control of the non-linear systems [73], [74]. ANN has several advantages like fast-tracking, robust operation, off-line tracking and non-linear mapping, high-speed response as mentioned in [75]. Therefore, the ANN algorithm can be applied in MPPT technique [75]–[82]. ANN technique normally has three layers viz., input, hidden and output as shown in Fig. 1.14.

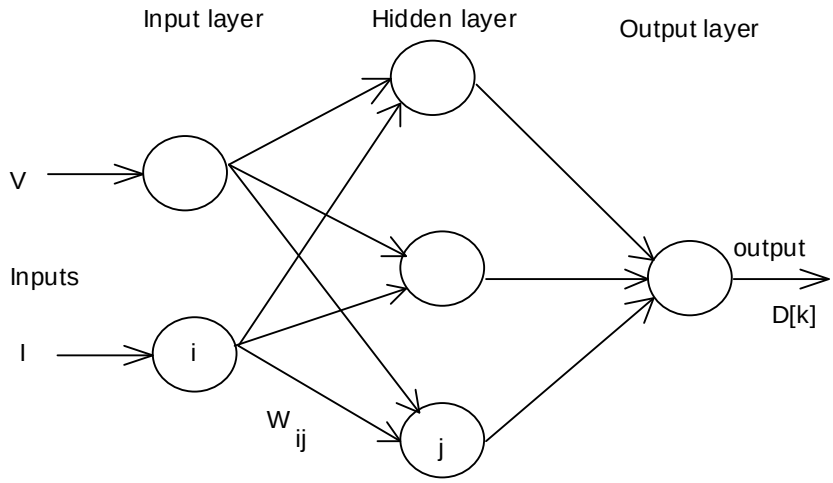

Fig. 1.14. A typical artificial neural network for MPPT technique

The number of nodes in each layer depends on the system designer. In this case, the input variables to the controller can be electrical and non-electrical types. The electrical parameters of the PV module such as PV array current (I_{PV}), voltage (V_{PV}), power (P_{PV}), short-circuit current (I_{SC}), open-circuit voltage (V_{OC}) are used as input [75], [77], [83]. On the other hand, non-electrical parameter like irradiance, temperature are used in [44],[64], [75]. Several studies have also used a combination of both electrical and non-electrical variables as input [84]–[86]. An ANN system may have one or several output(s). For the MPPT algorithm usually, the duty cycle is used as an output signal to drive the semiconductor switches of the converter. This technique is also capable to produce the duty cycle D[k] as an output variable. The closeness of the operating point to the MPP depends on the hidden layer and how well the network has been trained. As shown in Fig. 1.14, the link between ith and jth nodes has a

weight of w_{ij}. The weighting factors of the link should be carefully determined through a training process. As the PV module has different I-V characteristics an ANN has to be trained specifically for which it will be used. Hence, the cost of an ANN-based MPPT technique is high compared to other MPPT methods.

i) Load voltage or load current maximization technique:

The most of the MPPT techniques discussed so far, the controller sensed the input current, i_{in} and input voltage, v_{in} to the power converter to implement the MPPT algorithms. Alternatively, maximization of the output power (by sensing the output voltage, v_{out} and/or output current i_{out} of the converter) could be used to extract the maximum power from a PV module assuming a lossless power converter, as given in [87]–[92]. A simplified block diagram of the load current or the load voltage maximization technique has been given in Fig. 1.15. Although two sensors are shown at the output of the converter to show their location, only one will be needed, as described below.

For a near-constant voltage type load (such as a battery), the load current maximization will lead to extraction of maximum power from a PV module. Likewise, for a constant current type load, the load voltage maximization will lead to extraction of maximum power from a PV module. If the load is of constant resistance type, either voltage or current can be maximized to achieve the same goal. So, in these cases, a single sensor, either for voltage or for current, can be employed to implement the MPPT algorithm. Thus, this technique reduces the hardware as well as software complexity.

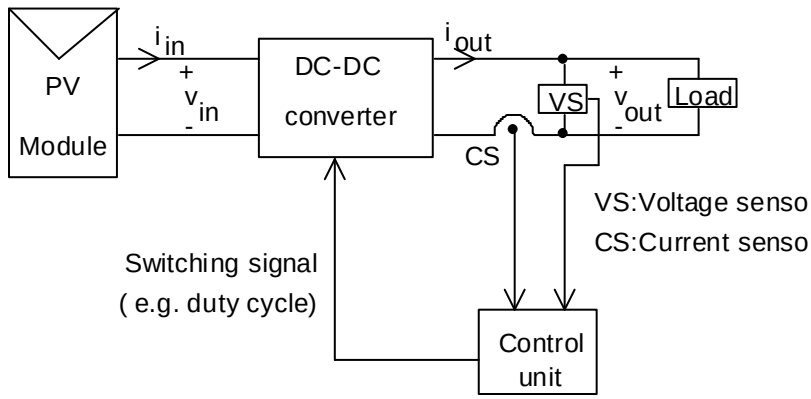

Fig. 1.15. Simplified block diagram of load current or load voltage maximization technique

The literature survey reveals that most of the MPPT techniques have been concentrated on maximizing the output power of the PV array. However, a more rational approach for the case of battery charging systems should be the maximization of the input power to the battery. This thesis thus aims to investigate whether the MPPT technique could be implemented to the output of the converter under variable insolation and temperature conditions. A detailed description of hardware and software implementation of this technique, as used in the present study, is given in Chapter 3.

1.7.2 LED driver

An LED driver is a self-contained power supply which has an output that matched to the electrical characteristics of the LED or LED string. The LED driver can be subdivided into two categories – AC supply driven and DC supply driven. We do not review the former variety because it is outside the scope of our present study. It is known that LED current is decided by two parameters, namely the threshold voltage V_γ and the incremental resistance r_d of the diode. Neither of these two parameters are constant for an LED of a given type. For a simplified two-part, piece-wise linear model the forward current I_F is related to the forward applied supply voltage V_S by the equation (1.23)

$$I_F = \frac{V_S - V_\gamma}{r_d} \quad \text{for } V_S > V_\gamma \qquad (1.23)$$

$$= 0 \quad \text{for } V_S < V_\gamma$$

The above equation indicates that the value of the forward current I_F for a given supply voltage V_S varies widely for two reasons. Firstly, the threshold voltage V_γ is a monotone decreasing function of the junction temperature and secondly, the value of the incremental resistance r_d has a wide unit to unit variation [93]. Characteristic of an LED lamp is voltage sensitive in the sense that for voltages below the threshold value the current is negligibly small. On the other hand, for voltages above this current increases vary rapidly. This has been approximated by the model described above equation 1.23. A slight increase of the applied voltage may cause an abrupt increase in current that may damage the LED permanently.

The strong temperature dependence of V_γ can be reduced by adding an external resistance, R_E in series with the LED. Hence, equation (1.23) can be modified as

$$I_F = \frac{V_S - V_\gamma}{r_d + R_E} \qquad (1.24)$$

Therefore, the simplest way to drive an LED from a constant-voltage (CV) source is by using a current limiting resistance as shown in Fig. 1.16. However, addition of R_E causes a loss of voltage $I_F R_E$ from the supply voltage VS. This causes a drop of efficacy of the LED.

A constant current (CC) LED driver circumvents the demerits of a CV driver. Such a driver can drive the LED at the rated current irrespective of the variations in threshold voltage, LED junction temperature and LED supply voltage. Hence, a CC driver is always recommended over the CV driver [93]–[98]. CC LED drivers with different topologies are available in the existing literature [99]–[106].

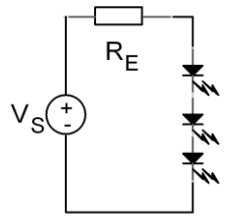

Fig. 1.16. A simple contant-voltage (CV) LED driver.

A simple low-side linear regulator example circuit for constant current (CC) driver has been shown in Fig. 1.17. The current through the LED series string is kept constant by dropping a part of the supply voltage V_F by means of N-channel MOSFET whose gate-to-source voltage V_{GS} is adjusted automatically. For a constant current of, say, 350mA the drop across current sensing resistor R_{cs}, with a value 1ohm, has a value of 350mV. This is compared with a 350mV reference in an error amplifier. Any increase of LED current due to an increase in supply voltage or decrease of the LED threshold voltage is followed by an increase of the input voltage to the inverting input of the error amplifier. This leads to a drop in the value of V_{GS} which, in turn, brings back the value of current to desired value. However, the method suffers from a major disadvantage. The drop across the drain and source terminals of the series-pass MOSFET causes a power loss. This loss is a considerable fraction of the electrical power input to the LED and this reduces the efficiency of the whole circuit. Also, a linear current regulator may require a bulky heat sink to dissipate the extra power. The above example shows the necessity of a non-dissipative or ‘switch-mode’ current regulator.

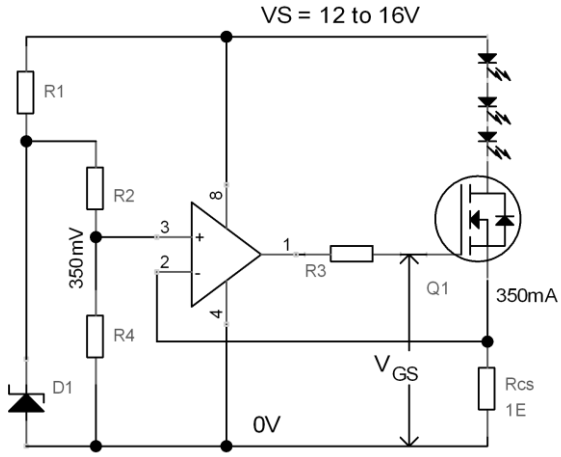

Fig. 1.17. A constant current (CC) linear LED driver

A simplified example of a switch mode current regulator is shown in Fig. 1.18. The MOSFET series switch Q1, instead of operating in linear mode, is either on or off. The drop V_{cs} across the current sense resistor decides the on or off state of the switch. The controller works on a hypothetical reference voltage V_{ref}, which is the product of the desired LED output current I_{ref} and R_{cs}. At the start, the Q1 is on and the LED current I increases according to the following equation

$$\frac{di}{dt} = \frac{V_s - V_F}{L_1} \tag{1.25}$$

where V_s and V_F are the values of supply voltage and LED forward drop, respectively. The current increases at the rate given above till V_{cs} reaches an upper threshold of, say, 1.02 V_{ref}. The controller output then turns off Q1. The current now continues through the freewheel diode D1 according to the following equation.

$$\frac{di}{dt} = -\frac{V_F}{L_1} \tag{1.26}$$

The negative sign in equation (1.26) indicates that the LED current decreases in this interval. It will continue to do so till V_{cs} reaches a lower threshold of, say, 0.98 V_{ref}. Attainment of this threshold will again turn on Q1. This cycle is repeated continuously keeping the instantaneous value of current within 0.98 I_{ref} and 1.02 I_{ref} Thus the average current will remain at I_{ref} with an associated peak-to-peak ripple of 4%. Due to negligible power loss in the MOSFET during both the on-and-off states the efficiency of the circuit remains very high as compared to the linear current regulator. Though, the linear current regulators are cost-effective solutions for low power application as they do not require any additional storage element such as a capacitor or inductor.

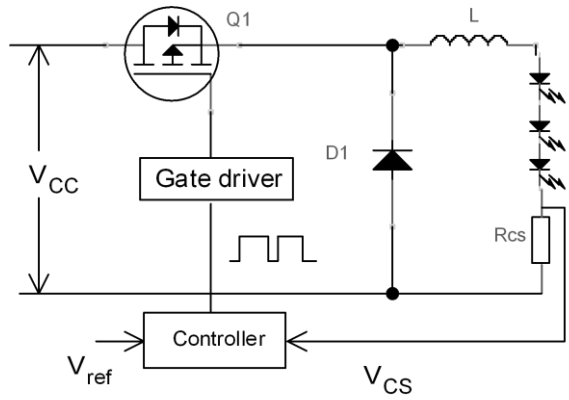

Fig. 1.18. A switch-mode constant current (CC) LED driver

In this study, a PWM dimmable LED driver (based on linear regulator) for tunable-CCT outdoor lighting system (TCOLS) and a three-step dimmable LED driver (based on switch mode regulator) for fixed-CCT outdoor lighting system (FCOLS) have been developed. A detailed description of hardware implementation, as used in the present study, is given in Chapter 4.

1.7.3 Wireless communication

Wireless communication is used to transfer data between two or more points, without any physical connection. In 1901, Guglielmo Marconi first demonstrated the transatlantic wireless signal at Signal Hill, St. John's, Newfoundland [107], [108]. The letter "S" was first transmitted and received by "mercury coherer" detector in series with a telephone. This novel wireless detection device was also invented by Sir Jagadish Chandra Bose of Presidency College, Kolkata, India. Almost simultaneously, Bose also invented seminal results on radio and microwave communication [107] [109]. He influenced other inventors trying to develop the radio wave as a communications medium [110], [111]. Since then, wireless communication has evolved into an essential element of modern society. The major advantages of a wireless network over the wired network are

- Lower cost: Wireless networks are cost-effective to install and maintain.
- Flexibility: Radio wave can travel freely through the air, so, any device can communicate irrespective of their location within a certain range.

- Scalability: Expansion of the wired network is costly and difficult to add new cables or reroute the existing cable, on the other hand, expansion of the wireless system is very easy.

- Reliability: In wireless communication system chances of communication failure is less as no cables are used.

Considering the advantages of wireless communication, it has become the dominant technology in the communication industry. A simplified realization of a wireless communication system is shown in Fig. 1.19.

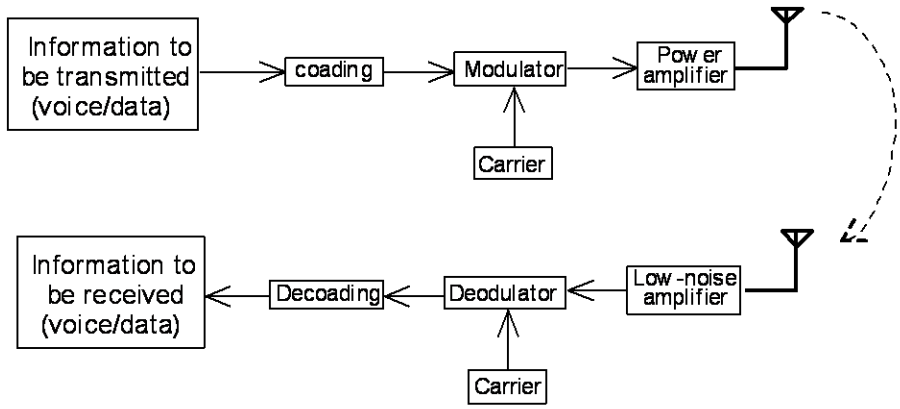

Fig. 1.19. Simplified realization of a wireless communication system

There are several research studies for remote control and/or monitoring system based on wireless communication technologies. The research carried out in this field can be broadly classified into the following categories:

A) Global System for Mobile Communication (GSM) based monitoring and/or control through Short Message Service (SMS).

B) Internet-based monitoring and/or control through General Packet Radio Service (GPRS).

C) Wireless monitoring and/or control using low-power wireless communication standards such as ZigBee, Wi-Fi, Bluetooth, IrDA, any other RF technologies.

D) Any combination of the aforementioned wireless technologies.

The recent research finding indicates that these types of wireless monitoring and/or controlling systems have a huge application areas such as home automation [112], [113],

security systems [114], industries[115]–[117], smart grids[118], lighting control[119], irrigation system[120], healthcare[121], [122] and so on.

In this proposed study, remote health monitoring and control of the solar-powered OLS are important issues, as the OLSs are usually installed outdoors or sometimes far away from a locality. Some of the research studies used low-power wireless communication technologies such as ZigBee, Wi-Fi, Bluetooth to monitor and/or control the lighting systems as well as the other systems [117], [123]–[126]. In recent years, wireless sensor networks (WSNs) have also gained popularity for monitoring and tracking, particularly after the advancement of micro-electro-mechanical-system (MEMS) [127]–[129]. A sensor network has a large number of sensor nodes with a wireless interface for communication with each other within a short distance. Ultimately, the network gathers the information to a central location for processing. Generally, WSNs use low-power wireless communication technologies such as ZigBee, Wi-Fi, Bluetooth for monitoring as mentioned in [123], [130], [131]. These technologies do not require any license for the spectrum use, though they suffer from the limited coverage range. Most of this wireless technology can monitor the system with a distance between 0 to 100 m [132]. Though in this study, we have considered to monitor and control a lighting system which may be placed several 100m from the central station. So, alone low-power wireless communication technology cannot serve the purpose of this study. This distance problem can be solved by using several repeaters at every few hundred meters apart, then continue through other communication lines. In this case, the cost and complexity of the communication network system will be high and also it will reduce the reliability of the system.

To solve the above problem, a GSM or GPRS based communication system may be used. GSM represents the second generation (2G) network technology, which was introduced in 1991 for the major use of voice communication. Over the last two decades, cellular phones have experienced exponential growth as it becomes an integrated part of our daily lives. As of 2017, the number of people connected to the mobile services surpassed 5 billion globally [133]. Thus, throughout the globe, two out of three people had a mobile subscription. In the last two decades, to provide service to the subscribers, the infrastructure of GSM network has significantly increased. So, without building the additional wireless network, readily available GSM network is a great choice to transmit/receive data to/from the remote locations. Similarly, GPRS technology (often termed as 2.5G technology) has also been used for controlling and/or monitoring of systems, depending upon the specific application area. In

general, GPRS is most suitable for the implementation that requires real-time monitoring, internet connectivity and higher data rate. The cost of the GPRS service and modem is higher compared to GSM technology, as real-time, packet-based data transfer at higher-rate is available in GPRS.

In this study, monitoring of the system parameters once a day is enough to take a prompt decision about the health of the lighting system. So, GSM-based SMS service is an excellent choice to serve the purpose of this study. The SMS can reach to all the locations at an affordable price. Also in GSM technology, SMS is the most convenient to understand for the general user. The other advantage of the GSM network is its high security, so the information transmitted or received through this network cannot be monitored by an eavesdropper.

In the last two decades, a lot of research work has been carried out on the use of SMS over GSM network. We reviewed some remote control and/or monitoring schemes based on GSM-SMS service which is the most relevant and affordable communication technology for this study as discussed below.

In [134], a GSM-SMS based intelligent control system has been developed and implemented for remote oil-well health monitoring and automatic oil-pumping control. This system can diagnose the nine most important oil-well malfunctions. After completion of malfunction detection, it can send the nature of fault to the handset of maintenance parsonel through SMS.

In [112], a home automation system has been proposed based on three remote controlling methods, they are GSM network, internet and speech. GSM network and internet are used to control the home appliances from the remote places, whereas the speech based control is used when the users are inside the house. Interactive software has been developed for Java-enabled mobile, which will allow the user to control and monitor any home appliances through SMS.

In [118], the authors proposed a GSM-based embedded system for monitoring and control of the smart grid. The system can monitor the load conditions of the smart grid. It will automatically shut down if the load increases beyond the rated capacity and inform the operator by sending an SMS through GSM network. It can also monitor the temperature of the devices present in the system.

A GSM-based street light control and monitoring system are designed and implemented in [135]. Every light pole has a single current sensor. If any fault detected in the system, it

will immediately send an SMS to the base station through the GSM network. So, fault detection and maintenance of the system will be very easy compared to the conventional system.

In [136], the authors describe the remote monitoring and control of a stand-alone PV plant. In general, the system records the different PV parameters and periodically sends the information to the remote station through the GSM-SMS service. In case of abnormal behavior, the system can immediately inform the operator through SMS. Based on this information, the operator can modify some elements and measurement setting of the plant from the remote place.

In this implementation, GSM-SMS technology has been used for monitoring and control of the remote outdoor lighting system. Details of the communication system are described in Chapter 5.

1.7.4 CCT controllable LED light

In order to explain the significance of the developed CCT control technique, a review of the existing techniques to produce tunable-CCT LED lighting system is provided in this section. Currently, LED based white light is produced either from a blue or a near-ultraviolet emitting chip coated with a suitable yellow phosphor, or by mixing of light from multiple monochromatic chips, usually, red, green and blue (RGB) [93]. In some of the previous studies, light from monochromatic red-green-blue (RGB) LEDs [137], [138] or red-green-blue-amber (RGBA) LEDs [139] were mixed to get different colour combination of white shade. These types of LED systems have some disadvantages like poor colour rendering index (CRI), chromaticity shifts [140] and requirement of three or more Pulse-Width Modulated (PWM) output channels. It is reported that the chromaticity shift for phosphor coated LED (PC-LED) system is less than that of the mixed-colour RGB LED (MC-LED) system, during similar dimming by both continuous current reduction and PWM method [140]. Also this type of LED system uses three (for RGB) [137], [141] or four (for RGBA) [139] independent converters to supply power as described by the authors. To resolve the issue, we are using a single constant voltage Power supply to drive multiple LED strings with individually programmable constant amplitude PWM current, which also increases the power density. Chromaticity of the RGB LED also shifts due to LED junction temperature variation [141], [142] and aging [143]. But the use of an MC-LED System allows the user to have dynamic control of colour and a life longer than that of a PC-LED system.

Tunable-CCT light sources have also been implemented by blending cool-white (CW) and warm-white (WW) LED sources [144]–[147]. A number of commercial, tunable LED lighting products e. g. Lutron® [148] , LuxiTune™ [149] are also available. Lutron® from Philips provides three types of colour tuning techniques, namely 'dim to warm', 'tunable white' and 'full colour tuning' [148]. In tunable white mode warm white (3000K) and cool white (5000K) LED are used to provide different colour temperatures ranging from 3000K to 5000K. In this mode colour temperature and intensity of the fixture are not completely independent as specified in the application note. LuxiTune™ from LED Engin is a tunable white light engine solution, with two tuning modes - Warm Dimming and CCT Tuning. CCT can be varied in the range 4300K - 2100K and 3000K - 1600K in CCT tuning mode and warm dimming mode respectively [149]. In such systems, the CRI can be greatly improved, but the CCT of the produced light is limited to a range between that of CW and WW LEDs. However, work on wide range CCT- and illuminance- tunable light sources, based on two-channel drive, have not been reported.

Precise colour control of PC white LED or RGB (red-green-blue) colour mixing LED system is still a challenging job for the lighting industry[137], [142], [150]. As luminous intensity and colour outputs of LED are influenced by LED junction temperature variation, which is caused by self-heating of the LED and ambient temperature variation, it has been suggested that a proper junction temperature compensated control strategy should be implemented to stabilize the luminous intensity as well as the colour of LED [142], [151], [152]. Various researchers proposed different control structures based on LED junction temperature feedback, light flux feedback, colour coordinate feedback or a combination of these techniques [137], [145], [153]. Use of external sensors, which is mandatory for flux feedback and colour coordinate feedback, increases the complexity and overall cost of the system. Sensor placement and regular calibration of sensors are important issues which may not be acceptable in all applications. In some previous studies, the junction temperature of an LED is estimated as a function of its heatsink temperature [142] or LED operating temperature [154]. However, when multiple LEDs are mounted on a common heatsink, the junction temperature of a particular LED is not only a function of the heatsink temperature but also of the power dissipation of the neighboring LEDs.

A detailed description of hardware and software implementation of wide-range CCT and illuminance control technique, as used in the present study, is given in Chapter 4. In this implementation, LED junction temperature has been estimated from the average forward drop

of the LED string. A model to evaluate the luminous parameters has also been presented in Chapter 4.

1.8 Scope of the thesis

This thesis describes a solar-powered outdoor lighting system with wireless remote control and monitoring facility. Most of the existing outdoor light lighting systems suffer from the shortcomings which are already been discussed in Section 1.6. This fact motivates to develop and integrate the several technological possibilities in the outdoor lighting system. A brief chapter-wise organization of the thesis is presented below.

Chapter 1 of the thesis describes the problems associated with the existing outdoor lighting system. The advantages of solar energy and LED for outdoor lighting applications are presented. A detailed literature survey based on the research area is also described in this chapter.

Chapter 2 devoted a broad outline of the solar-powered outdoor lighting system which is developed in this work. Some fundamental principle of solar photovoltaic system related to this work is also presented. A step-wise design procedure of a stand-alone solar electric system is described. Based on this calculation, the rating of system components have been chosen for the prototype.

Chapter 3 explores into the development of a solar-powered multi-stage battery charging system. The hardware, software and operation of the developed VRLA battery charging system are presented and explained. A novel MPPT-based bulk charging technique is described and implemented. To validate the multi-stage algorithm, the tracking behavior of the MPPT algorithm under variable irradiance and corresponding experimental results are also presented.

Chapter 4 presents the development of a dimmable, tunable-CCT and fixed-CCT LED lighting system. Based on a simple mathematical foundation, the design and operation of an LED lamp with wide-range CCT and illuminance control capability using two-component colour blending have been presented. The circuit diagram and operating principle of the developed LED drivers are also explained. This chapter ends with the experimental results to validate the performance of the CCT and illuminance control system. For the tunable-CCT lighting system, a comparison with the ANSI standard is also presented.

Chapter 5 describes the implementation of wireless monitoring and control of the outdoor lighting system. The software for wireless monitoring and control system is explained by using different flowcharts. Different health monitoring schemes for outdoor lighting system is also presented.

Finally, **Chapter 6** presents the concluding remarks and future scope of research. The limitations of the developed system are also discussed.

References

[1] J. B. Murdoch, *Illumination Engineering—From Edison's Lamp to Laser*, 1 st. New York: Macmillan Publishing Company, 1985.

[2] L. R. Brown, "World Electricity Consumption for Lighting By Sector and Potential Electricity Savings," *PhD Propos.*, vol. 1, p. 7, 2005.

[3] REN21, *Renewables 2017: global status report*, vol. 72, no. October 2016. 2017.

[4] "Solar Panel Cost Trends (Tons of Charts)." [Online]. Available: https://cleantechnica.com/2014/09/04/solar-panel-cost-trends-10-charts/. [Accessed: 27-May-2019].

[5] C. S. SOLANKI, *Solar Photovoltaics - fundamentals technologies and applications*. 2016.

[6] "Year End Review 2017 –MNRE." [Online]. Available: http://pib.nic.in/newsite/PrintRelease.aspx?relid=174832. [Accessed: 14-Mar-2019].

[7] U.S. Department of Energy, "Exterior Lighting Guide," *Guide*, p. 38, 2010.

[8] K. W. Houser, "The LED Surprise," *LEUKOS - J. Illum. Eng. Soc. North Am.*, vol. 11, no. 3, p. 107, 2015.

[9] M. Cole, H. Clayton, and K. Martin, "Solid-state lighting: The new normal in lighting," *IEEE Trans. Ind. Appl.*, vol. 51, no. 1, pp. 109–119, 2015.

[10] J. K. Kim and E. F. Schubert, "Transcending the replacement paradigm of solid-state lighting," *Opt. Express*, vol. 16, no. 26, p. 21835, 2008.

[11] M. Richards, P. Boyce, and S. Fotios, "Road lighting and energy saving," *Light. Res. Technol.*, vol. 41, no. 3, pp. 245–260, 2009.

[12] O. Rabaza, F. Aznar-Dols, M. J. Mercado-Vargas, and A. Espín-Estrella, "A new method of measuring and monitoring light pollution in the night sky," *Light. Res. Technol.*, vol. 46, no. 1, pp. 5–19, 2014.

[13] M. S. Rea and A. Bierman, "Spectral considerations for outdoor lighting: Consequences for sky glow," *Light. Res. Technol.*, vol. 47, no. 8, pp. 920–930, 2015.

[14] "DOE Publishes Report on LED Street Lighting's Impact on Sky Glow | Department of Energy." [Online]. Available: https://www.energy.gov/eere/ssl/articles/doe-publishes-report-led-street-lighting-s-impact-sky-glow. [Accessed: 14-Mar-2019].

[15] L. Bellia, F. Bisegna, and G. Spada, "Lighting in indoor environments: Visual and non-visual effects of light sources with different spectral power distributions," *Build. Environ.*, vol. 46, no. 10, pp. 1984–1992, 2011.

[16] W. van Bommel and G. van den Beld, "Lighting for work: a review of visual and biological effects," *Light. Res. Technol.*, vol. 36, no. 4, pp. 255–266, 2004.

[17] CIE and T. R. 158, "Ocular lighting effects on human physiology and behaviour," 2004.

[18] K. C. Lin and C. S. Lin, "The study of a novel control method of the mood lighting emulator," *Opt. Commun.*, vol. 350, pp. 71–76, 2015.

[19] R. S. McCloughan, C. L. B., Aspinall, P. A., & Webb, "The impact of lighting on mood," *Int. J. Light. Res. Technol.*, 1999.

[20] S. Jain and V. Agarwal, "A new algorithm for rapid tracking of approximate maximum power point in photovoltaic systems," *IEEE Power Electron. Lett.*, vol. 2, no. 1, pp. 16–19, 2004.

[21] C. Hua and J. Lin, "Fully digital control of distributed photovoltaic power systems," *ISIE*

2001. 2001 IEEE Int. Symp. Ind. Electron. Proc. (Cat. No.01TH8570), vol. 1, pp. 1–6, 2001.

[22] N. Femia, G. Petrone, G. Spagnuolo, and M. Vitelli, "Optimization of perturb and observe maximum power point tracking method," *IEEE Trans. Power Electron.*, vol. 20, no. 4, pp. 963–973, 2005.

[23] N. S. D'Souza, L. A. C. Lopes, and X. J. Liu, "An intelligent maximum power point tracker using peak current control," *PESC Rec. - IEEE Annu. Power Electron. Spec. Conf.*, vol. 2005, pp. 172–177, 2005.

[24] A. K. Abdelsalam, A. M. Massoud, S. Ahmed, and P. N. Enjeti, "High-Performance Adaptive Perturb and Observe MPPT Technique for Photovoltaic-Based Microgrids," vol. 26, no. 4, pp. 1010–1021, 2011.

[25] T. Esram and P. L. Chapman, "Comparison of Photovoltaic Array Maximum Power Point Tracking Techniques," *IEEE Trans. Energy Convers.*, vol. 22, no. 2, pp. 439–449, 2007.

[26] B. Subudhi and R. Pradhan, "A Comparative Study on Maximum Power Point Tracking Techniques for Photovoltaic Power Systems," *Sustain. Energy, IEEE Trans.*, vol. 4, no. 1, pp. 89–98, 2013.

[27] T. Shimizu, O. Hashimoto, and G. Kimura, "A novel high-performance utility-interactive photovoltaic inverter system," *IEEE Trans. Power Electron.*, vol. 18, no. 2, pp. 704–711, 2003.

[28] W. J. a. Teulings, J. C. Marpinard, a. Capel, and D. O'Sullivan, "A new maximum power point tracking system," *Proc. IEEE Power Electron. Spec. Conf. - PESC '93*, pp. 1–6, 1993.

[29] M. Veerachary, T. Senjyu, and K. Uezato, "Maximum power point tracking control of IDB converter supplied PV system," *IEE Proc. - Electr. Power Appl.*, vol. 148, no. 6, p. 494, 2001.

[30] W. Xiao and W. G. Dunford, "A modified adaptive hill climbing MPPT method for photovoltaic power systems," *PESC Rec. - IEEE Annu. Power Electron. Spec. Conf.*, vol. 3, pp. 1957–1963, 2004.

[31] M. I. Bahari, P. Tarassodi, Y. M. Naeini, A. K. Khalilabad, and P. Shirazi, "Algorithm For PhotoVoltaic Application," pp. 1041–1044, 2016.

[32] S. a Abuzed, M. P. Foster, and D. a Stone, "Variable PWM step-size for modified Hill climbing MPPT PV converter," *7th IET Int. Conf. Power Electron. Mach. Drives*, pp. 1–6, 2014.

[33] C. Carvalho, "A Step-up μ-Power Converter for Solar Energy Harvesting Applications , using Hill Climbing Maximum Power Point Tracking," *Sol. Energy*, pp. 1924–1927, 2011.

[34] P. J. Wolfs and L. Tang, "A single cell maximum power point tracking converter without a current sensor for high performance vehicle solar arrays," *PESC Rec. - IEEE Annu. Power Electron. Spec. Conf.*, vol. 2005, pp. 165–171, 2005.

[35] A. Pandey, N. Dasgupta, and A. K. Mukerjee, "High-performance algorithms for drift avoidance and fast tracking in solar MPPT system," *IEEE Trans. Energy Convers.*, vol. 23, no. 2, pp. 681–689, 2008.

[36] L. Piegari and R. Rizzo, "Adaptive perturb and observe algorithm for photovoltaic maximum power point tracking," *IET Renew. Power Gener.*, vol. 4, no. 4, p. 317, 2010.

[37] Y. Hsiao and C. Chen, "Maximum power tracking for photovoltaic power system," *Conf. Rec. 37th 2002 IEEE Ind. Appl. Conf.*, vol. 2, no. FEBRUARY 2002, pp. 1035–1040, 2002.

[38] A. F. Boehringer, "Self-Adapting dc Converter for Solar Spacecraft Power Supply," *IEEE Trans. Aerosp. Electron. Syst.*, vol. AES-4, no. 1, pp. 102–111, 1968.

[39] H. Al-Atrash, I. Batarseh, and K. Rustom, "Effect of measurement noise and bias on hill-

climbing MPPT algorithms," *IEEE Trans. Aerosp. Electron. Syst.*, vol. 46, no. 2, pp. 745–760, 2010.

[40] K. Kobayashi, I. Takano, and Y. Sawada, "A study of a two stage maximum power point tracking control of a photovoltaic system under partially shaded insolation conditions," *Sol. Energy Mater. Sol. Cells*, vol. 90, no. 18–19, pp. 2975–2988, 2006.

[41] W. W. W. Wu, N. Pongratananukul, W. Q. W. Qiu, K. Rustom, T. Kasparis, and I. Batarseh, "DSP-based multiple peak power tracking for expandable power system," *Eighteenth Annu. IEEE Appl. Power Electron. Conf. Expo. 2003. APEC '03.*, vol. 1, no. C, pp. 525–530, 2003.

[42] E. Koutroulis, K. Kalaitzakis, and N. C. Voulgaris, "Development of a microcontroller-based, photovoltaic maximum power point tracking control system," *Power Electron. IEEE Trans.*, vol. 16, no. 1, pp. 46–54, 2001.

[43] N. Chettibi, A. Mellit, and M. Drif, "FPGA-Based implementation of IncCond algorithm for photovoltaic applications," *Proc. Int. Conf. Microelectron. ICM*, no. Icm, pp. 0–3, 2012.

[44] B. Liu, S. Duan, F. Liu, and P. Xu, "Analysis and Improvement of Maximum Power Point Tracking Algorithm Based on Incremental Conductance Method for Photovoltaic Array," *2007 7th Int. Conf. Power Electron. Drive Syst.*, 2007.

[45] J. M. Enrique, J. M. Andújar, and M. A. Bohórquez, "A reliable, fast and low cost maximum power point tracker for photovoltaic applications," *Sol. Energy*, vol. 84, no. 1, pp. 79–89, 2010.

[46] and Y. K. F. Liu, S. Duan, Fei Liu, B. Liu, "A Variable Step Size INCMPPT Method for PV Systems," *IEEE Trans. Ind. Electron.*, vol. 55, no. 7, pp. 2622–2628, 2008.

[47] M. a. S. Masoum, H. Dehbonei, and E. F. Fuchs, "Theoretical and experimental analyses of photovoltaic systems with voltageand current-based maximum power-point tracking," *IEEE Trans. Energy Convers.*, vol. 17, no. 4, pp. 514–522, 2002.

[48] H.-J. N. H.-J. Noh, D.-Y. L. D.-Y. Lee, and D.-S. H. D.-S. Hyun, "An improved MPPT converter with current compensation method for small scaled PV-applications," *IEEE 2002 28th Annu. Conf. Ind. Electron. Soc. IECON 02*, vol. 2, pp. 1113–1118, 2002.

[49] B. Subudhi and R. Pradhan, "Characteristics evaluation and parameter extraction of a solar array based on experimental analysis," *2011 IEEE Ninth Int. Conf. Power Electron. Drive Syst.*, no. December, pp. 5–8, 2011.

[50] G. W. Hart, H. M. Branz, and C. H. Cox, "Experimental tests of open-loop maximum-power-point tracking techniques for photovoltaic arrays," *Sol. Cells*, 1984.

[51] T. Noguchi, S. Togashi, and R. Nakamoto, "Short-current pulse based adaptive maximum-power-point tracking for photovoltaic power generation system," *ISIE2000 Proc. 2000 IEEE Int. Symp. Ind. Electron. Cat No00TH8543*, vol. 1, no. 1, pp. 65–72, 2000.

[52] N. Mutoh, T. Matuo, K. Okada, and M. Sakai, "Prediction-data-based maximum-power-point-tracking method for photovoltaic power generation systems," *Power Electron. Spec. Conf. 2002. pesc 02. 2002 IEEE 33rd Annu.*, vol. 3, pp. 1489–1494 vol.3, 2002.

[53] A. Mohamed, N. Amin, and K. Sopian, "An Efficient Maximum Power Point Tracking Controller for Photovoltaic," vol. 5, no. 2, pp. 53–63, 2010.

[54] A. M. Farayola, A. N. Hasan, and A. Ali, "Curve Fitting Polynomial Technique Compared to ANFIS Technique for Maximum Power Point Tracking," no. Irec, pp. 0–5, 2017.

[55] S. Maharjan, J. C. H. Peng, and W. Xiao, "Improved Deterministic Real-Time Estimation of Maximum Power Point in Photovoltaic Power Systems," pp. 1–4, 2015.

[56] T. Esram *et al.*, "Dynamic Maximum Power Point Tracking of Photovoltaic Arrays Using Ripple Correlation Control," vol. 21, no. 5, pp. 1282–1291, 2006.

[57] A. M. Bazzi and P. T. Krein, "Ripple Correlation Control : An Extremum Seeking Control Perspective for Real-Time Optimization," vol. 29, no. 2, pp. 988–995, 2014.

[58] J. W. Kimball, S. Member, and P. T. Krein, "Digital Ripple Correlation Control for Photovoltaic Applications," no. 2, pp. 1690–1694, 2007.

[59] R. J. Turnbull, "Dynamic Maximum Power Point Tracker for Photovoltaic Applications," pp. 1710–1716, 1996.

[60] J. W. Kimball and P. T. Krein, "Discrete-Time Ripple Correlation Control for Maximum Power Point Tracking," vol. 23, no. 5, pp. 2353–2362, 2008.

[61] C. Barth and R. C. N. Pilawa-Podgurski, "Dithering Digital Ripple Correlation Control for Photovoltaic Maximum Power Point Tracking," *IEEE Trans. Power Electron.*, vol. 30, no. 8, pp. 4548–4559, 2015.

[62] Y. H. Lim and D. C. Hamill, "Simple Maximum Power Point Tracker for Photovoltaic Arrays," vol. 36, no. May, pp. 997–999, 2000.

[63] T. J. (University of N. M. Ross, *Fuzzy logic with engineering applications*. 2010.

[64] M. Veerachary, T. Senjyu, and K. Uezato, "Neural-Network-Based Maximum-Power-Point Tracking of Coupled-Inductor," vol. 50, no. 4, pp. 749–758, 2003.

[65] B. N. Alajmi, K. H. Ahmed, S. J. Finney, and B. W. Williams, "Fuzzy-Logic-Control Approach of a Modified Hill-Climbing Method for Maximum Power Point in Microgrid Standalone Photovoltaic System," vol. 26, no. 4, pp. 1022–1030, 2011.

[66] C. Cecati, F. Ciancetta, and P. Siano, "A Multilevel Inverter for Photovoltaic Systems With Fuzzy Logic Control," vol. 57, no. 12, pp. 4115–4125, 2010.

[67] Y. Yang, "A Fuzzy Logic Controller for Maximum Power Point Tracking with 8-bit Microcontroller," pp. 2895–2900, 2010.

[68] C. Won, D. Kim, S. Kim, W. Kim, and H. Kim, "A New Maximum Power Point Tracker," 1994.

[69] M. G. Simoes, N. Franceschetti, and M. Friedhofer, "A fuzzy logic based photovoltaic peak power tracking control," *Ind. Electron. 1998. Proceedings. ISIE'98. IEEE Int. Symp.*, vol. 1, pp. 300–305, 1998.

[70] H. E. L. K. M. N. F. Nashed, "Fuzzy logic implementation for photovoltaic maximum," pp. 155–160, 2000.

[71] N. Patcharaprakiti and S. Premrudeepreechacharn, "Maximum Power Point Tracking Using Adaptive Fuzzy Logic Control for Grid-Connected Photovoltaic System," pp. 372–377, 2002.

[72] N. Khaehintung and K. Pramotung, "RISC-Microcontroller Built-in Fuzzy Logic Controller of Maximum Power Point Tracking for Solar-Powered Light-Flasher Applications," *Ieee*, 2004.

[73] D. Kriesel, "A Brief Introduction to Neural Networks," *Retrieved August*, 2005.

[74] C. Gershenson, "Artificial Neural Networks for Beginners," *Networks*, 2003.

[75] L. M. Elobaid, A. K. Abdelsalam, and E. E. Zakzouk, "Artificial neural network-based photovoltaic maximum power point tracking techniques: a survey," *IET Renew. Power Gener.*, vol. 9, no. 8, pp. 1043–1063, 2015.

[76] T. Hiyama and K. Kitabayashi, "Neural network based estimation of maximum power generation from PV module using environmental information," *IEEE Trans. Energy Convers.*, vol. 12, no. 3, pp. 241–247, 1997.

[77] T. Hiyama, S. Kouzuma, T. Imakubo, O. O. Point, S. Member, and C. Science, "Identification of optimal operating point of PV modules using neural network for real time maximum power

tracking control," *Energy Conversion, IEEE Trans.*, vol. 10, no. 2, pp. 360–367, 1995.

[78] C. H. C. Hua and J. R. L. J. R. Lin, "DSP-based controller application in battery storage of photovoltaic\nsystem," *Proc. 1996 IEEE IECON. 22nd Int. Conf. Ind. Electron. Control. Instrum.*, vol. 3, pp. 1705–1710, 1996.

[79] K. Ro and S. Rahman, "Two-loop controller for maximizing performance of a grid-connected photovoltaic-fuel cell hybrid power plant," *IEEE Trans. Energy Convers.*, vol. 13, no. 3, pp. 276–281, 1998.

[80] A. Chatterjee and A. Keyhani, "Neural network estimation of microgrid maximum solar power," *IEEE Trans. Smart Grid*, 2012.

[81] Y.-H. Liu, C.-L. Liu, J.-W. Huang, and J.-H. Chen, "Neural-network-based maximum power point tracking methods for photovoltaic systems operating under fast changing environments," *Sol. Energy*, 2013.

[82] F. Giraud and Z. M. Salameh, "Analysis of the effects of a passing cloud on a grid-interactive photovoltaic system with battery storage using neural networks," *IEEE Trans. Energy Convers.*, 1999.

[83] M. C. Di Piazza, M. Pucci, A. Ragusa, and G. Vitale, "A growing neural gas network based MPPT technique for multi-string PV plants," *IEEE Int. Symp. Ind. Electron.*, pp. 544–549, 2010.

[84] P. C. Sekhar, S. Mishra, and R. Sharma, "Data analytics based neuro-fuzzy controller for diesel-photovoltaic hybrid AC microgrid," no. October 2014, pp. 193–207, 2015.

[85] E. M. Natsheh, A. R. Natsheh, and A. Albarbar, "Intelligent controller for managing power flow within standalone hybrid power systems," no. May, pp. 191–200, 2013.

[86] M. Carmela, D. Piazza, M. Pucci, A. Ragusa, and G. Vitale, "Analytical Versus Neural Real-Time Simulation of a Photovoltaic Generator Based on a DC – DC Converter," vol. 46, no. 6, pp. 2501–2510, 2010.

[87] J. Arias, F. F. Linera, J. Martin-Ramos, a. M. Pernia, and J. Cambronero, "A modular PV regulator based on microcontroller with maximum power point tracking," *Conf. Rec. 2004 IEEE Ind. Appl. Conf. 2004. 39th IAS Annu. Meet.*, vol. 2, pp. 1178–1184, 2004.

[88] a. S. Kislovski and R. Redl, "Maximum-power-tracking using positive feedback," *Proc. 1994 Power Electron. Spec. Conf. - PESC'94*, pp. 1065–1068, 1994.

[89] C. R. Sullivan and M. J. Powers, "A high-efficiency maximum power point tracker for photovoltaic arrays in a solar-powered race vehicle," *Proc. IEEE Power Electron. Spec. Conf. - PESC '93*, pp. 574–580, 1993.

[90] H. J. Beukes and J. H. R. Enslin, "Analysis of a new compound converter as MPPT, battery regulator and bus regulator for satellite power systems," *PESC Rec. - IEEE Annu. Power Electron. Spec. Conf.*, pp. 846–852, 1993.

[91] J. H. R. Enslin and D. B. Snyman, "Simplified feed-forward control of the maximum power point in PV\ninstallations," *Proc. 1992 Int. Conf. Ind. Electron. Control. Instrumentation, Autom.*, 1992.

[92] D. Shmilovitz, "Photovoltaic maximum power point tracking employing load parameters," *IEEE Int. Symp. Ind. Electron.*, vol. III, pp. 1037–1042, 2005.

[93] E. F. Schubert, *Light-Emitting Diodes*. 2006.

[94] Y. Wang, J. M. Alonso, and X. Ruan, "A Review of LED Drivers and Related Technologies," *IEEE Trans. Ind. Electron.*, vol. 64, no. 7, pp. 5754–5765, 2017.

[95] H. Van Der Broeck, G. Sauerl??nder, and M. Wendt, "Power driver topologies and control

schemes for LEDs," in *Conference Proceedings - IEEE Applied Power Electronics Conference and Exposition - APEC*, 2007.

[96] G. Carraro, "Solving high-voltage off-line HB-LED constant-current control-circuit issues," in *Conference Proceedings - IEEE Applied Power Electronics Conference and Exposition - APEC*, 2007.

[97] S. Winder, *Power supplies for LED driving*. 2008.

[98] A. Jha and B. Singh, "Power quality improvement using bridgeless-Landsman converter for LED driver," *IET Power Electron.*, vol. 9, no. 13, pp. 2591–2601, 2016.

[99] D. Xu, X. Liu, Q. Yang, and J. Xu, "High-efficiency multi-string LED driver based on constant current bus with time-multiplexing control," *Electron. Lett.*, vol. 52, no. 9, pp. 746–748, 2016.

[100] K. Chen, P. Xiao, A. Johnsen, and R. E. Saenz, "Turn-On Optimization for Class D Series-Parallel LCC-Type Constant Current High-Power LED Driver Design Based on Traditional Fluorescent Control IC," *IEEE Trans. Power Electron.*, vol. 31, no. 7, pp. 4732–4741, 2016.

[101] A. Jha and M. Kumar, "A Wide Range Constant Current LED Driver with Improved Power Quality and Zero Standby," *2018 IEEMA Eng. Infin. Conf.*, pp. 1–6.

[102] H. Deng, L. Shan, Y. Yin, G. Si, and Y. Sun, "Design of a LED Constant-Current Driver Using a Novel Hysteresis-Current Control Method with Adaptive Off-Time Control," no. 2014, pp. 1551–1555, 2015.

[103] C. Wang, J. Xi, and L. He, "A linear constant current LED driver with no off-chip inductor or capacitor," *IEEE Int. Symp. Ind. Electron.*, pp. 2524–2528, 2014.

[104] N. Narendran and Y. Gu, "Life of LED-based white light sources," *IEEE/OSA J. Disp. Technol.*, 2005.

[105] Q. Luo, S. Zhi, C. Zou, W. Lu, and L. Zhou, "An LED driver with dynamic high-frequency sinusoidal bus voltage regulation for multistring applications," *IEEE Trans. Power Electron.*, vol. 29, no. 1, pp. 491–500, 2014.

[106] P. D. Teodosescu, M. Bojan, and R. Marschalko, "Resonant LED driver with inherent constant current and power factor correction," *Electron. Lett.*, vol. 50, no. 15, pp. 1086–1088, 2014.

[107] P. K. Bondyopadhyay, "Sir J C bose's diode detector received marconi's first transatlantic wireless signal of december 1901 (The 'italian navy coherer' scandal revisited)," *IETE Tech. Rev. (Institution Electron. Telecommun. Eng. India)*, vol. 15, no. 5, pp. 377–406, 1998.

[108] J. ORRIN E. DUNLAP, *Marconi—The Man and His Wireless*. New York: THE MACMILLAN COMPANY, 1937.

[109] T. K. Sarkar and D. L. Sengupta, "An appreciation of J. C. Bose's pioneering work in millimeter waves," *IEEE Antennas Propag. Mag.*, vol. 39, no. 5, pp. 55–62, 1997.

[110] D. T. Emerson, "The work of jagadis chandra bose: 100 years of millimeter-wave research," *IEEE Trans. Microw. Theory Tech.*, 1997.

[111] C. A. Hempstead, *Wireless: From Marconi's Black-Box to the Audion*, vol. 36, no. 128. 2003.

[112] B. Yuksekkaya, A. A. Kayalar, M. B. Tosun, M. K. Ozcan, and A. Z. Alkar, "A GSM, internet and speech controlled wireless interactive home automation system," *IEEE Trans. Consum. Electron.*, vol. 52, no. 3, pp. 837–843, 2006.

[113] T. Perumal, A. R. Ramil, and C. Y. Leong, "Design and implementation of SOAP-based residential management for smart home systems," *IEEE Trans. Consum. Electron.*, vol. 54, no. 2, pp. 453–459, 2008.

[114] Y. Zhao and Z. Ye, "A Low Cost GSM / GPRS Based Wireless Home Security System," no.

6, pp. 567–572, 2008.

[115] M. Sha, M. Ieee, H. Gonzalez, M. Ieee, and D. Gunatilaka, “Real-Time Wireless Sensor-Actuator Networks for Industrial Cyber-Physical Systems,” 2015.

[116] F. Salvadori *et al.*, “Monitoring in Industrial Systems Using Wireless Sensor Network With Dynamic Power Management,” vol. 58, no. 9, pp. 3104–3111, 2009.

[117] H. Ramamurthy, B. S. Prabhu, R. Gadh, and A. M. A. M. A. M. Madni, “Wireless Industrial Monitoring and Control Using a Smart Sensor Platform,” *Sensors Journal, IEEE*, 2007.

[118] A. Sachan, “GSM Based Automated Embedded System for Monitoring and Controlling of Smart Grid,” vol. 7, no. 12, pp. 1258–1262, 2013.

[119] A. Pellegrino, V. R. M. Lo Verso, L. Blaso, A. Acquaviva, E. Patti, and A. Osello, “Lighting Control and Monitoring for Energy Efficiency : A Case Study Focused on the Interoperability of Building Management Systems,” vol. 52, no. 3, pp. 2627–2637, 2016.

[120] Y. J. Kim, R. G. Evans, and W. M. Iversen, “Remote Sensing and Control of an Irrigation System Using a Distributed Wireless Sensor Network,” vol. 57, no. 7, pp. 1379–1387, 2008.

[121] S. Chen, H. Lee, C. Chen, and H. Huang, “Adaptive Low-Power Design for Biometrics and Healthcare Applications,” vol. 3, no. 4, pp. 398–409, 2009.

[122] F. Hu, S. Lakdawala, Q. Hao, and M. Qiu, “Low-power, intelligent sensor hardware interface for medical data preprocessing,” *IEEE Trans. Inf. Technol. Biomed.*, vol. 13, no. 4, pp. 656–663, 2009.

[123] J. Zheng, M. J. Lee, and M. Anshel, “Toward Secure Low Rate Wireless Personal Area Networks,” *IEEE Trans. Mob. Comput.*, vol. 5, no. 10, pp. 1361–1373, 2006.

[124] B. Hu and W. Fan, “Design of Wireless Temperature Monitoring and Control System Based on ZigBee Technology in Communication Room,” *2010 Int. Conf. Internet Technol. Appl.*, pp. 1–3, 2010.

[125] T. Ramachandran, J. Temenggung, and B. M. Cheras, “ZigBee Wireless Communication for Monitoring Renewable Street Light System,” no. 22, 2014.

[126] Z. Kaleem, T. M. Yoon, and C. Lee, “Energy Efficient Outdoor Light Monitoring and Control Architecture Using Embedded System,” *IEEE Embed. Syst. Lett.*, vol. 8, no. 1, pp. 18–21, 2016.

[127] J. Yick, B. Mukherjee, and D. Ghosal, “Wireless sensor network survey,” *Comput. Networks*, vol. 52, no. 12, pp. 2292–2330, 2008.

[128] I. F. Akyildiz, W. Su, Y. Sankarasubramaniam, and E. Cayirci, “Wireless sensor networks : a survey,” vol. 38, pp. 393–422, 2002.

[129] L. Borges, F. Velez, and A. Lebres, “Survey on the Characterization and Classification of Wireless Sensor Networks Applications,” *IEEE Commun. Surv. Tutorials*, vol. XX, no. X, pp. 1–1, 2014.

[130] G. Shahzad, H. Yang, A. W. Ahmad, and C. Lee, “Energy-Efficient Intelligent Street Lighting System Using Traffic-Adaptive Control,” *IEEE Sens. J.*, vol. 16, no. 13, pp. 5397–5405, 2016.

[131] M. E. A. López, F. J. G. Mantiñan, and M. G. Molina, “Implementation of Wireless Remote Monitoring and Control of Solar Photovoltaic (PV) System,” *Transm. Distrib. Lat. Am. Conf. Expo. (T&D-LA), 2012 Sixth IEEE/PES*, pp. 1–6, 2012.

[132] F. Leccese and Z. Leonowicz, “Intelligent wireless street lighting system,” *2012 11th Int. Conf. Environ. Electr. Eng. EEEIC 2012 - Conf. Proc.*, pp. 958–961, 2012.

[133] G. Gobal System for Mobile communications Association, “The Mobile Economy,” *GSMA Intell.*, no. 35, pp. 11–11, 2018.

[134] D. Wang, R. He, J. Han, M. Fattouche, and F. M. Ghannouchi, "Sensor Network Based Oilwell Health Monitoring and Intelligent Control," vol. 12, no. 5, pp. 1326–1339, 2012.

[135] S. R. Parekar and M. M. Dongre, "An intelligent system for monitoring and controlling of street light using GSM technology," *Proc. - IEEE Int. Conf. Inf. Process. ICIP 2015*, pp. 604–609, 2016.

[136] M. Gagliarducci, D. A. Lampasi, and L. Podestà, "GSM-based monitoring and control of photovoltaic power generation," *Meas. J. Int. Meas. Confed.*, vol. 40, no. 3, pp. 314–321, 2007.

[137] F.-C. W. F.-C. Wang, C.-W. T. C.-W. Tang, and B.-J. H. B.-J. Huang, "Multivariable Robust Control for a Red, Green, and Blue LED Lighting System," *IEEE Trans. Power Electron.*, vol. 25, no. 2, pp. 417–428, 2010.

[138] S. Muthu, A. Member, F. J. P. Schuurmans, and M. D. Pashley, "Red , Green , and Blue LEDs for," vol. 8, no. 2, pp. 333–338, 2002.

[139] J. M. Gilman, M. E. Miller, and M. R. Grimaila, "A simplified control system for a daylight-matched LED lamp," *Light. Res. Technol.*, vol. 45, no. 5, pp. 614–629, 2013.

[140] M. Dyble, N. Narendran, A. Bierman, and T. Klein, "Impact of dimming white LEDs: chromaticity shifts due to different dimming methods," *Fifth Int. Conf. Solid State Light.*, vol. 5941, p. 59411H, 2005.

[141] X. Qu, S. C. Wong, and C. K. Tse, "Temperature measurement technique for stabilizing the light output of RGB LED lamps," *IEEE Trans. Instrum. Meas.*, vol. 59, no. 3, pp. 661–670, 2010.

[142] K. H. Loo, Y. M. Lai, S. C. Tan, and C. K. Tse, "On the color stability of phosphor-converted white LEDs under DC, PWM, and bilevel drive," *IEEE Trans. Power Electron.*, vol. 27, no. 2, pp. 974–984, 2012.

[143] S. K. Ng, K. H. Loo, Y. M. Lai, and C. K. Tse, "Color control system for RGB LED with application to light sources suffering from prolonged aging," *IEEE Trans. Ind. Electron.*, vol. 61, no. 4, pp. 1788–1798, 2014.

[144] C. H. Miao, "Color temperature adjustable lamp," US8159125B2, 2012.

[145] A. T. L. Lee, H. Chen, S. C. Tan, and S. Y. Hui, "Precise Dimming and Color Control of LED Systems Based on Color Mixing," *IEEE Trans. Power Electron.*, vol. 31, no. 1, pp. 65–80, 2016.

[146] K. Jonsson, "Light with changeable color temperature," US20120146505A1, 2012.

[147] H. T. Chen, S. C. Tan, and S. Y. R. Hui, "Nonlinear Dimming and Correlated Color Temperature Control of Bicolor White LED Systems," *IEEE Trans. Power Electron.*, vol. 30, no. 12, pp. 6934–6947, 2015.

[148] "Application note: Lutron®," Color Tuning with Lutron Controls"." [Online]. Available: http://www.lutron.com/TechnicalDocumentLibrary/048579.pdf.

[149] "Tunable white light engine for HCL | LED Engin." [Online]. Available: https://www.osram.us/ledengin/products/luxitune/. [Accessed: 16-Mar-2019].

[150] S. Muthu and J. Gaines, "Red, green and blue LED-based white light source: implementation challenges and control design," pp. 515–522, 2004.

[151] M. M. Sisto and J. Gauvin, "Accurate chromatic control and color rendering optimization in LED lighting systems using junction temperature feedback," *Thirteen. Int. Conf. Solid State Light.*, vol. 9190, no. September 2014, p. 919002, 2014.

[152] M. B. Yurtseven, S. Mete, and S. Onaygil, “The effects of temperature and driving current on the key parameters of commercially available, high-power, white LEDs,” *Light. Res. Technol.*, vol. 48, no. 8, pp. 943–965, 2016.

[153] P. Deurenberg, C. Hoelen, J. van Meurs, and J. Ansems, “Achieving color point stability in RGB multi-chip LED modules using various color control loops,” *Fifth Int. Conf. Solid State Light.*, vol. 5941, no. September 2005, p. 59410C, 2005.

[154] L. D. O. and T. E. Clary, “LED brightness compensation system and methods,” EP 1 901 587 A2, 2008.

Chapter 2

Outline of the Solar-Powered Outdoor Lighting Systems

2.1 Introduction

In this chapter, outline of the developed solar-powered outdoor lighting system (OLS) is presented. The first part of this chapter focuses on the fundamental of the solar photovoltaic system and the second part of this chapter deals with the proposed development. In this study, two remote control and monitoring enabled, 'smart', energy-efficient, long-life, low-cost and low-maintenance solar-powered OLSs have been developed and implemented. The advantages of solar energy and LED for OLS have already been discussed in chapter1.

The first OLS is a fixed-CCT outdoor lighting system (FCOLS) for single colour lighting applications such as streets, pathways, parking lots, industrial yards, security areas etc. The second one is a tunable-CCT outdoor lighting system (TCOLS) for colour-tunable lighting applications such as residential non-living areas, public buildings and structures, gardens, parks etc. The prototype TCOLS can independently produce a variable CCT ranging from 2500 to 12500 K and a variable illuminance ranging from 5 to 120 lx, at a distance of 1m - a value set for the purpose of this study. The colour-tunable LED (CTLED) light source also has a great impact on human psychology and biology which is discussed in Chapter 1. The OLSs can be controlled and monitored from a central monitoring station through a GSM network.

2.2 Fundamental of photovoltaic (PV) system

The word photovoltaic is derived from the Latin word photo (light) and voltaic (energy). Recently, Solar PV technology has emerged as one of the most matured and fast evolving renewable energy technologies. It is expected that it will play a vital role in the future global electricity generation.

2.2.1 Solar cell operating principle

The solar cell is a p-n junction semiconductor diode that has been designed and constructed to efficiently absorb the incident radiation from the sun and convert it into electrical energy.

In one method of construction, by alternate doping of an intrinsic silicon by a p-type and an n-type impurity, a metallurgical junction is formed. The n region is heavily doped and thin so light can penetrate through it. On the other hand, p region is lightly doped so that most of the depletion region lies in the p side. The transition region between n-type and p-type semiconductors is called space-charge region or depletion region [1].

One of the electrical contacts of the diode is formed by a metallic layer on the rear side of the solar cell. Another electrical contact of the diode is formed by a metallic grid at the front side. Since metal reflects light, metal coverage should be as small as possible in order to allow the sufficient light to enter the cell. Basic construction of a solar cell is shown in Fig. 2.1, where sunlight has fallen on the front side of the solar cell.

When the solar cell is in thermal equilibrium, the drift and diffusion currents for each carrier type exactly balance, therefore there is no net of current flow. Now, the semiconductor is taken out of equilibrium for instance by solar radiation and/or injection of current, the electron and hole tend to relax back towards their equilibrium values through a process called recombination. In this process electron falls from conduction band to valence band, thereby eliminating a valence-band hole. The photon particle hits the solar cell can be transmitted through the cell, reflected or absorbed. By absorbing the energy of photon, the electrons are excited and travel from the valence band to conduction band, where it can move freely. The electron can then be moved by the electric field across the p-n junction, through an external conductor resulting in the flow of electrons, which will continue as long as the solar cell is illuminated.

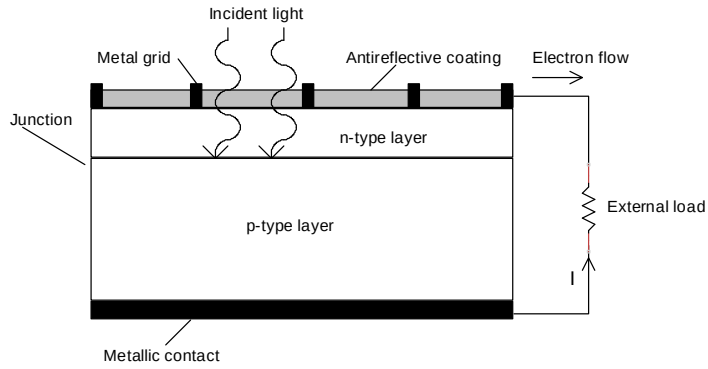

Fig. 2.1. The physical construction of a typical solar cell

2.2.2 Characteristic of the solar cell

An ideal solar cell can be considered as an irradiance-dependent, non-ideal current source, where the current produced by the solar cell is proportional to the solar intensity falling on it.

However, the practical behaviour of a solar cell deviates from ideal one due to the optical and electrical losses [2]. An involved model of a solar cell uses an irradiance-dependent current source in parallel with two diodes, a shunt resistance and a series resistance. The recombination losses are represented by the diodes connected parallel to the current source, but in reverse direction. Two diodes may be added to the circuit, one diode represents the recombination losses in the bulk and in the emitter region of the cell. The other diode represents the recombination in the space charge region of the cell. In a simple model, typically, the recombination in the space charge region is neglected, and only one diode is added in the equivalent circuit as shown in Fig. 2.2.

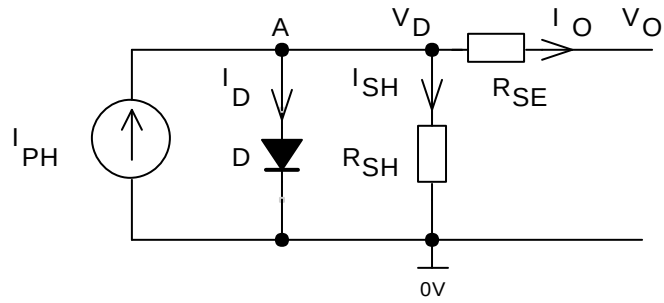

Fig. 2.2. Equivalent circuit of a solar cell

From the equivalent circuit of a solar cell in Fig. 2.2, applying KCL at node A, an equation for the terminal current I_O can be written in the following form

$$I_O = I_{PH} - I_D - I_{SH} \tag{2.1}$$

where,

I_{PH} is the photo-generated current

I_D is the diode current

I_{SH} is the shunt leakage current

The diode current I_D can be given by the well-known Shockley equation [3]

$$I_D = I_S \left(e^{\frac{qV_D}{\eta_i K_B T}} - 1 \right) \tag{2.2}$$

where,

q is electron charge equal to 1.6×10^{-19}C

η_i is the ideality factor of diode

K_B is the Boltzmann constant equal to 1.3806×10^{-23} JK^{-1}

T is the absolute temperature in K

V_D is the voltage across the diode

I_S is the dark saturation current

Substituting equation (2.2) in equation (2.1)

$$I_O = I_{PH} - I_S\left(e^{\frac{q\,V_D}{\eta_i K_B T}} - 1\right) - \frac{V_D}{R_{SH}} \qquad (2.3)$$

The cell terminal voltage V_O is given by

$$V_O = V_D - I_O R_{SE} \qquad (2.4)$$

where R_{SE} is the equivalent series resistance caused by the lead resistances and the bulk resistance of the semiconductor.

The output or I_O-V_O characteristic of a solar cell can be expressed from equations (2.3) and (2.4). Generally, solar cells are characterized and compared with each other with four parameters as discussed below, they are open circuit voltage (V_{oc}), short circuit current (I_{sc}), fill factor (FF) and efficiency (η).

Open circuit voltage (V_{oc}): Open circuit voltage is the maximum voltage which is generated across the terminal of a cell when kept open i.e. $I_O = 0$. Putting this condition in equation (2.3), an expression for V_{oc} can be derived as equation (2.5), assuming that the shunt resistance is high enough to neglect the term I_{SH}.

$$V_{oc} \approx \frac{\eta_i K_B T}{q} \ln\left(\frac{I_{PH}}{I_S} + 1\right) \qquad (2.5)$$

Short circuit current (I_{sc}): This is the maximum current which can be generated by a solar cell, when its terminals are shorted with each other, i.e. output voltage $V_O = 0$, when we put $V_D = 0$ in equation (2.6), the expression for I_{sc} will be, assuming very low series resistance

$$I_{sc} \approx I_{PH} \qquad (2.6)$$

Thus, I_{sc} is equal to the photo-generated current.

Fill factor (K_{FF}): Fill factor is the ratio of maximum power which can deliver a solar cell to the load and the product of V_{oc} and I_{sc}. K_{FF} can be expressed as [1]

$$K_{FF} = \frac{V_{mp} I_{mp}}{V_{oc} I_{sc}} \quad (2.7)$$

A very good quality crystalline silicon solar cell has a K_{FF} of nearly 0.8.

Efficiency (η): The efficiency of a solar cell can be defined as the ratio of output power to the input power. The power output should be at maximum power point, i.e. at P_{mp} of a cell and input power is the power of a solar radiation P_{rad}. According to standard test conditions (STC) P_{rad} is equal to 1000W/m^2. Thus the efficiency can be expressed as

$$\eta = \frac{P_{mp}}{P_{rad}} \quad (2.8)$$

Substituting, $P_{mp} = V_{mp} I_{mp}$ and equation (2.7) in equation (2.8) can be written in form as

$$\eta = \frac{V_{mp} I_{mp}}{P_{rad}} = \frac{V_{oc} I_{sc} K_{FF}}{P_{rad}} \quad (2.9)$$

Fig. 2.3 graphically represents I-V characteristic of a solar cell where the voltage and the current are shown in normalized forms. Normalization helps the system designer in comparing the performance of different ratings of cells from different manufacturers. The process of normalization of the quantities is discussed below.

The normalized current I_n is determined by using the short-circuit current as a normalizing factor

$$I_n = \frac{I_O}{I_{sc}} \quad (2.10)$$

Likewise, the normalized voltage V_n is determined by using the open-circuit voltage as a normalizing factor

$$V_n = \frac{V_O}{V_{oc}} \quad (2.11)$$

The normalized power P_n is calculated by taking the ratio of the actual output power $P_o = V_o I_o$ to the ideal output power $I_{sc} V_{oc}$

$$P_n = \frac{P_o}{I_{sc} V_{oc}} \quad (2.12)$$

Reconversion of the normalized quantity of voltage, current and power to actual quantity requires the use of corresponding normalization factors of V_{oc}, I_{sc}, and V_{oc} I_{sc}, respectively. Fig. 2.3 additionally points to a very special point, namely, the maximum power point (MPP).

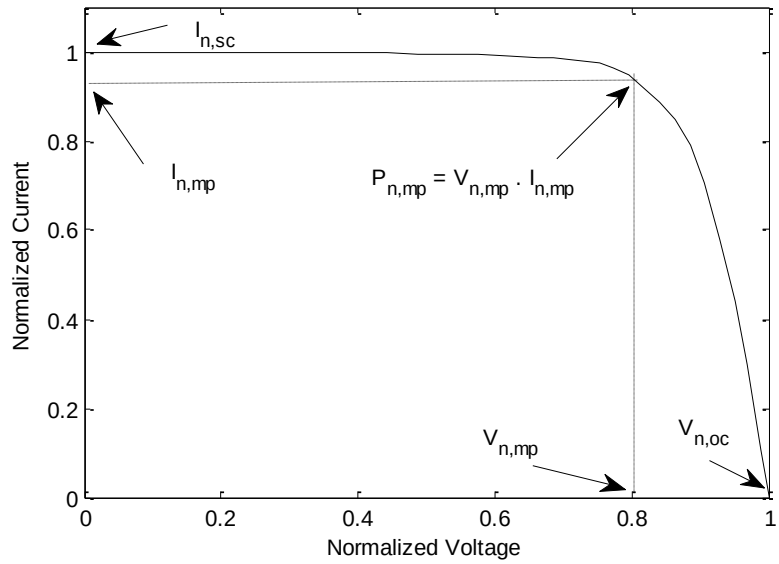

Fig. 2.3. Typical plot of solar cell I-V characteristic (scaled in normalized value)

2.2.3 Solar resource and radiation

The sun is the source of almost all energy on our planet, either directly as sunlight or indirectly as wind or waves. Even the coal was once living plants that gained their energy from photosynthesis: the process by which sunlight, carbon-di-oxide and water are converted to carbohydrates. The sun's seemingly endless energy supply is driven by a process known as nuclear fusion, where an atom of hydrogen combines to form an atom of helium releasing a large amount of energy in the process. The helium atom may then combine with other helium or hydrogen atom to release even more energy. The energy produces in the heart of the sun is emitted as electromagnetic radiation. Electromagnetic radiation is emitted in many useful forms including microwave radio-wave and visible light. Solar cell designers focus on capturing the energy carried in visible light.

Although radiation emitted from the sun is fairly consistent, there is significant variation received at the earth surface. This is caused by the earth's orbit, rotation on its axis and the albedo of certain areas. Solar array designers need to able to quantify how much solar radiation will be received throughout the year at a given site.

The incident solar energy per unit area is termed as insolation and will be denoted by I_S. As shown in Fig. 2.4, it is a function of time, t in hours where t=0 indicates the sunrise. Instead of a graph like Fig. 2.4, a quantity known as *peak sun hours* (PSH) is often used by the designers. The PSH, to be denoted by T_{PS}, for a particular day is the number of hours for which a constant insolation at the rate of 1000W/m^2 would give an energy that is equal to the energy that is actually available when I_S is a function of time.

The total energy ε_s in watt-hour, received per unit area (m^2) in a day can be expressed by

$$\varepsilon_s = \int_0^{24} I_s dt \tag{2.13}$$

where t is measured in hours.

T_{PS} is given by

$$T_{PS} = \frac{\varepsilon_s}{1000} \tag{2.14}$$

From the irradiance graph Fig. 2.4, the computed value of ε_s is 6320 Wh/ m^2, which is equivalent to a T_{PS} of 6.32 hours. In Section 2.4.3 it will be shown that value of T_{PS} plays a very significant role in the selection of solar module size.

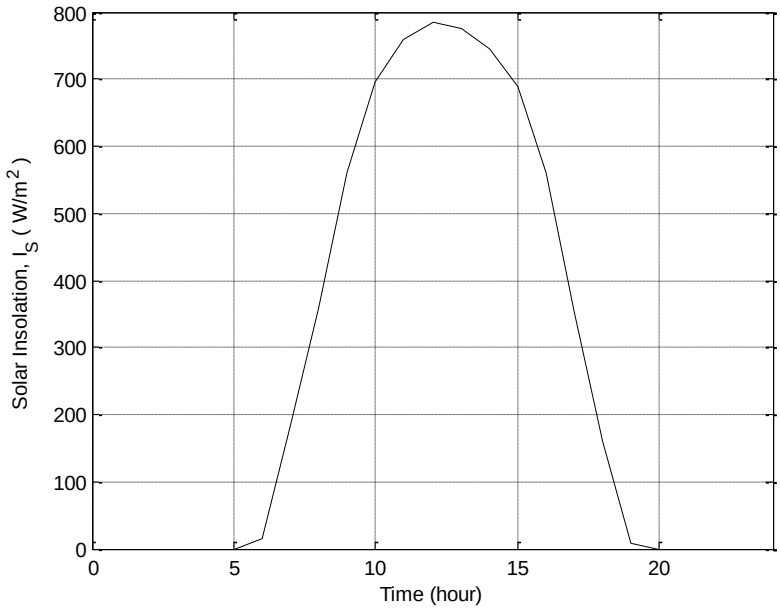

Fig. 2.4. Typical irradiance graph for a day

2.2.4 Solar electric systems

The photovoltaic systems are used to supply power to the electrical loads. The loads may be of DC or AC type and depending upon the application. Additionally, the load may require power during day-time only or night-time only or 24 hours a day. Since a PV module generates power only during the sunshine hours, the requirement of some energy storage arrangement is mandatory to supply the load during the non-sunshine hours. This energy storage is usually accomplished through batteries. During non-sunshine hours, the load may also be powered by auxiliary power sources such as diesel generator, wind generator or by connecting the PV system to the grid at daytime and draw power at night or some combination of these auxiliary sources. Solar PV systems are broadly classified into three types, each type is characterized by unique consideration in design, installation and operation.

2.2.4.1 Stand-alone or Off-grid systems

A stand-alone or off-grid solar electric system is designed to supplement or replace conventional grid supply. They are most commonly used in remote or rural areas where grid supply is not accessible due to very high cost of grid extension. A stand-alone PV system configuration may be straightforward, incorporating only two components, PV module and load or can be very complex, containing sophisticated controllers, several power sources, multiple energy storage units, smart inverters to meet stringent load requirements.

The off-grid PV system configurations can be broadly divided into four categories, depending on the different parameters such as load requirement, reliability of the system, cost of the system, resource availability, performance of the system etc. The configurations are discussed below in the order of increasing complexity.

Type-a: Unregulated stand-alone system with DC load: It is the simplest possible configuration of stand-alone PV system, where the PV panel is directly connected to the load as shown in Fig 2.5 (a). No arrangements have been made for optimum utilization of PV module. As the voltage and current of the PV module vary according to the insolation and load characteristic, this is called an unregulated system. In this type of configuration, no arrangements have been made for energy storage to operate the load at night. This kind of

configuration mostly used in raw DC loads like DC fan, DC pump (suitable for irrigation) etc.

Type-b: Regulated stand-alone system with DC load: It is similar to an unregulated PV system except that an electronics power converter has been used in between the PV module and the load as shown in Fig2.5 (b). The converter may be the voltage regulator, current regulator or a maximum power point tracker (MPPT) circuit. The power converter is required for smooth operation of the load. The MPPT-based charge controller is used to ensure maximum utilization of power from a PV module. A details discussion about the circuit for MPPT implementation and the proposed algorithm are presented in chapter 3.

Type-c: Regulated stand-alone system with battery and DC load: This kind of PV system is used when the night-time or non-sunshine hours operation of the load is required. In this configuration, a storage device (battery) is used to store the extra energy generated by the solar panel throughout the day, in turn, this stored energy can be used by a load during non-sunshine hours. Fig 2.5 (c) shows the block diagram for this configuration. Batteries in a PV system contribute to the recurring cost as the life of the battery is significantly shorter than the life of PV array. The life of the batteries affected by the manner in which they are used, commonly overcharging and deep-discharging considerably reduce the battery life, eventually increasing the operating cost of the PV system. Therefore, a proper control circuit is required to prevent overcharging and deep-discharging. The control circuit is also called a charge controller. To optimize the solar power in addition to the charge controller circuit, an MPPT circuit may also be incorporated in this configuration.

Type-c configuration expedites load voltage regulation, along with the battery ensures uninterruptable and smooth load operation. This type of configuration could be used for providing power to DC lighting, fan, motor and DC appliance etc. The system developed in this study has been implemented using type-c configuration, as it is most compatible with the LED-based OLS. The developed MPPT-based multi-stage charge controller circuit with its algorithm has been discussed in chapter 3.

Type-d: Regulated stand-alone system with battery and DC and AC load: This configuration is identical to the type-c configuration except the system can provide the power to the AC load. This system uses solar power to charge the batteries, then the stored charge is used to operate the appliances (e.g. lighting, pumps, motor etc.), either directly from the batteries as low voltage equipment (e.g. 12V DC light) or from an inverter. The inverter is connected to the batteries and converts the battery voltage to mains equivalent (i.e. 230V, 50Hz) for use in regular AC appliances (e.g., computer, television, fan, etc.).

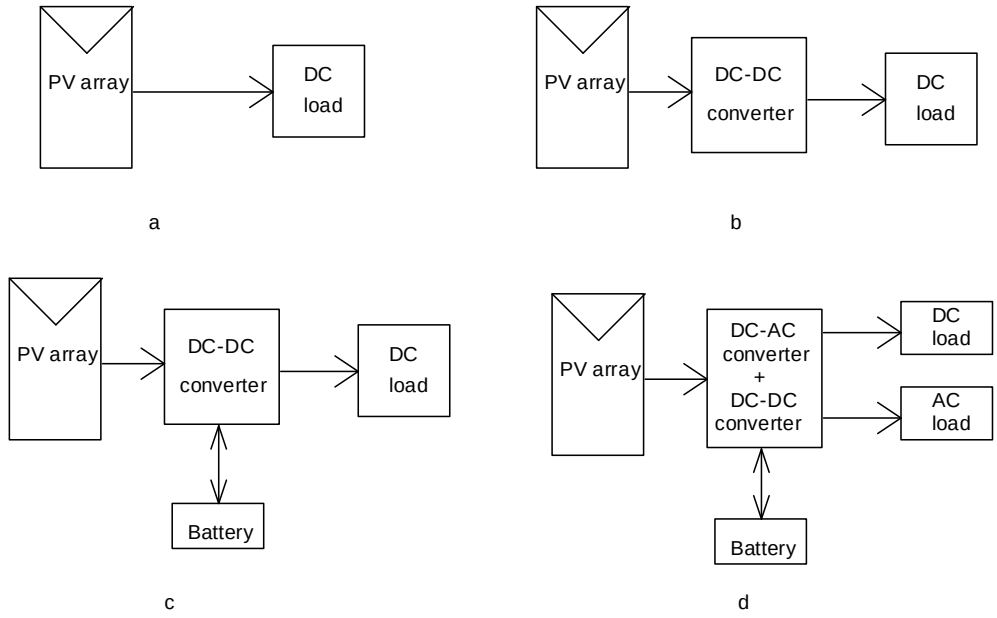

Fig. 2.5. Schematic representation of various standalone PV system configurations

2.2.4.2 Hybrid PV systems

Solar is an unreliable source of energy, as it can supply energy only when the insolation is available. i.e., during the daytime. A hybrid PV system is a system that comprises at least one or more than one sources, other than PV, to meet the electrical power demand of the loads. The other sources that are generally used in combination with the PV source are wind generator, diesel generator, fuel cell, micro-turbines etc. Hybrid PV systems are more relevant in the stand-alone or islanded applications than grid-connected PV system. In a grid-connected system, during night-time, the energy demand of the load can be met by the grid. However, in the PV based stand-alone applications may lead to total shut down of the load, due to several reasons. They are the system without storage device, cloudy weather, or partial

shedding of the PV module. Under such condition, to maintain the continuity of the energy, a configuration integrating a source other than PV is essential.

The hybrid systems are complex than the stand-alone system as it contains more than one energy sources. An abrupt change in the output power from any of the source can affect the system stability significantly. The same situation may arise when there is a sudden change in the load. Therefore, it is a challenging task to design a fast and accurate control scheme to ensure system stability, in such a situation.

2.2.4.3 Grid-connected PV systems

The grid-connected PV system is becoming more popular in urban areas because of their applications in distributed generation and for effectively using the power of a PV module. Unlike off-grid system battery backup is not mandatory to ensure MPPT. Installation as well as running cost for this type of system will be low as the battery is not required. Excess power generated by the PV module can be directly fed into the grid through a grid-connected inverter. The major components of grid-connected PV system include the PV module, inverter and bi-directional energy metering system.

2.2.5 Photovoltaic array performance

Two primary important factors that strongly affect the output power, as well as module characteristics of a PV module, are irradiance and temperature [1], [2]. To implement a true MPPT algorithm, the MPP must be continuously tracked as the power output of a module changes throughout the day depending upon the irradiance and temperature. Effect of irradiance and temperature are discussed below.

2.2.5.1 Irradiance

The amount of solar irradiance falling on a solar module will largely determine its power output. The power of a module decreases almost linearly with decrease in the intensity of solar irradiance. The power output of a solar module changes during the day as solar as solar radiation varies throughout the day. The current produced by a PV module is a linear function

of the irradiance. Thus, if the irradiance is decreased to half of the peak irradiance (i.e., 1000W/m^2), the module will produce half of the peak current. On the other hand, the voltage of a module has a logarithmic function of the irradiance. Therefore, the drop in module voltage is not significant for a large change in irradiance. A typical I-V characteristic [1] of a module at 25°C for different irradiance are shown in Fig. 2.6.

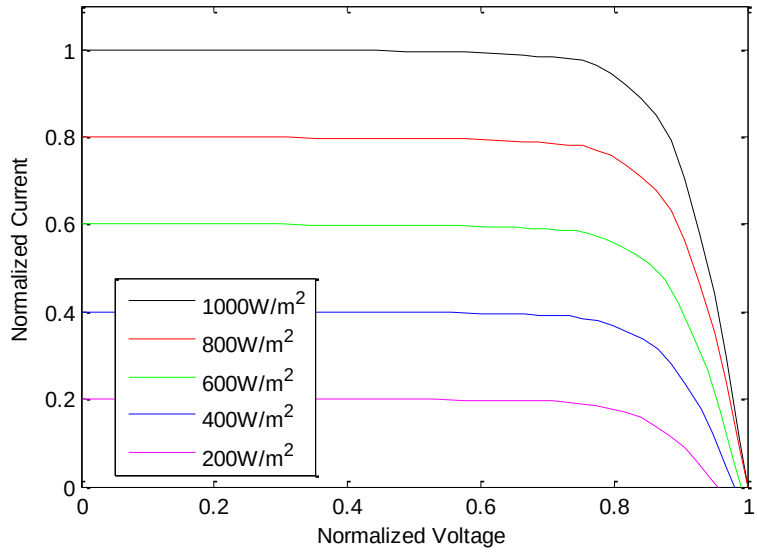

Fig. 2.6. I-V characteristic of a solar cell operating at different irradiance (at 25°C)

2.2.5.2 Temperature

The PV module are normally rated at STC, i.e. modules are rated at 25°C. However, in practice scenario the module temperature may vary from -40 °C to 80°C, depending on the different conditions such as ambition temperature radiation intensity, wind speed, mounting structure, etc. For example, a module mounted in a steel structure with air flowing around it will operate cooler, than one mounted directly on the top of a roof. As module temperature increases, the open circuit voltage V_{oc} decreases rapidly while the short-circuit current increases slowly, therefore, overall power output will decrease. PV module voltage and power temperature coefficient may range from -0.1/°C to -0.6/°C, depending on the module type and module material. A commonly used temperature coefficient for crystalline silicon is -0.5/°C. The power output of crystalline-silicon and CIS (Copper Indium Gallium) affected the most by temperature and amorphous-silicon and Cadmium-Telluride (CdTe) are affected the least. Sometimes, the temperature coefficient of the module is also available in the manufacturer specification sheet. Typical I-V characteristics [1] of a module at a fixed

irradiance for different temperatures are shown in Fig. 2.7. To calculate the module output voltage at different module temperature, the following equation can be used [1]

$$V_{mp}(T) = V_{mp}(25) + \alpha_{cv}(T - 25) \quad (2.15)$$

where

$V_{mp}(T)$ is the peak power voltage at the operating temperature of T°C.

$V_{mp}(25)$ is peak power voltage at STC.

α_{cv} is temperature coefficient of output voltage of the module.

The equation in the same form as (2.15) can be used to evaluate the power and current of a module if the temperature coefficients α_{cp} and α_{ci} are given, respectively.

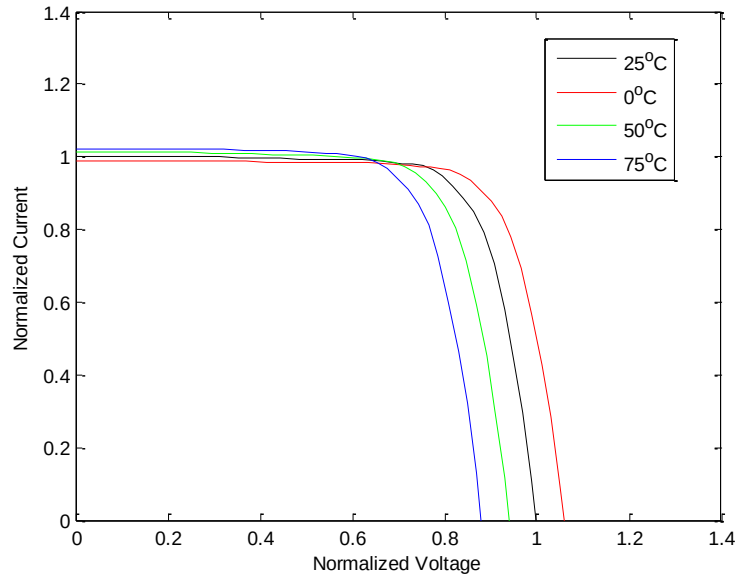

Fig. 2.7. I-V characteristic of a solar cell operating at different temperature

2.3 Overview of Backup Battery

The battery is an electrochemical device which converts the chemical energy contained in its active material directly into electrical energy and vice versa, by means of oxidation-reduction (redox) reactions. Nowadays, batteries are extensively used with renewable energy sources for the purpose of storing energy for later used. Several types of back up batteries are available in the market today, with various battery chemistries and features. In a PV system, the batteries are required as an energy storage medium. The are two main reasons for using the battery. Firstly, the solar radiation is not available during the non-sunshine hours or cloudy skies, therefore if solar energy is the only source of energy, it must be stored to supply

the load during non-sunshine hours. Secondly, for a stand-alone application during the daytime, it may not be possible to use the available solar energy produced by the PV module as energy requirement is determined by the load. In such a situation, to extract the maximum energy from the PV module (i.e. maximum power point tracking) a battery is used to store the extra energy which is generated by the PV module.

The most commonly used batteries in the PV system are the lead-acid batteries. Nickel-cadmium, lithium-ion and nickel-hydride batteries are also used, but to a much lesser extent. A short discussion about the different battery technology which is used in the PV system is given below.

Nickel-cadmium (Ni-Cd) batteries: The cells in this type of battery consist of nickel oxide and hydroxide as the anode and cadmium as the cathode with potassium hydroxide as the electrolyte. Merits of Ni-Cd batteries are fast changing, longer life, provide excellent performance under the rigorous condition, low-temperature operation etc. However, they have the relatively low energy to weight ratio and can suffer from memory effect. The memory effect can be observed in some rechargeable batteries. When the rechargeable battery is repeatedly recharged without being fully discharged, causes the battery to lose the original capacity, i.e., the performance of the battery deteriorates. Ni-Cd batteries are also not environmentally friendly due to use of cadmium [4].

Nickel-Metal Hydride (Ni-Mh) batteries: The chemical reaction at the anode is similar to that of NiCd cell. However, the cathode uses a hydrogen-absorbing alloy instead of cadmium. These types of batteries are less prone to the memory effect, which is described above. However, they are more expensive and have a relatively short storage life with a self-discharge rate than Ni-Cd battery [4].

Lithium-ion battery (Li-ion): Over the last few years, Lithium-ion (Li-ion) batteries are the most emerging battery technology, due to its highest energy density among all of the commercial battery chemistries. It captures the market for a portable electronic device like a camera, mobile, laptop, tablet, troy etc. The operation of Li-ion battery is based on Lithium ions migration between cathode and anode. During charging, the lithium ion in the cathode material migrate via a separator into the layer structure of carbon material that forms the anode and during discharging, the lithium ions in the carbon material migrate backward to cathode material. This is known as “rocking chair or shuttlecock or swing” principle.

Recently, Li-ion batteries are become popular in residential PV energy storage [4] mainly due to the following reasons

a) higher energy density(150Wh/kg) and hence very light weight of all battery chemistry
b) higher charging rate hence can be charged quickly
c) very high charge cycles (up to 7000) even during deep-cycled
d) higher cell voltage (3.5V for Li-ion battery compared to 2.0v for lead-acid battery)
e) low-temperature operation.

Nowadays, Li-ion batteries are also used in outdoor lighting applications by some manufacturing companies. Though at this moment, Li-ion batteries are too expensive compared to the lead-acid battery for mass energy storage applications. However, as this is an emerging technology, further cost reductions in the manufacturing processes are highly expected. Safety is an essential issue for Li-ion battery. It is vital to use protection circuitry into the battery pack so that thermal runaway does not cause the battery to light on fire and/or explode.

Lead-acid battery: Lead-acid batteries are almost universally used in solar PV systems because of their low cost and availability. The cells in a lead-acid battery consist of lead electrodes in an electrolyte of aqueous sulphuric acid. The anode and cathode are made up of lead (Pb) and lead oxide, respectively. At present, the lead-acid battery technologies used in PV system are divided into two major groups, namely vented (flooded) lead-acid batteries and valve-regulated lead-acid (VRLA) batteries. Generally, most PV systems are used vented and VRLA deep cycle batteries.

Vented (flooded) lead-acid batteries: Vented lead-acid batteries are used with aqueous electrolytes. In this type of battery, oxygen evolved at the positive plate and hydrogen evolved at the negative plate leave the battery, which causes loss of water. Thus, during operation, vented lead-acid batteries consume water. It requires routine maintenance like the addition of de-mineralized water at intervals to restore the concentration of the electrolyte. Proper ventilation is to be provided for oxygen and hydrogen removal. When maintained properly, the vented lead-acid battery offers a long and successful track record for application in the PV system. The batteries are topped up when required and therefore they are more

tolerant to the high-temperature operation, free electrolyte also facilities the cooling of the battery [4].

Valve regulated lead-acid (VRLA) batteries: VRLA batteries are first become available in the early 1980s and have steady growth in production since then. VRLA batteries now capture a significant portion of the solar PV battery market due to its maintenance-free features. In VRLA batteries the captive electrolyte is suspended in either a silica gel or in glass fibers called the absorbed glass mat (AGM). In-gel and AGM batteries, the H_2 ions produced at the negative plate and oxygen gas produced at the positive plate, then recombine electrochemically at the negative plates to conserve water, this feature allows the battery to use much less electrolyte. The VRLA battery occasionally releases a tiny amount of hydrogen and oxygen gas when it is under charge. The venting occurs when a low-pressure gas relief valve allows excess gas to vent when the battery reaches a predetermined maximum internal pressure, so VRLA batteries should be installed in a ventilated enclosure. VRLA batteries have the merit of high power density and require minimum maintenance as topping up is not required. At the same time, VRLA batteries degrade faster at high temperatures compared to vented lead-acid batteries.

In this study, we have proposed to use VRLA battery due to its several advantages as discussed above. VRLA battery requires more stringent charge control, which is discussed in chapter 3.

2.4 Proposed Solar-powered outdoor light control and monitoring system

In this study, two remote control and monitoring enabled, ‘smart’, energy-efficient, long-life, low-cost and low-maintenance solar-powered OLS has been developed and implemented in Illumination Engineering Laboratory of Electrical Engineering department, Jadavpur University. This systems run automatically with minimal manual intervention. Moreover, the system can send relevant information on a regular basis, related to management and maintenance of the system to the central monitoring station through a GSM network. After analyzing the received information, the central station can also control some parameters of the remote lighting system through the same network. Additionally, on receiving of the information the health and nature of the fault of the system can be predicted from the remote central station, accordingly, the maintenance personnel may be sent to the exact location.

Two separate OLSs are developed on the basis of the application area. The first one (FCOLS) is designed with cool-white LED (CWLED) for single colour lighting application such as streets, pathways, parking lots, industrial yards, security areas etc. the second one (TCOLS) is designed with colour-tunable LED (CTLED) light source for colour-tunable lighting application such as residential non-living areas, public buildings and structures, gardens, parks etc. Although, the solar-powered battery charging system is identical irrespective of CWLED and CTLED light sources. The block diagram of the solar-powered outdoor light control and monitoring system for CW LED source and colour-tunable LED source are shown in Fig. 2.8 and Fig. 2.9, respectively. The CWLED source is capable of producing 100%, 60% and 30% light output to optimize the power requirement and to maintain natural nocturnal atmosphere, simultaneously. On the other hand, a prototype is designed for colour tunable light source which can independently produce a variable CCT ranging from 2500K to 12500K and a changeable illuminance ranging from 5lx to 120lx.

The developed control algorithm is experimentally validated by a simple hardware implementation. The hardware of the system is designed by using readily available low-cost components and the control software is developed in Atmel Studio 6.2 IDE (free software from Microchip Technology Inc.) using C programming language. The IDE has been used to compile the source files to a hex code. A common USBasp programmer is then used to burn the hex file on to the target ATmega32A microcontroller unit (MCU). The supervisory MCU is used to accumulate the relevant information from different sensors and controllers, and then it processes the data according to proper scheduling.

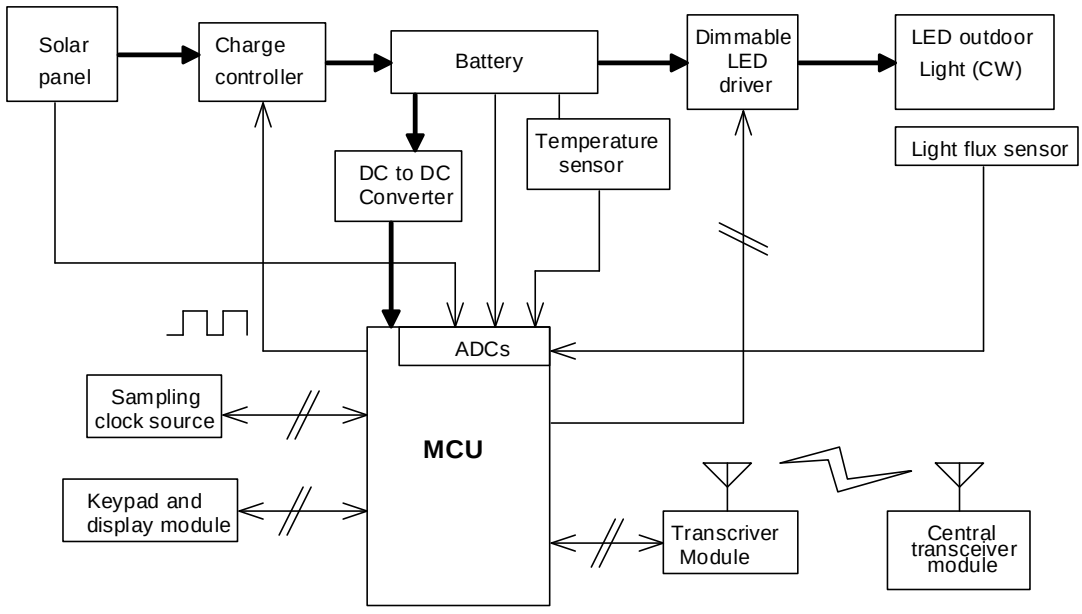

Fig. 2.8. Block diagram of the FCOLS

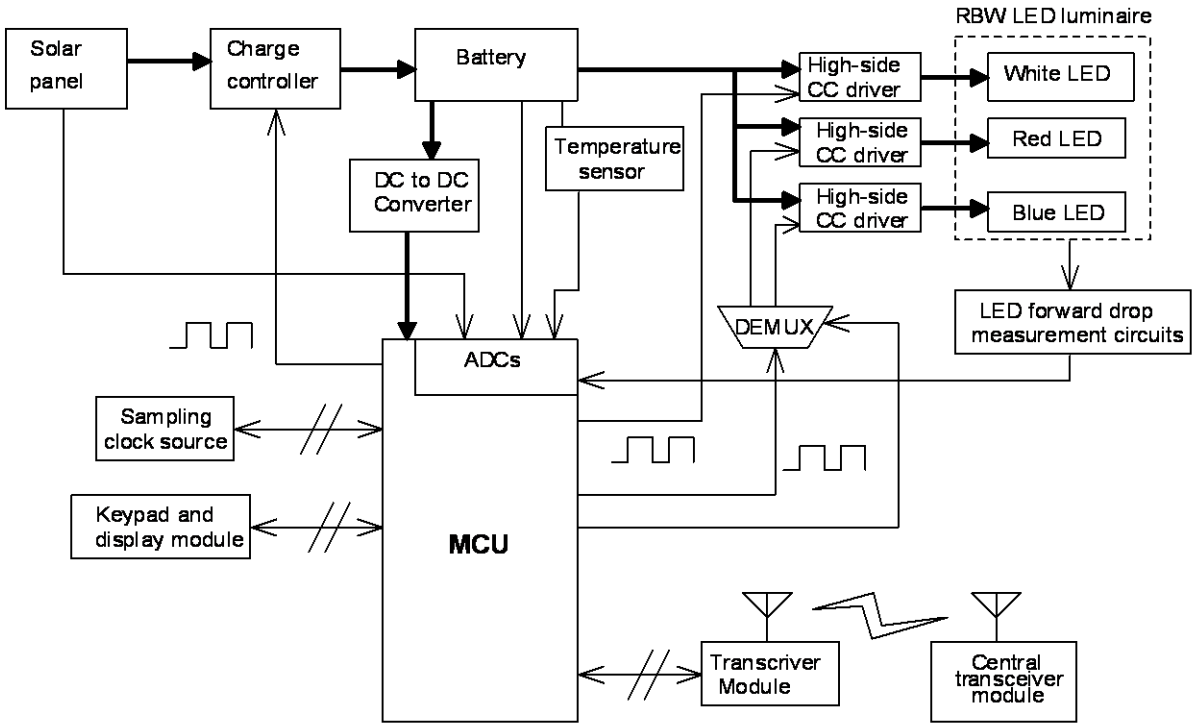

Fig. 2.9. Block diagram of the TCOLS

Short descriptions of each block of Fig. 2.8 and Fig. 2.9 are given below.

- **Solar panel:** The solar module is composed of solar cells that are responsible for collecting solar radiation and converting it into electrical energy. The solar panel arrays consist of a set of modules connected in series and/or parallel to provide the necessary energy for the load.
- **Battery:** A battery is a storage device that converts chemical energy into electrical energy and vice-versa. A storage device can prove very useful as it can store any unused energy generated by the solar panel throughout the day and, in turn, this stored energy can be used to energy a system when no sunlight is available to the solar panel.
- **Charge controller:** The charge controller or charge regulator is an electronic circuit whose function is to protect the battery by avoiding overcharge or excessive discharge through the load, which can also extend the battery performance or lifespan. Therefore, the charge controller is an energy manager in a stand-alone PV system.

- **DC to DC converter:** DC-DC converter transforms a continuous voltage to another continuous voltage with a different value. The DC-DC converter will provide the microcontroller unit (MCU) compatible voltage to power up the MCU.
- **LED driver:** An LED driver is a self-contained power supply which has an output that is matched to the electrical characteristics of the LED or LED string.
- **LED outdoor light (CW):** The outdoor luminaire is designed by using cool-white (CW) LED of 18W.
- **Temperature sensor:** The temperature sensor is mounted on the battery case for battery temperature measurement.
- **Transceiver module:** A GSM-based transceiver module SIM900 is used for SMS based GSM control and monitoring for the remote lighting system.
- **Centre transceiver module:** A desktop computer or a mobile handset is used for monitoring and control of the remote OLS.
- **Sampling clock source:** Sampling clock source provides the clock pulse at each sampling interval.
- **Keypad and display module:** A 3X1 keypad module is used for different parameter setting and a 16X2 LCD module (JHD162A) is used to display various parameters such as battery voltage, charging current, discharging current for user interfacing.
- **MCU:** A supervisory MCU is used to execute the implemented algorithm. In this study, a low-cost, CMOS, 8-bit, low-power MCU (ATmega32A) from Microchip Technology Inc. is used [5].
- **Light flux sensor:** A light dependent resistance (LDR) based light flux sensor is used to sense the intensity of the outdoor light.
- **DEMUX:** Demultiplexer (DEMUX) is used to drive blue LED or red LED string depending on the selection from MCU.
- **High-side CC driver:** A high-side, constant peak current LED driver has been designed to drive the each LED string from the battery.
- **RBW LED luminaire:** RBW LED luminaire comprises of red, blue, white LEDs which makes a colour-tunable light source.

2.4.1 Description of different states

In this implementation, the control algorithm of the OLS has been realized with six numbers of states, based on different functions of each state. The primary functions of each state are given below.

State 0: Send text messages. Wait for sufficient insolation

State 1: Bulk Charging (MPPT charging).

State 2: Absorption charging (two-level constant voltage charging).

State 3: Pulsed trickle charging and health check.

State 4: Receive administrator messages and wait for dusk.

State 5: Supply lighting load during night according to lighting schedule.

The state transition diagram of the control algorithm has been shown in Fig. 2. 10. Based on the different situations such as battery voltage, irradiance level, battery state of charge, battery health etc. the control algorithm automatically may go through six states or five states or four states throughout the day. For a specific state transition, a corresponding stimulus is required.

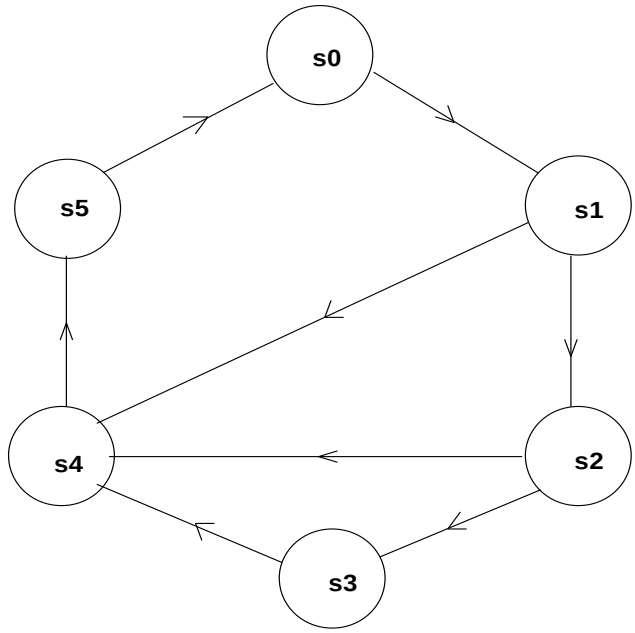

Fig. 2. 10. State transition diagram of the OLS

The flow chart of the main control algorithm is given in Fig. 2.11. At the start, some required parameters of the program are initialized. Afterward, at the beginning of each cycle, the algorithm will check the state number. After checking the state number, the program will go through a number of statements of the present state. During execution of different statements, it will simultaneously check the condition for state transition, based upon the condition the program may run through the same state or may jump to the specified state. After the execution of each statement of a state, the program will wait for the timer tick-pulse to start a fresh cycle. In this present study, the sampling period of 500ms is chosen for execution of each cycle.

The statements of each state also contain small handy modules for a specific task which is called a function in C language. This expedited the development and debugging process of the entire program due to the use of independent modules. Additionally, it is effortless to modify the program after the initial development. At the beginning of the program, some pre-defined values have also been initialized for the initial set parameter, which increases the speed of execution time of the program. These macros also facilitated the user to modify predefined set parameters. In summary, the whole program has been kept structured and readable as far as possible.

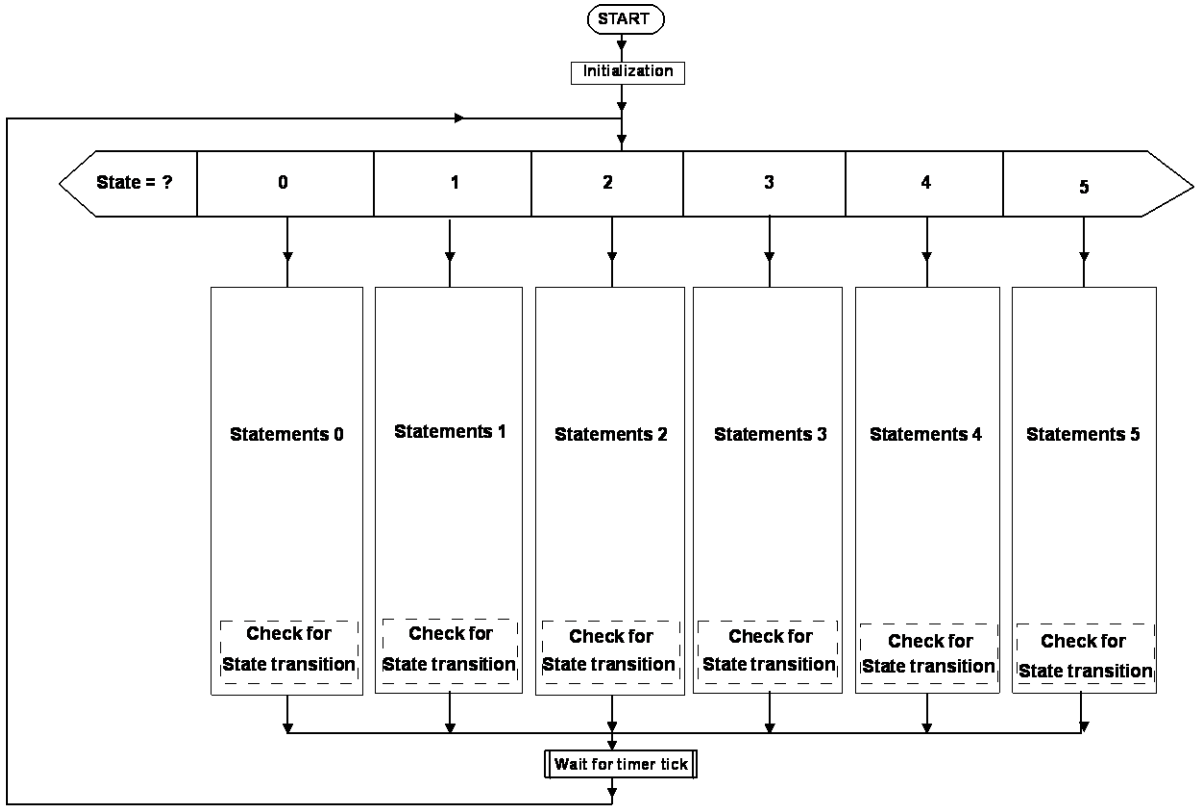

Fig. 2.11. Flowchart of the main control algorithm

2.4.2 Port allocation for the solar-powered OLSs

In this study, we have used ATmega32A microcontroller from Microchip Technology Inc. as a supervisory MCU [5]. ATmega32A is a low-power CMOS 8-bit microcontroller based on the AVR® enhanced RISC architecture. It has a very low cost and has features like 32Kbyte of in-system programmable flash memory, 32 Programmable I/O lines, 4 PWM channels, maximum clock speed of 16 MHz etc. Any other MCU, irrespective of the manufacturer, having at least six ADCs, one 8-bit resolution PWM channel, two 10-bit resolution PWM channel (for colour-tunable LED), one USART interface, one I^2C interface, 16 KB of flash memory and 16 programmable I/O lines, irrespective of the manufacturer, could also be used to implement the proposed OLS. The MCU is running at a clock frequency of 12 MHz. Port allocation of ATmega32A for FCOLS and TCOLS are given in Table 2.1 and Table 2.2, respectively. For better understanding the pin configurations of ATmega32A are given in Fig. 2.12 [5].

Table 2.1. Port allocation for FCOLS

PORT	BIT	I/O	Pin #	Function	Remarks
PA	0	I	40	Analog input	Measurement of PV module voltage
PA	1	I	39	Analog input	Measurement of battery voltage
PA	2	I	38	Analog input	Measurement of battery charging current
PA	3	I	37	Analog input	Measurement of battery discharging current
PA	4	I	36	Analog input	Measurement of battery case temperature
PA	6	I	34	Analog input	LED light level
PD	2	O	16	Heartbeat LED	
PD	3	O	17	LED_ON	To turn the light ON/OFF
PD	5:4	O	18, 19	Dimming	00 = high brightness, 01 = medium brightness,11 = low brightness
PD	7	I	21	TT2Hz	Sampling clock frequency
PD	1:0		15, 14	Serial Communication	TXD,RXD (GSM module)
PB	2:0	I	3:1	Keypad module	
PB	3	O	4	PWM output	To control duty cycle of the charger
PB	5	O	6	Backlight on/MOSI	Active low
PB	6	O	7	MISO	
PB	7	I	8	SCK	
PC	7:4 3:2	O O	29:26 25, 24	LCD data LCD control	DB 7:4 E, R/W
PD	6	O	20	LCD control	RS
PC	0:1		22,23	I2C bus	To RTC board

Table 2.2. Port allocation for TCOLS

PORT	BIT	I/O	Pin #	Function	Remarks
PA	0	I	40	Analog input	Measurement of PV module voltage
PA	1	I	39	Analog input	Measurement of battery voltage
PA	2	I	38	Analog input	Measurement of battery charging current
PA	3	I	37	Analog input	Measurement of battery discharging current
PA	4	I	36	Analog input	Measurement of battery case temperature
PA	6	I	34	Analog input	Measurement of forward drop of white LED for temperature compensation
PA	7	I	34	Analog input	Measurement of forward drop of red LED for temperature compensation
PA	8	I	34	Analog input	Measurement of forward drop of blue LED for temperature compensation
PD	2	O	16	Heartbeat LED	
PD	3	O	17	Companion LED selection	For select line of the DEMUX
PD	5	O	19	PWM dimming signal 1	For white LED
PD	4	O	18	PWM dimming signal 2	For companion LED
PD	7	I	21	TT2Hz	Sampling clock frequency
PD	1:0		15, 14	Serial Communication	TXD,RXD (GSM module)
PB	4	O	5	LED_ON	To turn the light ON/OFF
PB	2:0	I	3:1	Keypad module	
PB	3	O	4	PWM output	To control duty cycle of the charger
PB	5	O	6	Backlight on/MOSI	Active low
PB	6	O	7	MISO	
PB	7	I	8	SCK	
PC	7:4 3:2	O O	29:26 25, 24	LCD data LCD control	DB 7:4 E, R/W
PD	6	O	20	LCD control	RS
PC	0:1		22,23	I2C bus	To RTC board

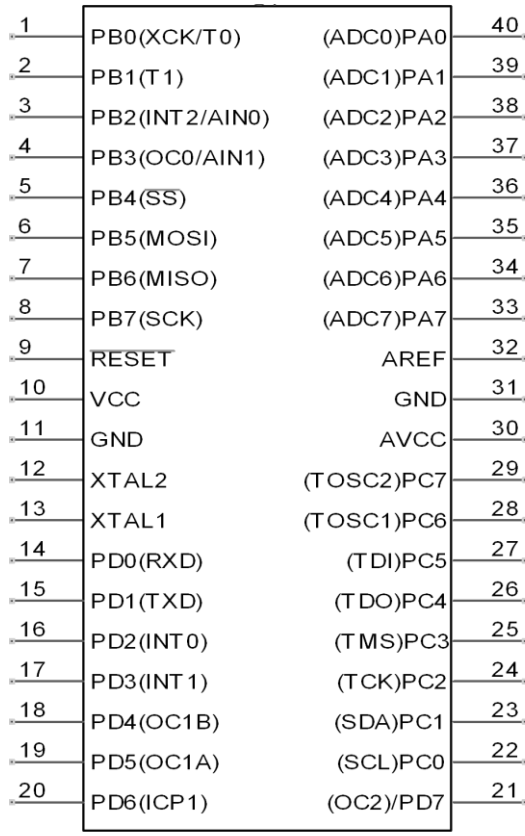

Fig. 2.12. Pin configurations of ATmega32A

2.4.3 Design of a solar electric system for the OLS

In this study, a stand-alone PV system has been designed to fulfill the daily electrical energy requirement for an LED-based OLS, where the lighting load is made on during night time. In such system, a battery is required to store the electric energy, which will be generated from a solar PV module. The battery will be charged from the PV module during the day, and the stored charge will supply the load during the night. Generally, a standalone PV system design requires the estimation of load (in terms of daily energy requirement), estimation of battery, estimation of the size of PV modules, charge controller rating etc. The design of a standalone PV system is usually done in four steps, the steps are given below:

Step 1: Estimation of daily electrical energy required.

Step 2: Estimation of system voltage and battery requirement

Step 3: Estimation of PV module requirements.

Step 4: Rating of charge controller

Step 1: Estimation of daily electrical energy requirement

In order to estimate the daily electrical energy requirement, one must know the power rating of the load and the number of hours of daily usage. The daily electrical energy consumption ε in watt-hour (Wh) is given below, where p is instantaneous power and t is the time in hours.

$$\varepsilon = \int p \ \mathrm{dt} \tag{2.16}$$

In a typical lighting system, p follows a box-car pattern as shown in Fig. 2.13, where, for simplicity, we have shown only four rectangular pulses. In such cases, the integral is replaced by summation given by

$$\varepsilon = \sum_{k=1}^{4} p_k t_k \tag{2.17}$$

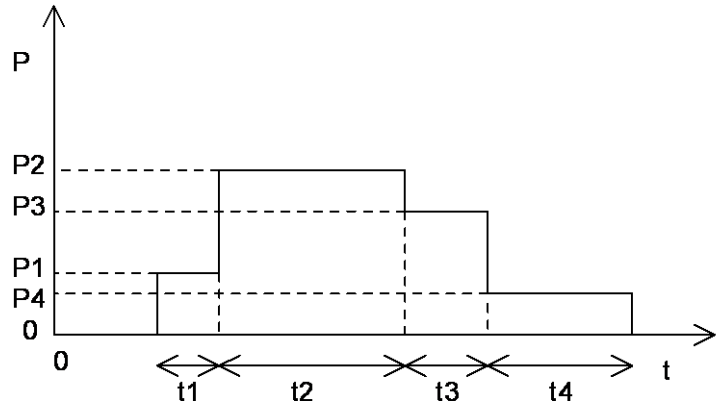

Fig. 2.13. Typical power consumption pattern of a dimmable lighting system

Step 2: Estimation of system voltage and battery requirement

Deciding the system voltage: The output voltage of the DC-DC converter is decided by the voltage at which the load operates. But the input voltage to the converter is decided by the other considerations. It depends on the battery voltage, line current, allowable voltage drop and power losses in the cables, etc. typically the terminal voltage of batteries used in PV system is 12 volts. In this study, we are considering the PV system voltage of 12V. If higher system voltage is required then it should be multiples of 12V, i.e. 24V, 36V, 48V, etc. Higher PV system voltage minimizes the current carried by the cable to reduce the power losses and voltage drop in the cable.

Rating of the battery requirement: The selection of a battery depends on two factors

I. The depth-of-discharge (DOD) of the battery.

II. System Voltage.

In lighting applications batteries with a DOD in the range of 55% - 65% are commonly used. Let us consider an ideal battery with a DOD of 100% and where the entire charge can be recovered during discharge. Under this condition the required battery capacity Q_1 can be calculated as below

$$Q_1 = \frac{\varepsilon}{E_b} \quad (2.18)$$

where E_b is the nominal battery voltage in V.

Now, the actual battery capacity Q_2 required depending on the DOD and battery efficiency can be calculated as

$$Q_2 = \frac{Q_1}{(\frac{D_d}{100})\,\eta_B} \quad (2.19)$$

where η_B and D_d are the ampere-hour efficiency and DOD of the battery, respectively.

If n_{da} is the number of days of autonomy required, the battery capacity has to be increased by a factor of $(1+ n_{da})$ that is,

$$Q = Q_2\ (\ 1+ n_{da}\ ) \quad (2.20)$$

where Q is the actual AH rating of the battery for n_{da} days of autonomy.

Step 3: Estimation of PV module requirements

To estimate the requirement of PV modules, the following parameters are required

- Commercially available Voltage, current and wattage of the module.
- Solar radiation at given location.
- The temperature of the field where the module will be installed.
- Dust level in the working environment.

The PV module capacity should be designed to supply the daily energy demand.

Peak power required P_{pv1} is given by

$$P_{pv1} = \frac{\varepsilon}{T_{PS}} \quad (2.21)$$

where T_{PS} is the peak sun hour as explained in Section 2.2.3.

Panel watt-peak required after considering the efficiency of system and module

$$P_{pv2} = \frac{P_{pv1}}{\eta_s \, \eta_{pv}} \quad (2.22)$$

where η_s is the estimated overall system efficiency considering the losses in the conducting wires and the losses in the charge controller, and η_{pv} is the average performance efficiency considering the effect of temperature and aging on the PV array.

Step 4: Estimation of charge controller rating

The output voltage rating of the charge controller is equal to the nominal voltage of the battery. The output current rating of the charge controller, by convention, is equal to the short-circuit current.

A proof-of-concept (POC) system has been developed and implemented for this study. The rating of different solar PV system after considering the factors is given below.

Step 1: Table 2.3 provides the lighting schedule in hours along with power ratings for the POC CW LED lighting system.

Table 2.3. Estimation of daily electrical energy requirement

Lighting schedule	Duration, t_k ,(hour)	Power requirement, p_k (watt)	Required energy, $p_k t_k$ (watt-hour)
17:00- 18:00	1	12	12
18:00- 22:00	4	18	72
22:00- 2:00	4	12	48
2:00- 6:00	4	09	36
Total daily electrical energy required, ε			168

Step 2: Calculated Q_2 is 27.45AH, considering V_b = 12V, D_d = 60% and η_B = 85%**.** In this case, we are considering one day of autonomy. Hence, one can select one 12 volts battery with AH capacity slightly greater than the calculated value of 56Ah Q_2. An unnecessarily large value increases the battery, and hence, system cost.

Step 3: Calculated W_{p2} is 68.57, considering global solar radiation for 5 hours, $\eta_s = 0.7$ and $\eta_{pv} = 0.7$. As the system has a one day of autonomy, 20% additional solar panel is required to charge the battery properly. So, here, one 12 volt, 85 watt-peak solar module is selected for optimal operation.

Step 4: In this case, we have considered a system voltage of 12volt, so solar charge controller voltage rating will be 12 volts. Charge controller current rating will be equal to the total short circuit current of PV array i.e. 6A in this case as specified in the datasheet.

To validate the whole system, a POC system has been built in our laboratory. In accordance with the availability of the system components, we have chosen a lower watt-peak of PV module and a lower AH of battery capacity. This does not in any way invalidate the generalized design concept developed here. For selection of module, in place of 85 watt-peak we have chosen 60 watt-peak PV module. Similarly, for selection of battery, in place of 56AH, we have chosen 26AH of VRLA battery.

2.5 Conclusion

The first part of this chapter has reviewed some fundamental of solar photovoltaic system which is required to develop the proposed system. Two primary important factors that strongly affect the module characteristics of a PV module are irradiance and temperature. Therefore, the maximum-power-point (MPP) must be tracked to extract the maximum possible power from a solar module continuously irrespective of variable irradiance and temperature. . The final part of this chapter has presented the design procedure of a stand-alone PV system. Based on this calculation, a POC system for solar-powered LED lighting has been developed and implemented, in the present work. Details of multi-stage battery charging system and LED lighting systems have been described in chapter3 and chapter4, respectively.

The methodology and implementation approaches used in this work is quite simple, straightforward, and do not require any complicated algorithm or costly component or costly tools. The hardware of the whole OLS has been implemented by using readily available components including a low-cost microcontroller.

References

[1] A. Luque and S. Hegedus, *Handbook of Photovoltaic Science and Engineering*. 2011.

[2] C. S. SOLANKI, *Solar Photovoltaics - fundamentals technologies and applications*. 2016.

[3] C. C. H. Jacob Millman, *INTEGRATED ELECTRONICS: ANALOG AND DIGITAL CIRCUITS*. NEW DELHI: Tata McGraw-Hill Publishing Company Limited, 1991.

[4] C. D. Rahn and C. Y. Wang, *Battery Systems Engineering*. 2013.

[5] "ATmega32A - 8-bit AVR Microcontrollers." [Online]. Available: https://www.microchip.com/wwwproducts/en/ATmega32A. [Accessed: 14-Mar-2019].

Chapter 3
Development of Solar-Powered Multi-Stage Battery Charger

3.1 Introduction

In this chapter, a description of the developed solar-powered multi-stage battery charging system is presented. A typical off-grid PV system consists of a PV array, charge controller, battery and load, as mentioned earlier. In such a PV system, the battery accounts more than 40% of its overall cost throughout the life [1]. So, increase of the life-span of the battery leads to a significant reduction in the system operating cost. Additionally, lead is hazardous for the environment due to the toxicity of its organometallic compound. Due to this reason, for the last two decades, lot of research work have been carried out for extending the life-span of the lead-acid batteries. Moreover, the increase of battery life also improves the reliability of the overall system. The life-span of a battery can be extended by adaptation of a proper battery charging scheme and avoiding excess overcharge and deep discharge. Charging process of a VRLA battery is fairly straightforward, but when the maximization of battery life and minimization of the charging time are considered, it becomes somewhat involved. The factors which mostly affect the life-span of a VRLA battery are discussed below.

Overcharging: During overcharge, excess cell voltage converts the electrolyte into hydrogen and oxygen gases, respectively, at the negative electrodes and positive electrodes. Now, when this pressure builds up to a sufficient high level due to overcharge, the pressure release valve of the battery opens automatically and releases the generated gas. Due to this process, an amount of electrolyte dries out which results in loss of battery capacity.

Undercharging: During undercharge, the cell voltage is lower compared to full charge voltage, which causes the charging current to be zero before reaching to the full charge capacity. This causes the crystal of lead-sulphate, which developed during discharge, to remain at the electrodes. Thus, it reduces the active surface area, consequently it reduces the battery capacities.

Operating temperature: Operating temperature of a battery has a significant effect on capacity, life-span, water consumption, etc. As a rule of thumb, for every 8° C to 10°C increment in the operating temperature reduces the battery lifespan by half [2]. The effect of battery temperature on charging voltage is discussed later.

Storage: If a battery is stored for long periods without charging, sulphation occurs due to undercharging on the battery terminal and the electrodes. This sulphation also reduces the charge capacity of the battery.

3.2 Requirement of the multi-stage charger for VRLA battery:

There are several VRLA battery charging schemes such as constant current (CC), constant voltage (CV), constant current-constant voltage (CC-CV), intermittent charging method (IC), interrupted charge control (ICC), three stage charging (TSC). Among them, CC and CV are the traditional charging technique for the VRLA batteries. They are discussed below with their limitations.

- **CC:** In this method, the charging current is set to the maximum rated current of the battery. However, small charging current will increase the charging time. Also, some cells of the battery may reach to full charge before others, so, it very unsuitable to decide when the battery has reached to full SOC. Thus, this technique is not recommended for charging a number of cells when connected in series.

- **CV:** In this method, a specified charging voltage is applied across the battery terminal. The specified voltage has been set in accordance with the manufacturer specification. However, this method needs to limit initial charging current. Otherwise, it draws a large initial current which may affect the battery performance and it also increases the battery temperature.

Keeping in mind the limitation of the traditional techniques, the modern charge control techniques are developed based on multi-mode control. Generally, the modern charge control techniques are CC-CV, intermittent charging (IC), three-stage charging (TSC) and interrupted charge control (ICC). These are being discussed below.

- **CC-CV:** In this method, a combination of CC and CV charging is used. In the first stage, the battery is charged using a constant current until the battery voltage reaches a set point

voltage. In the second stage, a constant voltage is applied and the current decreases. CC-CV battery charging scheme is shown in Fig. 3.1. The continuous voltage is present across the battery to keep the battery at 100% SOC. During this time, the battery can draw a small amount of current even after the battery is fully charged. So, the battery may be overcharged which results in grid corrosion, gassing and increase battery temperature, ultimately, affects the life-span of the battery [3].

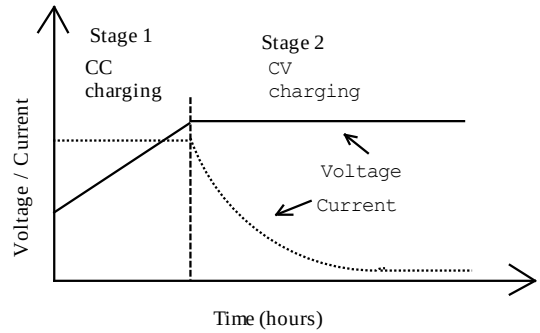

Fig. 3.1. CC-CV battery charging scheme

- **IC:** In this technique, the battery is charged in a short period up to an upper threshold voltage V_{BUT} and then it is kept open circuit until the battery voltage reaches a predefined lower threshold voltage V_{BLT}. When battery voltage reached V_{BLT}, it again starts to charge at full capacity. A typical current and voltage waveform of IC method is shown in Fig. 3.2. Usually, this method employs CC charging between V_{BUT} and V_{BLT} [2], [4], [5]. CC charging of upper threshold voltage 2.45V per cell does not ensure 100% SOC [6]. Thus, a battery may be undercharged even after completion of a charge cycle. Additionally, the battery may be kept for an open circuit for a long time, as a result, the battery cannot maintain full charge state continuously.

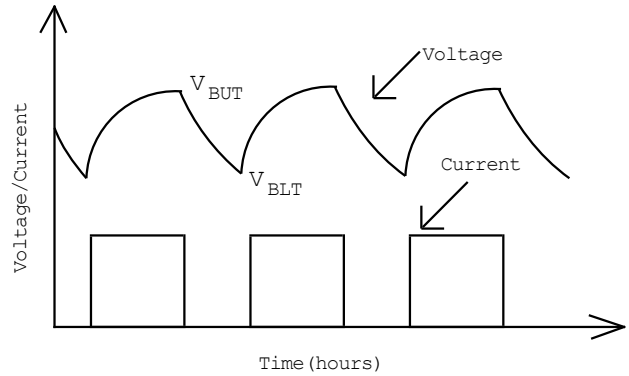

Fig. 3.2. Typical waveform of voltage and current for intermittent charging

- **TSC:** Three stage charging (TSC) method supplies power to the battery is three steps as shown in Fig. 3.3. The three stages are bulk charging, absorption charging and float charging. In the first step, the battery is charged up to a predefined upper threshold voltage at the rated maximum current. In the second step, the battery terminal voltage is maintained at a constant value while the charging current decreases. In the third step, a small amount of current is supplied to the battery to maintain the battery voltage.

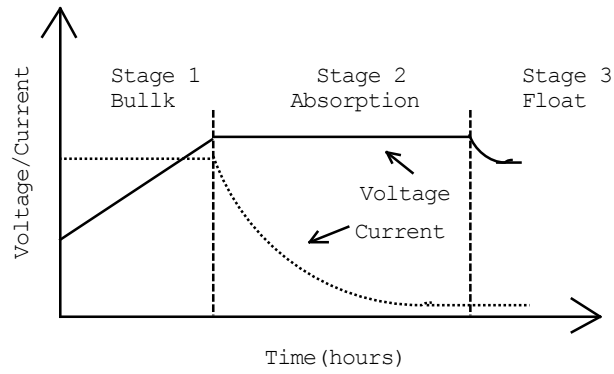

Fig. 3.3. Typical graph of voltage and current for three-stage charging

- **ICC:** Interrupted charge control (ICC) is a modification of the IC method where this method avoids the undercharging problem of IC method. This technique charges the battery in four modes as discussed below.

  Mode1: the battery is charged with a CC-mode at the rate of 0.1C. The battery voltage is continuously tracked during this mode.

  Mode2: when the battery voltage reaches a predefined upper threshold voltage V_{UTh}, the battery will be kept in open circuit until it reaches a lower threshold voltage V_{LTh}.

  Mode3: the battery is charged with a pulsed-current mode of 0.05C until the upper threshold voltage has been reached.

  Mode4: the charging current is then terminated and kept open circuit. Again modes 1, 2 and 3 are repeated when battery charge false to 97% of SOC. Typical graph of voltage and current for ICC method is shown in Fig. 3.4. The black-shaded portion of this figure indicates the pulse-current charging for small time interval.

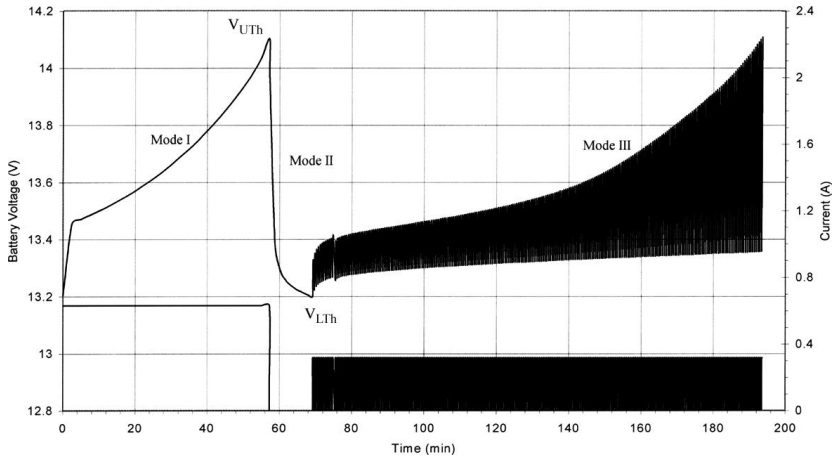

Fig. 3.4. A typical graph of voltage and current for ICC [2]

From the above discussion, it can be concluded that the multi-mode charger is essential to maximize the battery life and minimize the charging time for VRLA battery. The proposed multi-stage charger has been discussed in the next section.

3.3 Proposed multi-stage charging algorithm for VRLA battery

The proposed charging scheme has multiple objectives which ensure the optimum use of solar energy as well as the optimum performance of the VRLA battery. The objectives are given below.

- Objective 1: To ensure that the solar energy is harvested efficiently by the use of proper MPPT algorithm, which is discussed later in this chapter.
- Objective 2: To ensure that the battery is appropriately charged through the use of multi-stage charging algorithm with proper temperature compensation.
- Objective 3: To balance the power flow from PV module to the battery irrespective of temperature, irradiance and load.
- Objective 4: To estimate the state-of-charge (SOC) of VRLA battery by using a suitable algorithm.
- Objective 5: To monitor the health of the battery from the remote place by using GSM technology.

In this study, to achieve the multiple objectives the hardware as well as software is developed and implemented in a stand-alone solar PV system. A detailed block diagram of the proposed multi-stage battery charging system is shown in Fig. 3.5.

The traditional CC, CV or CC-CV charge controller uses analog ICs such as UC384x, L6561, etc to implement the algorithm. However, the circuit of compensation parameters is made up of capacitors and resistors. The value of this capacitor and resistor are dependent on the ambient temperature and aging. Thus, the set voltage/current may change throughout the life-span. Keeping in mind the disadvantages of the analog controller, our proposed technique uses digital control technique. In digital control, the required compensation and set parameters are stored digitally which helps to mitigate the aging and temperature issue. Additionally, it has some advantages such as programmable compensator, programmable parameter tuning, simplify the implementation of complex control technique, immune to signal noise etc. In this study, a low-cost microcontroller, ATmega32A from microchip is used as a supervisory controller.

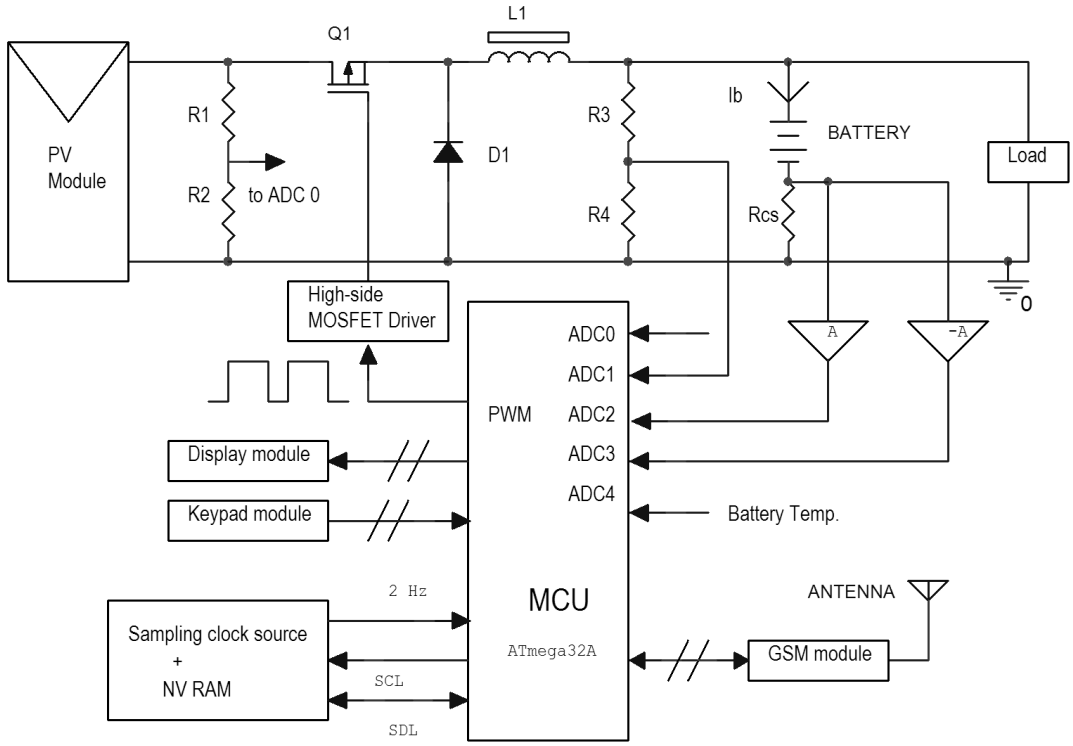

Fig. 3.5. Simplified block diagram of the multi-stage battery charging system

Comparing the modern charge control techniques of VRLA battery, TSC has the highest charging efficiency when the battery is charged from a PV module as discussed in [7]. IC and

ICC methods disconnect the battery from the PV module if a predefined upper-threshold voltage has been reached and kept open-circuit for a long time until a lower threshold voltage is reached. During this time battery is not charged from the PV module, as a result, the available solar energy cannot be utilized properly to maintain a continuous full charge condition. Hence, at the end of the day, the battery may not be charged to 100% SOC. Specifically, these two methods (IC and ICC) are suitable for standby applications where the battery is not regularly discharged. Hence, in this study, we have proposed a modified multi-stage charging algorithm, where the bulk charging is based on MPPT algorithm for better efficiency and absorption charging is modified to two-stage constant voltage charging for avoiding over-charge. A typical voltage and current waveform of the proposed multi-stage battery charging technique is shown in Fig. 3.6. In this implementation the charging process consists of following three stages.

- **Stage1:** In this stage, the charging process is started when sufficient solar radiation falls on the solar module. The MPPT-based battery charging scheme has been adapted to charge the battery up to a predefined upper threshold voltage, V_{BREFH}. During this stage, the battery voltage is continuously monitored. This stage restores around 70-80% of SOC.

- **Stage 2:** When the battery voltage reaches to V_{BREFH}, the charging algorithm automatically jumps from MPPT charging to CV charging. In this stage, the battery voltage goes through two-stage CV charging process. In the first and second step the output voltage of the converter has been set to a higher threshold voltage, V_{BREFH} and a lower threshold voltage V_{BREFL}, respectively, as shown in Fig. 3.6. In this state, the battery current is monitored continuously.

- **Stage3:** When the battery current reaches to a lower threshold current denoted by $I_{OTL,}$ the charging process automatically jumps to State3. This state maintains the battery at 100% SOC. It has two stages. In the first stage, the battery is charged to constant voltage for a given time interval and then the battery is kept open circuit for a given time. This stage is also known as trickle charging stage. In the second stage, the health of the battery is monitored by comparing the battery voltage with a predefined value. These two stages repeat until low solar insolation detected by the system.

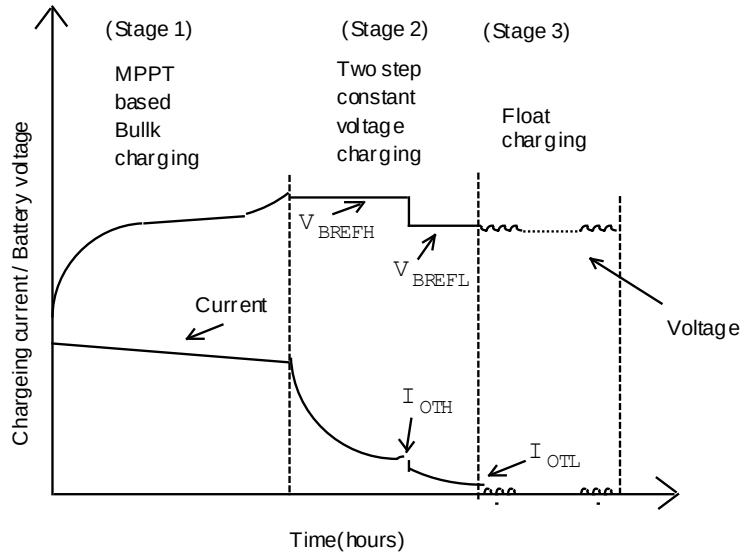

Fig. 3.6. Typical voltage and current waveforms of the proposed three-stage battery charging technique

3.3.1 MPPT-based bulk charging

In most of the previous studies, bulk charging has been implemented by using a constant current charging algorithm. In our case, the battery is charged from the PV module. Therefore, constant current cannot be maintained during bulk charging especially during rapidly variable atmospheric condition throughout the day. Hence, the CC based bulk charging has been substituted by the MPPT-based charging algorithm to charge the battery more efficiently from the PV module.

After reviewing various MPPT algorithms as discussed in chapter 1 of this study, the MPPT method has been implemented at the load side, as the system proposed by us has some advantages over other MPPT techniques. In most of the stand-alone PV systems, monitoring of the battery current and voltage are required for the sake of battery protection and implementation of different charge control techniques. Additionally, in our case, it is also necessary to monitor the SOC of the battery. For implementation of SOC monitoring, an accurate measurement of battery current is mandatory as explained in Section 3.4.2.8. Thus, the MPPT algorithm is implemented using the same output voltage and current sensors without the use of additional sensors. This consequently reduces the hardware cost as well as the computational burden of the controller.

MPPT-based buck charging is the first charging stage and in this stage the battery capacity is replenished to 70-80% of SOC at a fast rate. The battery is charged in the bulk charging mode until its terminal voltage reaches a specified threshold voltage of V_{BREFH}. The IEEE Standard 1361^{TM}-2014 [8] specifies a value of V_{BREFH} as 2.4V/cell (i.e., 14.4V for a 12 V battery) at 25°C for VRLA gel batteries. This predefined upper threshold voltage V_{BREFH} value may also be specified in the manufacturer specification sheet. Accordingly, the value of V_{BREFH} should be programmed in the control algorithm to get optimum battery performance.

In the present implementation, the employed MPPT technique is based on a modified perturb and observation (P&O) technique.

3.3.1.1 Proposed P & O technique

Generally, in conventional P & O technique, the fixed perturb signal is either PV reference voltage or current [9]–[11]. The basic principle of this technique and its implementation has already been discussed in Section 1.7.1 of Chapter 1. For ready reference, we reproduce an equation formed by combination of equations (1.4) and (1.5) as

$$V_{PV,\,r}\,(k+1) = V_{PV,\,r}\,(k) + m\,V_{PV,\,st} \qquad (3.1)$$

where k and (k+1) are the present and the next sampling instants, respectively. $V_{PV,st}$ is the search step of constant magnitude by which the reference $V_{PV,r}$ [k] is incremented or decremented depending on whether m is +1 or -1. In addition, there is a special condition in which m is given a value of 0 and this occurs when the MPP has been reached. A large value of $V_{PV,st}$ contributes to faster dynamics (i.e. attainment of MPP) but in conjunction with excessive undesirable steady-state oscillation. On the other hand, a small value of $V_{PV,st}$ leads to slower dynamics of the converter which results in inefficient use of the PV array. Therefore, for a fixed perturbation system a suitable value of $V_{PV,st}$ should be chosen, so that, a satisfactory tradeoff between excessive oscillation and slow dynamics is achieved.

Currently, most of the MPPT techniques use the duty cycle of the converter as a perturb signal to implement the MPPT algorithm [12]. This method simplifies the whole control system as duty cycle is directly manipulated instead of indirect manipulation by PV current or voltage control loop. The technique is based on the principle that the duty cycle versus power (D-P) curve has a unique maximum power point corresponding to a specific duty cycle. For fixed perturbation method, the following expression can be used to reach the MPP.

$$D\,(k+1) = D\,(k) \pm \Delta D \qquad (3.2)$$

where D is the duty cycle and ΔD is the constant search step. This scheme with fixed perturbation suffers from speed versus oscillation tradeoff problem. To mitigate the problem a variable, or adaptive, step size is recommended in literature. For voltage perturbation with variable step size, the following simple expression can be used to implement the MPPT algorithm [13].

$$V_r\,(k+1) = V_r\,(k) \pm Q \left|\frac{\Delta P_i}{\Delta V_i}\right| \tag{3.3}$$

where the coefficient Q is the scaling factor, which is tuned by the system designer. ΔP_i and ΔV_i are the increments in input power and voltage of the DC-DC converter, respectively, for two consecutive sampling instants.

For duty cycle perturbation with variable step size, the following basic equation can be used to evaluate the MPP [14], [15].

$$\Delta D(k) = \pm Q \left|\frac{P_i(k)-P_i(k-1)}{D(k)-D(k-1)}\right| \tag{3.4}$$

where ΔD(k) is defined to be D(k+1) – D(k). One major difficulty of adaptive step size is to find an appropriate value of Q, as it determines the optimum performance of the MPPT algorithm. Manual tuning of Q is laborious and the evaluated value is only applicable for a given system and environmental condition [15]. Therefore, an automatic evaluation of parameter Q at the startup is needed for a good MPPT tracking system. The determination process of Q is discussed below.

It is suggested in [15] that the approximate derivative of power with respect to voltage (ΔP/ΔV) is a better suited parameter for deciding the perturbation step size than (ΔP/ΔD). It is shown in Fig. 3.7 that the true derivative dp/dv varies smoothly with the output voltage of the module. Therefore, the following equation can be used to evaluate the duty cycle for the optimum operation.

$$\Delta D(k) = \pm Q \left|\frac{P_i(k)-P_i(k-1)}{V_i(k)-V_i(k-1)}\right| \tag{3.5}$$

As discussed in Chapter 1, most of the adaptive P & O techniques are implemented at the output of PV module i.e., the output voltage and current of a PV module are directly measured to implement the algorithm. However, a more rational approach for the case of battery charging systems should be the maximization of the input power to the battery (which is the output power of the PV module) under variable insolation and temperature conditions. In this

study, we have developed a system which maximizes the latter power. This would require the PV array and DC-to-DC converter to be considered as a single cascaded system whose output power has to be maximized

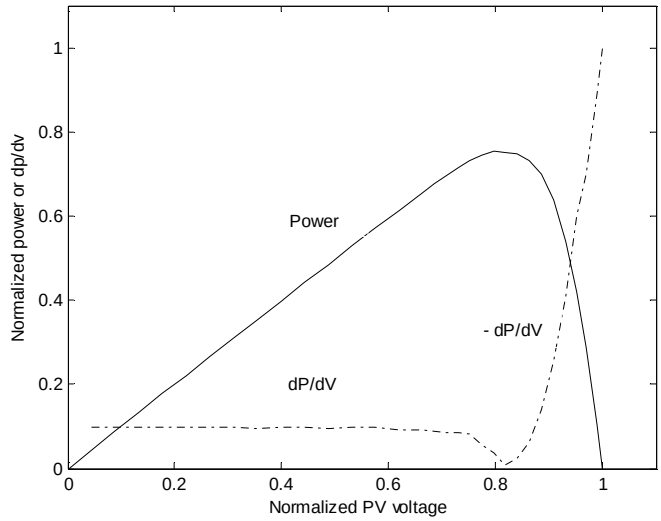

Fig. 3.7. Variation of dP/dV with PV voltage

The relationship between the input power P_i and the output power P_o of the DC-to-DC converter is given by the power balance equation

$$P_i = P_o + P_L \tag{3.6}$$

where P_L is the power loss in the converter. For most power converters of any practical interest the value of P_L is kept small compared to the rated P_o in order to attain a high efficiency, η:

$$\eta = \frac{P_o}{P_i} \tag{3.7}$$

A simple loss model of a DC-DC converter can be given by the sum of a constant loss and a variable loss proportional to the output power:

$$P_L = \alpha_1 + \alpha_2 P_o \tag{3.8}$$

where α_1 and α_2 are constants. In general P_i and P_O are functions of the input voltage V_i. Substitution of equation (3.8) to equation (3.6) yields

$$P_i = \alpha_1 + (1+ \alpha_2) P_o \tag{3.9}$$

Taking the derivative of both sides with respect to V_i

$$\frac{dPi}{dV_i} = (1+ \alpha_2) \frac{dPo}{dV_i} \quad (3.10)$$

At MPP (of converter input power) $dP_i/dV_i = 0$, which from equation (3.10) implies $dP_o/dV_i = 0$. In other words, both the input and output powers have their respective maximums at the same input voltage V_i. This fact has been graphically demonstrated in Fig. 3.8. Our proposed algorithm tries to find out the point at which dP_o/dV_i is zero. For the loss model assumed this will ensure the maximum of both the input and output power of the converter. It may be noted here that the proposed loss model includes both the 'constant loss' ($\alpha_2 = 0$) and 'only linearly variable loss' ($\alpha_1 = 0$) as special cases. Thus our proposed method is valid for these two cases also.

In this study, we implemented the P & O technique based on the following basic equation

$$\Delta D(k) = \pm Q \left| \frac{P_o(k) - P_o(k-1)}{V_i(k) - V_i(k-1)} \right| \quad (3.11)$$

Although, there are apparent ambiguities in the signs of the right hand sides of equations (3.4), (3.5) and (3.11), it is resolved by considering the sign of $(P_o (k) - P_o (k-1))/ (V_i(k) – V_i(k-1)$ as will be shown in the next section.

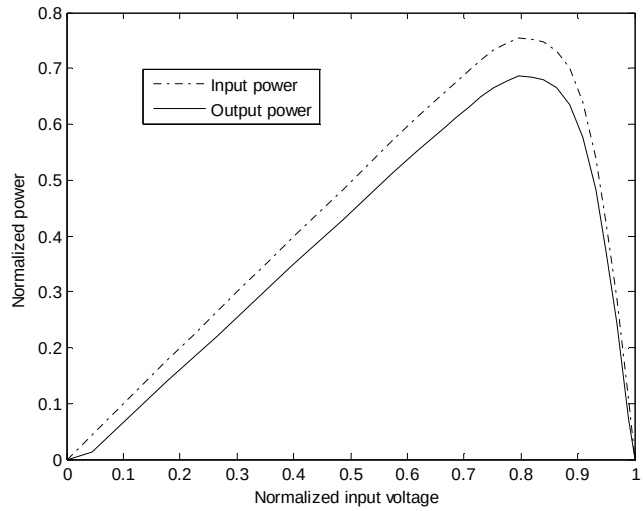

Fig. 3.8. P_i - V_i and P_o - V_i characteristics for the variable loss converter

The factor $Q > 0$ plays a very important role in equation (3.11). Firstly, one may observe that the magnitude of ΔD at a particular sample is obtained by multiplication of the magnitude of $\Delta P_o/\Delta V_i$ in the previous sample, a process that justifies the name 'scale factor'.

The second observation is that Q is not dimensionless and specifically, in this case, has a dimension of current. The value of Q can be determined from equation (3.11) as

$$Q = |\Delta D| \left|\frac{\Delta V_i}{\Delta P_o}\right| \tag{3.12}$$

where the increment ΔD refers to that between the k^{th} and $(k+1)^{th}$ sampling intervals and ΔP_o and ΔV_i refer to those between the $(k-1)^{th}$ and k^{th} sampling intervals. A slight reinterpretation of equation (3.12) will be utilized in finding a suitable value of Q at start-up of the MPPT algorithm.

3.3.1.2 Description of the implemented MPPT algorithm

The flowchart of the proposed MPPT algorithm, which is an expansion of the path corresponding to state1 in Fig. 2.11, is illustrated in the flowchart of Fig. 3.9. In this figure, ψ and ψ_old will indicate the value of variable ψ in the current and the previous sampling instants, respectively. To start the algorithm, different values of user defined constants and run-time variables are needed to be initialized for state1. The values of user defined constants and variables are given in Table 3.1 and Table 3.2, respectively. Two different variables, D and DuCy, both of which are used to represent the duty cycle of the DC-DC buck converter, are present in the flowchart. While D is a floating point number in the range (0, 1), DuCy is a positive integer in the range (0, 255). The variable DuCy can be straightaway loaded to the PWM register of Timer 0 of the MCU used as mentioned in Tables 2.1 and 2.2 of Section 2.4.2. The value of DuCy is converted to the duty cycle of the rectangular pulses at the OCR0 pin whose actual value is (DuCy+1)/256. The ideal value of the duty cycle D computed anywhere in this flowchart is converted to DuCy firstly by rounding off 256D to the nearest integer and then subtracting 1 from the result. This may, in general, give rise to a small difference between the ideal D and the actual outputted D. The other alternative of using a single variable DuCy and computation of a change of the same would have caused an unnecessary oscillation of the output due to the large granularity in DuCy.

State1 has three phases (or, sub-states) namely phase0, phase1 and phase2. In phase0, when adequate insolation has been detected at the beginning of a day, the controller will increment the value of the duty cycle D in very small steps of about 0.01 till it reaches a specific value D_1 where the output current is equal to or a little greater than a predefined value of I_{OMIN}. The system remains in this phase for a number of sampling intervals

depending on the available insolation and the state-of-charge of the battery. On attaining this condition, it measures and records the corresponding input voltage V_{i1} and output power P_{o1}.

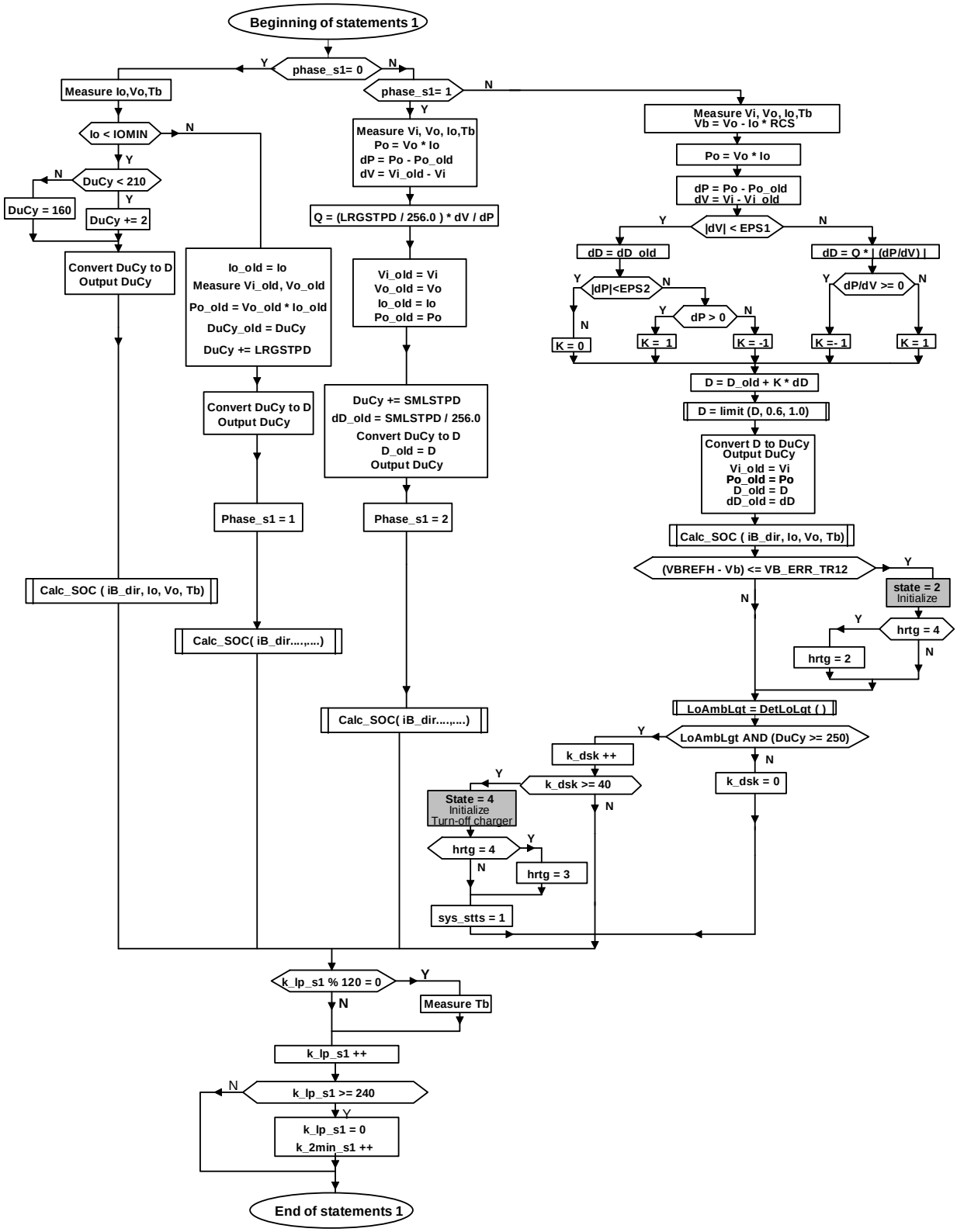

Fig. 3.9. Flowchart of the proposed MPPT algorithm

The system remains in this phase for only one more sampling period in which it collects data from which a value of the scaling factor Q can be computed. Towards this goal, a large increment in D equaling D_{LRG} is then applied. A value of D_{LRG}= 0.1 worked very well in our system. This produced a new value of duty cycle $D_2 = D_1 + D_{LRG}$. After this the system moves to phase1, when it is ready with the responses V_{i2} and P_{o2}.

Table 3. 1: User define constants for state 1

Constants	value
EPS1	0.02
EPS2	0.1
I_{OMIN}	0.25
SMLSTPD	10
LRGSTPD	25
RCS	0.02
VB_ER_TRR12	0.05
V_{BREFH}	14.4

Table 3. 2: Initialization of run time variables for state 1

Variables	value
phase_s1	0
k_lp_s1	0
k_2min_s1	0
k_dsk	0

At start of phase1, the values of V_{i2} and P_{o2} are measured so that $\Delta V_i = V_{i2} - V_{i1}$ and $\Delta P_o = P_{o2} - P_{o1}$ are known. Strictly speaking, for use in equation (3.12), ΔD cannot be equated to D_{LRG} because this is not the value of ΔD that is calculated by the algorithm for use in the next sample but is the value of ΔD in the current sample. Our experience indicates that a highly satisfactory value of Q, in terms of speed of response and stability, can be obtained by substituting $\Delta D = D_{LRG}$ in equation (3.12). Following this a small increment in $\Delta D = D_{SML}$ is applied and the system enters phase2. A value of D_{SML} = 0.04 worked satisfactorily.

The charge controller remains in phase2 of state1 till MPPT charging ends. In this phase the controller output D is generated in every sampling period T_S of the system. If the incremental output voltage dV is less than a small positive value EPS1, the algorithm maintains the same dD as in the previous sample. This is used to mitigate a large change in D that may be caused by division by a small number. Additionally, if the incremental power dP is less than a preassigned power, EPS2, the algorithm maintains same D as in the previous sample to avoid unnecessary changes in D. In this algorithm, the values of EPS1 and EPS2 are chosen 20mV and 0.1W, respectively.

A direction variable K is used to indicate the increment in duty cycle. K= +1, -1 and 0, respectively, indicate $\Delta D > 0$, < 0 and $= 0$. By taking $K = -\text{sgn}(\Delta P_o / \Delta V_i)$, the direction of the next step is automatically obtained. For example, if $\Delta P_o / \Delta V_i \leq 0$, K becomes 1 and D has to be increased. On the other hand, if $\Delta P_o / \Delta V_i > 0$, K becomes -1 and D has to be decreased. The apparent ambiguity in the sign of ΔD in equation (3.11) is thus resolved.

A large change in D may occur due to a high value of incremental power ΔP_o, therefore the system may be pushed far away from the MPP. This situation is similar to that of a classical integral controller. This necessitates the limiting of D to avoid *wind up* of the control. The upper and lower limits have been kept at 1.0 and 0.6, respectively, to obtain speedy recovery from the saturation condition. The limit values have been fixed experimentally.

3.3.2 Two-stage constant voltage charging (Absorption charging)

State2 represents the control algorithm for two-stage constant voltage charging. Once the battery voltage reaches a predefined upper threshold voltage V_{BREFH}, the charger algorithm automatically moves from bulk charging stage to absorption charging stage i.e. the controller transits from MPPT charging to constant voltage charging. In MPPT-based bulk charging stage, the battery recovers approximately 70-80% of the SOC. The remaining 20-30% of the SOC is replenished at the constant voltage mode in order to protect from the over-charging of the battery. The algorithm for two-level constant voltage charging and its controller have been discussed in the next sub-sections.

3.3.2.1 Algorithm for two-stage constant voltage charging

In state2, the battery voltage is gone through two-stage constant voltage charging namely "high absorption charge" and "low absorption charge". In high absorption charge, the battery voltage was set to $V_{BREFH,}$ in this case 14.4V and the controller monitors the charging current continuously. If the charging current falls below a high threshold current $I_{OTH,}$ the controller moves to the second stage, i.e. low absorption charge. In this stage, the controller will maintain a lower constant voltage $V_{BREFL,}$ in this implementation, 14.1V until the charging current reaches a lower threshold current I_{OTL}. The two-stage constant voltage is implemented by using the same MCU as a PI controller which is explained in the next section.

The flowchart of two-stage constant voltage charging algorithm is illustrated in Fig. 3.10. In this figure, ψ and ψ_old will indicate the value of variable ψ in the present and previous sampling instant, respectively. To start the algorithm, different values of user define

constant and run-time variables are needed to be initialized for state2. The values of user defined constants and variables are given in Table 3.3 and Table 3.4, respectively.

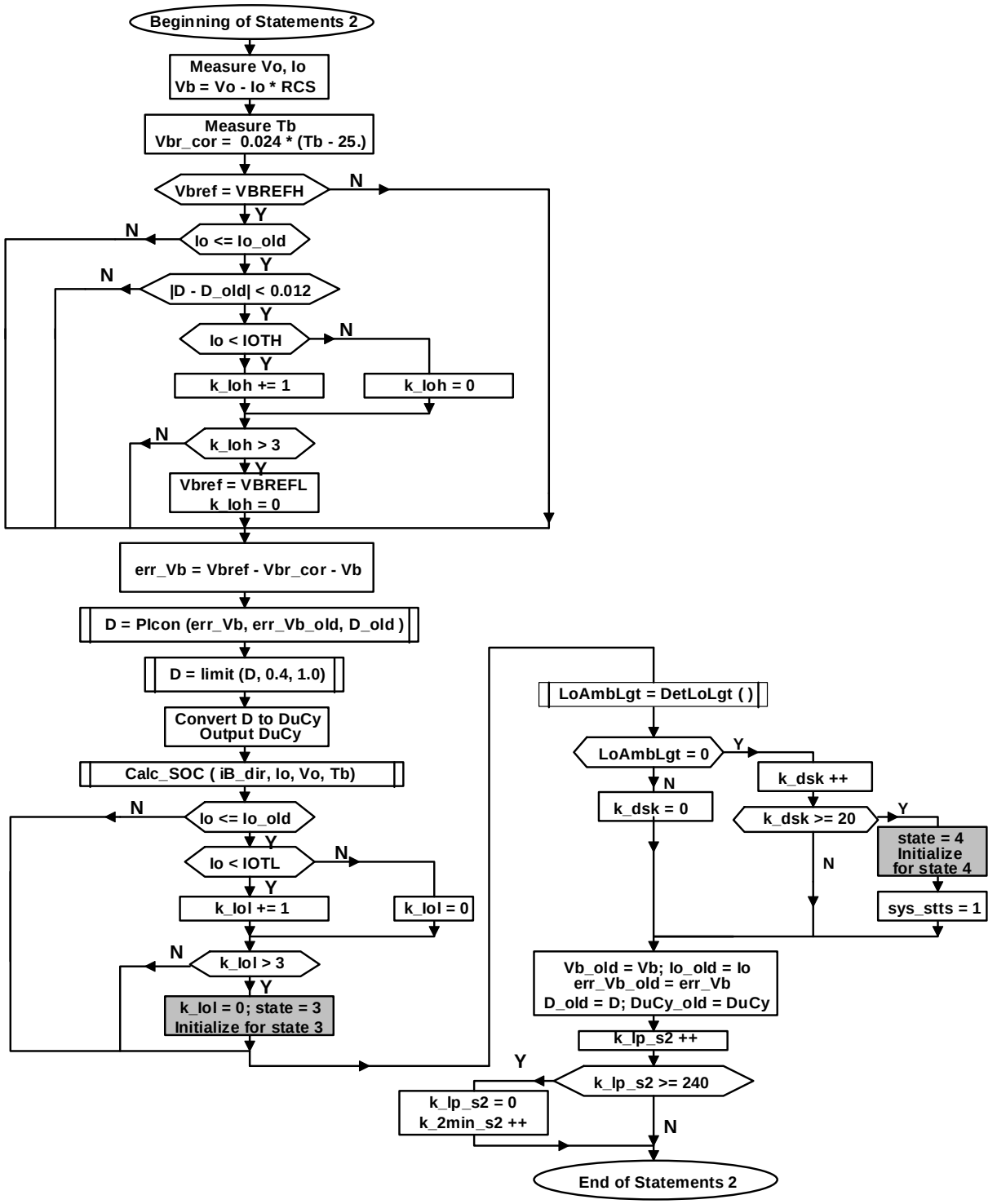

Fig. 3.10. Flowchart of two-stage constant voltage charging

The loop counters k_lp_s2 and k_2min_s2 are incremented in every 500ms and 2 min, respectively. In general, during charge or discharge, case temperature of the battery varies

slowly with respect to T_S, therefore, it can be measured at an interval of one minute for temperature compensation of the set point voltage. In this case, the case temperature has been measured in each cycle (i.e., at interval of 500ms), as the controller gets enough time for measurement of battery temperature.

Table 3. 3: User define constants for state 2

Constants	value
V_{BREFH}	14.4
V_{BREFL}	14.1
I_{OTH}	0.8
I_{OTL}	0.4
RCS	0.02
VB_ER_TR12	0.05

Table 3. 4:Initializations of run time variable for state 2

Variables	value
V_{bref}	V_{BREFH}
k_lp_s2	0
k_2min_s2	0
k_dsk	0
k_Ioh	0
K_Iol	0
err_Vb_old	VB_ERR_TR12

3.3.1.3 Description of PI controller

The output voltage of the DC-DC converter is kept constant by using a digital proportional-integral (PI) controller. In this implementation, PI controller is used to eradicate the steady state error resulting from a proportional (P) controller. The algorithm of PI controller is implemented by using the same hardware setup. To explain the working principle of the CV charging stage a simplified block diagram is shown in Fig. 3.11. In the discussions to follow ψ [k] will indicate the k^{th} sample of a variable ψ.

In order to ensure that the reference and the actual values of battery voltage V_B are equal in the steady state, the error $V_{b,\,e}$[k] is computed as

$$V_{b,\,e}[k] = V_b\,[k] - V_{b,ref}\,[k] \tag{3.13}$$

where $V_{b,r}$ is the reference voltage of the controller. To maximize battery life and minimize charging time, the battery charging voltage needs to be temperature compensated (i.e. reduced at higher temperature and increased at lower temperature). Therefore, in this realization, the expression for actual reference voltage $V_{b,ref}$ can be given as follows

$$V_{b,\,ref} = V_{BREFL} - V_{b,\,tcor} \tag{3.14}$$

where $V_{b,tcor}$ is the correction of reference voltage based on battery temperature and V_{BREFL} is the lower constant voltage i.e., 14.1V . The expression of $V_{b,tcor}$ is given by

$$V_{b,tcor} = 0.024\ (T_b - 25) \tag{3.15}$$

where T_b indicates case-temperature of the battery. The temperature is measured by a solid-state sensor connected to the MCU as discussed in Section 3.4.2.6. In this case, a typically compensation voltage of -0.004V/^{o}C/cell is chosen which results in 0.024V/^{o}C for 12V battery (i.e., comprises of six cells).

The error signal $V_{b,e}[k]$ is fed to a direct-acting PI controller which produces the output duty cycle D[k] of the converter. The controller generates the control signal D[k] to keep a constant V_b irrespective of the load and input voltage variations. D[k] is computed as

$$D[k] = K_P V_{b,e}[k] + K_I \sum_{n=0}^{k-1} V_{b,e}[n] \tag{3.16}$$

where the proportional constant K_P and integral constant K_I have been set to 0.2 and 0.25, respectively. The constant values have been fixed experimentally. If the overall system is stable the presence of the integral term in the controller will ensure that the reference and actual values of V_b are equal.

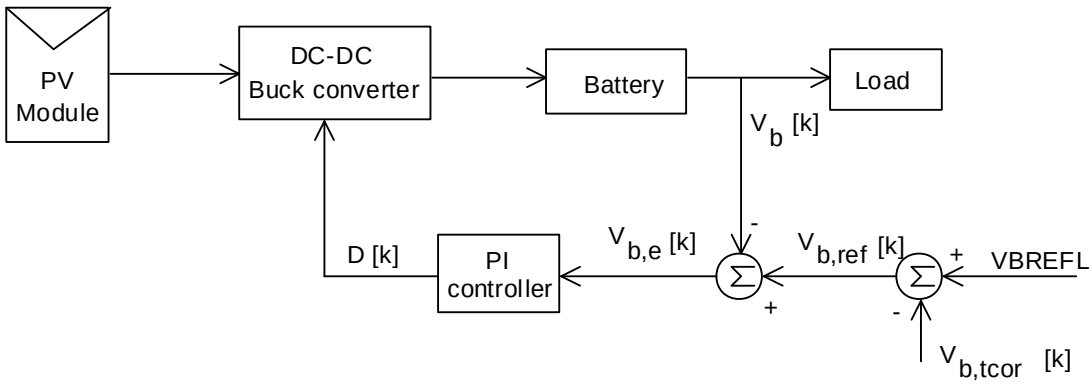

Fig. 3.11. Simplified block diagram of CV charger with PI controller

3.3.3 Pulsed trickle charging and health check

In the present implementation, state3 consists of two phases, namely, phase0 and phase1. Phase0 and phase1 represent the pulsed trickle charging and health checking of the battery, respectively. Phase0 is used for mainly two reasons. Firstly, to avoid over-charging of the

battery. Secondly, to replenish the drain-out current of the battery due to the system current (i.e., current required to supply the MCU, LCD, GSM module etc) as well as the self-discharge current. Therefore, this phase increases the battery life and at the same time it also maintains the SOC at 100%. In phase1, health of the battery is monitored. The process of health monitoring is discussed in Section 3.3.3.2.

3.3.3.1 Different methods for checking the health of a VRLA battery

State-of-health (SOH) prediction of VRLA battery is an important issue due to several reasons. They are as follows

- Prediction of precise time for replacement of battery.
- Optimal usage of the battery.
- Better charge or discharge schedule management of the battery
- Determination of life-span of the battery and based on that battery selection may be done by the user.

Several methods have been proposed by the researchers to determine the SOH of batteries. In the present implementation, SOH has been predicted by using two methods. In the first method, open-circuit voltage of the battery is measured after a given time and compared with pre-defined values to predict the SOH. In actual case, the battery voltage falls with respect to time just after disconnection of the charger. This basic principle is used in the first method to determine the SOH. In the second method, internal resistance of the battery has been measured to predict the SOH. This method is based on the fact that the internal-resistance of a VRLA battery increases with age due to the chemical degradation of the active material. A detail description of internal resistance measurement process is given in chapter 5.

3.3.3.2 Algorithm for pulse trickle charging and health check

As discussed earlier, stage 3 has two phases trickle-charging phase and health-checking phase. The trickle-charging phase can be further divided in two modes, namely, voltage control mode and stand-by mode.

The flowchart of pulse trickle charging and health checking algorithm are illustrated in Fig. 3.12. In this figure, ψ and ψ_old will indicate the value of variable ψ in the present and

previous sampling instant, respectively. To start the algorithm, different values of user define constant and run-time variables are needed to be initialized for state2. The values of user defined constants and variables are given in Table 3.5 and Table 3.6, respectively.

In voltage control stage, the battery voltage is maintained at a lower constant voltage i.e. at V_{BREFL} for one minute. The voltage of battery is kept constant by using the same digital proportional-integral (PI) controller which has already been explained in Section 3.3.2.3. In stand-by mode, the battery is kept open-circuit for another one minute. During this time, the duty cycle of the converter has been fixed to 0.5 instead of zero so that the control algorithm can attain the desired dutycycle quickly in the next mode i.e. voltage control mode. The user define constant, k_2MIN_MAX is used to set the time duration for trickle -charging.

After completion of trickle charging phase, in health checking phase, the battery is kept open-circuit for a given time. During this time, V_B falls as battery is not charging. For healthy battery the open-circuit voltage falls slower with time than unhealthy battery. Now the battery voltage has been measured at the end of given time and compared with four pre-defined voltage levels. Based on this comparison a health rating variable (hrtg) has been assigned to 1, 2, 3 or 4, respectively, to represent excellent, good, fair or poor health condition of the battery.

The function LoAmbLgt has already been discussed in Section 3.3.2.2. During operation in state3, if low ambient light is detected, the control algorithm jumps to state 4 for receiving administrator message. The variables k_lp_s3 and k_2min_s3 are used as a loop counters. Based on these variables, the float charging state has been implemented. The loop counter k_lp_s3 and k_2min_s3 are incremented in every 500mS and 2 min, respectively.

Table 3.5: User define constants for state 3

Constants	value
V_{BREFL}	14.1
K_TC_ON	120
K_2MIN_MAX	2
RCS	0.02

Table 3. 6:Initializations of run time variable for state 3

Variables	Value
V_{bref}	V_{BREFL}
k_lp_s3	0
k_2min_s3	0
k_dsk	0
hchk	0
k_hc_s3	0
err_Vb	0

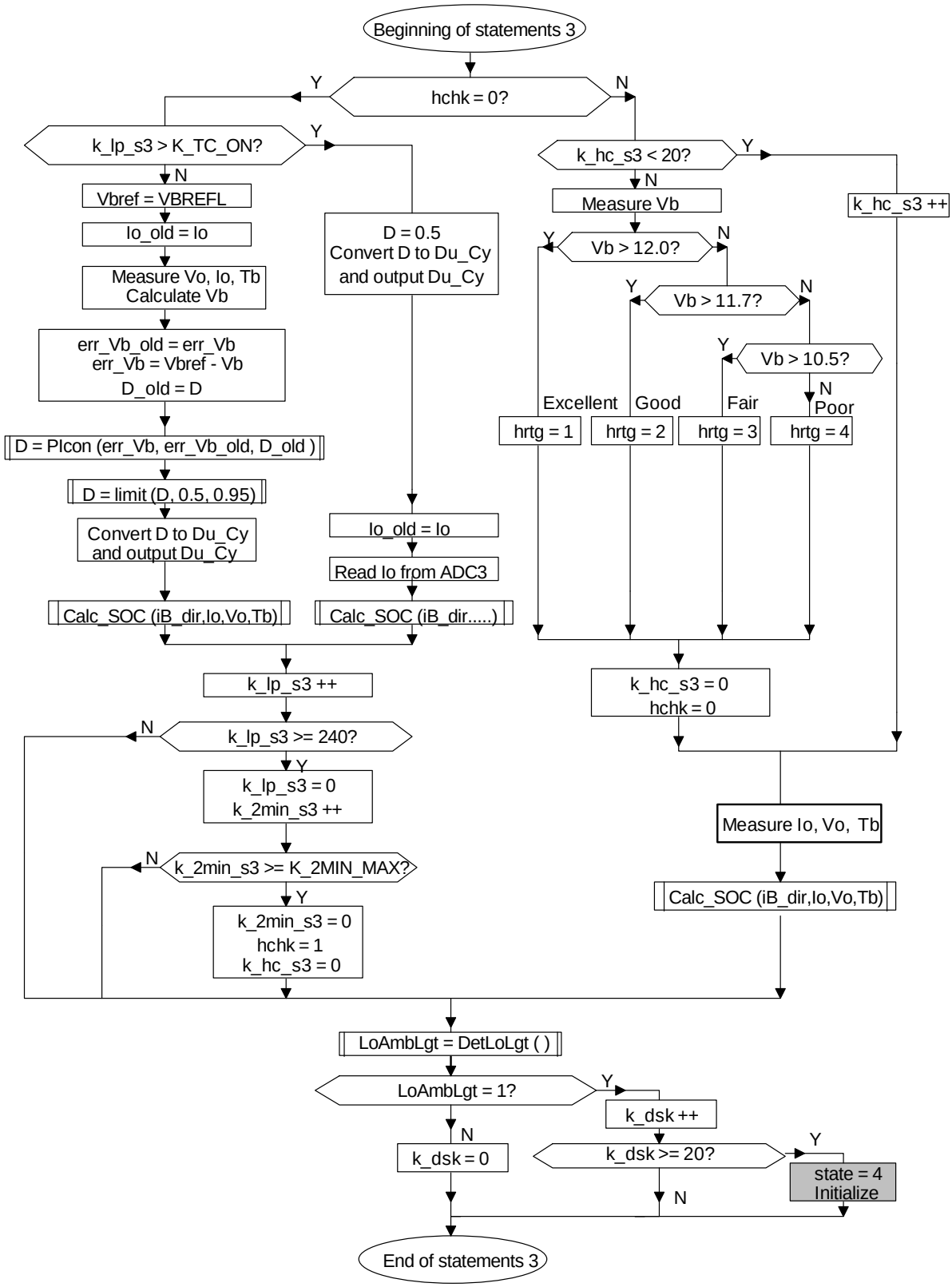

Fig. 3.12. Flowchart of pulse trickle charging and health check

3.4 Hardware implementation and experimental analysis of charger

Generally, three types of popular topologies are used to implement a basic switched-mode converter. They are buck, boost, and buck-boost. Among them, the buck converter normally offers the most efficient solution over the others. It also has a low component count. Therefore, in this study, the buck converter topology is used to implement the multi-stage battery charger algorithm.

Normally, the PV voltage V_{mpp} at the maximum power point for a rated 12V solar module approximately varies from 14.5V to 18.0V, at a typical insolation condition. In our case, 12V, 42 AH battery is used. Hence, to charge the battery, output voltage of the converter should be always lower than the input voltage. Thus, a buck converter can change the battery more efficiently from the solar module. Circuit diagram of the developed multi-mode battery charger based on buck converter is shown in Fig. 3.13. The whole circuit diagram is divided into six blocks based on different circuit operation. The basic requirement of each block is given below.

Block [1]: Buck converter

Block [2]: Auxiliary power supply for the control circuit.

Block [3]: Voltage interface to the ADC for PV voltage measurement.

Block [4]: Voltage interface to the ADC for battery voltage measurement.

Block [5]: Current sensing scheme and ADC interfaces.

Block [6]: Discrete component based high-side MOSFET driver.

A brief explanation of the operating principle of the blocks is given in the following sub-sections.

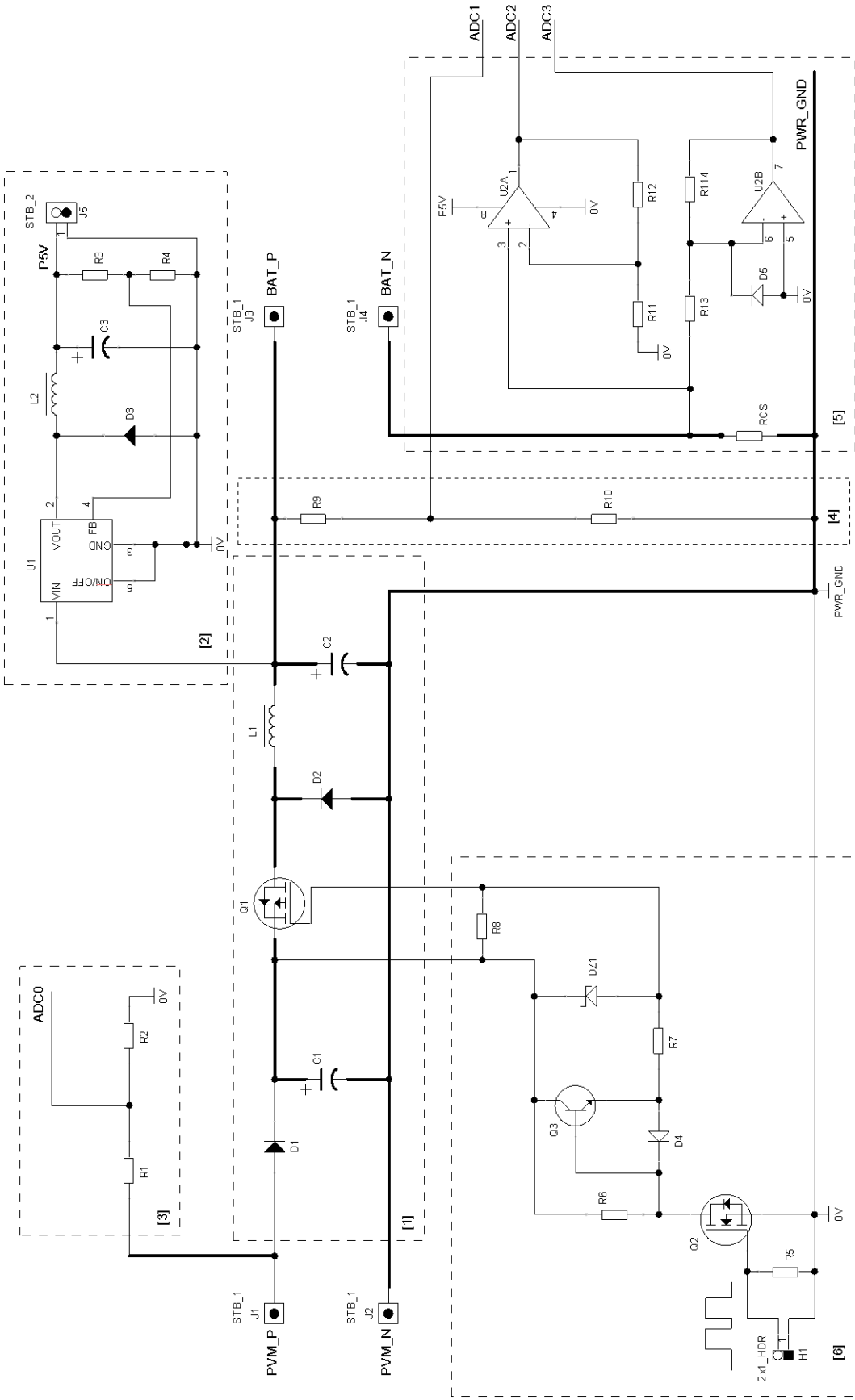

Fig. 3. 13. Multi-stage battery charger

An assembled printed circuit board (PCB) of the battery charger and LED driver is shown in Fig. 3.14. A discussion on the design and implementation of the LED driver is given in chapter4.

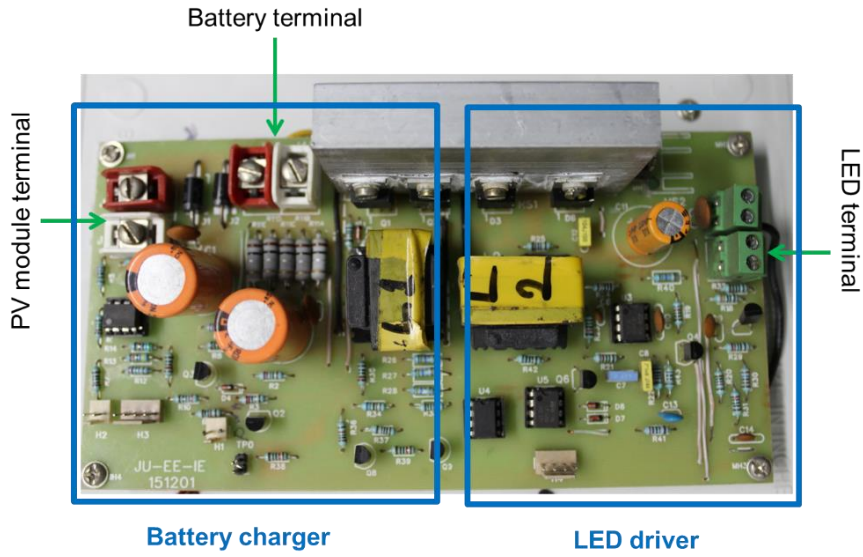

Fig. 3.14 The prototype of battery charger and fixed-CCT LED driver

3.4.1 Analysis and preliminary design of the converter

DC choppers can be used as a switch-mode regulator to provide regulated DC voltage. In a step-down or buck converter, the average output voltage V_o is less than or at most, equal to the input voltage. In this section, the working principle of a buck converter is described.

In this study, a buck converter is used to charge the battery from the PV module in an optimal fashion. The circuit diagram of a buck converter using a p-channel MOSFET as a switch is shown in Fig. 3.15. Important waveforms explaining the principle of operation of the converter are shown in Fig. 3.18. For the purpose of analysis, it is assumed that the PV voltage, V_{PV} is ripple free. However, as shown in Fig. 3.18(c), the input current to the converter is in the form of trapezoidal pulses that cause voltage ripples in v_{PV}, unless suitable measures are adopted. Placement of a capacitor C1 of suitable value can reduce the voltage ripple to a negligible amount. For a fixed switching frequency f_S, a fixed inductor L and a range of load current i_O from a certain minimum up to the rated value, the inductor current i_L lies in the range ($I_{L,min}$, $I_{L,max}$) where $I_{L,min} > 0$. Since the current i_L is never zero over a period $T = 1 / f_S$, this mode of operation is called the *continuous conduction mode* or CCM. At the end of this section it will be shown that there are two more modes of operation of this type of

converter, namely, the *boundary conduction mode* (BCM) and the *discontinuous conduction mode* (DCM), both of which are of relatively small importance in this study.

Depending on the state of the series switch, the operation of the converter in CCM can further subdivided into two modes, namely, interval 1, $0 \leq t < T_{ON}$, when S1 is on, and interval 2, $T_{ON} \leq t < T$, when S1 is off. Assuming T to be fixed, the output voltage Vo can be controlled by adjusting the value of T_{ON}. The length of the second interval is $T_{OFF} = T - T_{ON}$. The operation in the two intervals is discussed below.

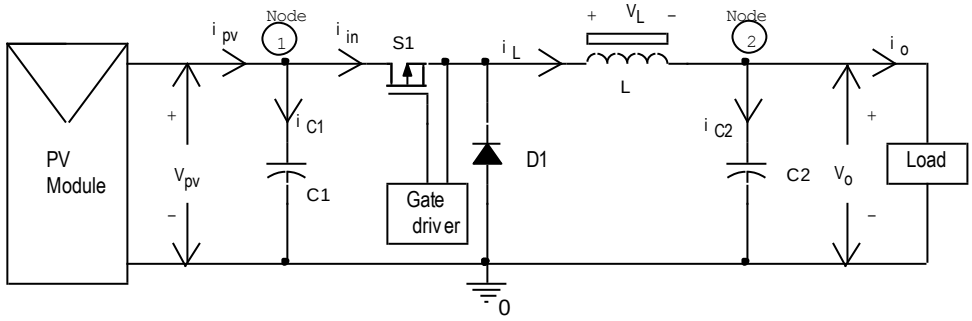

Fig. 3.15. Simplified circuit diagram of the buck converter

Interval 1: Starts at t=0, when switch S1 is closed, the freewheel diode D1 becomes reverse biased and the PV module provides energy to the load. i.e., the battery as well as the inductor L. The equivalent circuit in interval 1 is shown in Fig. 3.16. The rate of increase of inductor current is given by

$$\frac{di_L}{dt} = \frac{v_L}{L} = \frac{V_{PV} - V_o}{L}, \text{ for } 0 \leq t < DT \tag{3.17}$$

where D is the duty cycle given by

$$D = \frac{T_{ON}}{T_{ON}+T_{OFF}} = \frac{T_{ON}}{T} = T_{ON} f_S \tag{3.18}$$

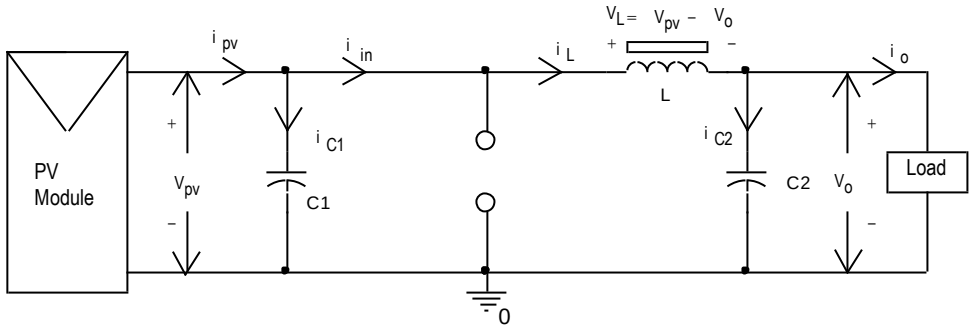

Fig. 3.16. Equivalent circuit for Interval 1 (S1 closed, D1 blocking)

Since the right-hand side of equation (3.17) is a positive constant, the inductor current increases linearly with time as shown in Fig. 3.18(b). The rate of rise of current can therefore be equated to $\frac{\Delta i_L}{DT}$ thereby modifying equation (3.17) as

$$\frac{\Delta i_L}{DT} = \frac{V_{PV} - V_o}{L} \tag{3.19}$$

From equation (3.19), the increase in inductor current in this interval is given by

$$\Delta i_L = \frac{V_{PV} - V_o}{L} \text{ DT} \tag{3.20}$$

Interval 2: starts at t = DT, when switch S1 opens. The freewheel diode D1, in order to maintain the continuity of inductor current, becomes forward biased and the inductor current flows through it. Part of the stored energy of the inductor is transferred to the load-capacitor parallel combination. The equivalent circuit in interval 2 is shown in Fig. 3.17. Now, i_L decreases at the rate of

$$\frac{di_L}{dt} = \frac{v_L}{L} = \frac{-V_o}{L}, \text{ for DT} \leq t < T \tag{3.21}$$

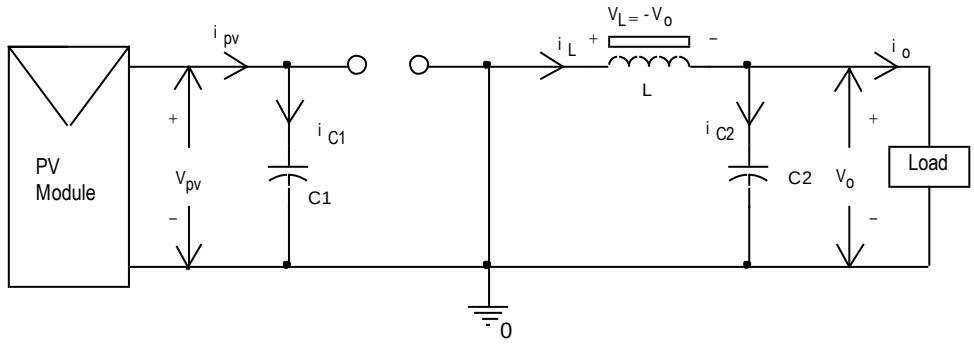

Fig. 3.17. Equivalent circuit for Interval 2 (S1 open, D1 conducting)

Since the right-hand side of equation (3.21) is a negative constant, the current i_L decreases linearly with time as shown in Fig. 3.18(b). So, the rate of change of i_L in this interval can be rewritten as

$$\frac{\Delta i_L}{(1-D)T} = \frac{-V_o}{L} \tag{3.22}$$

Rearranging equation (3.18) the increase in i_L can be expressed by

$$\Delta i_L = \frac{-V_o}{L}(1\text{-}D)\,T \qquad (3.23)$$

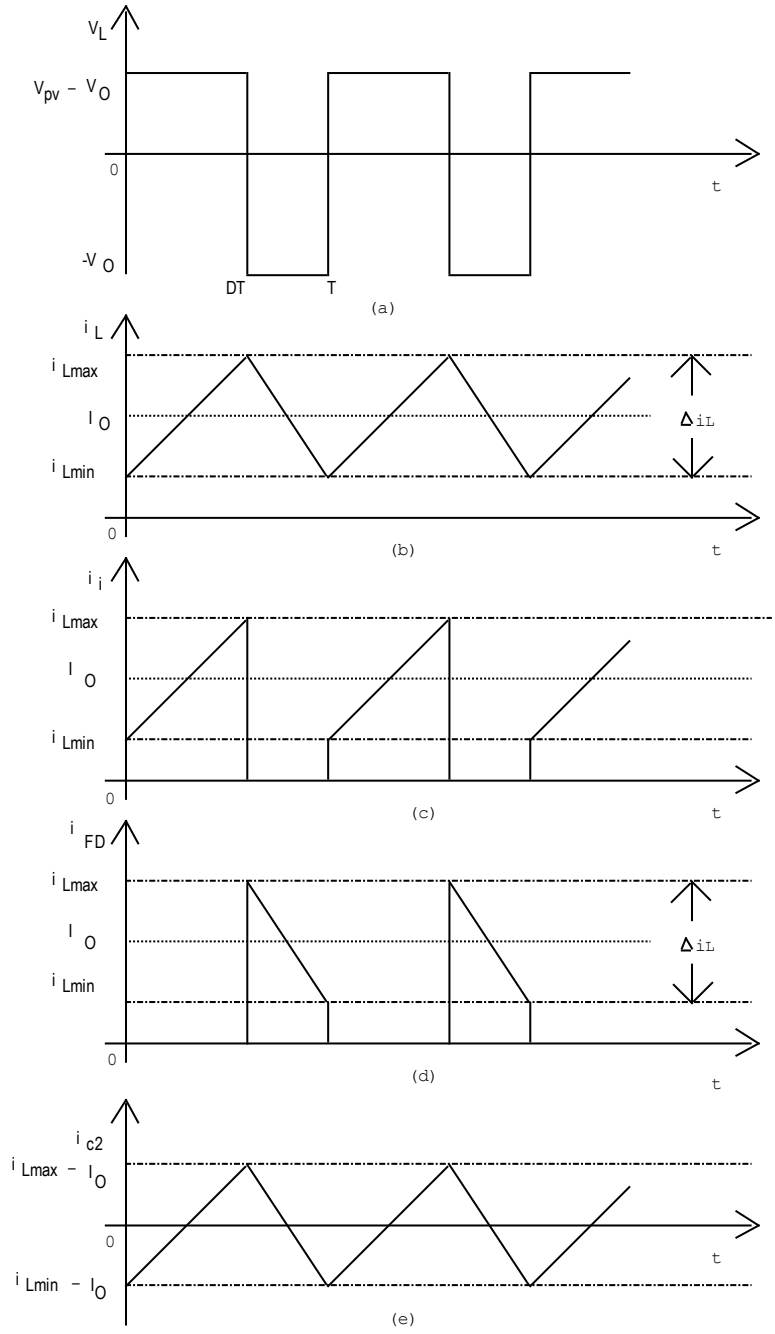

Fig. 3.18. Waveforms of the buck converter for CCM (a) Inductor voltage (b) Inductor current (c) Input current (d) Freewheel diode current (e) Capacitor current

Based on the discussions above, wave shapes of the inductor voltage and current are shown in Fig. 4(a) and Fig. 4(b), respectively. For periodic operation in a cycle, i_L will be

same at the beginning and end of a switching period T. Therefore, the resultant change in inductor current is zero in a cycle. This condition is represented by equation (3.24)

$$\Delta i_L \text{ (Interval 1)} + \Delta i_L \text{ (Interval 2)} = 0 \quad (3.24)$$

Now, equations (3.20) and (3.23) when substituted in equation (3.24) gives

$$\frac{V_{PV} - V_o}{L} \text{ DT} + \frac{-V_o}{L} \text{ (1-D) T} = 0 \quad (3.25)$$

Solving equation (3.25), the expression for output voltage, V_o will be

$$V_o = D\ V_{PV} \quad (3.26)$$

Equation (3.26) describes the operation of the buck converter. For a fixed input voltage, the output voltage is directly proportional to D and is, therefore, less than or equal to the input.

Equations (3.20) and (3.23) give the change in inductor current Δi_L. Now the maximum and minimum value of inductor current, respectively, I_{Lmax} and I_{Lmin} can be expressed as

$$I_{L,max} = I_{L,avg} + \frac{\Delta i_L}{2} = I_{L,avg} + \frac{V_o(1-D)}{2Lf_s} \quad (3.27)$$

$$I_{L,min} = I_{L,avg} - \frac{\Delta i_L}{2} = I_{L,avg} - \frac{V_o(1-D)}{2Lf_s} \quad (3.28)$$

For steady-state operation, the average capacitor current is zero. Thus, the average inductor current $I_{L,avg}$, must be the same as the average load current I_O:

$$I_{L,avg} = I_O \quad (3.29)$$

The required value of the inductance can be obtained by observing that the minimum instantaneous current $I_{L,min}$ occurs for the combination of minimum output current, minimum inductance and minimum duty cycle. In order to have continuous conduction mode (CCM) even under this condition, $I_{L,min}$ has to be zero. If any of the three required quantities is more than its respective minimum, CCM is automatically ensured. Imposition of $I_{L,min}$= 0 along with equation (3.29) yields

$$I_{o,\,min} = \frac{V_o(1-D_{min})}{2L_{min}f_s} \quad (3.30)$$

A rearrangement of the above equation gives

$$L_{min} = \frac{V_o(1-D_{min})}{2I_{o,min}f_S} \quad (3.31)$$

From equation (3.31), it can be seen that the inductance value is inversely proportional to the switching frequency, f_S of the converter. So, if the switching frequency increases, the output filter inductor and/or capacitor values could be smaller which also reduces the cost as well as converter size. On the other hand, if frequency increased, the switching-loss is also increased. Therefore, a suitable tradeoff between inductor value and switching loss must be made. In this case, a typical switching frequency of 50 KHz is chosen. Generation of exact 50 KHz is not possible as f_S of the converter is governed by the MCU. The PWM frequency for ATmega32A [16] can be calculated by the following equation

$$F_{PWM} = \frac{F_{clk}}{256\ X\ N_{psc}} \quad (3.32)$$

where the variable N_{psc} represents the prescaler factor (1, 8, 32, 64, 128, 256 or 1024) and F_{clk} is the system clock frequency.

In this study, F_{clk} of 12MHz is chosen, which is generated by using a standard crystal oscillator. The required value of N_{psc} for generation of 50 KHz f_S is therefore 0.937. Due to the limited choice of the prescaler value, we are bound to select a nearest value of one. Putting N_{psc} = 1 in equation (3.32) produces a 46.78 KHz of f_S. In this realization, Timer 0 of ATmega32A is used to generate f_S. Timer0 can work in four different modes, namely, normal, phase correct PWM, CTC and fast PWM. Among them we have chosen fast PWM mode as it provides a high frequency PWM waveform generation option. This mode can be set by programming the bits B6 = 1 and B3 = 1 of registrar TCCR0. By programming bit0, bit1 and bit2 of timer/counter control register TCCR0, a prescaler value of one has been set. This requires B2 = 0, B1 = 0, and B0 =1.

Now the duty cycle of f_S can be controlled by proper setting of the Output Compare Register (OCR0) whose value may vary from 0 to 255. The relationship of duty cycle and OCR0 register is given as follows

$$D = \frac{\text{Content of OCR0} + 1}{256} \quad (3.33)$$

The value of OCR0 register is set at the appropriate value by the charging controller. Hence, the desired output will be available at pin 4 of the MCU.

In the previous analysis, the output capacitor, C2 is assumed to be very large to maintain V_o at a constant value. As the cost of a capacitor for a certain voltage rating approximately increases linearly with its value, C2 cannot be increased indefinitely. A method for designing an economic value of C2 is described below.

The output voltage ripple, ΔVo can be determined from the voltage-current relationship of the capacitor.

Applying KCL at node 2 of Fig. 3.15, the capacitor current i_{c2} can be given by

$$i_{c2} = i_L - i_o \tag{3.34}$$

Assuming, the entire ripple component of i_L flows through the capacitor and its average value I_o flows through the load, the shaded area of Fig. 3.19 graphically shows the change in charge ΔQ due to positive current. Hence, the peak-to-peak voltage ripple of the capacitor can be expressed as

$$\Delta V_o = \frac{\Delta Q}{C} = \frac{1}{C}\frac{1}{2}\left(\frac{\Delta i_L}{2}\right)\left(\frac{T}{2}\right) = \frac{T\Delta i_L}{8C} \tag{3.35}$$

Substituting the value of Δi_L from equation (3.23) to equation (3.35) gives

$$\Delta V_o = \frac{V_o\,(1-D)}{8LC2{f_s}^2} \tag{3.36}$$

A factor is known as voltage ripple factor, γ_v is often specified as a ratio of ripple voltage to average voltage, i.e.

$$\gamma_v = \frac{\Delta V_o}{V_o} \tag{3.37}$$

For an ideal DC output γ_v must be zero. On the other hand, for a specified γ_v the actual voltage ripple in output can be calculated using equation (3.37). Therefore, if γ_v and V_o are known the value of output capacitance C2 can be calculated by rearranging the terms of equation (3.30).

The minimum value of output capacitance C2 is thus given by

$$C2_{,min} = \frac{(1-D_{min})}{8L\,\gamma_v {f_s}^2} \tag{3.38}$$

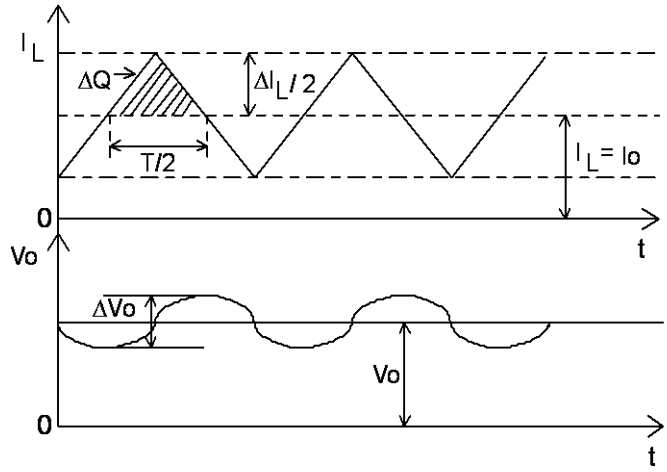

Fig. 3.19. Inductance current and output voltage ripple of a buck converter

The expression of output voltage ripple of equation (3.34) is established, by assuming C2 as an ideal capacitor, although, a practical capacitance can be modeled by a capacitor with an equivalent series resistant (ESR) and an equivalent series inductance (ESL). The ESL of the capacitor is not a significant factor at typical f_s. On the other hand, the ESR of the capacitor may have a remarkable effect on the output voltage ripple. Thus, C2 can be modeled as shown in Fig. 3.20. Considering the ESR of the capacitor, in worst case condition, the peak-to-peak ripple voltage due to the ESR may be added to the peak-to-peak ripple voltage due to the pure capacitor. Thus, equation (3.35) can be modified as follows

$$\Delta V_o < \Delta V_{o,\,ESR} + \Delta V_{o,c} \tag{3.39}$$

where $\Delta V_{o,\,ESR}$ is the voltage variation due to the ESR of the capacitor and $\Delta V_{o,c}$ is the voltage variation due to the pure capacitor, as in equation (3.35).

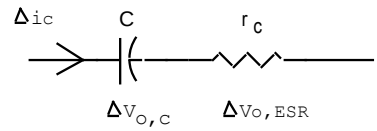

Fig. 3.20 An equivalent circuit of capacitor C2

It may happen that $\Delta V_{o,\,ESR}$ is much higher than $\Delta V_{o,c}$, in that case, C2 is chosen based on ESR instead of capacitor value. Therefore, a low ESR capacitor is always preferred as an output capacitor.

A buck converter can be operated in two more modes: *boundary conduction mode* (BCM) and *discontinuous conduction mode* (DCM). In our case, the battery charging current varies with solar irradiance and battery charge status. In BCM, the inductor current i_L equals 0 at the end of a time period T and again linearly increases when the switch is closed. As the battery charging current decreases from a high value to a lower value, the BC mode is entered only momentarily. With a further decrease of charging current the converter enters into DCM. Hence, the converter normally operates in either CCM or DCM modes depending on the requirement of output current.

In DCM, to maintain the output current and voltage at their specified values, the sum of on time $T_{ON} = DT$ and off time $T_{OFF} = D_1T$ is less than the period T. The inductor current reaches a zero value at $t = T_{ON} + T_{OFF}$ and remains there for the remaining time D_2T, where $D_2 = 1 - (D + D_1)$. The relevant voltage and current waveforms are shown in Fig. 3.21. In this mode, when the inductor current is zero, the load current is entirely provided by C2, i.e. $i_o = -i_{c2}$. During the time D_2T the inductor voltage is zero. Since the average inductance voltage is zero for a period, from the waveform of inductance voltage of Fig. 3.21, it can be written as

$$(V_{PV} - V_o)DT + (-V_o)D_1T = 0 \tag{3.40}$$

Rearranging equation (3.40), the relationship between output voltage and PV voltage can be written as follows

$$V_o = V_{PV} \left(\frac{D}{D+D_1}\right) \tag{3.41}$$

where $D + D_1 < 1$

Thus, in DCM the output voltage is controlled by a closed loop system that adjusts the values of D and D_1 so that it is maintained at the required value.

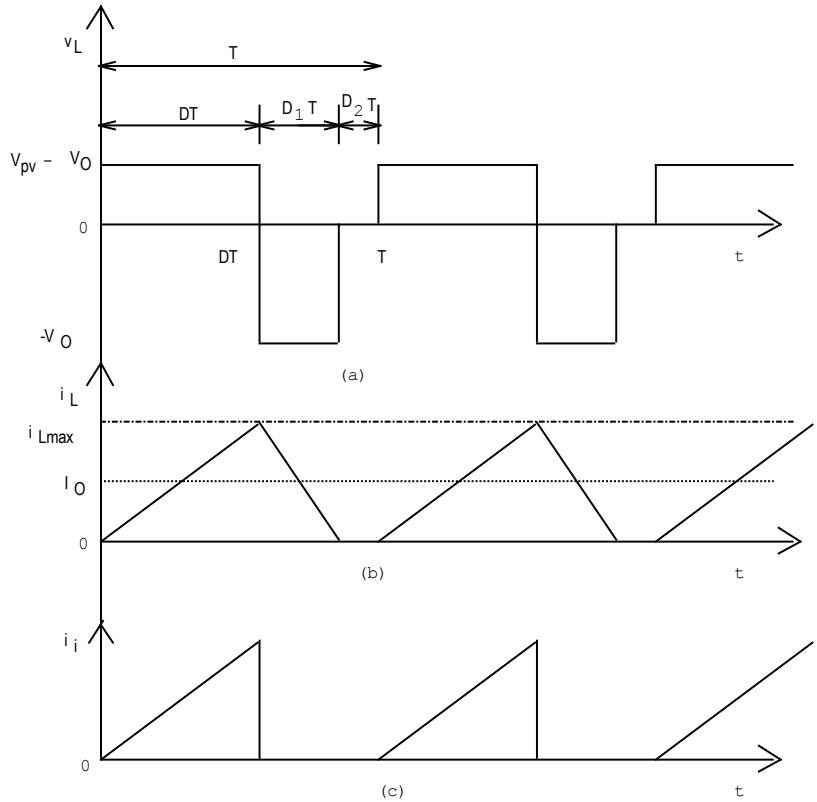

Fig. 3.21. Waveforms of the buck converter for discontinuous inductor current (a) Inductor voltage (b) Inductor current (c) Input current

Selection of major components of the prototype

The voltage, V_{mpp} at maximum power for a rated 12V solar module approximately varies from 14.0V to 18.0V, at a typical insolation condition. In our case, 12V, 42 AH battery is used. Thus, a buck converter can change the battery from the solar module. Now a sample calculation to determine the component value of a buck converter for CCM operation is given below. For calculation, we have chosen the following parameters.

Maximum open-circuit PV voltage, $V_{OC,max} = 21V$

Minimum input PV voltage at MPP, $V_{pv,min} = 12V$

Maximum input PV voltage at MPP, $V_{pv,max} = 18V$

Nominal output voltage, $V_o = 12V$

Maximum output current, $I_{o,max} = 5A$

Switching frequency of the converter $f_S = 46.87$ KHz

Power rating of the PV module = $100W_p$

Inductor

The average inductor current can be calculated by the following equation

$$I_{L,avg} = \frac{P}{V_b \ \eta} \quad (3.42)$$

Substituting the values of P =$100W_p$, V_b =12V and η = 90% in equation (3.42), yield, $I_{L,avg}$ = 9.25A

Assuming the allowable inductor current ripple is 20% of the average inductor current, hence, the change in inductor current will be 1.85A.

To evaluate the inductance value using equation (3.31), one should know the minimum duty cycle of the buck converter. The minimum duty cycle of the buck converter can be calculated by using the following equation.

$$D_{min} = \frac{V_o}{V_{pv}\,\eta} \quad (3.43)$$

where η is the efficiency of the converter.

In our case, the minimum duty cycle, D_{min} = 0.74. Considering efficiency = 90%, the inductance value for CCM operation will be 35.3uH. One can select higher inductor value which will consequently reduce the ripple current of the inductor.

Output capacitor

Capacitor voltage ripple = 2% is chosen for selection of the output capacitor, C2. Thus, change in capacitor voltage ripple is 0.24V. Substituting the values of D =0.74, L =35.3uH, and f_S = 46.87 Khz, γ_v = 0.02 in equation (3.36), yield, C2 = 20.1uF.

MOSFET rating

From the 3rd waveform of Fig.4, it can be proved that the average value of drain current of MOSFET Q1, $I_{D,av}$ is given by

$$I_{D,av} = \frac{1}{2}(i_{Lmax} - i_{Lmin})\,D = I_o\,D \quad (3.44)$$

Taking the maximum value of the quantity of RHS (Io = 5A) and D = 1, the maximum value of $I_{D,av}$ is 5A accordingly any p-channel MOSFET with an $I_{D,av}$ of 5A can be used.

The maximum voltage V_{DS} across the MOSFET occurs when it is OFF and has a value equal to $V_{PV} + V_F$ where V_F is the forward drop across the freewheel diode D_2. The freewheel rectifier D2 in this realization is a schottky rectifier so that the forward conduction loss kept at a minimum. Considering V_{PV} = 21V and V_F = 0.5V, the voltage rating of the MOSFET should be at least 21.5V. In the present implementation, a low-cost MOSFET IRF9540 with a voltage and current rating of 100V and 13A, respectively, has been used. This gives rise to a voltage safety factor of 4.6 and a current safety factor of 2.6.

Freewheel diode rating

The freewheel diode is forward biased when the MOSFET is OFF, therefore, the forward average current $I_{FD,av}$ is given by

$$I_{FD,av} = \frac{1}{2} (i_{Lmax} - i_{Lmin}) (1-D) = I_o (1-D) \quad (3.45)$$

The theoretical maximum occur when D=0. The average current rating of the freewheel diode is therefore the maximum output current. In our case, the maximum rated current is 5A.

The maximum reverse voltage to which the freewheel diode is subjected is V_{PV} (while Q1 is ON). Thus, the freewheel diode must have a voltage rating of V_{PV}. We have realized this with a dual schottky diode MBR2045 [17]. The voltage and current rating of MBR2045 are 45V and 10A, respectively. This gives rise to a voltage safety factor of 2.1 and a current safety factor of 2.

In addition to component shown in Fig.1, it is necessary to connect a blocking diode D_{BL} between the positive terminal of the PV array and the source terminal of MOSFET Q1. This diode prevents in case of a flow battery current towards the PV array for $V_{PV} < V_B$, where V_B is the battery voltage. In worth case the maximum reverse voltage is V_B (when the PV are accidentally short circuited). The average current through this diode is same as that of the MOSFET drain current. Owing to the finite forward voltage drop across this diode the efficiency of the converter is somewhat reduced. We have selected two low-cost SR360 each rated for 60V and 3A. Paralleling two diode reduces the effective forward drop their by increasing efficiency.

3.4.2 Analysis and design of auxilary sub-systems

In this section, we will discuss about the auxiliary sub-systems which are required to implement the hardware as well as the charging algorithm.

3.4.2.1 Auxiliary power supply circuit

In this study, the auxiliary power (+5V supply) required by the MCU, the LCD and the other ICs is obtained from a switch-mode buck-regulator fed from the 12V battery. The regulator uses LM2576 [18] which provides all the active functions for a switching converter in a single chip. It is used as a replacement of inefficient three-terminal linear voltage regulator (such as LM7805, LM317 etc). The device has a capability to drive 3-A load with excellent line and load regulations. The regulator also requires a minimum number of external components to produce a fixed output voltage of +5V. A typical circuit diagram is shown in Fig. 3.22. As discussed in Section 3.4.1, the values of L2, C3 and D3 can be calculated on the basis of the fixed operating frequency of 52Khz. The values are 100uH, 330uF and 1N5822 schottky diode, respectively.

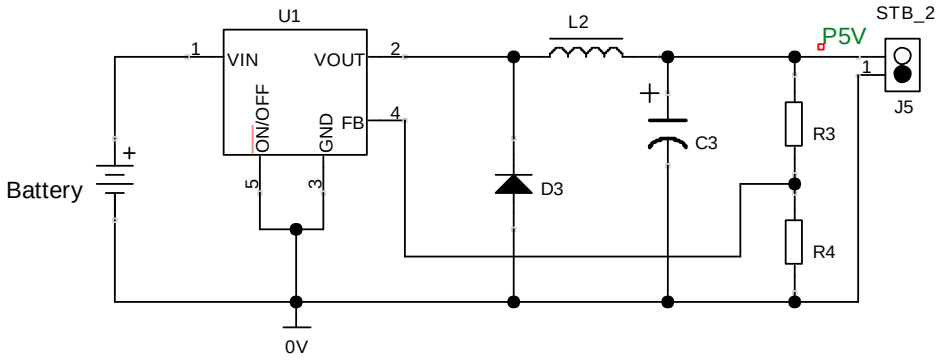

Fig. 3.22. Circuit diagram of the step-down switching regulator using LM2576-ADJ

To calculate the value of R_3 and R_4, the output voltage equation of LM2576 as given below

$$V_{out} = V_{ref}\left(1 + \frac{R3}{R4}\right) \tag{3.46}$$

Equation (3.46) can be rearranged by taking R_3 left hand side as

$$R_3 = R_4\left(\frac{V_{out}}{V_{ref}} - 1\right) \tag{3.47}$$

where the value of V_{ref} is 1.23V and the recommended value of R_4 is between 1K and 5K. Selection of R_4 = 1.5K yields R_3 = 4.59K. Taking a standard value of 4.7K gives V_{out} = 5.08V. In addition, if +3% tolerance of V_{ref} is considered, the highest possible value of V_{out} becomes 5.23V. This voltage is safe for all 5-V rated devices.

3.4.2.2 General introduction to A-D conversion

The major analog signals that require conversion to digital form for control and monitoring of the system are PV array voltage, battery bus voltage, battery charging and discharging currents and the battery temperature. The selected MCU has 8 10-bit A-D converters with the same input range. For the following discussion the definition of a parameter known as the resolution q of the converter is required. It is given by

$$q = \frac{U_R}{2^N} \tag{3.48}$$

where U_R and N are the reference voltage and the number of bits of the ADC, respectively. In the present implementation, U_R has been programmed to have a value of 2.56V, so that q has a value of 2.5mV.

The input to output, or *forward*, transformation involves the conversion of a input analog voltage $u_{i,AD}$ in the range $(0 \leq u_{i,AD} \leq U_R)$ to a positive integer n_{ad} governed by the following equations

$$n_{ad} = 0, \quad \text{for } 0 \leq u_{i,AD} < \frac{q}{2} \tag{3.49}$$

$$= m, \quad \text{for } \left(mq - \frac{q}{2}\right) \leq u_{i,AD} < \left(mq + \frac{q}{2}\right)$$

$$= 2^N - 1 \text{ for } 2^N q - \frac{3q}{2} \leq u_{i,AD} \leq U_R$$

A value of $u_{i,AD} > U_R$, although not recommended, creates output saturation to produce $m = 2^N - 1$.

Equation (3.49) clearly shows the discontinuous nature of the *many-to-one* transformation involved in the forward conversion. In other words, the output m does not refer to an unique input voltage u_i – instead it is a band.

The inverse, or *backward*, transformation should convert the number m to a voltage u_i. Due to the nature of forward transformation this conversion will not be unique. A common practice is to use the following equation

$$u_i = q\ m \tag{3.50}$$

Clearly the regenerated input, instead of being a continuous voltage from 0-U_R now becomes a discrete number of points of u_i. This causes a quantization error whose maximum value is q/2 and random in nature.

As discussed earlier the reference voltage of all ADC channels have been fixed to 2.56V internally irrespective of the supply voltage. This requires B7 =1, B6 = 1 of ADC multiplexer selection register (ADMUX). The clock frequency of the ADC for ATmega32A can be selected by programming bit2, bit2, bit0 of ADC control and status register (ADCSRA). To select conversion time one can select any of f_{clk} /2, f_{clk} /4, f_{clk} /8, f_{clk} /16, f_{clk} /32, f_{clk} /64, f_{clk} /128 for the ADC clock. It is also recommended in the specification sheet of ATmega32A [16] that the ADC clock frequency should be less than 200KHz for the maximum accuracy. In our case as conversion time is not a vital issue, the ADC clock has been set to f_{clk} /128 or 93.75KHz. this requires B2 = 1, B1 = 1, B0 = 0 of ADCSRA register. For normal conversion, the ADC rwquires a conversion time of 13 cycles i.e. 138.67 uS which is very small compared to the system-sampling time of 500mS.

3.4.2.3 Attenuators for voltage measurement

Both the voltages discussed in the previous section have ranges more than the input range of the converters. Specifically, input range of PV array voltage is 0-21V and that of the battery bus voltage is 0-15V. Thus in both cases passive attenuators of suitable gain value G will suffice as input interfaces to the ADCs. For a typical attenuator shown in Fig. 3.23, consisting of resistances RA and RB, the gain G given by

$$G = \frac{u_{i,AD}}{ei} = \frac{RB}{RA+RB} \tag{3.51}$$

The required value of G for PV array voltage is therefore 2.56/21 or 0.122. Using a standard value of RB = 2.2KΩ the value of RA is obtained as 15.8KΩ. Use of a standard value of 18K results in G = 0.1089.

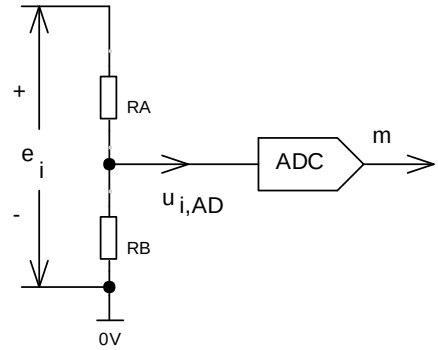

Fig. 3.23. Typical attenuator for ADC interface

During the operation of the converter, the value of m has to be converted to the physical variable e_i. Combination of equation (3.50) and (3.51) gives

$$e_i = \frac{u_{i,AD}}{G} = (\frac{q}{G})m = G_V\, m \qquad (3.52)$$

the gain factor G_V converting to e_i has the unit of Volt.

The same principle is applied for interfacing the battery bus voltage. The value of G required in this case 2.56/15 or 0.171. Keeping the value of RB = 2.2KΩ as before, and standardizing the value of RA = 12KΩ results in G = 0.155. In this implementation, the measurement resolution of PV array voltage and bus voltage are 23mV and 16mV, respectively.

3.4.2.4 Amplifiers for current measurement

In this study, a current sensing resistance R_{CS} is used to measure the charging as well as discharging current of the battery. R_{CS} converts the battery current I_B to a proportional voltage u_{CS}, which is given by

$$u_{CS} = I_B\, R_{CS} \qquad (3.53)$$

To reduce the power loss a low-value of sensing resistance should be placed in the current path. However, a very low voltage drop across R_{CS} will require the use of a high gain amplifier. The amplifier not only amplifies the low level signal but also the noise thus leading to inaccurate measurement of current. Therefore, a suitable tradeoff between high power loss and accuracy of measurement must be made for selection of R_{CS}. For typical design procedure, the shunt drop at maximum rated current should be kept 1% or less of the nominal battery voltage. In this design, a low-side current sensing scheme is adapted as MCU can

directly measure the ground-referenced output signal. R_{CS} is connected between the battery and ground as shown in Fig. 3.24.

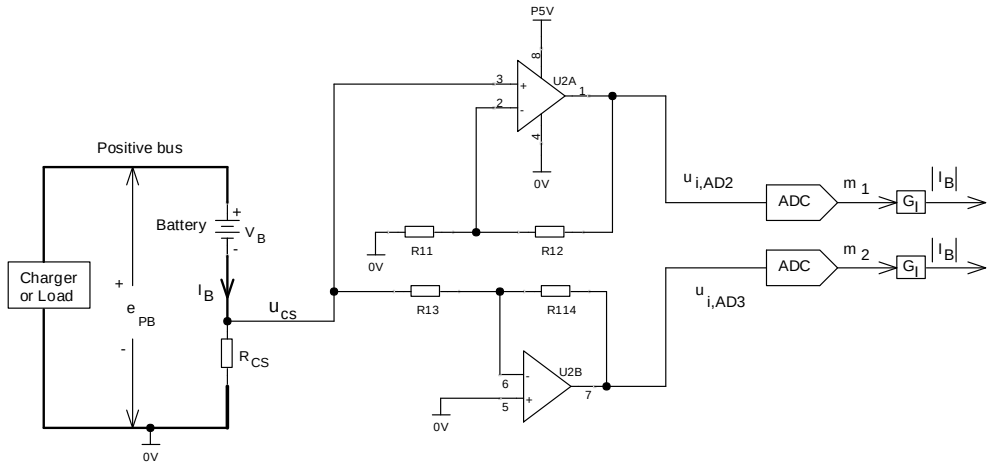

Fig. 3.24. Low-side battery current sensing scheme and ADC interfaces

In our case, to evaluate the actual battery voltage V_B, the drop across R_{CS} is subtracted from the battery positive bus voltage:

$$V_B = e_{PB} - I_B R_{CS} \tag{3.54}$$

where I_B is the battery current which is positive when the battery is charging and negative when it is discharging. Accordingly the drop across the current sense resistance is either positive or negative. The full scale value of u_{CS} is very small compared to the reference voltage of the ADC. Hence u_{CS} must be amplified by a suitable gain of proper polarity so as to make it compatible with the ADC. When u_{CS} is positive the amplifier should be a non-inverting amplifier. On the other hand when u_{CS} is negative the amplifier should be an inverting one. Thus in both cases an amplifier of suitable gain value A_V will suffice as input interfaces to the ADCs. The gain magnitude A_V can be decided by taking the value of full scale reference U_R and full scale value of u_{CS}. Thus, the required value of A_V is given by

$$A_V = \frac{u_{i,AD}}{u_{CS}} \tag{3.55}$$

A value of R_{CS} = 0.02Ω has been used in the present system so that at a maximum battery current of 5A the loss in RCS is 0.5W which is only 0.83% of the output power. The corresponding value of u_{CS} is 100mV. The required value of A_V for measurement of battery current is therefore 2.56/0.1 or 25.6.

For the non-inverting amplifier the gain A_{V1} is given by

$$A_{V1} = \left(1 + \frac{R_{12}}{R_{11}}\right) \quad (3.56)$$

Using a standard value of R11 = 22KΩ the value of R12 is obtained as 541KΩ. Use of a standard value of 470KΩ and 68KΩ in series results in A_{V1} = 25.45.

For the inverting amplifier, the value of A_{V2} is given by

$$A_{V2} = \left(-\frac{R_{14}}{R_{13}}\right) \quad (3.57)$$

For R13 = 22KΩ the required value of R14 for a gain of -25.6 comes out to be 563.2 KΩ. Using a standard value of R14 = 560 KΩ, A_{V2} is obtained as -25.45. Since the two gain are equal we can use the same gain magnitude A_V = 25.45. In case A_{V1} and A_{V2} are not equal in magnitude R12 can be trimmed so that the value of A_{V1} and A_{V2} are within 1%.

During the operation of the converter, the value of m has to be converted to the physical variable I_B. Combination of equations (3.50), (3.54) and (3.55) gives

$$I_B = \frac{u_{i,AD}}{A_V\, RCS} = \left(\frac{q}{R_{CS}\, A_V}\right) m = G_I\, m \quad (3.58)$$

where the gain factor $G_I = \frac{q}{R_{CS}\, A_V}$ (3.59)

converts the ADC output m to the battery current I_B and has the unit of ampere . In this implementation, the measurement resolution of charging and discharging current are 4.91mA.

Equation (3.49) can be further modified in terms of the magnitude of I_B as follows

$$V_B = e_{PB} - |I_B|\, R_{CS} \text{ for } I_B > 0 \quad (3.60)$$

$$= e_{PB} + |I_B|\, R_{CS} \text{ for } I_B < 0$$

Since in the realization above the value of m is always positive and is converted to the magnitude of I_B, equation (3.60) is easier to implement than equation (3.54) in software.

Since sufficient number of A-D converter channels are available in the MCU used, the output of two amplifiers are connected to two separate ADC channels. Otherwise a 2-to-1 analog multiplexer can be used to feed the amplifier outputs to one ADC channel. For accurate measurement a TLC272 [19] dual op-amp with low values of offset voltage and drift is used in this implementation.

3.4.2.5 High-side MOSFET driver

A MOSFET is a voltage driven device. For turning on the device a typical gate-to-source threshold voltage in excess of a threshold value of the order of 3-7 V must be used. The sign

of the voltage V_{GS} is positive for an N-channel MOSFET and is negative for the other variety. In this study, a P-channel MOSFET (IRF9540) [20] is used as a switch in the positive bus connecting the PV array and the battery of the charger circuit. A driver capable of driving the MOSFET switch at the command of a ground-referenced TTL signal is therefore required. The TTL signal is generated by using the MCU.

Although suitable high-side driver ICs for this required are available we used a driver based on discrete components in consideration of the following points. The IC based drivers (such as International Rectifier IR2122) are somewhat expensive and are not easy to find. In addition such drivers often require the use of an auxiliary voltage source. On the other hand, the discrete component based driver that has been designed and used in the present study is based on standard low-cost off-the-shelf components. It consists of a BJT, a small-signal MOSFET, four resistors, a fast-switching diode and a Zener diode. The circuit diagram of high-side MOSFET driver is shown in Fig. 3.25.

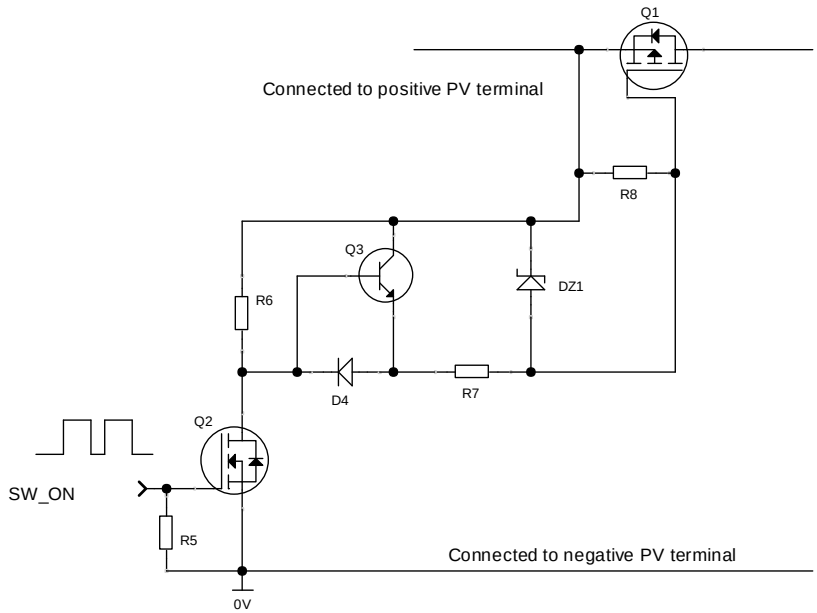

Fig. 3.25. High-side MOSFET driver using low-cost discrete components

The requirement of the driver circuit is when the TTL drive signal SW_ON is logical 1 the main MOSFET Q1 should turn on. On the other hand, for SW_ON = 0, Q1 must be off. An explanation of the operating principle of the high-side driver is given below.

For logic input 1, MOSFET Q2 is turned on, consequently, the gate terminal of Q1 goes very close to ground through the resistance R7 and diode D4. So V_{GS} is very close to supply voltage whose magnitude is much larger than that of the threshold voltage. Therefore, the effective gate-to-source capacitance C_{GS} gets quickly charged and Q1 turns on. During this

time, the NPN transistor Q3 remains cut-off as its base-emitter junction is reverse biased and it does not affect the operation of the circuit. A 18-V Zener diode DZ1 is connected across the gate-source terminal of Q1 to protect the gate of the MOSFET from gate-to-source breakdown voltage.

Corresponding to SW_ON = 0, the MOSFET Q2 turns OFF, so the transistor Q3 goes to linear mode with its base current supplied via R6. The diode D4 is now reverse biased. Due to the high gain of Q3 large collector and base current are produced which in turn quickly discharges C_{GS}. As a result Q2 turns off. SW_ON signal with the corresponding gate and drain signal of MOSFET Q1 are shown in Fig. 3.26 and Fig. 3.27, respectively. From Fig. 3.27 it is apparent that the turn off delay is about 200ns and the turn on delay is negligible small compared to it. The turn off delay is only 0.94% of time period of 21.3uS of the drive signal.

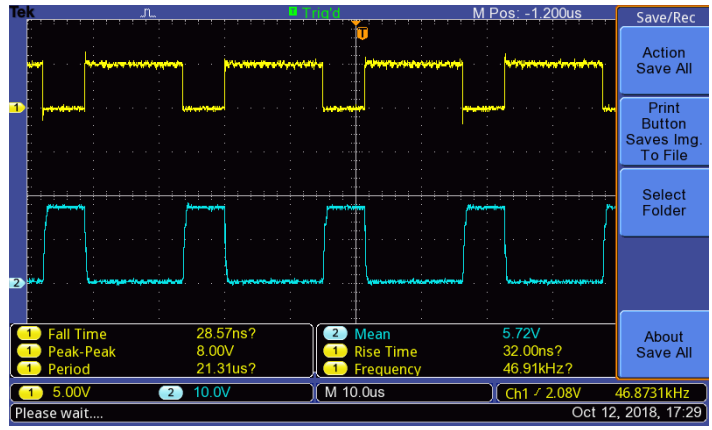

Fig. 3.26. SW_ON signal (CH1–5V/div), Gate signal of Q1 (CH2–10V/div). Time scale: 10µs/div

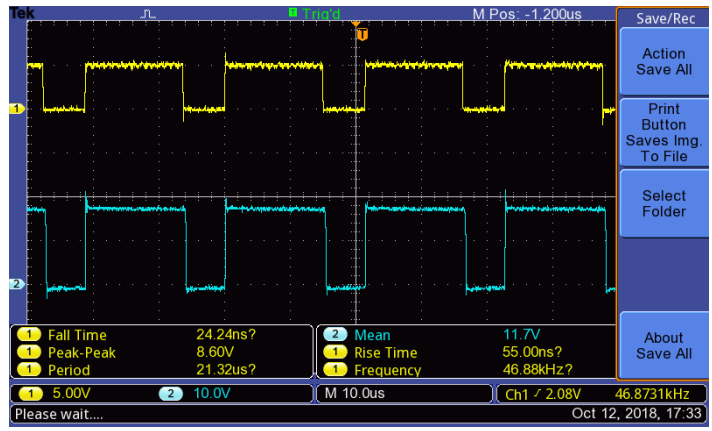

Fig. 3.27. SW_ON signal (CH1–5V/div), Drain signal of Q1 (CH2–10V/div). Time scale: 10µs/div

3.4.2.6 Battery temperature measurement

The battery temperature is measured to implement different charging algorithms which have already been discussed in the earlier section. In this implementation, a temperature sensor LM35 [21] is mounted on the battery case for battery temperature measurement. The sensor has an output voltage which is linearly-proportional to the Celsius temperature. The output voltage increases by 10mV for every 1°C rise in temperature. It does not require any external calibration to provide an accuracy of ± 0.25 °C at room temperature and ± 0.75°C over a full temperature range from −55°C to 150°C. ADC interface for the battery case temperature sensor using LM35 is shown in Fig. 3.28. The output voltage $u_{i,AD}$ related to the battery temperature T_b as follows

$$u_{i,AD} = S_{tmp} \times T_b \tag{3.61}$$

where S_{tmp} is the temperature sensitivity. For LM35 S_{tmp} = 10 mv/°C.

The output signal is directly connected to the on-chip ADC4 of the MCU. During the operation of the converter, the value of m has to be converted to the physical variable $T_{b,}$ combination of equation (3.50) and (3.61) give

$$T_b = \frac{u_{i,AD}}{S_{tmp}} = \left(\frac{q}{S_{tmp}}\right)m = G_T\, m \tag{3.62}$$

the gain factor G_T converting to T_b has the unit of °C .In this implementation, the measurement resolution of temperature is 0.25 °C.

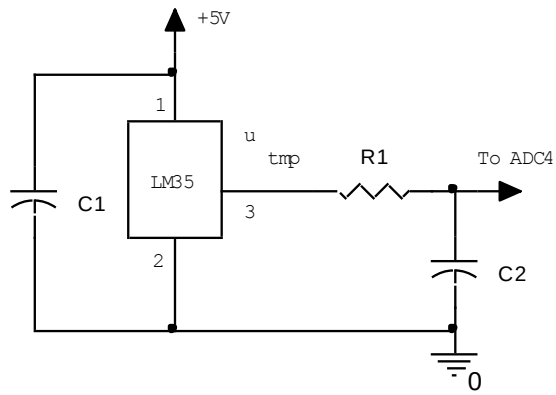

Fig. 3.28. ADC interface for battery case temperature sensor using LM35

3.4.2.7 Sampling pulse generation

In this study, a sampling pulse generator circuit of 2Hz is realized by using a binary ripple counter and a serial RTC chip as shown in Fig.3.29. The RTC chip (DS1307) consumes very low-power and has the features like full binary-coded decimal (BCD) clock/calendar, 56 bytes of nonvolatile (NV) RAM, I^2C interface, etc [22]. This IC requires a 32.768 kHz crystal as its time-base. To program DS1307 the address and data are transferred serially through an I^2C bidirectional bus. The bit4 of this IC, when set to logic 1, enables the oscillator output. The frequency of the square-wave output depends upon the value of bit1 and bit0 of the control register. In this case, we are chosen B1 = 1 and B0 = 0, so that a frequency of 8.192 kHz obtained at pin7. This is further divided by a factor of 2^{12} (= 4096) a CD4040 [23] CMOS frequency divider. This results in an output frequency of 2 Hz to be used as system sampling tick pulse. This signal is polled to initiate the beginning of a controller sampling interval of 500mS for all states. The NV RAM of DS1307 is also used in this study to store the value of SOC which in discussed in the next section.

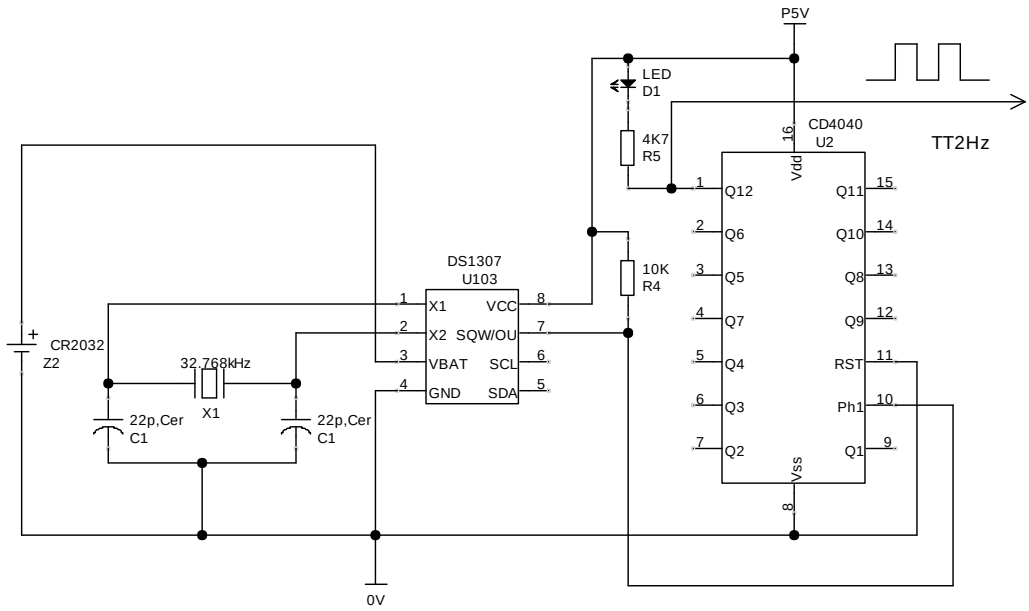

Fig. 3.29. Circuit diagram of 2Hz tick pulse generator

3.4.2.8 Battery state-of-charge (SOC) estimation

The state-of-charge (SOC) of a rechargeable battery is a numerical index in the range 0-100 that indicates the usable amount of percentage amp-hour (Ah) capacity of the battery at a given time. The zero value indicates a fully discharged battery, while 100 indicates a fully

charged one. The SOC cannot be determined by merely integrating the battery terminal current over a period of time from t_1 to t_2, where $t_2 > t_1$. In an ideal case, if the battery is being charged by a terminal current i_T, time is measured in seconds and there is no *gassing*, the value of SOC, indicated by S_c at time t_2 is given by

$$S_c(t_2) = S_c(t_1) + K_{cs} \int_{t_1}^{t_2} i_T \, dt \quad (3.63)$$

where C_{10} is the 10-hr ampere-hour rating of the battery and $K_{cs} = 1/(36\ C_{10})$ is the multiplying factor that converts coulomb (A.s) to a dimensionless quantity S_c.

In reality, a part of the terminal current is spent in gassing. If this current is indicated by i_g the actual charging current becomes (i_T - ig) and equation (3.63) modified as

$$S_c(t_2) = S_c(t_1) + K_{cs} \int_{t_1}^{t_2} (i_T - i_g) \, dt \quad (3.64)$$

Likewise, if the battery is discharging with a terminal current - i_T, equation (3.63) is modified as

$$S_c(t_2) = S_c(t_1) - K_{cs} \int_{t_1}^{t_2} (i_T + i_g) \, dt \quad (3.65)$$

Although, i_T can be measured by a suitable sensor, i_g can, at best, be estimated. Researchers at Fraunhoffer Institute [1] have done considerable work on VRLA batteries to estimate the variation of i_g as a function of the battery voltage per cell and its case temperature. In this study, the value of i_g at a specified condition of battery cell voltage u_B = 2.23V and cell temperature T = 20 ºC is indicated by its nominal value of i_{g0}. The actual value of i_g at any other condition of u_B and T varies exponentially as given by

$$i_g = i_{g0}\, e^{\alpha} \quad (3.66)$$

where α is a weighted sum of the increase of cell voltage and cell temperature from their respective nominal values and is given by

$$\alpha = \alpha_v\ (u_B - 2.23) + \alpha_t\ (T - 20) \quad (3.67)$$

According to reference [1], the values of α_v and α_t for a VRLA battery are 10/V and 0.06/ºC, respectively.

i_{g0} linearly varies as the Ah capacity C_{10} of the battery given by

$$i_{g0} = 3.6X\,10^{-4}\,C_{10} \quad (A) \tag{3.68}$$

For better understanding, the DC power distribution of our system with battery model is shown in Fig. 3.30. Apply KCL at node p gives

$$Io = iB\_net + i_g \tag{3.69}$$

where i_g is greater than zero and i_g flows from positive to negative terminal of the battery.

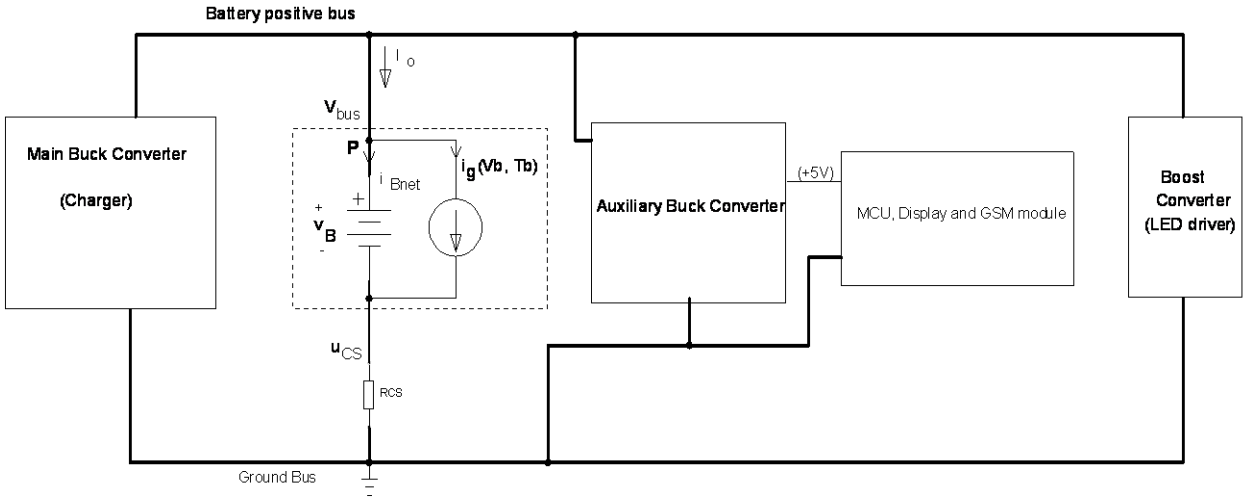

Fig. 3.30. DC power distribution of the system showing the battery model

Computationally, in a digital system, the increment or decrement of the value of S_c in a sample period can be computed easily if the charging/discharging status is known and the battery terminal current, cell voltage and case temperature are measurable, by using the digitized version of either equation (3.64) or equation (3.65), as the case may be. Backward rectangular integration usually gives good accuracy. Calibration of the SOC can be done by charging a new battery to a condition when other criteria indicate that it has been fully charged and then manually setting the S_c value to 100. Theoretically, this calibration has to be done only once in the lifetime of the battery provided the SOC evaluation routine always runs in the background for all states.

The function calc_SOC calculates the increase (or decrease) of 100 times the state-of-charge (socX100) of the battery over a sampling interval and stores the integral part of it in two consecutive bytes of a non-volatile (battery backed-up) RAM. The floating point value of socX100 is stored in the main RAM. The integer value of socX100, limited between 0 and 10000, is returned as an unsigned integer. The function requires four parameters to calculate

the SOC. They are battery current direction (iB_dir), battery current (Io), converter output voltage (Vo) and battery case temperature (Tb). The flowchart for this function is shown in Fig. 3.31. Depending on the direction of battery current, iB_dir is assigned to either +1 (for charging) or -1 (for discharging).

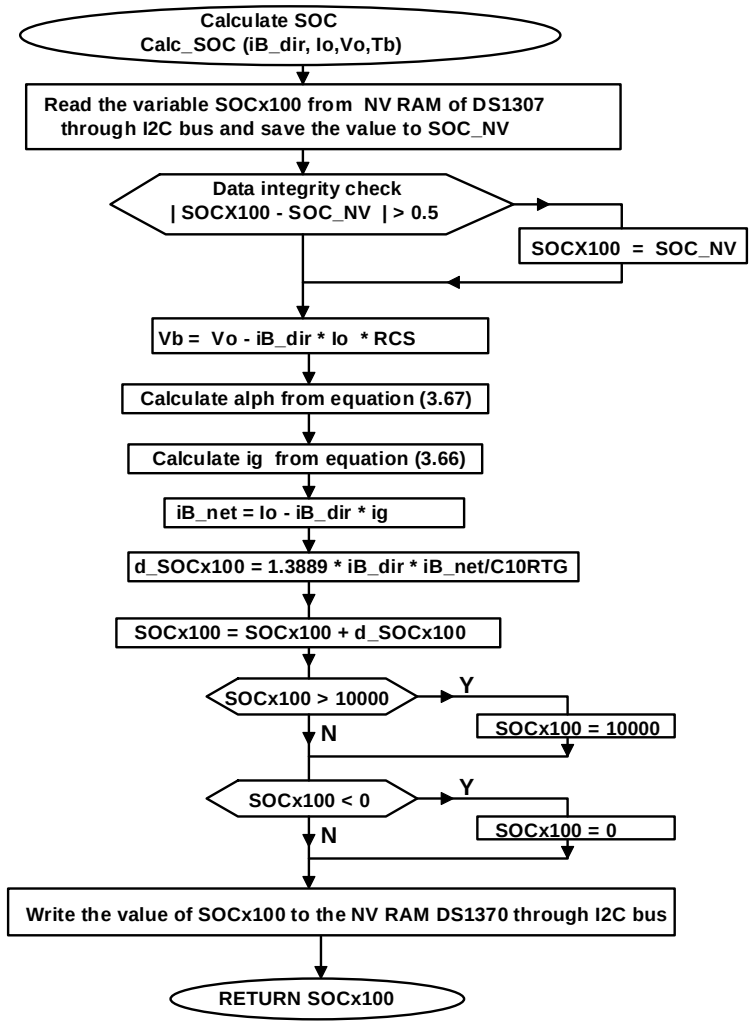

Fig. 3.31. Flowchart of the SOC estimation for VRLA battery

3.4.3 Experimental results

To validate the proposed battery charging system, a prototype has been made in the laboratory. The experimental setup for laboratory is shows in Fig. 3.32. In the laboratory, for experimental purpose, the solar module is replaced by a solar emulator. In this implementation, we have used 26AH, 12V VRLA battery and 12Volt, 100 watt-peak solar module.

An experiment was conducted to verify the tracking behavior of the proposed MPPT algorithm under variable irradiance. In this experiment, the irradiance was suddenly decreased from 1000W/m^2 to 500W/m^2 using a solar simulator to monitor the tracking performance of the controller to reach the maximum power point (MPP). The corresponding waveforms of input voltage (i.e., output of the PV array) and output current (i.e., battery charging current) are shown in Fig. 3.33. It can be observed that the controller takes five cycles (i.e., 2.5s at a 500ms sampling period) to reach the MPP. Similarly, corresponding waveforms of the input voltage and output current are shown in Fig. 3.34, for sudden increase in irradiance from 500W/m^2 to 1000W/m^2. It also takes 4-5 cycles to reach the MPP. Therefore, the controller can track the maximum power immediately (within 2.5s) under step decrease or increase of irradiance.

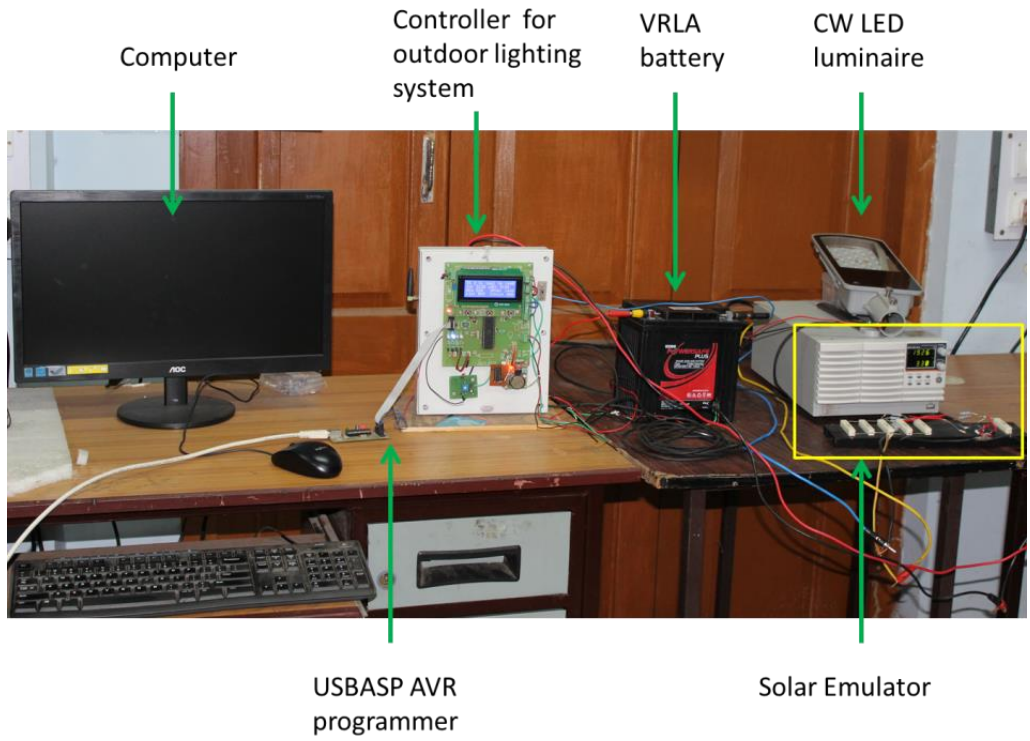

Fig. 3.32. Hardware setup of VRLA battery charger

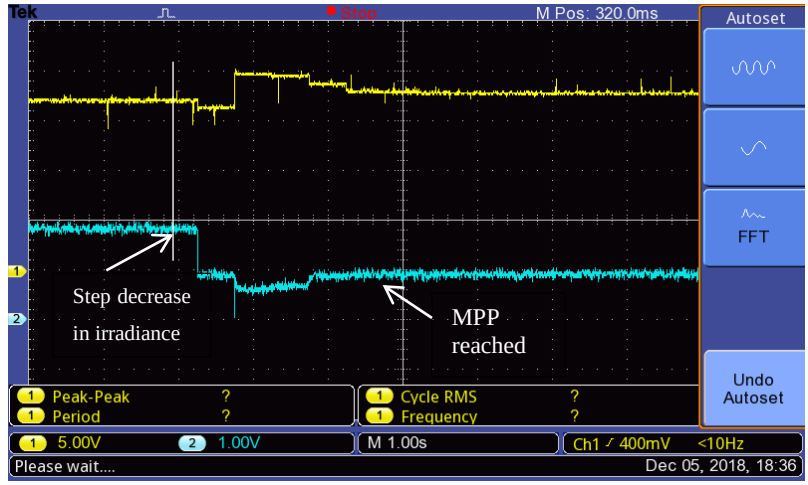

Fig. 3.33. Converter waveforms of input voltage (CH1: 5V/div) and output current (CH2:2.006A/div) when irradiance step changes from 1000W/m^2 to 500W/m^2,Time scale - 1 s/div

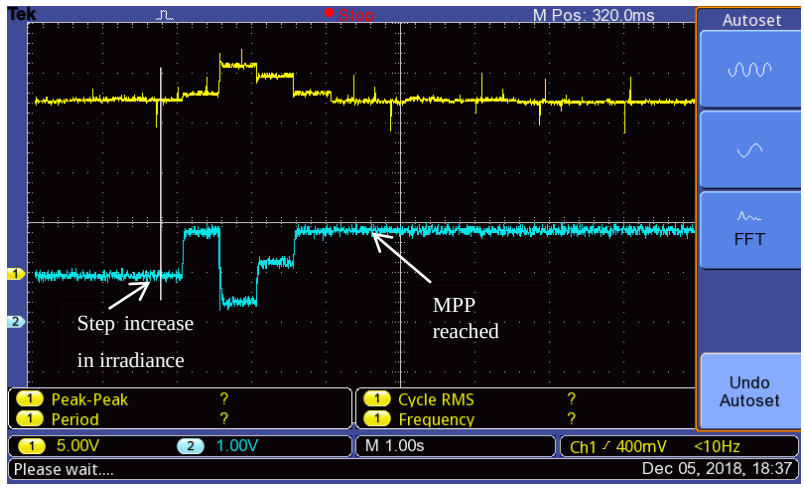

Fig. 3.34. Converter waveforms of input voltage (CH1: 5V/div) and output current (CH2: 2.006A/div), when irradiance step changes from 500W/m^2 to 1000W/m^2, Time scale-1 s/div.

It has been demonstrated in Fig. 3.35 that the output voltage is nearly constant during MPPT tracking when the irradiance was suddenly increased from 500W/m^2 to 1000W/m^2 using a solar simulator. Therefore, for quick tracking of MPP, in the proposed technique dP_O/dV_i has been chosen as perturbation parameter of D instead of dP_O/dV_O. Similarly, the corresponding waveforms of input voltage and output current are shown in Fig. 3.36 for suddenly decreased in irradiance from 1000W/m^2 to 500W/m^2. In this case, the output voltage is also constant during MPPT tracking.

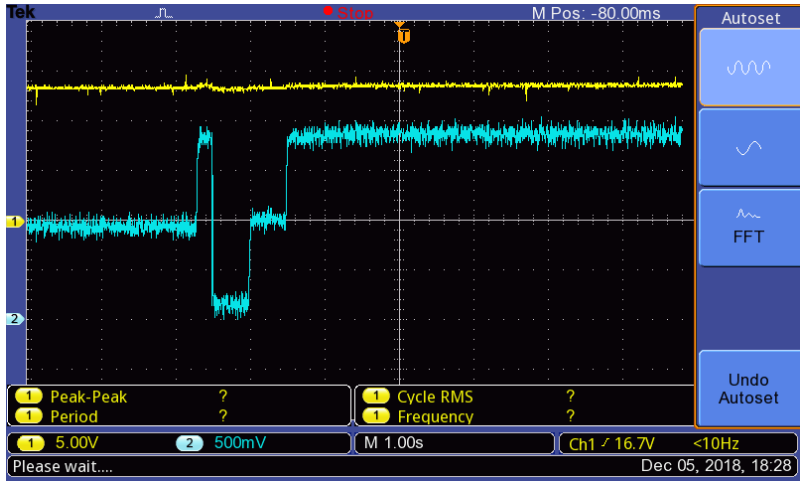

Fig. 3.35. Converter waveforms of input voltage (CH1: 5V/div) and output current (CH2: 1.003A/div), when irradiance step changes from 500W/m^2 to 1000W/m^2, Time scale-1 s/div

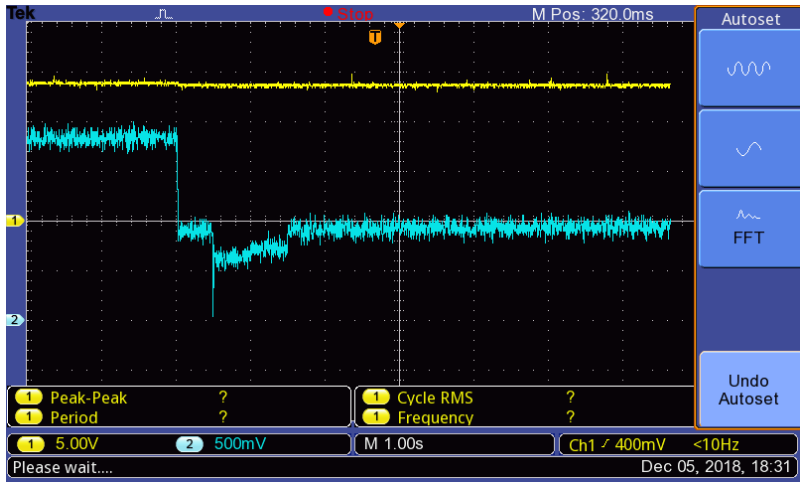

Fig. 3.36. Converter waveforms of input voltage (CH1: 5V/div) and output current (CH2: 1.003A/div), when irradiance step changes from 1000W/m^2 to 500W/m^2, Time scale-1 s/div

Another experiment was performed to know the characteristic of the battery voltage battery charging current, and dutycycle of the converter as a function of time. The measured V_B, I_B and D for MPPT stage (i.e., for state1) and two-stage CV stage (i.e., for state2) are shown in Fig. 3.37, Fig. 3.38 and Fig. 3.39, respectively. For better presentation the results were recorded at intervals of 15min, 10 min and 5 min, respectively, for MPPT stage, CV stage with high threshold voltage and CV stage with low threshold voltage.

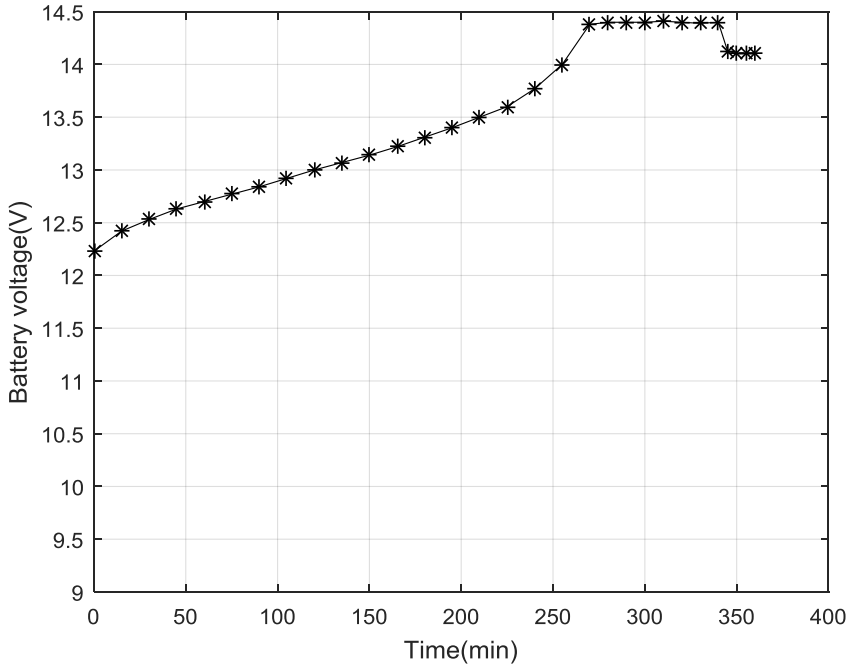

Fig. 3.37. Measured battery voltage with time for state 1 and state 2

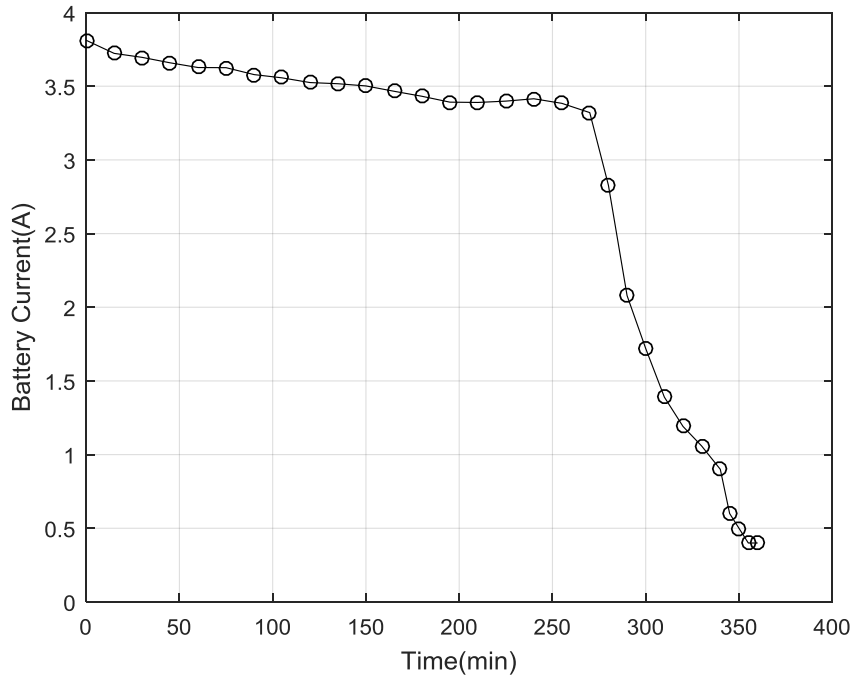

Fig. 3.38. Measured battery current with time for state 1 and state 2

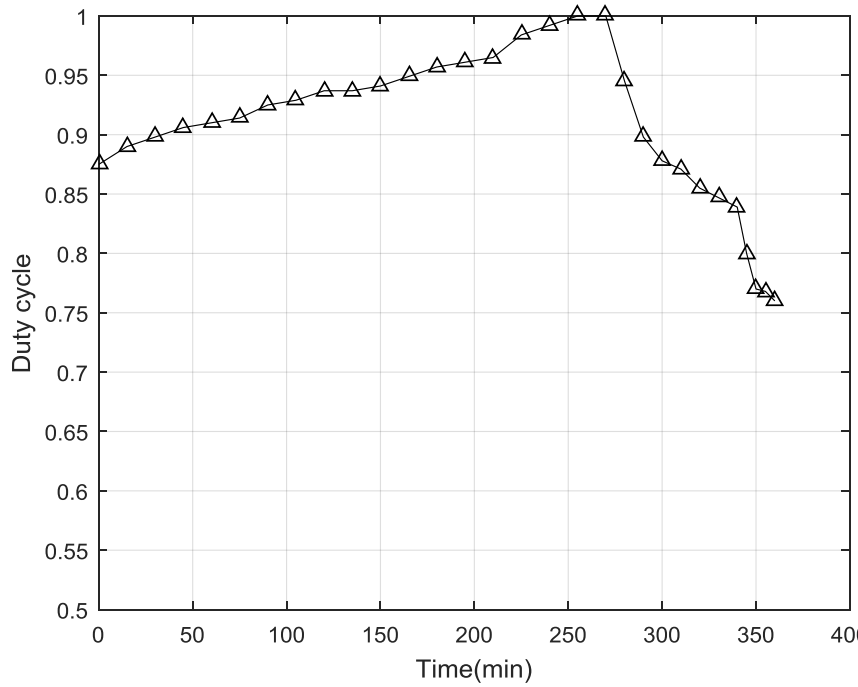

Fig. 3.39. Measured duty cycle of the converter during charge for state 1 and state 2

For better visibility, V_B , I_B and D for trickle charge are shown separately in Fig. 3.40, Fig. 3.41 and Fig. 3.42, respectively. In this experiment, the actual values were recorded at interval of 10 sec.

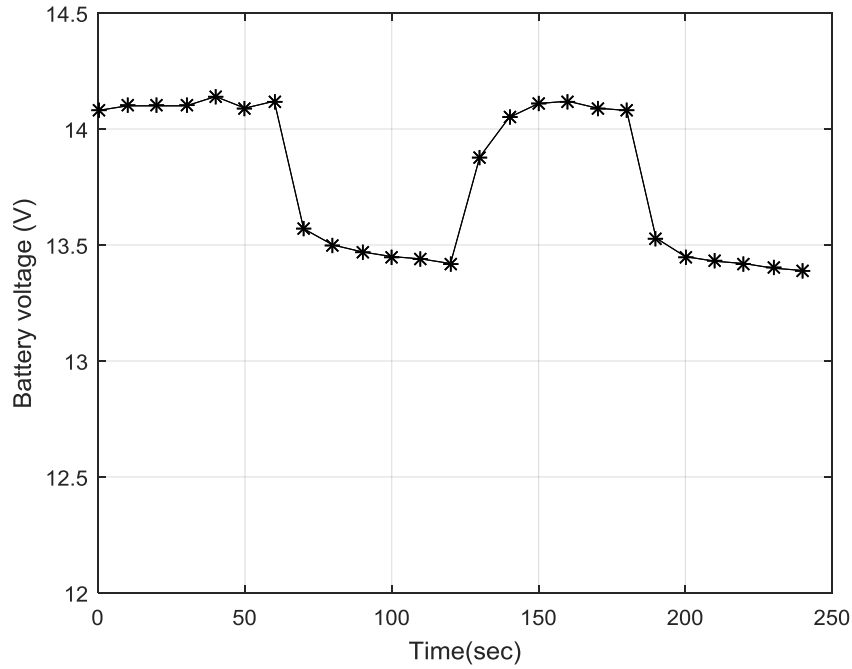

Fig. 3.40. Measured battery voltage as a function of time for state 3

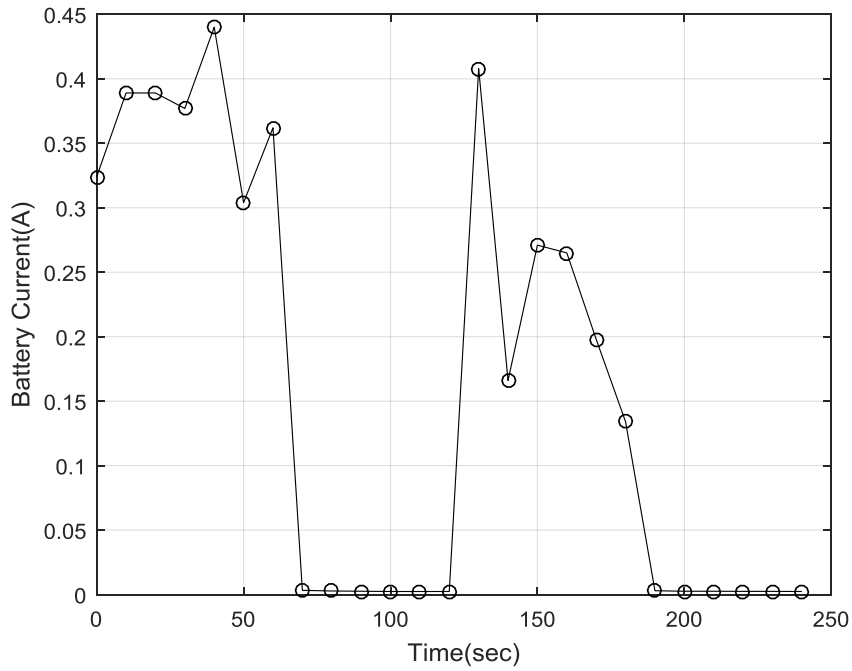

Fig. 3.41. Measured battery current as a function of time for state 3

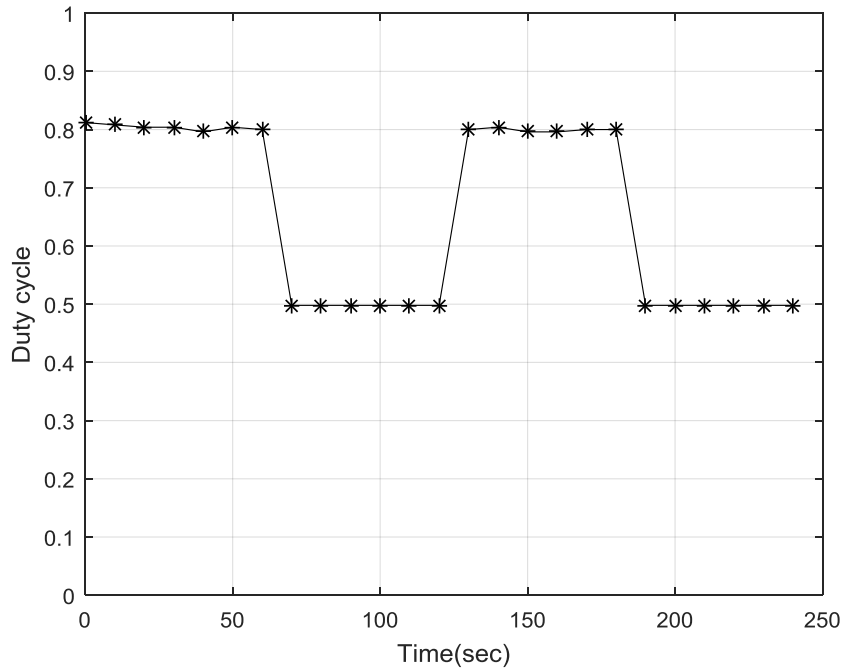

Fig. 3.42. Measured duty cycle as a function of time for state 3

The prototype of the solar-powered outdoor lighting system and the battery box has been shown in Fig. 3.43 and Fig. 3.44, respectively. In this prototype, a PV module of 60 W_p and a VRLA battery of 26AH have been used.

Fig. 3.43 Pictorial view of the developed solar-powered OLS

Fig. 3.44 Close-up view of the OLS controller

3.5 Conclusion

This chapter has discussed the solar-powered, multi-stage battery charger using a simple converter topology. The charger is capable to charge the VRLA battery efficiently from a PV module without overcharging. The charging scheme has multiple objectives which ensure the optimum use of solar energy as well as the optimum performance of the VRLA battery. For MPPT (i.e., state1), a modified perturb and observe technique has been presented to maximize the output power of the charger. For absorption charging (i.e., state2), a two-stage constant voltage charging method has been adopted which protects the battery from being overcharged. Trickle charge is also implemented to maintain the battery at full SOC. Additionally, SOC and health of the battery are also estimated. For state-of-charge (SOC) estimation of the battery, an accurate measurement of battery current is mandatory. Thus, adaptive perturbation based P&O technique is implemented using the same output voltage and current sensor with the addition of a PV voltage sensor. This consequently reduces the hardware cost as well as the computational burden of the controller.

The algorithm is experimentally validated by hardware implementation. The implementation uses only readily available components including a low-cost microcontroller (ATmega32A). The experimental results demonstrate that the proposed algorithm is working in proper manner under variable insolation condition.

References

[1] S. D. ; S. I. ; W. Lawrance, "A battery management system for stand-alone photovoltaic energy systems," *IEEE Ind. Appl. Mag.*, no. June, pp. 67–72, 2001.

[2] M. Bhatt, W. G. Hurley, S. Member, and W. H. Wölfle, "A New Approach to Intermittent Charging of Valve-Regulated Lead – Acid Batteries in Standby Applications," vol. 52, no. 5, pp. 1337–1342, 2005.

[3] D. A. J. Rand, D. P. Boden, C. S. Lakshmi, R. F. Nelson, and R. D. Prengaman, "Manufacturing and operational issues with lead-acid batteries," vol. 107, pp. 280–300, 2002.

[4] E. Rossinot, C. Lefrou, F. Dalard, and J. P. Cun, "Batteries in standby applications : comparison of alternate mode versus ¯ oating," vol. 101, 2001.

[5] P. Waltari and R. Tenno, "The Effects of Intermittent Charging on VRLA Battery Life Expectancy in Telecom Applications," pp. 121–127.

[6] K. Jana, "Charging pure lead-tin batteries :," vol. 9301.

[7] S. Armstrong, M. E. Glavin, and W. G. Hurley, "Comparison of Battery Charging Algorithms for Stand Alone Photovoltaic Systems," pp. 1469–1475, 2008.

[8] 1361™-2014 IEEE-SA-Standards-Board, "IEEE Guide for Selecting, Charging, Testing, and Evaluating Lead-Acid Batteries Used in Stand-Alone Photovoltaic (PV) Systems," 2014.

[9] D. Behavior, "Dynamic Behavior of a Class," *Power*, vol. 00, no. 9, 1983.

[10] Y. . Jung, G. . Yu, J. . Choi, and J. . Choi, "High-frequency DC link inverter for grid-connected photovoltaic system," *Conf. Rec. IEEE Photovolt. Spec. Conf.*, pp. 1410–1413, 2002.

[11] N. Femia, G. Lisi, G. Petrone, G. Spagnuolo, and M. Vitelli, "Distributed maximum power point tracking of photovoltaic arrays: Novel approach and system analysis," *IEEE Trans. Ind. Electron.*, vol. 55, no. 7, pp. 2610–2621, 2008.

[12] M. Veerachary, T. Senjyu, and K. Uezato, "Maximum power point tracking control of IDB converter supplied PV system," *IEE Proc. - Electr. Power Appl.*, vol. 148, no. 6, p. 494, 2001.

[13] P. Huynh and B. H. Cho, "Design and analysis of a microprocessor-controlled peak-power-tracking system," *IEEE Trans. Aerosp. Electron. Syst.*, vol. 32, no. 1, pp. 182–190, 1996.

[14] P. J. Wolfs and L. Tang, "A single cell maximum power point tracking converter without a current sensor for high performance vehicle solar arrays," *PESC Rec. - IEEE Annu. Power Electron. Spec. Conf.*, vol. 2005, pp. 165–171, 2005.

[15] A. Pandey, N. Dasgupta, and A. K. Mukerjee, "High-performance algorithms for drift avoidance and fast tracking in solar MPPT system," *IEEE Trans. Energy Convers.*, vol. 23, no. 2, pp. 681–689, 2008.

[16] "ATmega32A - 8-bit AVR Microcontrollers." [Online]. Available: https://www.microchip.com/wwwproducts/en/ATmega32A. [Accessed: 14-Mar-2019].

[17] "MBR2045CTG, MBRF2045CTG Switch-mode Power Rectifier." [Online]. Available: https://www.onsemi.com/pub/Collateral/MBR2045CT-D.PDF. [Accessed: 15-Apr-2019].

[18] "LM2576xx Series SIMPLE SWITCHER ® 3-A Step-Down Voltage Regulator Fixed Output Voltage Version Typical Application Diagram," 1999. [Online]. Available: http://www.ti.com/lit/ds/symlink/lm2576.pdf. [Accessed: 29-Mar-2019].

[19] "TLC272 Dual Single Supply Operational Amplifier | TI.com." [Online]. Available: http://www.ti.com/product/TLC272. [Accessed: 15-Apr-2019].

[20] "Power MOSFET IRF9540, SiHF9540." [Online]. Available: https://www.vishay.com/docs/91078/91078.pdf. [Accessed: 29-Mar-2019].

[21] "LM35 Precision Centigrade Temperature Sensors," 1999. [Online]. Available: http://www.ti.com/lit/ds/symlink/lm35.pdf. [Accessed: 29-Mar-2019].

[22] "DS1307 64 x 8, Serial, I2 C Real-Time Clock." [Online]. Available: https://datasheets.maximintegrated.com/en/ds/DS1307.pdf. [Accessed: 29-Mar-2019].

[23] "CD4040B CMOS 12-Stage Ripple-Carry Binary Counter/Divider | TI.com." [Online]. Available: http://www.ti.com/product/CD4040B. [Accessed: 15-Apr-2019].

Chapter 4

Development of Dimmable, Tunable-CCT and Fixed-CCT LED Lighting Systems

4.1 Introduction

In this chapter, a description of the developed tunable-CCT and fixed-CCT LED lighting system is presented. Recently, high-brightness light emitting diodes (HB-LEDs) are becoming the prime candidates for general lighting applications. HB-LEDs have the notable advantages of high luminous efficiency and consequently reduced energy consumption, very low ultraviolet emission, high environment friendliness and longer operating lifetime over conventional lamps (e.g., incandescent and fluorescent, high-pressure sodium, low-pressure sodium, metal halide lamps, etc) [1], [2]. In this study we have developed two types of LED lighting systems, each suitable for a specific application area.

The first one is a tunable-CCT, variable-illuminance LED lighting system for colour-tunable outdoor lighting applications (e.g., residential non-living areas, public buildings and structures, gardens, parks etc.). The prototype LED lighting system can independently produce a variable CCT ranging from 2500 to 12500 K and a variable illuminance ranging from 5 to 120 lx.

The second one is a fixed-CCT, three-step dimmable LED lighting system for single colour outdoor lighting applications (such as streets, pathways, parking lots, industrial yards, security areas etc.). For the fixed-CCT lighting system, generally, three types of phosphor-coated (PC) LEDs are commercially available. They are warm-white (around 2700K), natural-white(around 4000K), cool-white (at 5000K or more). Among them in our implementation, we have chosen cool-white LED for availability in our laboratory. A details description of both the light sources and its driving techniques are discussed in this chapter.

4.2 Development of tunable-CCT, variable-illuminance LED lighting system

In the present realization, a wide-range, open-loop and decoupled control of CCT and illuminance of a composite LED lamp has been presented that employs two-component

colour blending. A literature survey of tunable-CCT LED lighting system has already been presented in chapter 1. Light from the main CW (cool-white) PC-LED source is mixed in required proportion with that from a companion source which is either a blue or a red LED. Both the sources are fed by linear pulse-width (PW) modulators. Mathematical formulations necessary for selection of the companion source and determination of the duty cycles of the PW modulators for obtaining the desired CCT and work plane illuminances are derived. Using hardware made of readily available components and a simple software built for the purpose, a proof-of-concept system has been built. The forward drop of an LED fed by a constant current is a linearly decreasing function of its junction temperature. In our case, no attempt was made to estimate the junction temperature. Instead, the chromaticity coordinates of an LED source and its luminous flux contribution have been estimated from its forward drop, when driven under PWM control with a fixed peak current. The system is capable of providing a CCT range of 2500 to 12500 K and an illuminance range of 5 to 120 lx. The principle of operation, the mathematical formulations and the hardware and software features of the system have been described and performance evaluation of the system has been made through laboratory experiments.

4.2.1 Principle of Two-component Colour Blending

To resolve the issue related to the limited CCT tunable facility as described in the literature section of Chapter1. In this study, a hybrid LED colour mixing scheme has been implemented, where light from a main CW PC-LED source is blended with that from a companion red or a blue LED source to get, respectively, a CCT lower or higher than that of the CW LED. For a required CCT, since only two sources are involved, the colour shift of the blended light due to drift of the chromaticity of the constituent sources is less pronounced, provided the luminance and chromaticity shift of the sources are estimated at the run time and the blending ratio is adjusted accordingly.

For the tunable-CCT light source, a separate prototype has been made to demonstrate the proposed system. In this system, the CCT and illuminance have been set locally for testing the major part of the algorithm by using two 10K potentiometer (POT) instead of remote place (i.e., through SMS). Although, in the actual implementation, this system has been integrated to the main system whose pin allocation is given in Table 2.2 of Chapter 2. A block diagram of the proposed LED lighting system with decoupled control of CCT and

illuminance is shown in Fig. 4.1 Blending of light from the main CW LED with that of companion LED is implemented using pulse-width-modulation (PWM) dimming technique. The combination of the microcontroller unit (MCU), the de-multiplexer (DEMUX), and the human interfaces, shown inside the left-hand rectangle will be termed as CCT and illuminance control unit (CICU). The three voltages, ufa_W, ufa_R and ufa_B given as inputs to three analog-to-digital converters (ADC) in the CICU are the average forward drops of the three LED strings, which, in turn, are obtained by passing the instantaneous rectangular pulse waveforms through adequate low-pass active filters. Further details of the filters are available in Section 4.2.2.2. Other salient hardware features of the system are also given in the same section.

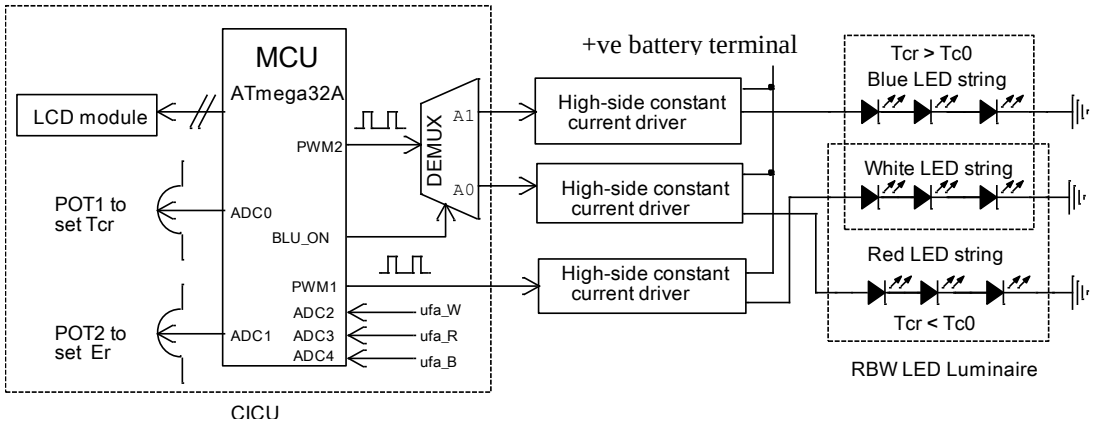

Fig. 4.1. Block diagram of the proposed CCT and illuminance controllable LED lighting system

4.2.1.1 Mathematical Foundation of Control Strategy

Two primary light sources S_1 and S_2 of two different colours with CIE (Commision Internationale de l'Eclairage) 1931 chromaticity coordinates of (x_1, y_1) and (x_2, y_2), respectively, are used to illuminate the same surface (the work plane). Y_1 and Y_2 are their respective luminance values, and E_1 and E_2 are the respective illuminance contributions on the work plane. Grassmann's law [3] also known as the law of linear combination of colours, states that the chromaticity coordinates (x_b, y_b) of the blended colour is given by the linear weighted sums of the chromaticity coordinates of S_1 and S_2 given below

$$x_b = x_1 a_1 + x_2 a_2, \quad \text{and} \quad y_b = y_1 a_1 + y_2 a_2, \tag{4.1}$$

where the weighting coefficients a_1 and a_2 are given by

$$a_1 = \frac{\frac{Y_1}{y_1}}{\frac{Y_1}{y_1} + \frac{Y_2}{y_2}} \quad \text{and} \quad a_2 = \frac{\frac{Y_2}{y_2}}{\frac{Y_1}{y_1} + \frac{Y_2}{y_2}} \tag{4.2}$$

It may be observed here that, by virtue of definitions of a_1 and a_2,

$$a_1 + a_2 = 1 \tag{4.3}$$

Use of simple analytical geometry shows that, due to equation (4.3), the position of (x_b, y_b) coordinate pair in the xy plane cannot be arbitrary – it must lie on the straight line joining the coordinate pairs of the constituent sources.

For the purpose of control of the blended colour, the two source luminances have to be controlled over a wide range. While analog control of the LED currents is a theoretical option, it cannot be used in this application due to several reasons[4], [5] . The first is that the linearity of the luminance vs. current graph is rather poor [5]. Secondly, the chromaticity changes with change of current [5]. Another important reason is that the generation of an analog current command from a microcontroller requires additional hardware like a digital-to-analog converter (DAC) or a PWM-to-analog converter.

In the present study, the two source luminances are controlled by two linear PWM dimmers described in Section 4.2.2. If D_1 and D_2 are their respective duty cycles, the values of Y_1 and Y_2 will be given by

$$Y_1 = Y_{M1}\, D_1, \text{ and} \tag{4.4}$$

$$Y_2 = Y_{M2}\, D_2, \tag{4.5}$$

where Y_{M1} and Y_{M2} are the maximum values of Y_1 and Y_2 corresponding to the maximum values of D_1 and D_2, namely, unity. Equations (4.1) to (4.5) clearly indicate that by changing the values of D_1 and D_2, the chromaticity coordinates of the blended colour (indeed, the colour) can be changed.

In many situations, where the distance between the sources and the illuminated surface is fixed, the transmittance of the medium is fixed, reflectances of nearby objects are fixed, and there is no stray light, the following equations in terms of the illuminances E_1, E_2 can be written

$$E_1 = k_{YE}\, Y_1, \tag{4.6}$$

$$E_2 = k_{YE}\, Y_2, \tag{4.7}$$

where k_{YE} is constant.

In view of the linearity of the PWM process, the average or apparent illuminances E_1 and E_2 are related to their respective maximum values E_{M1} and E_{M2} as below:

$$E_1 = E_{M1}\, D_1, \text{ and} \tag{4.8}$$

$$E_2 = E_{M2}\, D_2. \tag{4.9}$$

Equation (4.2) is thus modified as

$$a1 = \frac{\frac{E_{M1}\, D_1}{y_1}}{\frac{E_{M1}\, D_1}{y_1} + \frac{E_{M2}\, D_2}{y_2}} \quad \text{and} \quad a2 = \frac{\frac{E_{M2}\, D_2}{y_2}}{\frac{E_{M1}\, D_1}{y_1} + \frac{E_{M2}\, D_2}{y_2}} \tag{4.10}$$

If we define the a_2/a_1 ratio as r_a

$$r_a = \frac{a_2}{a_1} \tag{4.11}$$

its value, in view of equation (4.10), will be given as

$$r_a = \frac{E_{M2}}{E_{M1}}\, \frac{D_2}{D_1}\, \frac{y_1}{y_2}, \text{ or, equivalently,}$$

$$\frac{D_2}{D_1} = r_a \frac{E_{M1}}{E_{M2}}\, \frac{y_2}{y_1} \tag{4.12}$$

The following additional definitions are now made.

$$\text{Peak illuminance ratio, } r_E = \frac{E_{M2}}{E_{M1}} \tag{4.13}$$

$$\text{y-coordinate ratio, } r_y = \frac{y_2}{y_1} \tag{4.14}$$

$$\text{Blending ratio, } r_D = \frac{D_2}{D_1} \tag{4.15}$$

Equations (4.13), (4.4) and (4.15), when substituted in equation (4.12) yield the value of blending ratio r_D as

$$r_D = \frac{r_a\, r_y}{r_E} \tag{4.16}$$

Equation (4.3) along with the first of equation (4.1) results in a value of $r_a = a_2/a_1$ as

$$r_a = \frac{x_1 - x_b}{x_b - x_2} \tag{4.17}$$

Thus if the chromaticity coordinate x_b of the required blended light is known, the use of equation (4.16) will evaluate the required blending ratio r_D.

The chromaticity coordinates of the two constituent sources and that of the blended light is shown in Fig. 4.2. For convenience, the line segment joining the two points S_1 and S_2 will be called the blending line. The equation of the blending line can be shown to be given by

$$y = m\,x + (y_2 - m\,x_2) \tag{4.18}$$

where (x, y) is the coordinate of an arbitrary point on the line and

$$m = \frac{y_2 - y_1}{x_2 - x_1} \tag{4.19}$$

is the slope of the line. Two blending lines WB (for S_2 = blue) and WR (for S_2 = red), used in this study, are shown in Fig. 4.2. McCamy's formula [6] for evaluation of the correlated colour temperature, Tc of a source with known xy chromaticity coordinates involves calculating a number n given by

$$n = \frac{x - x_e}{y_e - y} \tag{4.20}$$

where (x_e, y_e) is the coordinate of an epicenter in the xy plane from which all constant Tc lines emanate. x_e and y_e have values of 0.3320 and 0.1858, respectively. Clearly, n is the negative inverse slope of the line joining (x, y) with (x_e, y_e). The value of T_{cr}, as given by McCamy's formula is

$$T_{cr} = 449\,n^3 + 3525\,n^2 + 6823.3\,n + 5520.33 \tag{4.21}$$

In the range of T_c from 2856 to 6500 K, McCamy's formula provides a maximum absolute error of 2 K, and is, therefore, very accurate. Even for a wider range of 2000 to 12500 K it is reasonably accurate. Equation (4.22) is a mapping from a real number n to another real number T_{cr}. The present method proposes to use two mathematically simple, yet very accurate, inverse mappings from T_{cr} to n. One will be used for $T_{cr} \leq T_{c0}$, while the other for $T_{cr} > T_{c0}$, where T_{c0} is the value of the CCT for the source S_1.

Equation (4.20) can be rearranged as the equation of a straight line given, in slope-intercept form, by

$$y = -\frac{1}{n}x + \left(\frac{x_e}{n} + y_e\right) \quad (4.22)$$

We observe that for a fixed n, a fixed T_{cr} can be obtained from equation (4.21) and such a value of T_{cr} is obtained anywhere on the line given by equation (4.22). This line is therefore called an isotherm or an isoCCT line. Fig. 4.2 shows two isoCCT lines PQ_1 and PQ_2, corresponding to T_{cr} = 10000K and 2500K, respectively.

In the range ($0.075 \leq n < 0.725$), or, equivalently, ($6052K \leq T_{cr} < 12491K$), McCamy's formula can be closely fitted by a quadratic equation of the form:

$$an^2 + bn + c = 0 \quad (4.23)$$

where $a = 4064$; $b = 6640$; $c = 5536 - T_{cr}$ (4.24)

Similarly, in the range ($-0.68 \leq n < 0.12$), or, equivalently, ($2369\ K \leq T_{cr} < 6390\ K$) the quadratic equation (4.24) has coefficients:

$$a = 3148; \qquad b = 6766; \qquad c = 5524 - T_{cr} \quad (4.25)$$

The advantage of replacing the original McCamy's formula by two piecewise quadratic equations is that, for a given T_{cr}, a closed form solution for n can be easily obtained from equations (4.23) and (4.24), or (4.23) and (4.25), depending on the range of T_{cr}. The closeness of the fits are verified by worst-case deviation in T_{cr} of 5K and 10K, for ($-0.68 \leq n < 0.12$) and ($0.075 \leq n < 0.725$), respectively, from that given by McCamy's formula.

Once n is known from equation (4.23), we can find (x_b, y_b), the chromaticity coordinates of the intersection of two straight lines given by equations (4.18) and (4.22). This (x_b, y_b) coordinate pair produce the desired T_c and can be generated by mixing light fluxes from S_1 and S_2 using a blending ratio $r_D = D_2 / D_1$.

The intersection points lie within the hollow rectangular boxes shown in Fig. 4.2 The solution for x_b, obtained from substitution of x by x_b and y by y_b in equation (4.18) and (4.22), is given by

$$x_b = \frac{x_e + n\,(y_e - y_2 + mx_2)}{mn + 1} \quad (4.26)$$

Substitution of equation (4.26) into equation (4.17) yields r_a, from where r_D can be calculated using (4.16).

Computation of the individual values of D_1 and D_2 is rather straightforward considering the fact that the total required illuminance E_r on the work plane is the sum of the illuminance contributions E_1 and E_2:

$$E_r = E_1 + E_2 \tag{4.27}$$

Substitution of equations (4.8), (4.9), (4.13) and (4.14) into equation (4.27) finally yields

$$D_1 = \frac{Er}{E_{M1}\,(1 + r_D\, r_E)} \tag{4.28}$$

D_2 is determined from equation (4.15) as

$$D_2 = r_D\, D_1 \tag{4.29}$$

The values of the controlled outputs of the CCT and illuminance controller should ideally be the two duty cycles D_1 and D_2. But since D_1 and D_2 are two real numbers in general, they can not be directly transferred to the PWM registers of a microcontroller. The have to be converted to integers by the expessions below

$$p_k = \text{round}\,(D_k \,.\, 2^N) - 1, \qquad k = 1, 2 \tag{4.30}$$

where N is the word length of the PWM registers. It is clear that the actual values of the duty cycles are not D_1 and D_2, in general, but $(p_1+1) / 2^N$ and $(p_2 + 1) / 2^N$. Consequently, the actual value of r_D is modified to $(p_2 + 1) / (p_1 + 1)$. This causes a quantization error and its effect on system performance will be examined in Section 4.4.3. The notion of a transition value D_{Tk} may be introduced here. The transition value of D_k is a value D_{Tk} such that, if for $D_k = D_{Tk}^-$, $p_k = p$, for $D_k = D_{Tk}+$, $p_k = p + 1$. This implies a step discontinuity in the transformation. An expression for D_{Tk} can be derived from equation (4.30) to be

$$D_{Tk} = (p_k + 1.5) / 2^N \tag{4.31}$$

In summary, the control system, which is digital and algebraic in nature, accepts two reference inputs E_r and T_{cr} and depending on the chromaticity coordinates and luminance of the two sources- collectively termed as luminous parameters in this study- decides the selection of the colour of the companion source S_2 in the form of a binary variable BLU_ON and calculates two more integer outputs p_1 and p_2. It should be noted here that the luminous parameters are not constants but are functions of their respective junction temperatures. However, the controller sample time T is small compared to the rise time of the junction

temperatures corresponding to small step changes in Ds that may occur between two consecutive cycles. This validates the assumption that the values of the luminous parameters are constants over a sampling period. A method for estimating the luminous parameters in every sample interval at runtime is presented in the next section.

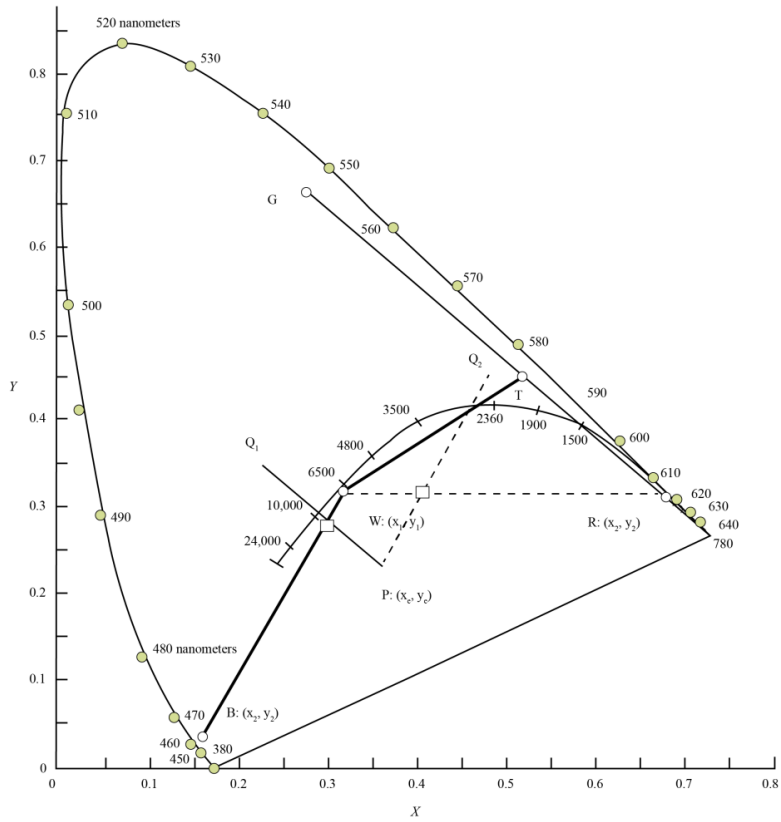

Fig. 4.2. Blending line, isoCCT line and Planckian locus shown on CIE 1931 chromaticity diagram

4.2.1.2 Runtime Estimation of Luminous Parameters

A runtime estimation of the luminous parameters E_M, x and y of each LED requires an a priori knowledge of the variation of the parameters as functions of their respective junction temperatures. One-time, off-line measurement and evaluation of some model parameters, discussed below, are necessary for the purpose.

The system hardware has been designed in such a way that the average value of forward drop of each LED, fed by a constant amplitude, constant frequency, variable pulse-width current, is connected to one channel of an on-chip ADC of the CICU. The average forward

voltage of a particular LED, u_{fa} is a function of its duty cycle D and its junction temperature θ_J. The output of the ADC, n_a being directly proportional to u_{fa} can be expressed as

$$n_a = n_a (D, \theta_J) \tag{4.32}$$

An experiment is now conducted in which the values of n_a are recorded for two different ambient temperatures of 27±2 ^{0}C and 40±2 ^{0}C and at three values of D = 0.1, 0.5 and 0.9 for white LED, and D = 0.1, 0.35 and 0.6 for red and blue LEDs. The higher ambient temperature is usually taken as the maximum operating ambient temperature of the lamp. For brevity, the lower ambient temperature condition will be termed as the S (or, 'standard ambient') condition and the higher ambient temperature condition will be termed as the H (or, 'high ambient') condition. Symbols like $\psi|S$ or $\psi|H$ will denote the value of a variable ψ in standard ambient condition or high ambient condition, respectively. Each n_a is then expressed as a quadratic expression in D of the form

$$n_a = A_0 + A_1 D + A_2 D^2 \tag{4.33}$$

The values of the constants A_0, A_1 and A_2 at S and H conditions for the three LEDs are shown in Table 4.1.

Table 4.1. Experimentally evaluated polynomial coefficients of ADC output for the three LEDs

Colour →	White			Red			Blue		
Ambient temp, ^{0}C ↓	A_0	A_1	A_2	A_0	A_1	A_2	A_0	A_1	A_2
27±2	9.39	979	-27.2	2.86	683	-21.5	7.4	905	-16.9
40±2	9.01	962	-24.9	2.97	657	-15.5	6.45	890	-15.9

For the white LED, a plot of equation (4.33) for a limited range of D is shown in Fig. 4.3. We take D = 0.6 as an example and show $n_a|S$ and $n_a|H$ by points A and B, respectively, in Fig. 4.3. The values of $n_a|S$ and $n_a|H$ can be determined by using equation (4.33) along with appropriate values of A_0, A_1 and A_2 given in Table 4.1. The actual value of n_a measured at runtime for the same D and shown by point X, may be, in general, different from either of them. We, therefore, define a variable d given by

$$d = (n_a|S - n_a) / (n_a|S - n_a|H) \tag{4.34}$$

As will be shown, this variable d, which is the ratio of the lengths of the line segments AX and AB, plays an important role in determining the values of the luminous parameters. Experiments have shown that the parameters very nearly follow the equations of straight lines given in slope-intercept form by

$$E_M(D)|S = E_M(0)|S + m_E|S \,.\, D \quad (4.35a)$$

$$E_M(D)|H = E_M(0)|H + m_E|H \,.\, D \quad (4.35b)$$

$$x(D)|S = x(0)|S + m_x|S \,.\, D \quad (4.36a)$$

$$x(D)|H = x(0)|H + m_x|H \,.\, D \quad (4.36b)$$

$$y(D)|S = x(0)|S + m_y|S \,.\, D \quad (4.37a)$$

$$y(D)|H = x(0)|H + m_y|H \,.\, D \quad (4.37b)$$

The slope and the intercept parameters from equation (4.35a) to equation (4.37b) can be determined from the values of the left hand sides for two extreme values in the working range of D (0.1 and 0.9 for white LED and 0.1 and 0.6 for the companion LEDs). Caution is taken so that a dependent variable reaches its steady-state before recording its value. The values of the parameters so obtained are given in Tables 4.2, 4.3 and 4.4. The evaluation of the present 12 slope and intercept constants and the earlier 6 constants $A_0|S$, $A_1|S$, $A_2|S$, $A_0|H$, $A_1|H$ and $A_2|H$ for each LED, although done offline and only once, is time consuming and therefore, adds to the system cost.

In the discussions to follow we shall, for the sake of brevity, use a common variable φ to indicate the luminous parameters because each will be estimated in the same manner at the runtime and the meaning of φ will become clear from the context. Since the value of duty cycle D is constant over a sampling period of the controller, each φ is a function of n_a only and assuming further that each such function is continuous in the interval ($n_a|S$, $n_a|H$), any φ for a given n_a can be determined by the linear interpolation formula

$$\varphi = \varphi|S - (\varphi|S - \varphi|H) / (n_a|S - n_a|H) \,.\, (n_a|S - n_a) \quad (4.38)$$

In view of the variable d defined earlier in equation (4.34), (4.38) simplifies to

$$\varphi = \varphi|S - (\varphi|S - \varphi|H) \,.\, d \quad (4.39)$$

Replacing φ by the required luminous parameter E_M, x or y in equation (4.39), these parameters for the two active LEDs are estimated at runtime. If the LEDs are operated at

lower ambient temperature than that in S condition, the value of n_a will be higher than n_a |S and d will become negative. Although equation (4.38) and equation (4.39) are still valid, the actual mathematical process becomes one of linear extrapolation rather than that of linear interpolation.

Once the values of the luminous parameters are estimated, the remaining calculations for determining the controller outputs, as described in the previous subsection are rather straightforward. The algorithmic steps are given in flowchart form in Section 4.2.2.1

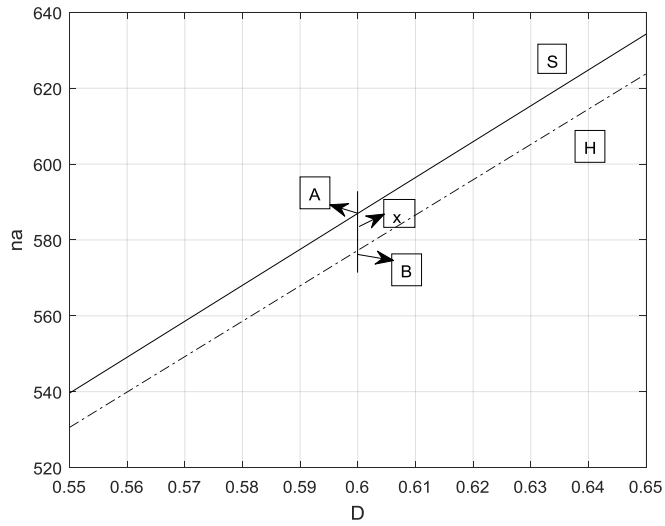

Fig. 4.3. Graphs showing the plot of equation (4.33) at two different ambient temperatures.

Table 4.2. Experimentally evaluated intercept and slope values for white LED

Ambient temperature, ^{0}C	$E_M(0)$, lx	$m_{EM,}$ lx	x (0)	m_x	y (0)	m_y
27±2	150.8	-9.256	0.3222	-3.6047E-3	0.3342	-5.4651E-3
40±2	140.9	-10.95	0.3172	-4.6512E-3	0.3273	-6.2791E-3

Table 4.3. Experimentally evaluated intercept and slope values for red LED

Ambient temperature, ^{0}C	$E_M(0)$, lx	$m_{EM,}$ lx	x (0)	m_x	y (0)	m_y
27±2	72.8	-10.35	0.6919	2.2093E-3	0.3072	-1.8605E-3
40±2	56.2	-10.35	0.6954	1.7742E-3	0.3035	-1.3953E-3

Table 4.4. Experimentally evaluated intercept and slope values for blue LED

Ambient tempearature, ^{0}C	$E_M(0)$, lx	m_{EM}, lx	x (0)	m_x	y (0)	m_y
27±2	6.77	-0.5116	0.1391	-1.1628E-4	0.0342	1.2791E-3
40±2	6.71	0.093	0.1390	-3.4884E-4	0.0381	9.3023E-4

Fig. 4.4 shows the variation of the estimated and measured luminous parameters of the white and the red LEDs at different heat sink temperatures. The normalized values of parameters have been obtained by dividing the actual value with that of the same at 30 ^{0}C. It is observed that the peak illuminance decreases with temperature for both the LEDs.

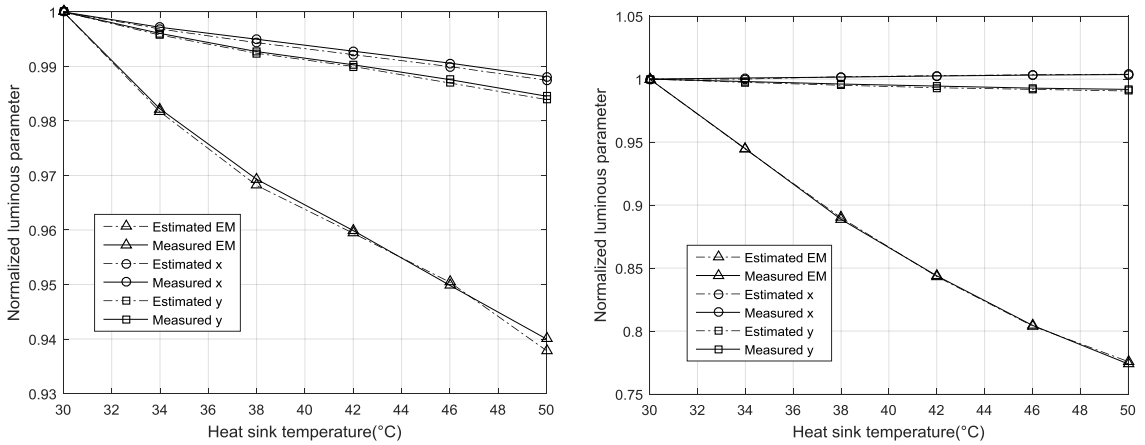

(a) (b)

Fig. 4.4. Normalized luminous parameters of the LEDs as a function of heat sink temperature (a) White LED (b) Red LED

4.2.2 Features of the CCT and Illuminance Control System

The features of CCT and illuminance control system have been sub-divided into software and hardware which are discussed below.

4.2.2.1 Software features of the CICU

The computational algorithm for the CICU is shown in the flowchart of Fig. 4.5, where the numbers in parenthesis indicate the equation numbers. The controller outputs BLU_ON, p_1 and p_2 are generated in every sampling period T of the system. The calculations can be broadly divided into two groups: the aperiodic or once-only type and the periodic or inside-

the-loop type. The fixed calculations, which do not depend on the reference inputs T_{cr} and E_r are kept in the aperiodic group.

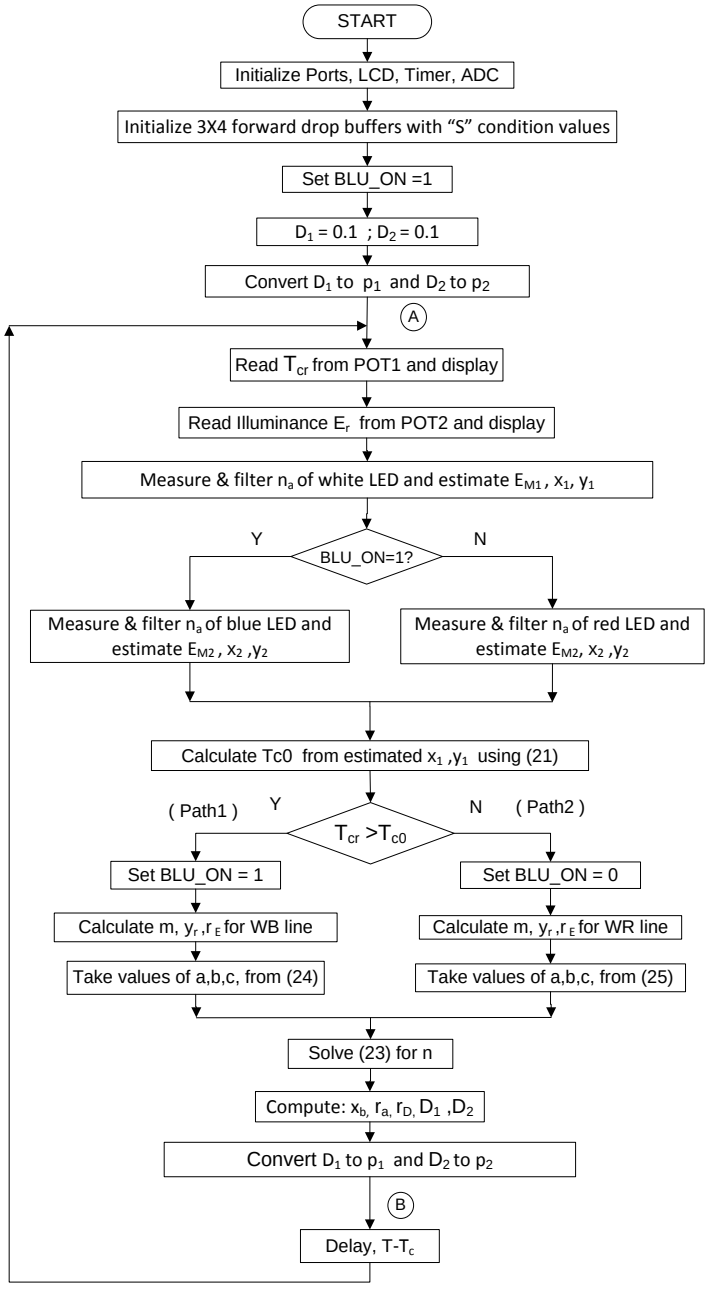

Fig. 4.5. Flow chart of the proposed CCT and illuminance control algorithm

The buffers mentioned in the third block from top are used for digital, low-pass, moving-average filtering of ADC outputs n_a mentioned earlier in Section 4.2.1.2. The branching in the loop to paths 1 and 2 occurs due to different values of parameters shown for WB and WR blending lines, respectively. The paths 1 and 2 finally merge together and the remaining

common calculations are then made. The average value of the code execution time T_c from node A to node B decides the delay time T_d according to the equation

$$T_d = T - T_c \tag{4.40}$$

For the ATmega32A microcontroller [7], used in the CICU, running at a clock frequency of 12 MHz, the average value of T_c is about 5.5 ms. Thus, a delay time of 994 ms will produce the desired sampling period of 1s.

The human interface of the system is extremely simple. The CCT and illuminance set points are supplied to the system in a convenient form using two analog voltages from two potentiometers, POT1 and POT2, respectively. The CCT can be set in the range of 2500 K to 12500 K, with a resolution of 100 K and an illuminance in the range of 5 to 120 lx, with a resolution of 1 lx. Both of these data are displayed on a common liquid crystal display (LCD).

4.2.2.2 Hardware features of the developed system

The hardware features of the developed system are discussed below.

a) The CCT and illuminance control unit (CICU)

The main tasks of the CCT and illuminance controller unit (CICU) have already been mentioned. The CICU comprises of an ATmega32A MCU, a common JHD162A, 16x2 LCD display, a demultiplexer (DEMUX) using a CD4011 CMOS quad, 2-input NAND gate and two linear 10KΩ potentiometers (POT). Any other MCU, irrespective of the manufacturer, having at least five ADCs, two 10-bit resolution PWM channels, 8 KB of flash memory and eight programmable I/O lines, could also be used to implement the proposed CICU. To avoid visible flicker, it has been customary to use a PWM frequency of more than 100 Hz [8], [9]. However, a recent IEEE Standard, 1789™-2015 [10] recommends that the PWM dimming frequency should be higher than 1.25 kHz. Also at this frequency and above there is no restriction on modulation percentage of the PWM dimming. We have used a frequency of 1.46 kHz, a value that is easily programmable for the above mentioned MCU operating at a clock frequency of 12MHz, for both the 10-bit PWM channels.

The DEMUX is shown in Fig. 4.1 is implemented using a common quad, 2-input, NAND CMOS IC CD4011. Depending on the state of the select line BLU_ON the DEMUX will

drive the red LED or the blue LED string from PWM2 channel. If BLU_ON is high, the PWM signal generated at the PWM2 channel of the MCU is steered to A1 to drive the blue LED string. On the other hand, if BLU_ON is low, the PWM signal is steered to A0 to drive the red LED string. The PWM1 channel of the MCU is used to drive the white LED string.

b) PWM dimmable high-side LED driver

A TTL-logic controllable, high side, constant peak current LED driver has been designed to drive the LED strings. The circuit diagram of a typical driver is shown in Fig. 4.6. When the logic control input LED_ON is 1, the LEDs turn-on at a programmed value of peak current decided by R_{CS}, the value of the current sensing resistor R4. On the other hand, for LED_ON = 0, the LEDs are off. The LED_ON signals, depending on the LED to be driven, are the PWM outputs obtained either from the MCU (for white LED) or from the demultiplexer (for red or blue LED). An explanation of the operating principle of the driver follows.

For logic input 0, the output of the TTL open-collector inverter U1 goes to Hi-Z state and the transistor Q1 goes to linear mode with a low value of collector-to-emitter voltage U_{CE} slightly greater than its base-to-emitter voltage U_{BE}. As a result, the magnitude of gate-to-source voltage U_{GS} of the output P-channel MOSFET Q3 goes below its threshold level. Q3 thus turns off, resulting in zero current through the LED string. Since the drop U_{CS} across the current sensing resistor R4 is zero, the PNP transistor Q2 remains cut-off and does not affect the operation of the circuit.

Corresponding to a logic input of 1, the output voltage of the inverter goes close to ground and the effective gate-to-source capacitance C_{GS} of Q3 starts to get charged. Q1 turns off now due to reverse biasing of its base-emitter junction caused by forward current flow in D1. When the resulting magnitude of U_{GS} crosses the threshold, the source current of Q3, which is also equal to the LED current I_{LED}, starts to increase. This increase of $I_{LED} = I_S$ does not take place indefinitely but instead is limited to a value at which U_{CS} equals the base-emitter threshold voltage $U_{T,BE}$ of Q2. Any increase of I_{LED} causes an increase in the base current of Q2 resulting in drop of magnitude of its U_{CE}, which is also the magnitude of U_{GS} of the MOSFET. This restores the value of I_{LED}, provided the current control loop is stable. The preceding discussions, under the assumption of stability, gives an expression for I_{LED} given below.

$$I_{LED} = U_{T,BE} / R_{CS} \tag{4.41}$$

The current control loop has a very high low-frequency loop gain and, if the voltage U_{CS} is directly coupled to the base of Q2 through a resistor R3 alone, causes an instability in the form of a high-frequency oscillation in I_{LED}. A common remedy in the form of putting a lead network in the feedback path works in this case. It was realized by shunting the resistor R3 by a 10 nF capacitor C2.

The change in the output LED current in response to the logic control signal cannot be instantaneous – instead, there are finite turn-on and turn-off delays of t_{don} and t_{doff}, respectively. Experimentally it was found that t_{don} and t_{doff}, respectively, have values of 3.5μs and 1μs. Since $t_{don} > t_{doff}$, the output pulse-width will become less than the input one by an amount of $(t_{don} - t_{doff})$. This is circumvented by adding a correction term in D, whose value is $(t_{don} - t_{doff}) / T_{PWM}$, where $T_{PWM} = 683$ μs is the time period of the PWM drive signal.

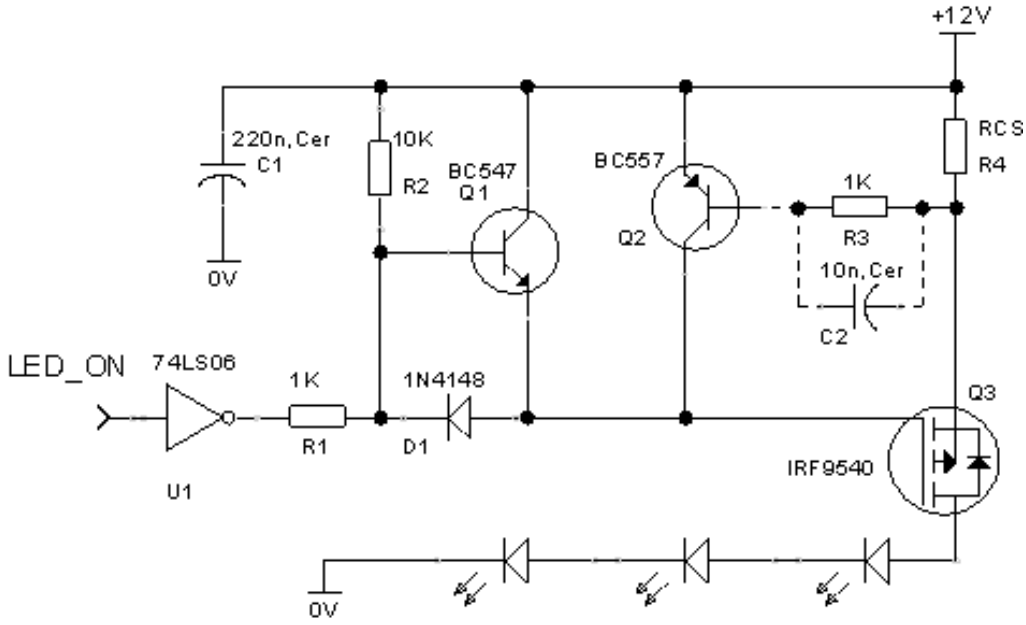

Fig. 4.6. High-side constant current LED driver

The values of R_{CS} and the corresponding current amplitudes along with some other parameters are shown in Table 4.5. The data in the 6th column is calculated from the average illuminance for D = 0.5. The prototype of white, red and blue LED driver with DEMUX circuit is shown in Fig. 4.7.

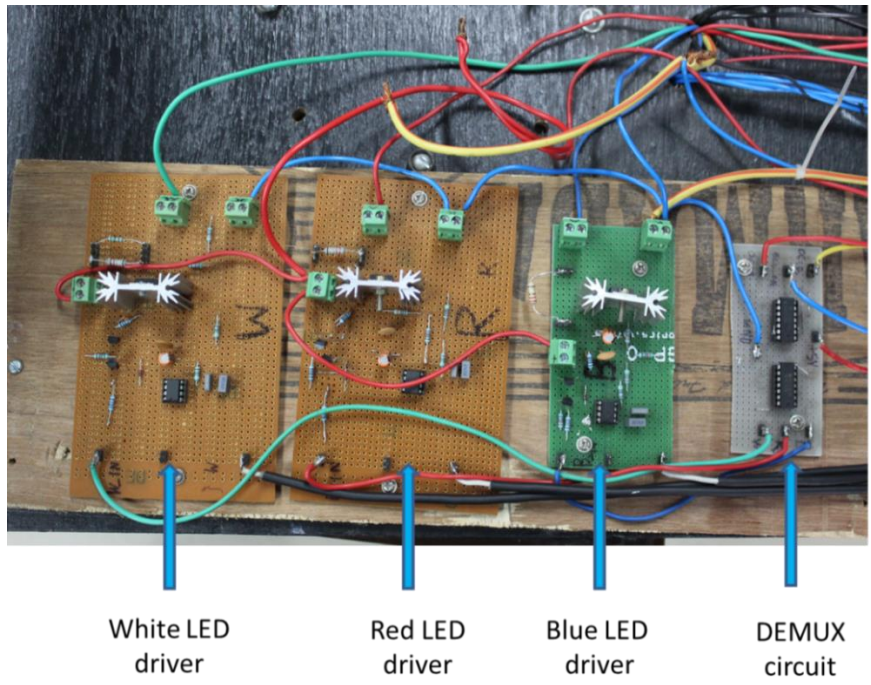

Fig. 4.7. Prototype of white, red and blue LED driver with DEMUX circuit

Table 4.5. Important parameters of the LED and its driver circuit

LED Colour	Power rating of each LED (W)	Number of LEDs in series	R_{CS} (Ω)	$I_{LED\text{-}Pk}$ (mA)	Approximate peak illuminance at work plane(lx)
White	1	3	1.9	316	146
Red	1	3	2.2	275	68
Blue	1	3	5.6	108	6.5

C) LED average forward drop measurement circuit

The instantaneous forward voltage across a series-connected LED string is a periodic rectangular pulse with a time period T_{PWM}, a duty cycle D and an amplitude that is the sum of the forward drops of the LED at the constant level of peak current. A fraction of this voltage, decided by the attenuation ratio R7 / (R6 + R7), when given to a low-pass filter (LPF) with a proper lower cut-off frequency will produce an output with a dc component u_{fa} along with a negligible ripple. The circuit diagram of the attenuator and the LPF is shown in Fig. 4.8. The output of the LPF is finally converted by the respective on-chip ADC to an integer n_a given by

$$n_a = \text{round}\,(u_{fa} / U_{R,AD}) \,.\, 2^{Nad} \qquad (4.42)$$

where $U_{R,AD}$ is the reference voltage and N_{ad} is the number of bits, respectively, of the ADC.

n_a is also, by design, internally clamped to an upper limit of $2^{Nad} - 1$. The input attenuator is so chosen that full input range of the ADC is utilized ensuring that the maximum value of u_{fa}, corresponding to D = 1 does not exceed $U_{R,AD}$, which has a value of 2.56V in our case.

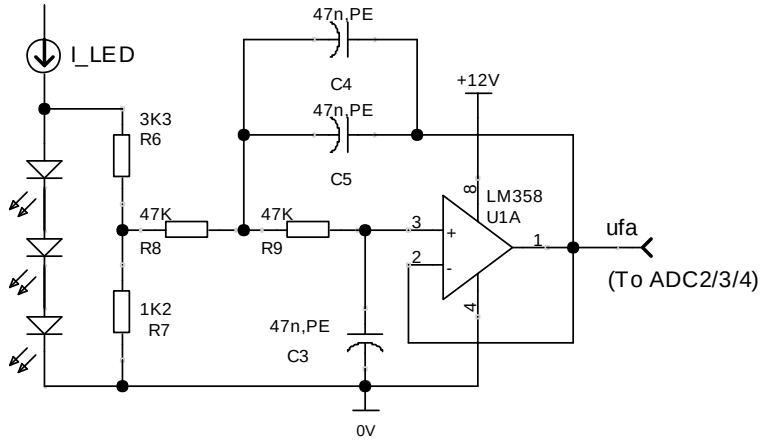

Fig. 4.8. Measurement of average forward drop of the LED string

A 2^{nd} order Butterworth LPF was used in our implementation and its lower cut-off frequency was chosen to be 1/20th that of the input fundamental frequency of 1.46 kHz. For the standard component values used, the lower cut-off frequency turns out to be 72 Hz, a value very close to the design target. A further filtering of the ripple is effected by taking 4 samples of the ADC output at intervals of T_{PWM} / 4 or, approximately 170 μs and taking the average of 4 resulting values of n_a. Although this effectively increases the ADC conversion time to T_{PWM}, it is, since $T_{PWM} << T_c$, of no serious concern.

d) The arrangement of the LEDs

A primitive arrangement of the LEDs was done in the prototype to meet the basic optical and thermal requirements. To facilitate adequate colour mixing, free of colour patches, the LEDs were placed in such a way that the distance between the farthest LEDs was small compared to the distance of the assembly from the work plane. The centres of the three CW-PC LEDs constituting the main source S_1 were located equally spaced on a pitch circle of diameter 40 mm. The six companion red and blue LEDs were placed alternately so that their centres were on a concentric circle of 80 mm diameter with two consecutive LEDs making an angle of 60^0 at the centre. The heatsink was a 1.6 mm thick circular aluminum plate 110 mm in diameter. At the maximum light output level, the temperature rise of the heatsink centre was only approximately 8^0C above the ambient. The placement of the power LEDs on the flat surface of an aluminum heat sink is shown in Fig. 4.9.

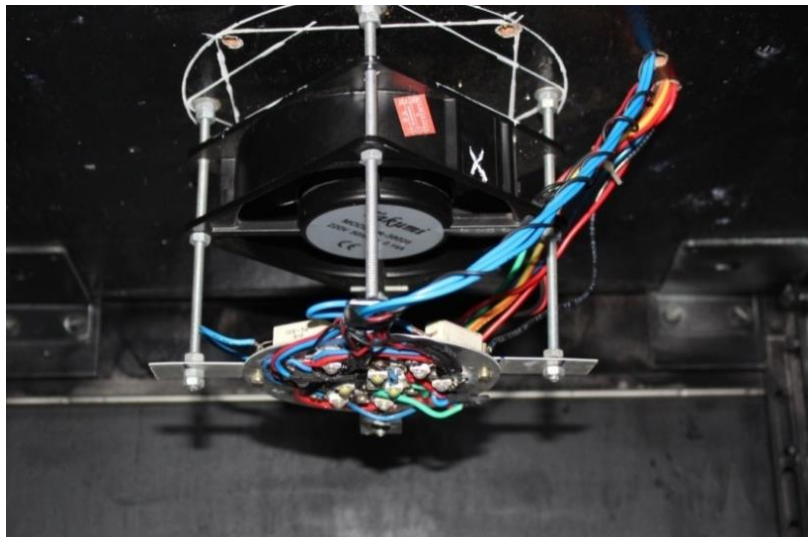

Fig. 4.9. Placement of power LEDs on an aluminum heat sink.

4.3 Hardware implementation of fixed-CCT, three-step dimmable LED driver

Generally, three types of popular topologies are used to implement a basic switched-mode converter. They are buck, boost, and buck-boost. Among them, in our case, the boost converter is chosen as a higher voltage than the battery nominal voltage requires to drive the LED strings. The input power of the converter is fed from the battery which is charged from PV module. In this study, a three-step dimmable LED driver has been developed and implemented.

The circuit diagram of the boost converter is shown in Fig 4.10a and the scheme for LED current and voltage control is shown in Fig 4.10b, the interconnections between the two figures are shown by means of symbols A, B and C. The converter circuit is built around UC3843, a fixed frequency, current mode PWM controller IC. This IC controls the peak value of instantaneous current in the choke L2 so that the input energy stored in a cycle is equal to the output energy required by the LED string and the energy losses in the circuit in the same period.

The load to the boost converter consists of a combination of 9 LEDs in series in a string and 4 such string in parallel. Corresponding to the maximum lumen output of luminaire the total current in the string has to be controlled at a value 4 times the rated current of each LED. The lumen output can be manipulated by control of the total LED current I_{LED}. I_{LED} is

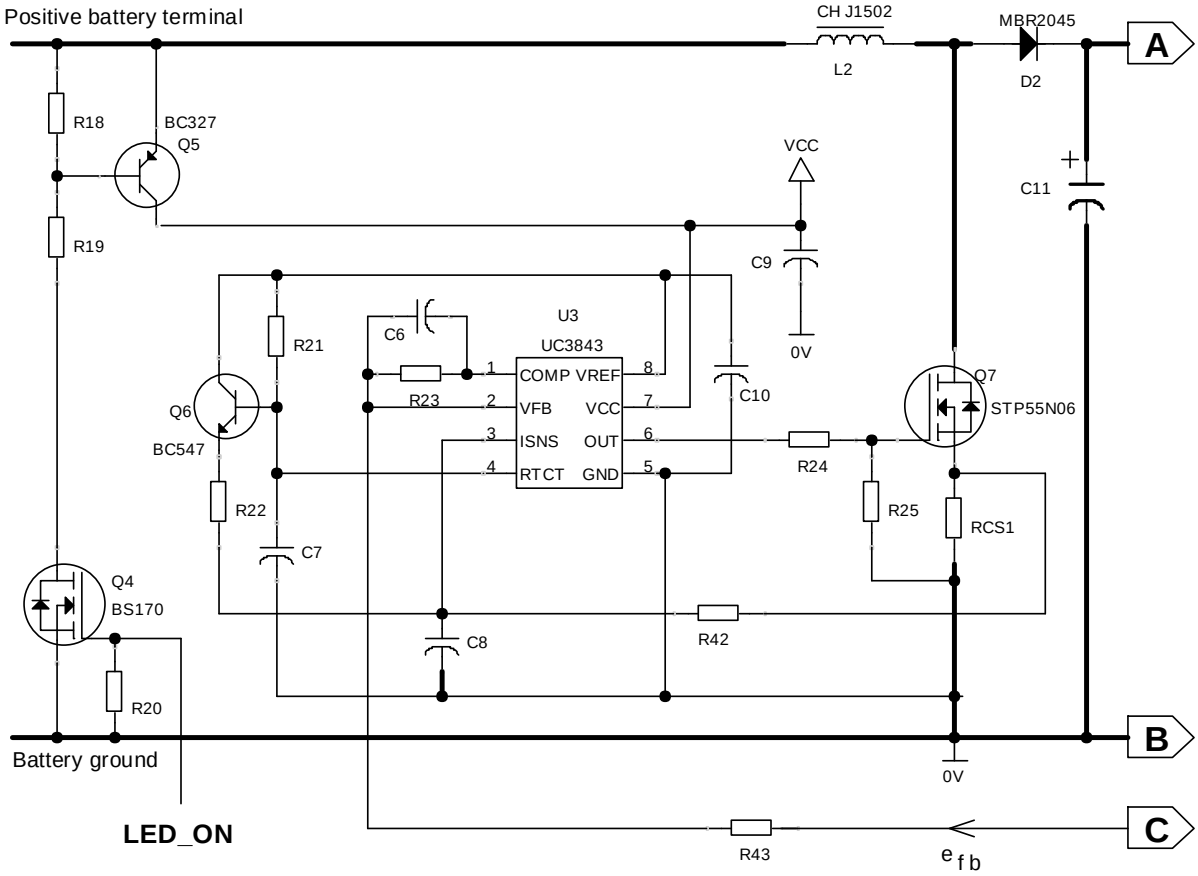

Fig. 4.10. (a) Boost converter with logic shut-down arrangement

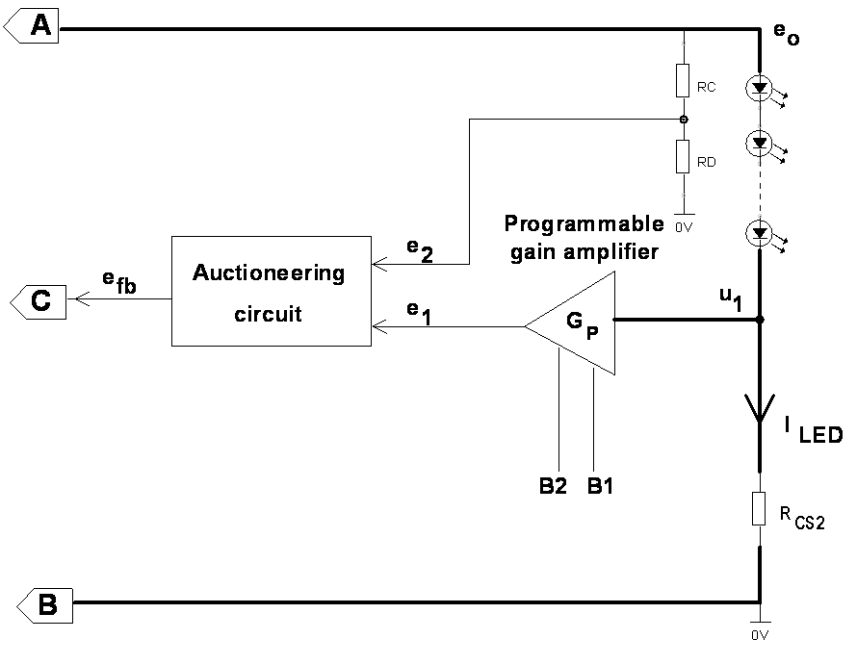

Fig. 4.10 (b) Scheme for LED current and voltage control

passed through a current sense resistor R_{CS2}, resulting in a voltage drop $u_1 = I_{LED} R_{CS2}$. In order to keep a high efficiency the value of R_{CS2} is chosen in such a way that the drop u_1 under rated condition is very small compared to the total LED drop. This requires the use of a non-inverting amplifier so that the output is compatible to the required value of feedback voltage of the PWM controller IC. It will be shown in Section 4.3.2.2 that this amplifier should be of a programmable-gain variety so that I_{LED} can be preset at different required value. Additionally, under the fault condition of open-circuit in the LED string, a boost converter can produce a very high voltage at its output. This conditions can be prevented by taking a feedback of the output voltage e_o employing a passive voltage divider consisting of resistors RC and RD. The output e_2 of the divider is given by $e_2 = RD/(RC + RD)\ e_o$. The converter operates in one of the two following modes. In the normal mode, current control takes place and e_1 should be fed back to the PWM controller IC. On the other hand, in the abnormal mode the voltage e_2 should be use as feedback so that the converter output within safe limits. Section 4.3.2.2 will show how an automatic switching between e_1 and e_2 takes place where the auctioneering block shown in Fig. 4.10 (b) is realized by using suitable hardware.

A brief explanation of the operating principle of boost converter and its control scheme are given in the following sub-sections.

4.3.1 Analysis and preliminary design of the boost converter

DC choppers can be used as a switch-mode regulator to provide a regulated DC voltage. In a step-up or boost converter, the average output voltage V_o is greater than or at least, equal to the input voltage. In this section, the working principle of a boost converter is described.

In this study, a boost converter is used to drive the LED strings from the battery at the specified current. The circuit diagram of a boost converter using a power MOSFET as a switch is shown in Fig. 4.11. Important waveforms explaining the principle of operation of the converter are shown in Fig. 4.14. For a fixed switching frequency f_S, a fixed inductor L and a range of load current i_O from a certain minimum up to the rated value, the inductor current i_L lies in the range ($I_{L,min}$, $I_{L,max}$) where $I_{L,min} > 0$. Since the current i_L is never zero over a period $T = 1 / f_S$, this mode of operation is called the continuous conduction mode or

CCM. Depending on the state of the series switch, the operation of the converter in CCM can further be subdivided into two modes, namely, interval 1, $0 \leq t < T_{ON}$, when S1 is on, and interval 2, $T_{ON} \leq t < T$, when S1 is off. Assuming T to be fixed, the output voltage V_o can be controlled by adjusting the value of T_{ON}. The length of the second interval is $T_{OFF} = T - T_{ON}$. The operation in the two intervals is discussed below.

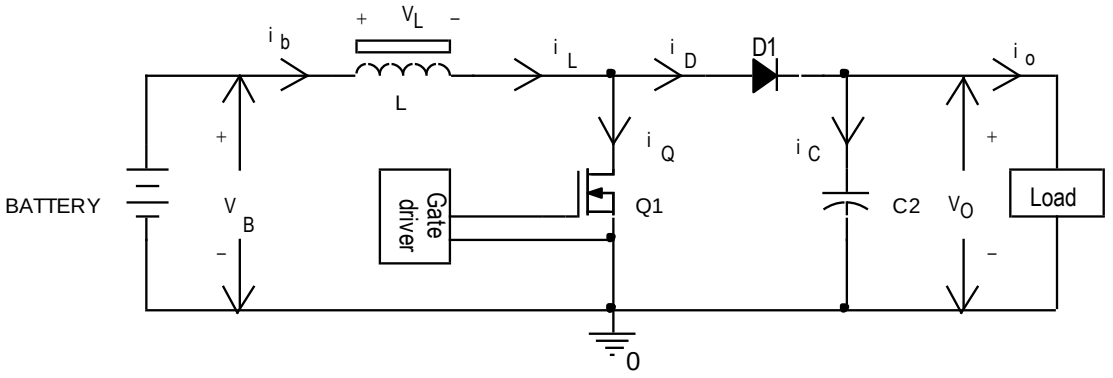

Fig. 4.11. Simplified circuit diagram of the boost converter

Interval 1: Starts at t=0, when switch S1 is closed, the diode D1 becomes reverse biased which isolates the output stage and at the same time input current flows through the inductor L and MOSFET Q1.The equivalent circuit in interval 1 is shown in Fig. 4.12. The rate of change of inductor current is given by

$$\frac{di_L}{dt} = \frac{v_L}{L} = \frac{V_B}{L}, \text{ for } 0 \leq t < DT \tag{4.43}$$

where D is the duty cycle given by

$$D = \frac{T_{ON}}{T_{ON}+T_{OFF}} = \frac{T_{ON}}{T} = T_{ON} f_S \tag{4.44}$$

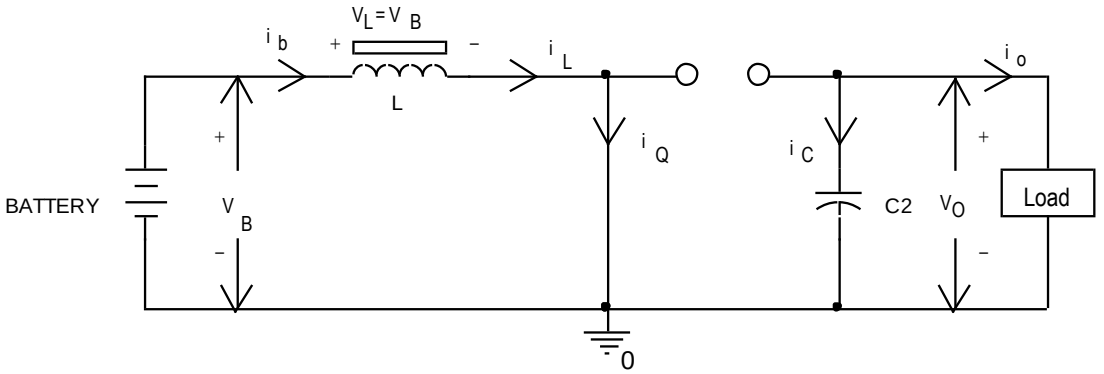

Fig. 4.12. Equivalent circuit for Interval 1 (Q1 closed, D1 blocking)

Since the right-hand side of equation (4.43) is a positive constant, the inductor current increases linearly with time as shown in Fig. 4.14(b). The rate of rise of current can therefore be equated to $\frac{\Delta i_L}{DT}$ thereby modifying equation (4.43) as

$$\frac{\Delta i_L}{DT} = \frac{V_B}{L} \tag{4.45}$$

From equation (4.45), the increase in inductor current in this interval is given by

$$\Delta i_L[T_{ON}] = \frac{V_B}{L} DT \tag{4.46}$$

Interval 2: Starts at t = DT, when switch Q1 opens. In order to maintain the continuity of inductor current, diode D1 becomes forward biased and then current which was flowing through the MOSFET Q1 would now flow through L, D1, C1 and load. The equivalent circuit in interval 2 is shown in Fig. 4.13. Now, i_L changes at the rate of

$$\frac{di_L}{dt} = \frac{V_B - V_o}{L}, \text{ for } DT \leq t < T \tag{4.47}$$

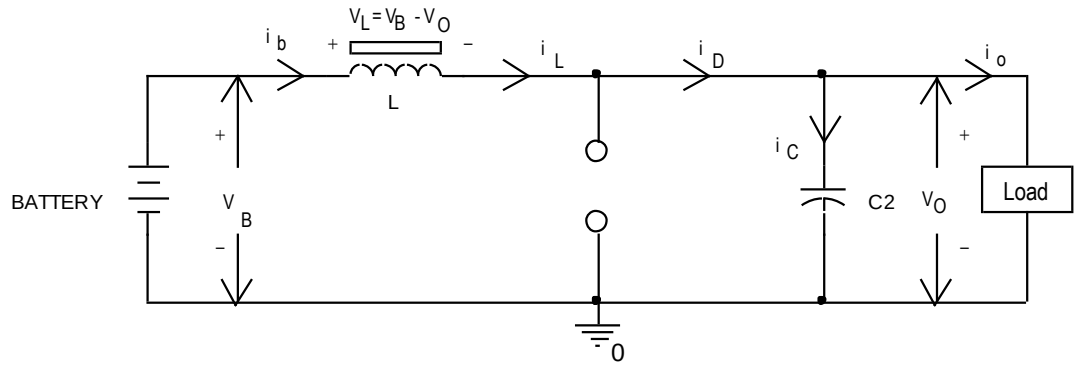

Fig. 4.13. Equivalent circuit for Interval 2 (Q1 open, D1 conducting)

Since the right-hand side of equation (4.47) is a negative constant, the current i_L decreases linearly with time as shown in Fig. 4.14(b). So, the rate of change of i_L in this interval can be rewritten as

$$\frac{\Delta i_L}{(1-D)T} = \frac{V_B - V_o}{L} \tag{4.48}$$

Rearranging equation (4.48) the increase in i_L can be expressed by

$$\Delta i_L[T_{OFF}] = \frac{(V_B - V_O)(1-D)T}{L} \tag{4.49}$$

Based on the discussions above, wave shapes of the inductor voltage and current are shown in Fig. 4.14(a) and Fig. 4.14(b), respectively. For periodic operation in a cycle, i_L will be same at the beginning and end of a switching period T. Therefore, the resultant change in inductor current is zero in a cycle. This condition is represented by equation (4.50)

$$\Delta i_L [T_{ON}] + \Delta i_L [T_{OFF}] = 0 \quad (4.50)$$

Now, equations (4.46) and (4.49) when substituted in equation (4.50) gives

$$\frac{V_B}{L} DT + \frac{(V_B - V_O)(1-D)T}{L} = 0 \quad (4.51)$$

Solving equation (4.51), the expression for output voltage, V_O will be

$$V_O = \frac{V_B}{(1-D)} \quad (4.52)$$

Equation (4.52) describes the operation of the boost converter. For a fixed input voltage, if duty cycle is increased, the output voltage of the converter also increases as the denominator of equation (4.52) becomes smaller. Therefore, the output of the boost converter can be greater than or at least equal to the input voltage.

Equations (4.46) and (4.49) give the change in inductor current Δi_L. Now the maximum and minimum value of inductor current, respectively, I_{Lmax} and I_{Lmin} can be expressed as

$$I_{L,max} = I_{L,avg} + \frac{\Delta i_L(ON)}{2} = I_{L,avg} + \frac{V_B DT}{2L} \quad (4.53)$$

$$I_{L,min} = I_{L,avg} - \frac{\Delta i_{L(ON)}}{2} = I_{L,avg} - \frac{V_B DT}{2L} \quad (4.54)$$

An expression for the average current can be found by assuming the converter to be loss-less as

$$V_o I_o = V_B I_{L,avg} \quad (4.55)$$

Substitution of V_o from equation (4.52) to equation (4.55), the average inductor current can be given by

$$I_{L,avg} = \frac{I_O}{(1-D)} \quad (4.56)$$

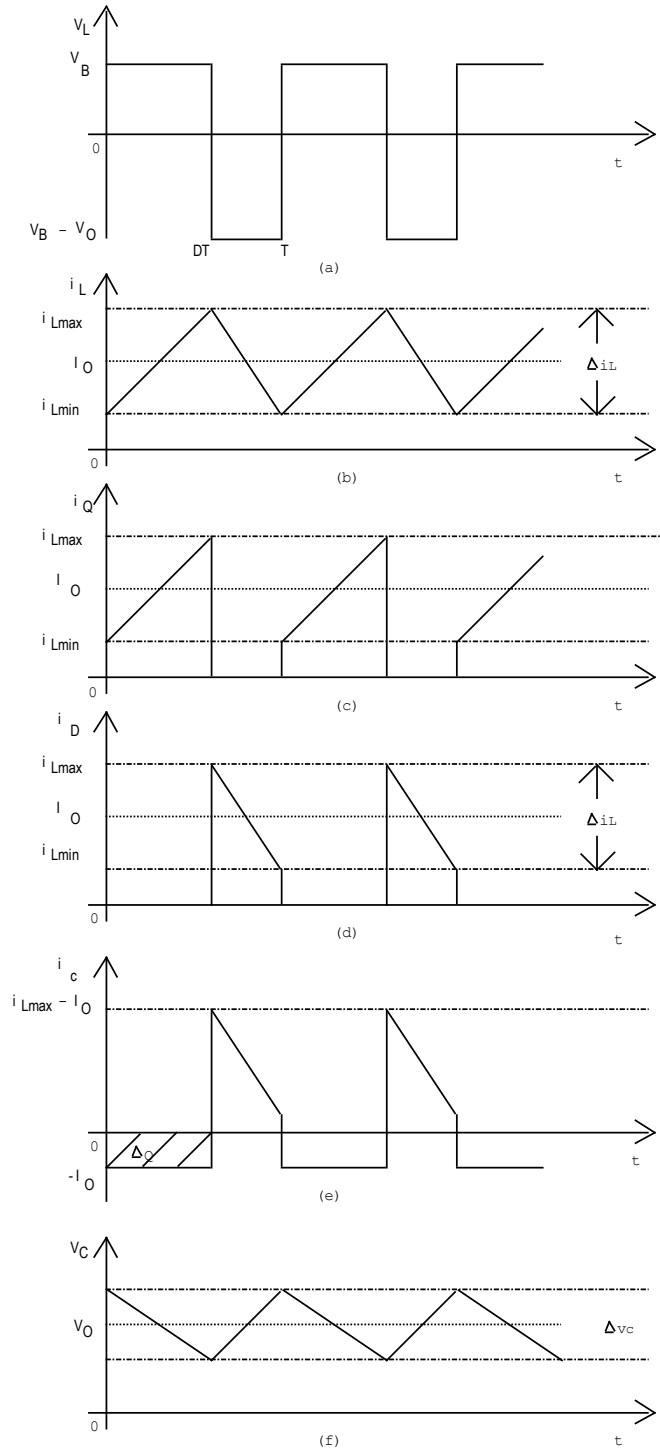

Fig. 4.14. Waveforms of the buck converter for CCM (a) Inductor voltage (b) Inductor current (c) MOSFET current (d) Diode current (e) Capacitor current (f) Capacitor voltage

Two important things can be observed from equation (4.54). Firstly, for a fixed load current I_o, which by virtue of equation (4.56), also means a fixed $I_{L,avg}$ and a fixed D, if the value of L is decreased, a point is attained when $I_{L,min}$ has a zero value implying that the

converter is about to leave the continuous conduction mode. Secondly, the same critical condition occurs when for a fixed L and fixed D, the value of I_o is decreased. The required value of the inductance can be obtained by observing that the minimum instantaneous current $I_{L,min}$ occurs for the combination of minimum output current and minimum inductance. As the duty cycle D is also a determining factor in the design of L, its value is obtained from equation (4.52) by substituting the minimum value of V_B. This value of D is used in the following two equations.

Imposition of $I_{L,min}$= 0 and substitution of equation (4.56) to equation (4.54) yields

$$I_{o,\,min} = \frac{V_o\, D\, (1-D)^2}{2L_{min} f_s} \tag{4.57}$$

A rearrangement of the above equation gives

$$L_{min} = \frac{V_o\, D\, (1-D)^2}{2I_{O,min} f_s} \tag{4.58}$$

In the previous analysis, the output capacitor, C2 is assumed to be very large to maintain V_o at a constant value. As the cost of a capacitor for a certain voltage rating approximately increases linearly with its value, C2 cannot be increased indefinitely. A method for designing an economic value of C2 is described below.

To calculate the peak-to-peak voltage ripple ΔVo, it is assumed that all ripple current component of i_D flows through C1 and the average current flows through the load. The change in capacitor charge ΔQ is shown in Fig. 4.14(e). The voltage ripple ΔVo can be expressed as

$$\Delta Vo = \frac{\Delta Q}{C} = \frac{I_O\, DT}{C} \tag{4.59}$$

From (4.59) the values of output capacitance can be expressed as

$$C_{min} = \frac{I_O\, D}{\Delta Vo\, f_s} \tag{4.60}$$

Selection of major components of the prototype

In the present realization, the input power of the boost converter has been fed from a VRLA battery whose voltage may vary from 10.5V-14.5V. The output of the converter circuit s fed to the LED strings. The required output voltage to drive the LED string at rated

current is nearly 31.5V (considering 8 LEDs connected in series and each LED has forward drop of 3.5V). A sample calculation to determine the component value of a boost converter for CCM operation is discussed as follows. For this calculation, the following design parameters are chosen.

Minimum input voltage, $V_{b,min}$ = 10.5V

Maximum input voltage, $V_{b,max}$ = 14.5V

Nominal output voltage, Vo = 31.5V

Maximum output current, $I_{o,max}$ = 604mA

Switching frequency of the converter f_S = 46.7 kHz

Inductor:

The average inductor current can be calculated from equation (4.55) as

$$I_{L,avg} = \frac{V_o I_O}{V_{b,min}} \quad (4.61)$$

Considering the converter efficiency of η, from equation (4.61), $I_{L,avg}$ can be rewritten as

$$I_{L,avg} = \frac{V_o I_O}{\eta V_{b,min}} \quad (4.62)$$

Substituting the values of V_o = 31.5V, $V_{b,min}$ = 10.5V, I_o = 604mA and η = 85% in equation (4.62), yield, $I_{L,avg}$ = 2.13A. Considering allowable inductor ripple current is 40% of $I_{L,avg}$, calculated ΔI_L = 852mA

Rearranging equation (4.52) the duty cycle can be calculated as

$$D = 1 + \frac{V_B}{V_o} \quad (4.63)$$

Considering the converter efficiency of η for realistic calculation equation (4.63) can be modified as

$$D = 1 + \frac{\eta V_{B,min}}{V_o} \quad (4.64)$$

Substituting the values of $V_{B,min}$ = 10.5V and Vo = 31.5V, η = 85% in equation (4.64), yield, D = 0.667.

Substituting the values of V_b = 10.5, D = 0.667, ΔI_L = 852mA, f_S = 46.7 kHz, yield, L = 176uH.

Output capacitor

The minimum output capacitor can be calculated from equation (4.60), substituting, $I_{o,max}$ = 604mA, D = 0.667 , ΔV_o = 0.63V (Considering ΔV_o = 2% of output voltage) and f_S = 46.7 kHz, yield, C_{min} = 13.7uF.

4.3.2 Analysis and design of auxiliary sub-systems

The auxiliary sub-systems required for the fixed-CCT LED driver are given in the following sub-sections.

4.3.2.1 Switching frequency generator and controller

The PWM controller IC UC3843 [11] offers the necessary features to implement DC-to-DC fixed frequency current-mode control schemes with a minimal external part count. The circuit diagram of the frequency generator and controller is shown in Fig. 4.10(a). The IC provides a high-frequency square wave with a high-current totempole output for driving the power MOSFET Q7 of the boost converter. The converter switching frequency can be selected by connecting to the designated pin through a resistor R21 to V_{REF} pin and a capacitor C7 to the ground. Oscillator timing capacitor C7 is charged from VREF (5V) through R21 and discharged by an internal current source. The output frequency of U3 can be expressed as

$$f_S = \frac{1.8}{R21 * C7} \quad (4.65)$$

In this implementation, an operating frequency is chosen to be in the range of 40 - 50 kHz. Use of standard values of R21 = 8.2KΩ and C7 = 4.7nF produces a switching frequency of 46.7 kHz. To ensure that the system can operate at high values of duty cycle D, a slope compensation circuit configured around Q6, R21 and R22, as suggested in reference [11], is used.

The instantaneous drain current of MOSFET Q7 is sensed by a low-value resistor RCS1. To filter the high frequency switching noises a passive low-pass filter consisting of R42 and C8 is used between the sensed voltage and the current sense (or, feedback) terminal ISNS.

An examination of the current sensing circuit of UC3843 reveals that if the error amplifier output is given by e_{EA}, the peak instantaneous MOSFET current I_{Lmax} (which is also the inductor peak current) is given by

$$I_{Lmax} = \frac{\frac{1}{3}(e_{EA-} 2V_F)}{RCS1} \quad , \tag{4.66}$$

provided the numerator is $\leq$ 1V. The V_F term included in the equation represents a near-constant forward drop of 0.7V in two internal diodes.

In the prototype, RCS1 consists of three standard 0.47Ω resistors parallel, giving rise to a value of 0.157Ω. Corresponding to the limit value of the numerator of equation (4.66) results in I_{peak} = 6.38A.

During operation, the feedback voltage e_{fb} is compared with the internal reference voltage (in this case 2.5V) of the PWM controller IC which generates an error signal, if any, and manipulates the dutycycle of the output of U3.

4.3.2.2 Scheme for LED current and voltage control

In this implementation, the LED driver can operate in constant current (CC) or in constant voltage (CV) mode. In general, most of the time, the driver operates in CC mode. The CV mode is activated to protect the circuit components and LED from overvoltage caused by open circuit condition in one or more LEDs in the string or open-circuit condition of the current sense resistor.

A suitable control circuit is used to select either output current feedback (I_{of}) or voltage feedback (V_{of}) depending on the mode of control. The circuit diagram for auctioneering control is shown in Fig. 4.15(a). Feedback control of LED output current requires that a voltage proportional to the current must be fed back to a common controller with a fixed reference. Similarly, when the output voltage of the LED string has to be controlled, a voltage proportional to the total LED voltage should be fed back to the same controller. The selection of the feedback variable, current or voltage, must be automatic. This requires the use of an auctioneering circuit to be discussed below.

If $e_1 > e_2$ and it is assumed that the output e_{fb} at the common cathode of D7 and D8 is equal to e_1. This voltage is fed back to the inverting inputs of U5A and U5B. This will force

the output of U5A to negative saturation (since $e_1 > e_2$). As a consequence, D7 is reverse biased and the output of U5A is decoupled from the final output e_{fb} to the inverting input of U5B, the output automatically is e_1. Likewise, if $e_2 > e_1$ U5B will become inactive and U5A, acting as a voltage buffer will enforce $e_{fb} = e_2$. Thus analytically

$$e_{fb} = \max (e_1, e_2) \tag{4.67}$$

Since the maximum of e_1 and e_2 is transferred to the output, the circuit is very aptly called an auctioneering circuit. Therefore, the LED driver operates in CC mode and CV mode, respectively, for $e_1 > e_2$ and $e_2 > e_1$.

In CC mode, the chosen current can be selected to three pre-defined values by setting two bits. These two bits are used to program the gain value of the current amplifier. Referring to Fig 10(b), the voltage drop $u_1 = I_{LED} . R_{CS2}$ across current sense resistor R_{CS2} is amplified by a non-inverting programmable gain amplifier (PGA), as shown in Fig.4.15 (b). Thus the output voltage e_1 of the PGA can be expressed as

$$e_1 = I_{LED} * R_{CS2} * G_P \tag{4.68}$$

where I_{LED}, R_{CS2} and G_P are the LED current, LED current sense resistor and gain of PGA, respectively.

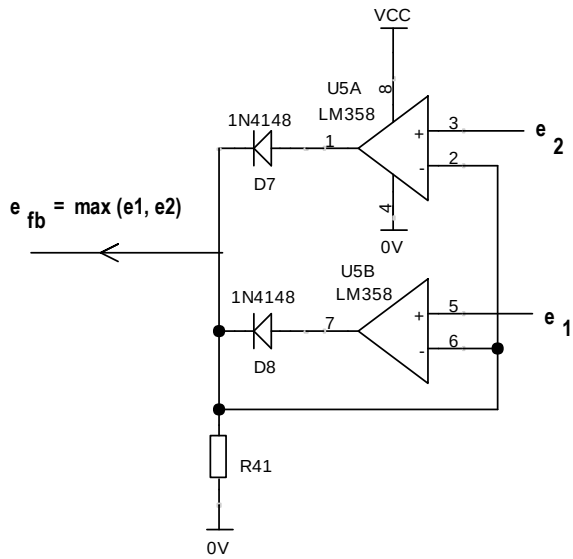

Fig. 4. 15. (a) Auctioneering circuit to select current or voltage control mode

As shown in Fig. 4.15(b), a standard non-inverting amplifier can be converted to a programmable gain variety if one of the gain determining resistors RA and RB can be made electronically adjustable. We prefer to use RB since one side of it is grounded. In the circuit

shown in Fig. 4.15(c) RB has been realized by using three equal-valued resistors R35, R36 and R37 along with two small-signal n-channel MOSFETs Q8 and Q9.With the application of logic 1 level (=5V) at the gate of a particular MOSFET the corresponding series-connected resistor is connected in parallel with the fixed resistor R35. Thus depending on the binary variable B2 and B1 (available from PD5 and PD4 pins of the MCU), different values of RB are obtained as shown in Table 4.6.

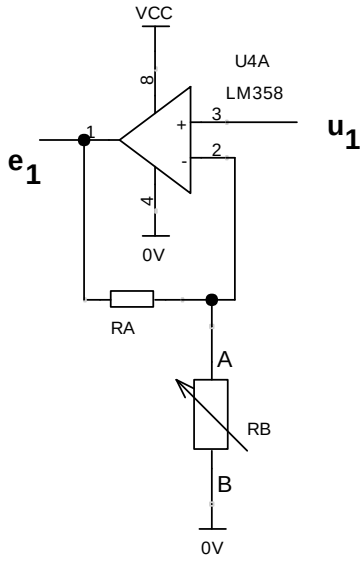

Fig. 4.15 (b) Topology of PGA

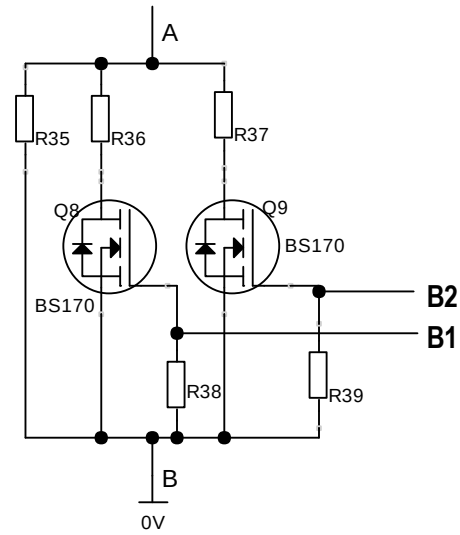

Fig. 4.15 (c) Realization of variable RB

In the prototype circuit, RA has a value of 78 KΩ, comprising of a 68 KΩ and a 10 KΩ resistor in series. The three resistors R35, R36 and R37 have the values of 10 KΩ each. The available value of P_G as a function of a 2-bit gain control word consisting of bits B2 and B1 are shown below in Table 4.6.

Rearranging equation (4.68), I_{LED} can be expressed as

$$I_{LED} = \frac{e_1}{G_P \ R_{CS2}} \tag{4.69}$$

A value of $R_{CS2} = 0.47\Omega$ has been used in the prototype. The output voltage e_{fb} has been fed to the inverting input (pin2) of an internal error amplifier of UC3843. The non-inverting input of the error amplifier is connected to an internal reference voltage of 2.5V. Therefore, during steady-state operation, and under assumption of zero steady-state error e_{fb} should be equal to 2.5V which is an internal reference voltage of the error amplifier. Form equation (4.67), for constant current mode $e_1 = e_{fb}$, i.e., $e_1 = 2.5V$. From equation (4.69), calculated values of I_{LED} with respect to logical bit settings are given in Table 4.6. The fourth

combination [B2, B1] = [1 0] is not shown in this table because it gives rise to the same value of RB as in the second row, and consequently, the same value of I_{LED}.

Table 4.6. RB, PGA gain and I_{LED} as functions of the gain control word B2 B1

B2	B1	RB(KΩ)	$G_P = 1+RA/RB$	I_{LED} (mA)
0	0	10	8.8	604
0	1	5	16.6	320
1	1	3.33	24.4	218

In CV mode, form equation (4.67), $e_{fb} = e_2$ as discussed earlier $e_2 = 2.5V$. In this mode, the output voltage of the driver can be expressed as

From Fig 4.10(b), the voltage e_2 is obtained by using a potential divider consisting of RC and RD as

$$e_2 = \frac{RD}{(RC + RD)} V_{LED} \tag{4.70}$$

Since in the normal condition, the system operates in constant current mode the value of e_2 should be less than the reference voltage of 2.5V. In this implementation, the LED string has nine LEDs in series. Thus output voltage of the driver at rated current should be around 31.5V (considering a typical forward drop 3.5V for white LED). Assuming a fixed value of RD = 2.2KΩ, and a value of $e_2 = 2.4V$, RC is obtained as 26.7KΩ. Choosing a standard value of 27KΩ, e_2 becomes 2.37V which is lower than the required value of 2.5V. Under open circuit condition, DC bus voltage, V_{BUS} can be expressed as

$$V_{BUS} = \frac{2.5\ (RC + RD)}{RD} \tag{4.71}$$

which has a value of 33.18V. This value is safe for converter operation under open circuit condition.

4.3.2.3 Logic shout-down arrangement

In the present implementation, the LED lamp is turned on or off by the logic input LED_ON. The circuit diagram of logic shout-down arrangement has already been shown in Fig. 4.10 (a), but redrawn here as Fig. 4.16. For LED_ON = 1, MOSFET Q4 is turned on, and consequently, PNP transistor Q5 turns on. Thus the positive terminal of the battery is

connected to the VCC pin of UC3843. Therefore the PWM output is available to drive the MOSFET of the boost converter which turns on the LED lamp.

On the other hand, for LED_ON = 0, MOSFET Q4 turns off so the transistor Q5 goes to cut-off mode. Thus the battery is disconnected from the VCC terminal of the controller IC. Hence, deprived of the gate drive, the main MOSFET Q7 turns off. This shuts down the boost converter thereby turning off the LED lamp.

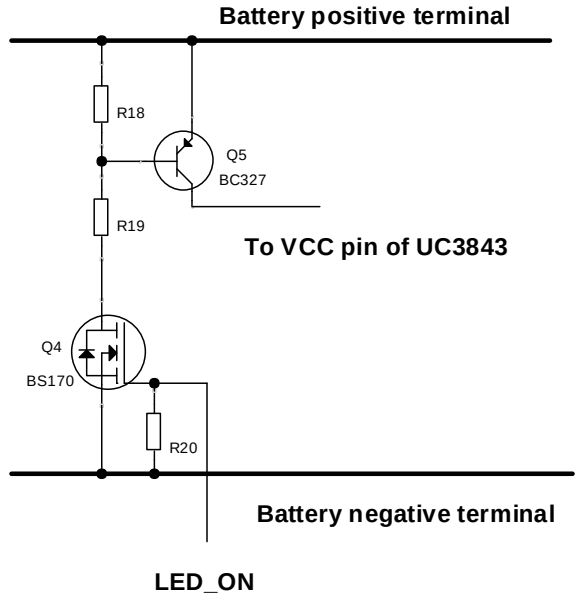

Fig. 4.16. Circuit of logic shout-down arrangement

4.4 Experimental Results and Observations

For the tunable-CCT system, the experimental studies were conducted in a windowless dark-room. The luminaire was mounted at the top of a black-painted aluminum-enclosed structure. Readings of the optical quantities were taken using a Konica- Minolta CL200A chroma meter. The meter was placed on the work plane 1 m below the composite LED source for measurement of CCT and illuminance. The experimental setup for CCT and illuminance measurement is shown in Fig. 4.17.

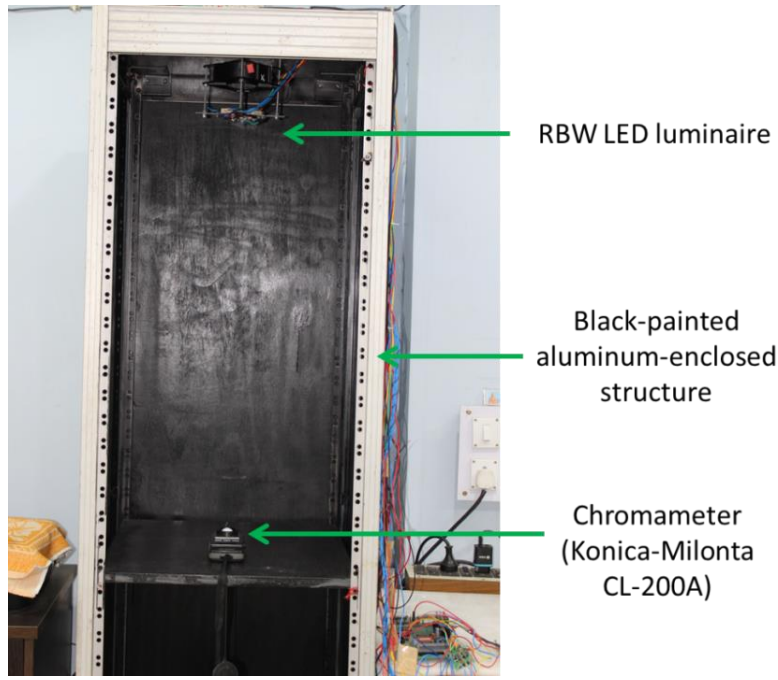

Fig. 4.17. Experimental setup for CCT and illuminance measurement

4.4.1 Performance of the CCT and Illuminance Control System

The system was first operated with fixed luminous parameters measured at $D_1 = 0.5$ and $D_2 = 0.35$ for the main and companion LEDs, respectively. Twenty four different combinations, corresponding to four values of E_r (30, 60, 90 and 120 lx) and six values of T_{cr} (2500, 4000, 6000, 8000, 10000 and 12500K) at each E_r are set for measuring the CCT and E errors. The readings of the photometric quantities have been taken by using a Konica-Minolta CL200A Chroma Meter which was used for determining the LED parameters as described in Section 4.2.1.2. The experimental plots of set point and measured values for ambient temperatures of 27°C and 45°C are shown in Fig. 4.18 (a) and Fig. 4.18 (b), respectively. Two performance indices, namely, RMS error and maximum absolute error are also chosen to evaluate the system performance at these sample set point combinations. The results are shown in Table 4.7.

The results in Table 4.7 show that the performance of the system, both in terms of RMS error and absolute error, for T_c and E are quite high, especially when one compares the corresponding figures for the compensated system to be considered next.

Table 4.7. Error performance indices of the system with fixed luminous parameters

Ambient temp(°C)	RMS error in T_c(K)	RMS error in E(lx)	Maximum absolute error in T_c (K)	Maximum absolute error in E (lx)
27±2	172.2	4.09	610 @T_{cr} = 12500K; Er = 120 lx	7.2 @T_{cr} = 12500K; E_r = 120 lx
45±2	1148.4	9.28	2810 @T_{cr} = 12500K; E_r = 120 lx	18.5 @T_{cr} = 2500K; E_r = 120 lx

The system was next operated in temperature compensated mode using the parameter estimation algorithm discussed in Section 4.2.1.2. The experimental results for ambient temperatures of 10°C, 27°C and 45°C are shown in Fig. 4.19, Fig. 4.20 and Fig. 4.21 in the form of scatter plots. The performance indices at different ambient temperatures are given in Table 4.8, where operation at a low ambient temperature of 10°C has also been included. At the low temperature the luminous parameters are estimated at runtime by extrapolation. Fig. 4.19, Fig. 4.20 and Fig. 4.21, when compared with Fig. 4.18(a) and Fig. 4.18(b) exhibit much lower errors in CCT and E for the compensated system. A comparison of the results in Tables 4.7 and 4.8 clearly indicates the superiority of the compensated system over the uncompensated one. It also shows that the system can be operated over a wide ambient temperature excursion between 10°C to 45°C.

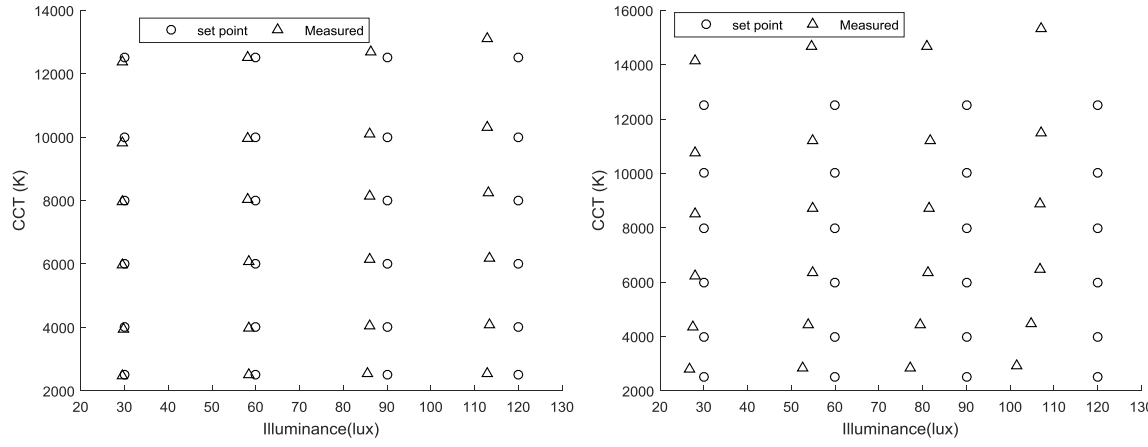

(a) (b)

Fig. 4.18. CCT and Illuminance measurement for (Fixed luminous parameters) (a) at 27°C (b) at 45°C

Table 4.8. Error performance indices of the system with runtime parameter estimation

Ambient temp(°C)	RMS error in T_c(K)	RMS error in E(lx)	Maximum absolute error in T_c (K)	Maximum absolute error in E (lx)
10±2	167.5	0.46	286	0.8
27±2	161.5	0.61	319	1.1
45±2	167.2	0.31	400	0.8

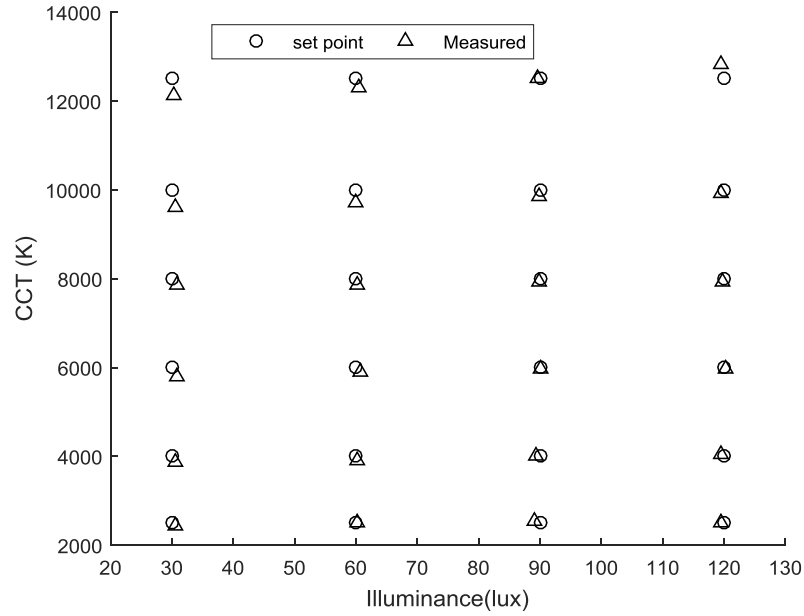

Fig. 4.19. CCT and Illuminance measurement at 10°C (Run-time estimated parameters)

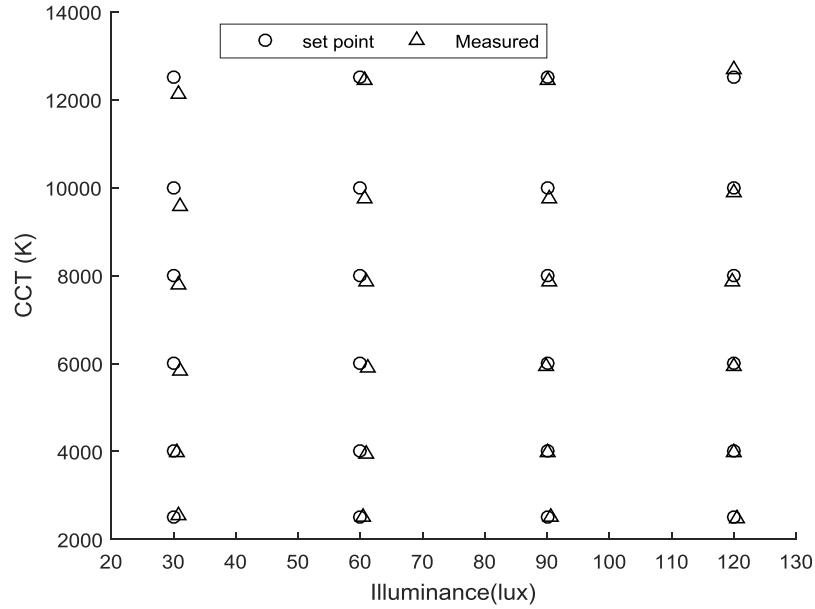

Fig. 4.20. CCT and Illuminance measurement at 27°C (Run-time estimated parameters)

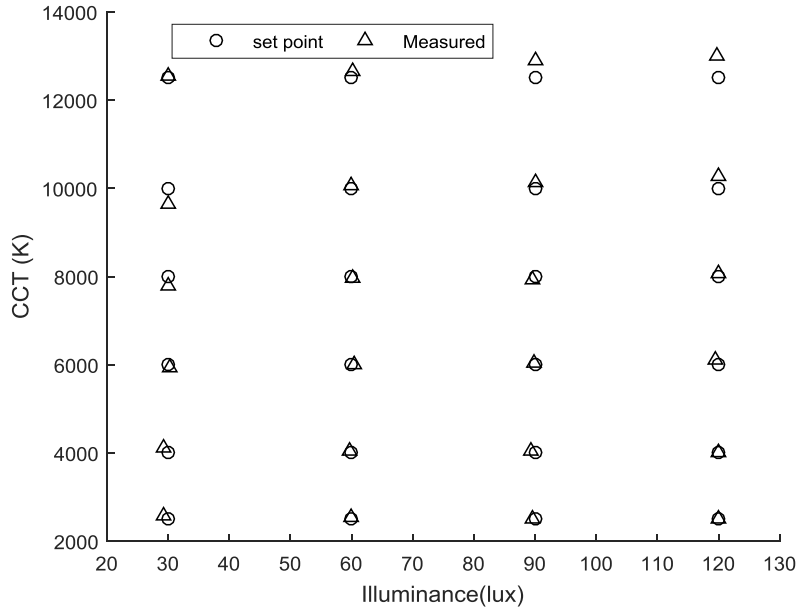

Fig. 4.21. CCT and Illuminance measurement at 45°C (Run-time estimated parameters)

Maintaining the temperature compensated system at the standard ambient temperature of 27±2^{0}C, the CCT and illuminance errors as functions of the set point CCT, at various illuminance set points were evaluated. The data are plotted in Fig. 4.22 and Fig. 4.23.

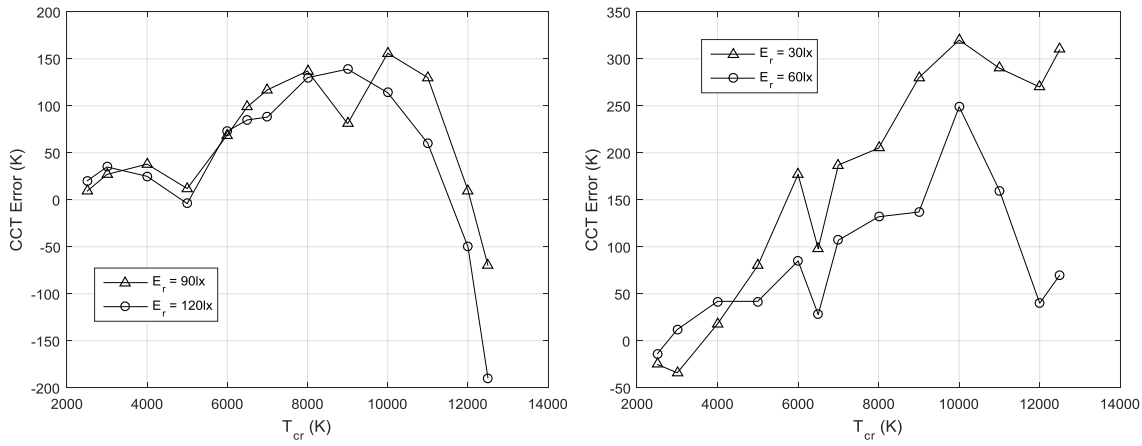

(a) (b)

Fig. 4.22. Graphs showing the error in CCT as a function of set point CCT. (a) E = 120 lx and 90 lx. (b) E = 60 lx and 30 lx with runtime parameter estimation.

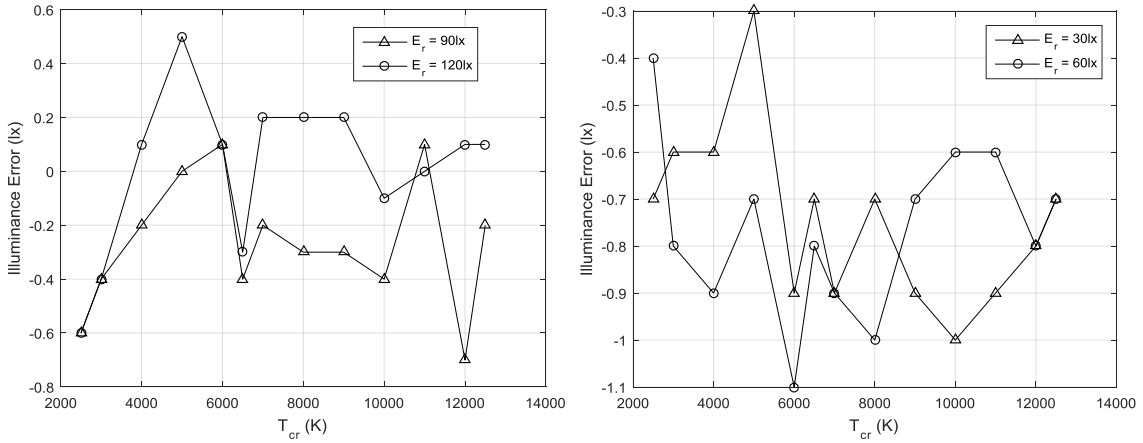

(a) (b)

Fig. 4.23. Graphs showing the error in illuminance as a function of set point CCT. (a) E = 120 lx and 90 lx. (b) E = 60 lx and 30 lx with runtime parameter estimation.

The following three plots show the internal functioning of the controller at an ambient temperature of 27±2 ^{0}C. The ratio r_a, which determines the position of x_b on the blending line is plotted as a function of set CCT in

Fig. 4.24. It is observed that r_a is not affected by the illuminance set point. Fig. 4.25 shows how the duty cycles D_1 and D_2 change with set CCT at two different values of setpoint E. It is apparent from this figure that the value of $r_D = D_2/D_1$ increases on both sides of $D_2 = 0$ point where the only source is S_1. In Fig. 4.26, the computed values of the luminance contributions $E_{M1}.D_1$ and $E_{M2}.D_2$ are plotted as functions of set CCT. It is obvious that at a different ambient temperature, while the values of the dependent variables in these three graphs will change, the shapes of the graphs will be retained.

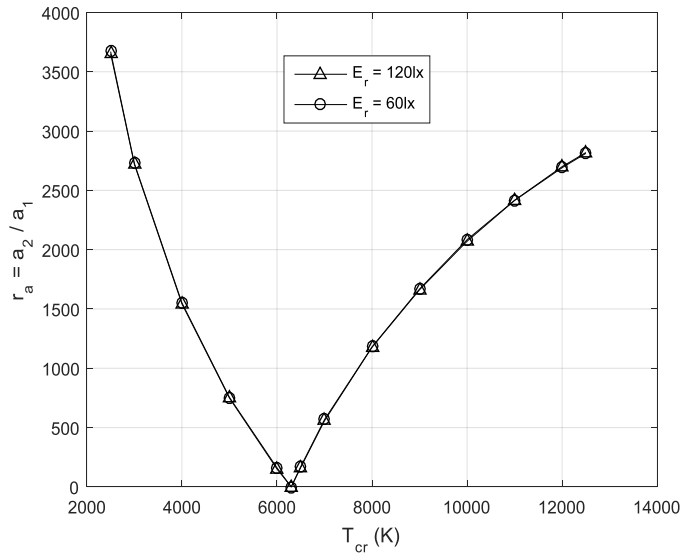

Fig. 4.24. Ratio r_a as a function of set CCT at 60 lx and 120 lx

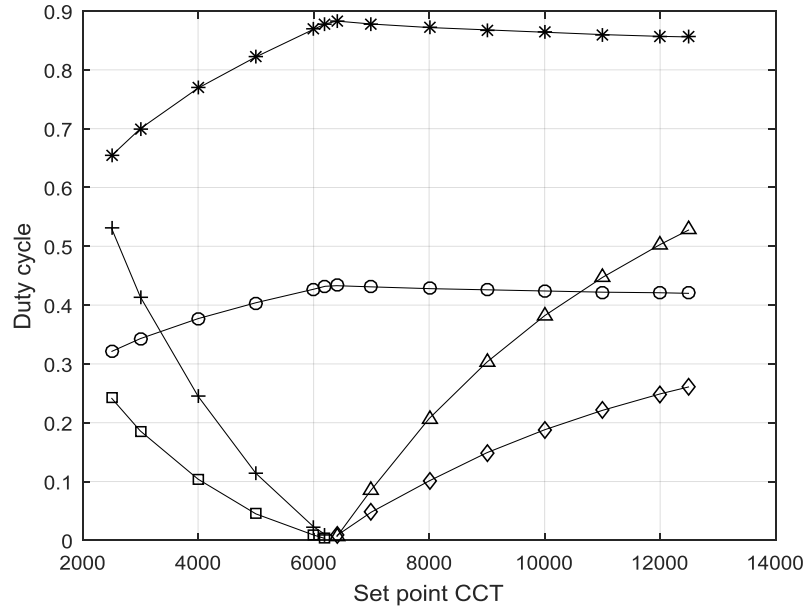

Fig. 4.25. D1 and D2 as functions of set CCT at 60lux and 120lux

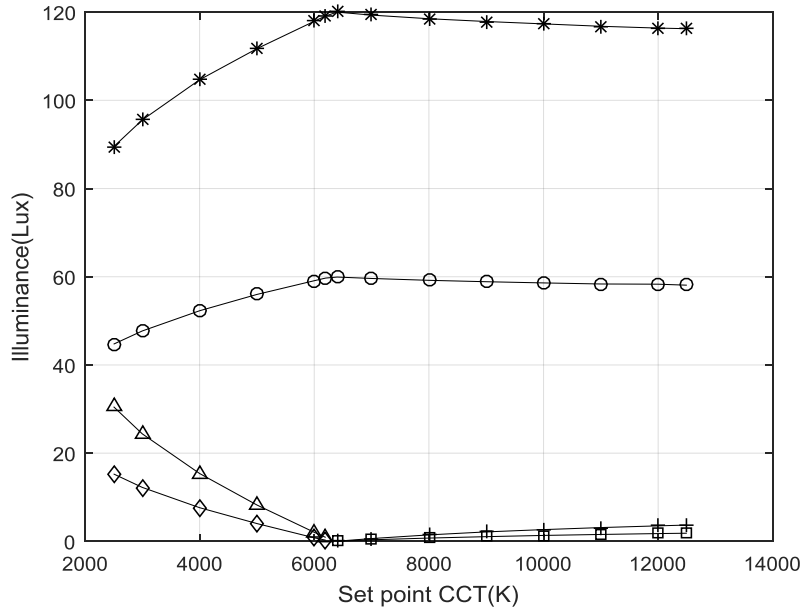

Fig. 4.26. Illuminance contribution from individual sources as functions of set CCT at 60 lx and 120lx

The relative efficiency as functions of set CCT at 120lx has been plotted in Fig. 4.27. The figure shows that for fixed lumen output the efficiency is decreasing for both RW and BW mixing as the efficacy of companion LED is less than that of the white LED.

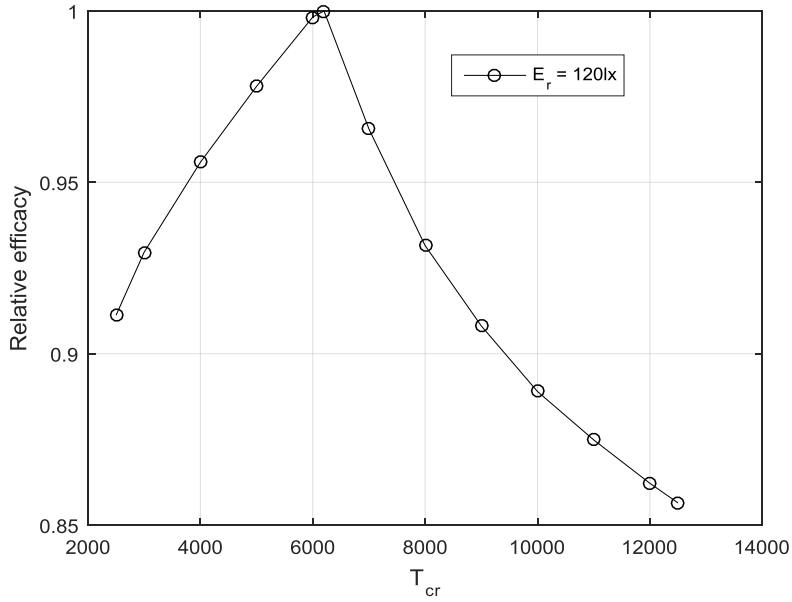

Fig. 4.27. Relative efficiency as functions of set CCT at 120lx

4.4.2 Measurement of Duv and Colour Rendering Index (CRI)

Although the requirements of a wide range of CCT and of illuminance have been met, the deviation of the locus of the operating points, namely the WB and WR line segments, from the Planckian locus is clearly visible. To quantify the deviation, a commonly used measure, D_{uv}, is used. The values of D_{uv} at selected values of CCT are computed by transformation of the CIE 1931 xy coordinates to the CIE 1960 uv coordinates system and subsequent evaluation of the linear distance between the actual operating point and the corresponding point on the Planckian locus the in the uv plane. By definition, as the R-W-B locus is always below the Planckian locus, D_{uv} is negative for all the points. A plot of D_{uv} as a function of CCT is shown in Fig. 4.28. Studies conducted at NIST (National Institute of Standards and Technology, USA) [12] indicate that for a CCT range of 2700K to 6500K, an approximate D_{uv} of – 0.015 appeared to be most natural. For the CCT range of 2500K to 4000K, our system has a larger magnitude of D_{uv}. A possible way to mitigate the problem is discussed at the end of this section.

To ascertain the colour quality of the light produced by the system over the entire range of CCT at 120 lx, the full-scale value of the illuminance set point, the most common colour rendition metric CRI Ra was used. It was measured by a Konica-Minolta CL-70F CRI-Illuminance meter. The values obtained are shown in Table 4.9. For a CCT range of 4000K to 12500K, the value of CRI is more than 82, a figure that is often seen for many commercial

quality, fixed CCT, LED lights. The reason for a fall of CRI for a CCT below 4000K is the marked deviation of the WR blending line from the Planckian locus and an excessive red content in the mixed light. At the end of this section, we present a possible solution to this problem also.

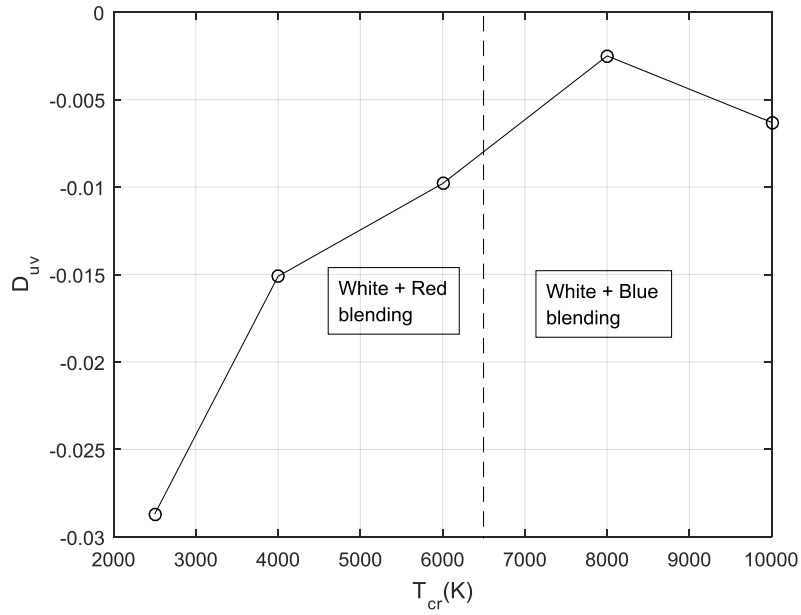

Fig. 4.28. Plot of experimental D_{uv} as a function of set point CCT

Table 4.9. CRI measurement

Set CCT (K)	2500	3000	4000	5000	6000	6200	6400	7000	8000	9000	10000	11000	12000	12500
Measured CRI	71.3	74.0	82.4	86	90.1	90.3	90.5	88.3	84.8	84.2	84.2	84.1	84.1	84.0

Fig. 4.29 shows the spectral power distribution (SPD) of the proposed RBW LED lighting system at 4000K, 5000K, 6000K and 7000K. Measured CRI at 6000K-7000K is found to lie in the band 88.3 to 90.1 as given in Table 4.9. From the SPD curve, it has been seen that the peaky nature in the red region is less for 6000K-7000K, that leads to high CRI value in this region.

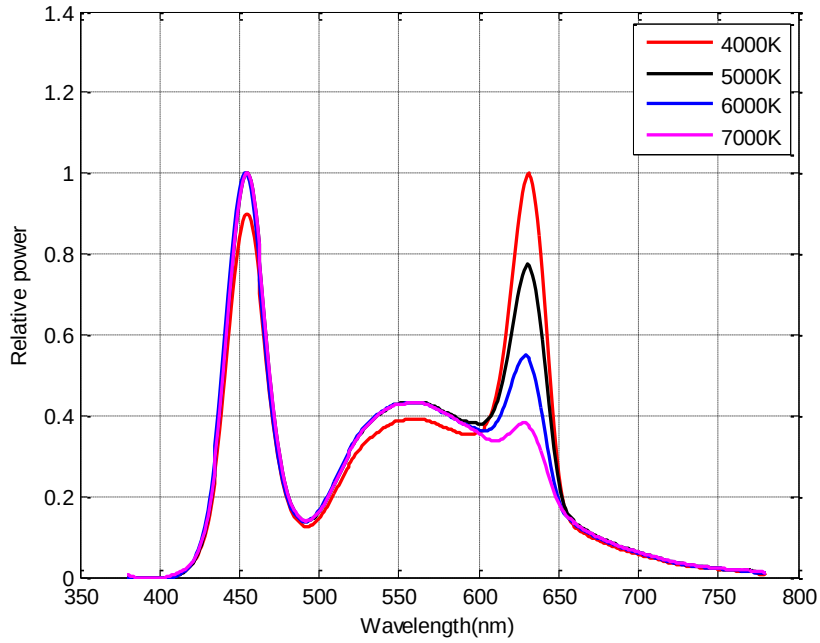

Fig. 4.29. Spectral power distribution of CCT (4000K, 5000K, 6000K and 7000K)

4.4.3 Observation regarding output quantization error

One of the major source of error in CCT, as already pointed out in Section 4.2.1.1 is the quantization of the controller output. Before presenting the observed effect, a little detailed exposition of the phenomenon is in order. One can, by use of (31), find two successive transition values of a particular D. For example, by setting p = (47, 48, 49) the values of D_T obtained are 0.04736 and 0.04834 for the 47-to-48 and 48-to-49 transitions, respectively. Thus, for D in the range of (0.04736, 0.04834), p remains unchanged at 48. Consequently, the value of the duty cycle of the PWM drive signal remains unchanged and no control over E or CCT can be exercised. To demonstrate the effect of this output quantization, we had, with a goal of obtaining a CCT of 9200K and an E of 30 lx, manually set the values of p_1 to 212 and 213, and p_2 to 48 and 49 and measured the CCT at the four possible combinations of p_1 and p_2. For our previously fixed value of $E_M\_B(0)$ = 6.77 lx, the results are shown in Table 4.10 . It is clear that the set CCT cannot be met in general due to the availability of a limited number of choices of the manipulated variables p1 and p2, resulting due to quantization. The last observation is true even when the controller works in automatic mode.

Table 4.10. CCT values (K) at different values of p1 and p2. EM_B (D = 0) = 6.77 lx

$p_1 \rightarrow$ / $p_2 \downarrow$	210	211
94	9192	9157
95	9237	9210

While selecting the peak LED current and the resulting peak illuminance for the blue LED shown in Table 4.5, much lower values were chosen compared to those of the red LED. It was accepted that, due to the limited accuracy caused by the limited resolution of the luxmeter, the measurement of peak illuminance was subject to a large error. However, the range of the manipulated variable p_2 was about 0 to 120 giving a resolution of 1 in 120. The consequential quantization error has been demonstrated in Table 4.10. The error band in CCT for a fixed $p_1 = 210$ is 45K. To see the effect of choice the peak illuminance on quantization error, its value was raised to 12.07 lx and the same experiment was repeated. The results are reproduced in Table 4.11. The range of the manipulated variable p_2 was about 0 to 60 giving a resolution of 1 in 60. As expected, the error band in CCT for a fixed $p_1 = 212$, increases to 117K. It is thus concluded that a trade-off between the possible error in measuring E_M for the least contributing S_2 (Blue LED in the present case) and the resulting quantization error must be made

Table 4.11. CCT values (K) at different values of p1 and p2. EM_B (D = 0) = 12.07 lx

$p_1 \rightarrow$ / $p_2 \downarrow$	212	213
48	9140	9122
49	9257	9233

4.4.4 Comparison of the proposed LED lighting system with ANSI

The ANSI standard C78.377A-2008 [13] for the chromaticity of solid-state lighting products is reproduced in Table 4.12 for ready reference. Form Fig. 4.30 it is observed that the CCT tolerance requirement is satisfied for both the CCTs for all the values of set illuminances. The D_{uv} values for WR line, which are not plotted in Fig. 4.31, are always negative and higher than the ANSI specified values. On the other hand, from the D_{uv} values for WA (white-amber) blending plotted in Fig. 4.31, it is observed that the D_{uv} is within the specified range for 3700K- 6200K. The ANSI C78.377 standard state that the tolerance range specified in

Table 4.12 is applicable for indoor lighting, higher tolerance values are often acceptable for other applications.

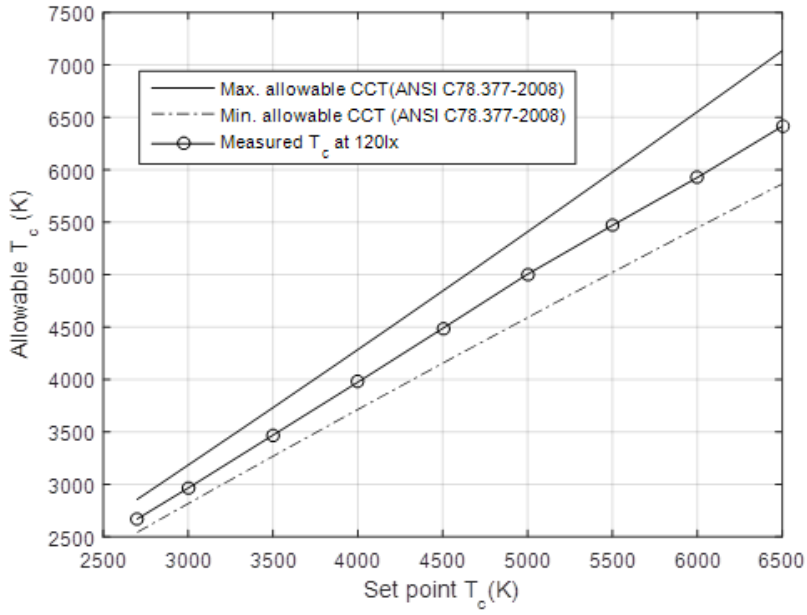

Fig. 4.30. Comparison of measured CCT with ANSI standard

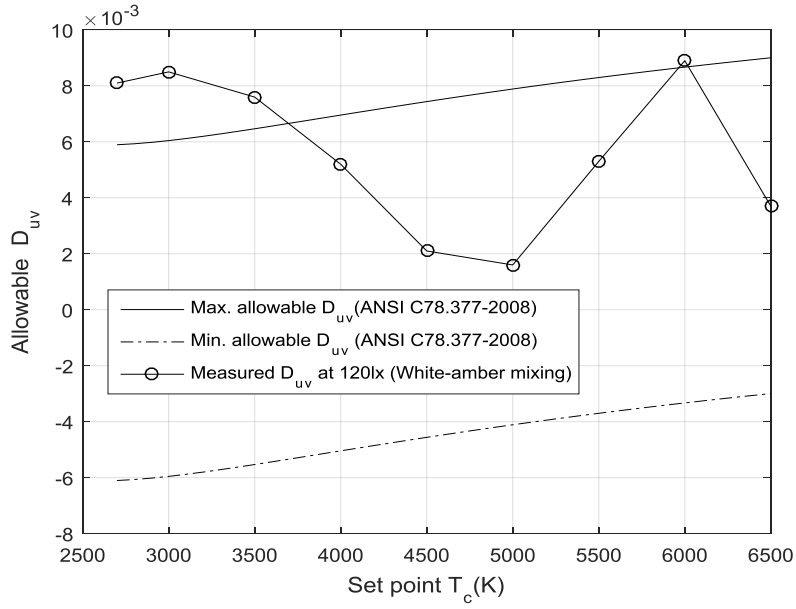

Fig. 4.31.Comparison of measured D_{uv} with ANSI standard for white-amber blending

The expression for the ΔT and D_{uv} of Table 4.12 for the flexible CCT have been given in the specified standard [13]**.** In accordance with the standard, the maximum and minimum tolerance range of CCT and D_{uv} have been plotted in Fig. 4.30 and Fig. 4.31, respectively.

Table 4.12. ANSI C78.377A standard for chromaticity specifications

Nominal CCT (K)	Target CCT and tolerance (K)	Target D_{uv} and tolerance
2700	2725 ± 145	0.000 ± 0.006
3000	3045 ± 175	0.000 ± 0.006
3500	3465 ± 245	0.000 ± 0.006
4000	3985 ± 275	0.001 ± 0.006
4500	4503 ± 243	0.001 ± 0.006
5000	5028 ± 283	0.002 ± 0.006
5700	5565 ± 355	0.002 ± 0.006
6500	6530 ± 510	0.003 ± 0.006
Flexible CCT (2700K-6500K)	T ± ΔT	D_{uv} ± 0.006

4.4.5 Improvement of D_{uv} and CRI

To improve the value of D_{uv} value for CCTs lower than that of S_1, the red LED source can be replaced by a source, say T, such that the blending line WT, as shown in Fig. 4.2, is closer to the Planckian locus. In an initial trial, the red LED was replaced by an amber LED whose measured xy coordinates in 'S' condition and a duty cycle of 0.1 were 0.5685 and 0.4295, respectively. The peak current value was kept same as that of the red LED. The value of D_{uv} at 2500K had remarkably improved to -0.007. However, the spectral response characteristic of the amber LED had a negligible red content as observed by the Konica-Minolta CL-70F CRI-Illuminance meter. Owing to this, the value of CRI in the 2500K to 4000K band cannot be improved by the use of this LED. Therefore, no further results were collected.

4.5 Conclusion

This chapter describes the implementation of fixed-CCT and tunable-CCT LED lighting systems. For the fixed-CCT system, a three-step dimmable LED driver has been implmentaed. The implementation uses only readily available components.

For the tunable-CCT system, a CCT and illuminance controllable LED lamp using two-component colour blending has been implemented. It is based on a simple mathematical foundation. A simple non-iterative algorithm for the controller has been used to implemenat the algorithm. The algorithm is experimentally validated by hardware implementation. The

implementation uses only readily available components including a low-cost microcontroller. The average forward voltages of active LEDs are measured at runtime and the luminous parameters of the LEDs are estimated by using a simple algorithm. The method of estimation of parameters, which does not need any temperature measurement, demonstrates the capability of operation of the system over a wide ambient temperature range. Experimental results demonstrate that the proposed approach for luminous parameter estimation yields more accurate results than those produced under the assumption of fixed luminous parameters. The developed RBW LED lighting system has been compared with the ANSI standard for solid-state lighting products. Considering the wide range of available CCT, the error in CCT, D_{uv} and measured CRI of the blended light are acceptable for a large class of applications.

References

[1] K. W. Houser, "The LED Surprise," *LEUKOS - J. Illum. Eng. Soc. North Am.*, vol. 11, no. 3, p. 107, 2015.

[2] M. Cole, H. Clayton, and K. Martin, "Solid-state lighting: The new normal in lighting," *IEEE Trans. Ind. Appl.*, vol. 51, no. 1, pp. 109–119, 2015.

[3] J. B. Murdoch, *Illumination Engineering—From Edison's Lamp to Laser*, 1 st. New York: Macmillan Publishing Company, 1985.

[4] M. Dyble, N. Narendran, A. Bierman, and T. Klein, "Impact of dimming white LEDs: chromaticity shifts due to different dimming methods," *Fifth Int. Conf. Solid State Light.*, vol. 5941, p. 59411H, 2005.

[5] N. Pousset, B. Rougié, and A. Razet, "Impact of current supply on LED colour," *Light. Res. Technol.*, vol. 42, no. 4, pp. 371–383, 2010.

[6] C. S. McCamy, "Correlated color temperature as an explicit function of chromaticity coordinates," *Color Res. Appl.*, 1992.

[7] "ATmega32A - 8-bit AVR Microcontrollers." [Online]. Available: https://www.microchip.com/wwwproducts/en/ATmega32A. [Accessed: 14-Mar-2019].

[8] J. D. Bullough, K. Sweater Hickcox, T. R. Klein, and N. Narendran, "Effects of flicker characteristics from solid-state lighting on detection, acceptability and comfort," *Light. Res. Technol.*, 2011.

[9] C. C. Wu, N. C. Hu, J. N. Chen, and H. I. Chang, "Parameterised LED current regulator for pulse width modulation switch delay for accurate colour mixing in multi-LED light sources," *Light. Res. Technol.*, vol. 46, no. 2, pp. 171–186, 2014.

[10] *IEEE Recommended Practices for Modulating Current in High-Brightness LEDs for Mitigating Health Risks to Viewers*, IEEE Standard 1789-2015, Jun. 2015.

[11] "UC1842 UCx84x Current-Mode PWM Controllers," 2016. [Online]. Available: http://www.ti.com/lit/ds/symlink/uc3843.pdf. [Accessed: 01-May-2019].

[12] Y. Ohno, "Color Quality of Lighting and Metrics-Where are we going to?," 2016. [Online]. Available: https://www.energystar.gov/sites/default/files/asset/document/Energy Star webinar Presentation - Ohno 2.pdf. [Accessed: 16-Mar-2019].

[13] "American National Standard, Specifications for Chromaticity of Solid State Lighting Products, ANSI C78.377," 2008.

Chapter 5

Wireless Monitoring and Control of the Outdoor Lighting Systems

5.1 Introduction

In this chapter, the implementation of wireless monitoring and control of the OLS has been described. Based on the literature survey given in Section 1.7.3 of Chapter 1, the GSM-based SMS service has been chosen to monitor and control the remote outdoor lighting system (OLS), in the present study. The controller sends the relevant information related to the management and maintenance of the OLS on a regular basis to the central monitoring station. The information has been sent through the GSM-SMS technology. On receiving the message in the central monitoring station, one can assess the different health parameters of the OLS. In turn, after analyzing the data, the administrator commands can be sent by the human supervisor to control various parameters of the OLS. The most relevant information which are sent via SMS is battery system health, SOC, dust/insect accumulation in the LED luminaire etc. Additionally, depending on the received information, the maintenance personnel can be sent to the exact location. Some of the information are displayed on an LCD panel locally, which also helps the maintenance personnel to predict the system fault. A detailed description of hardware and software implementation of GSM-SMS technology, as used in the present study, is given in this chapter. In Sections 5.1- 5.6, a detailed implementation of the communication features of the Fixed CCT Outdoor Lighting System (FCOLS) is presented. Section 5.7 deals with the software addition and deletions necessary for the TCOLS.

5.2 Overview of the proposed monitoring and control system

A block diagram of the proposed GSM-based remote monitoring and control system is shown in Fig. 5.1. This figure shows that the information of a remote OLS is transmitted through a GSM network to a central station for monitoring. After processing the information, the central station can also control the remote OLS through the same network. The MCU is programmed to send /receive SMS at a specified time-slot by using the GSM module

(SIM800). Generally, the central monitoring station stores the information in a database for analysis in the future. In this study, the memory of a mobile phone has been used as a storage device for SMS.

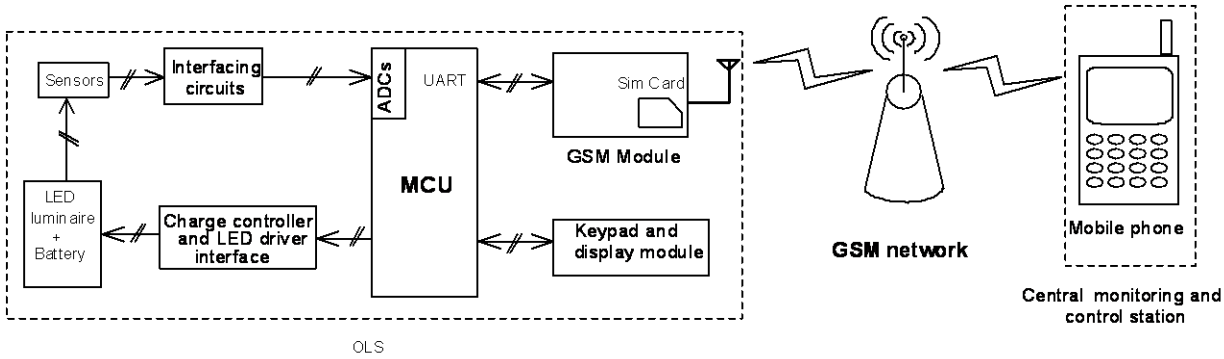

Fig. 5.1. Block diagram of the proposed GSM-based remote monitoring and control system.

Short descriptions of the important blocks of Fig. 5.1 are given below.

GSM module: A GSM-based transceiver module SIM800 is used for monitoring and control of the OLS through SMS.

Sensors: Different types of sensors (such as light sensor, temperature sensor**,** battery voltage/current sensors etc.) are used to collect the relevant information regarding the electrical and physical parameters of the OLS. Usually, the sensor produces the electrical equivalent values of any physical quantity.

Interfacing circuits: Output of the sensors are being fed to the MCU through the interfacing circuits. These circuits are used to produce a compatible voltage for the ADCs of the MCU.

GSM network: GSM (Global System for Mobile communication) is a digital mobile network that is extensively used by mobile phone users throughout the globe.

Centre monitoring and control station: A low-cost, mobile handset with the messaging facility is used as a GUI (graphical user interface) for the central monitoring and control station.

Keypad and display module: A 3X1 keypad module is used for different parameter setting and a 16X2 LCD module (JHD162A) is used to display various parameters such as battery voltage, charging current, discharging current for user interfacing.

5.3 Lighting load control and health monitoring

In the present implementation, the lighting load has been controlled in accordance with the administrator command or the pre-defined dimming control. Additionally, the health of the battery (by measurement of internal resistance) is estimated by using the same load. Therefore, the algorithm for lighting load control and health monitoring has been realized in the same state, i.e., at state 5. At the beginning of this state, the internal resistance of the battery has been measured in accordance with the standard IEC 61951-1. Then the battery power is optimized based on the administrator command or on pre-defined dimming control. In absence of administrator command, the total lighting period is controlled by the pre-defined three-step dimming level to optimize the battery power. For better visibility, the flowchart of State 5 has been split into two figures which are shown in Fig. 5.2 and Fig. 5.3. To start the algorithm, different values of user defined constants and run-time variables are needed to be initialized for state5. The values of user-defined constants and variables are given in Table 5.1 and Table 5.2, respectively.

In Fig. 5.2, the function low ambient light (LoAmbLgt) is used to detect the ambient light level at which the LED lamp turns off. This function measures the panel voltage to compare with a pre-defined voltage and return a value of 0 if high-ambient light detected. In our case, a predefined threshold value (panel voltage) of 10V is chosen to detect the dawn condition. To ensure the dawn, the algorithm will detect high-ambient light 40 times, i.e., the variable k_dwn should be equal to 40 for state transition as shown in the flowchart of Fig. 5.2. The loop counters k_lp_s5 and k_2min_s5 are incremented in every 500ms and 2 min, respectively. The values of loop counters are also displayed in the LCD screen to monitor the running time of state 5.

In State 5, the battery voltage, V_b is continuously monitored to protect the battery from deep-discharge. Therefore, the battery is disconnected from the load, if the battery voltage reaches a pre-defined lower threshold voltage, VBLO. In this case, VBLO = 11.4 has been chosen (i.e., 1.9V/cell) in accordance with the IEEE standard [1]. Other features of these flowcharts are discussed in the following sub-sections. To start the algorithm, different values of user defined constants and run-time variables are needed to be initialized for state5. The

values of user-defined constants and variables are given in Table 5.1 and Table 5.2, respectively.

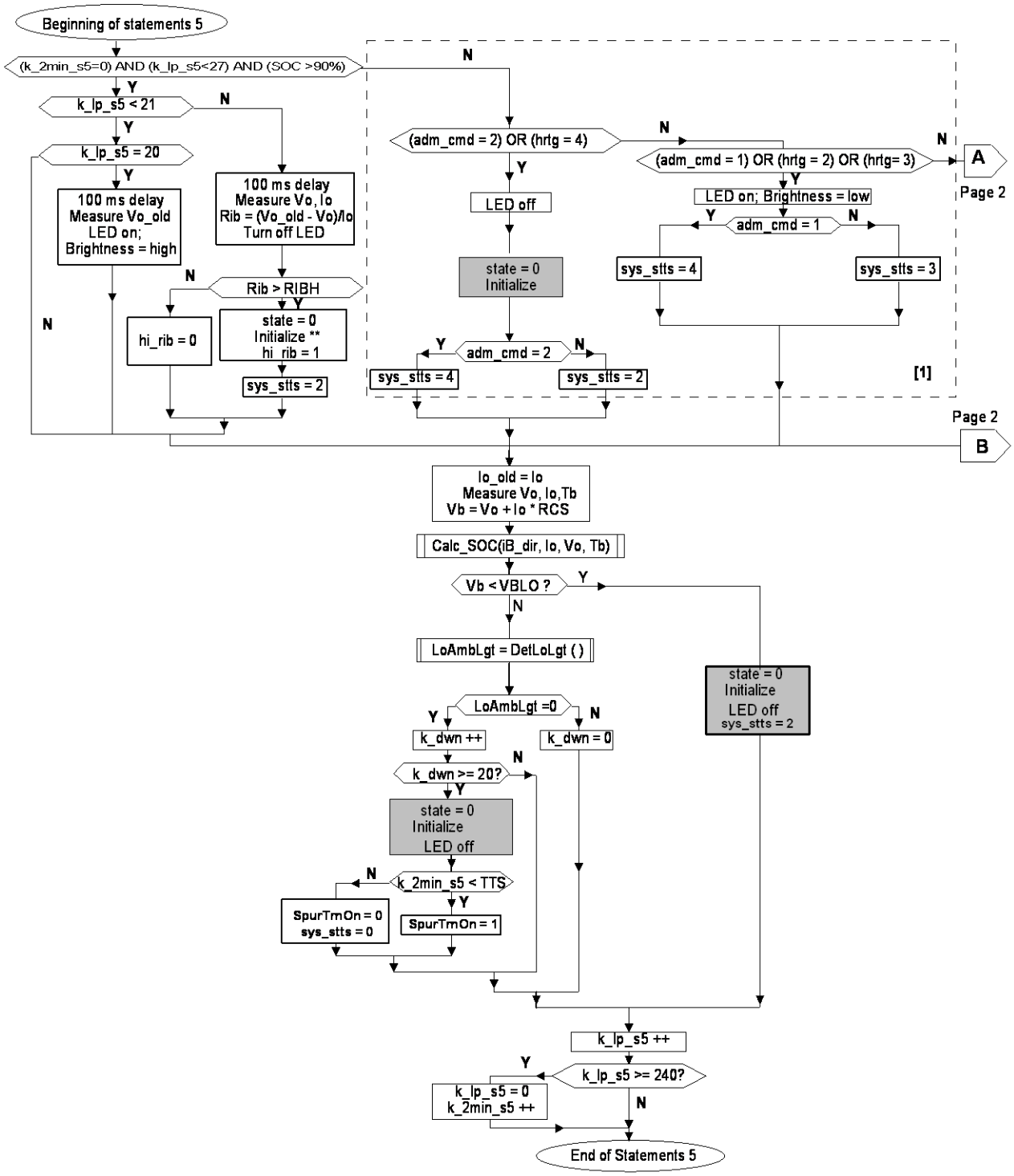

Fig. 5.2. Flowchart of lighting load control and battery health monitoring (State 5)

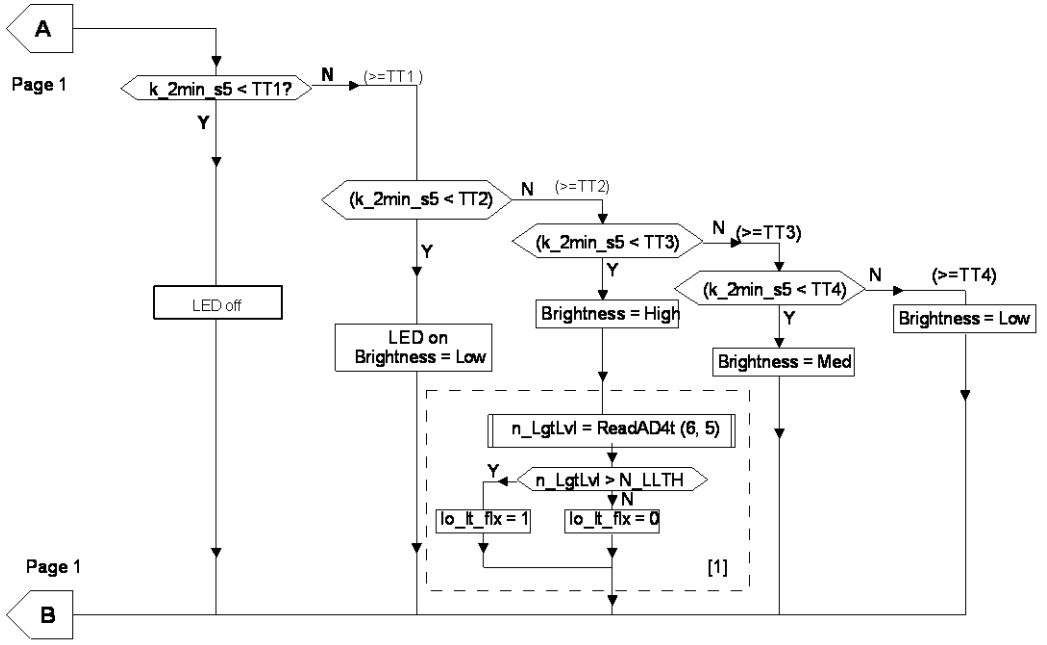

Fig. 5.3. Flowchart of lighting load control and battery health monitoring (continuation of State 5 from Fig. 5.2)

Table 5.1. User defined constants for state 5

Constants	Value
RIBH	0.18
VBLO	11.4
RCS	0.02
N_LLTH	2500
TT1	3
TT2	8
TT3	143
TT4	293

Table 5.2. Initialization of run time variables for state 5

Variables	Value
k_lp_s5	0
k_2min_s5	0
k_dwn	0

5.3.1 Load control based on predefined timing

To optimize the power consumption of the load, a predefined lighting schedule has been used in this implementation. For normal operation, the total lighting period has been sub-divided into five parts with respect to the brightness level. The principle and implementation of three-step dimming for brightness control have already been discussed in chapter4. The flowchart and timing diagram of the lighting schedule are shown in Fig. 5.3 and Fig. 5.4, respectively. In Fig. 5.4, the pre-defined brightness levels with the corresponding period have been shown. If any change in the time-slot is necessary for any other application, the pre-defined constants (TT1, TT2, TT3, and TT4) can be suitably modified.

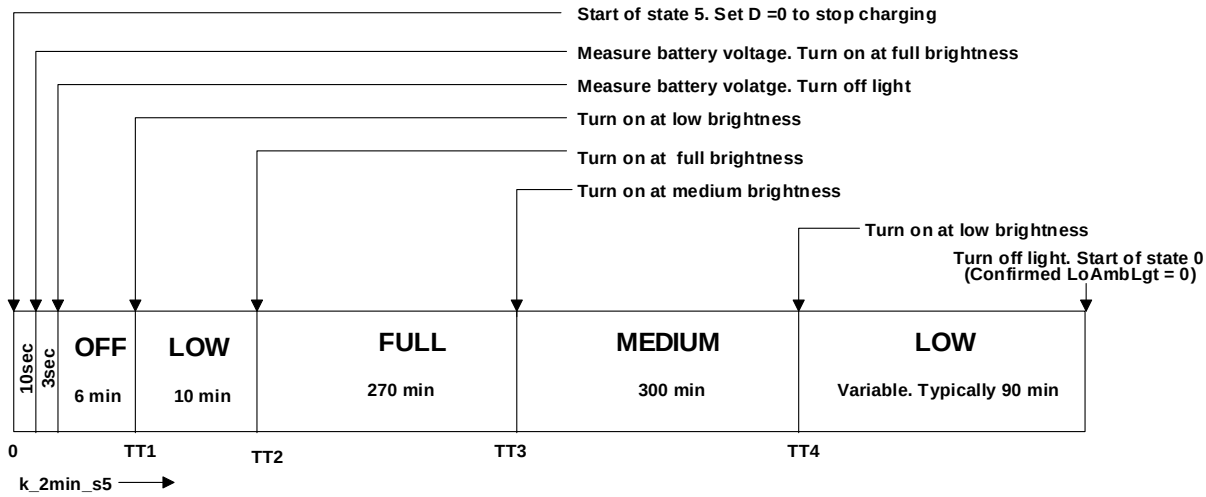

Fig. 5.4. Timing diagram of the lighting schedule for normal operation (State 5)

5.3.2 Load control based on administrator command

In the present implementation, the load can also be controlled from the remote place through GSM-SMS technology, based on the health record of an OLS. The SMS contains the administrator command to control the lighting load. A description of extraction of administrator command from the SMS has been given in details in Section 5.4. For FCOLS, two commands have been used to control the lighting load which is also shown in Fig. 5.2. The administrator command and the corresponding action have been given in Table 5.3. If any addition in the administrator command is necessary for any application, the flowchart can be suitably modified.

Table 5.3. Administrator command and the corresponding action for FCOLS.

Administrator command	Action
1	Turn on LED at low brightness to save the stored energy
2	Turn off the LED luminaire.

5.3.3 Health monitoring of the OLS

In state5, the DC internal resistance R_{DC} and light output of the luminaire are measured to predict the state-of-health (SOH) of the OLS. If the value of internal resistance increases

beyond a pre-defined value, the load turns off automatically to protect the battery. A system status message of "High internal resistance" is also sent to the central monitoring station so that the administrator can take actions accordingly. Additionally, the controller sends a message 'High lumen degradation' to the remote station, if the light output falls below a set-point value.

In this present study, R_{DC} has been measured in accordance with the recommendation of standard IEC 61951-1. In this method, the battery is discharged at a constant current of I_1 for a period of 10 s. In our case, this constant current is equal to the auxiliary supply current (i.e., supply required for MCU, LCD, ICs etc.). At the end of the discharge period of 10s, the voltage V_{B1} is measured and recorded. Then the discharge current is immediately increased to a constant value of I_2 for a period of 3s and at the end of this period, the battery voltage V_{B2} is measured. The current I_2 is generated by turning on the LED at full brightness. During this process, it has been assumed that I_2 is constant as LEDs are driven from a CC LED driver. The principle of operation and implementation of CC LED driver have already been discussed in Chapter 4. Based on the recorded values mentioned above, R_{DC} can be calculated as follows

$$R_{DC} = \frac{V_{B1} - V_{B2}}{I_2 - I_1} \tag{5.1}$$

It is known that the internal resistance increases as SOC decreases. Therefore, the value of R_{DC} varies with SOC of the battery, so, R_{DC} has been measured when the SOC reached to a pre-defined value of 90%. In the present implementation, R_{DC} is measured without using any additional load. This measuring process also does not affect system operation. A pre-defined high internal resistance value RIBH = 0.18Ω has been chosen. The value has been fixed experimentally. If the internal resistance increases beyond the set point value, a variable hi_rib has been set to 1, and a corresponding message for battery maintenance has been sent to the remote monitoring station. SOH of the battery is also predicted by measuring the battery voltage which has already been explained in Section 3.3.3.

A light dependent resistance (LDR) based light sensor is used to sense the intensity of the outdoor light. The sensor is placed at the inside of the luminaire so that it can measure indirect light from the LED source. In this realization, an ADC channel is used to measure the output voltage of the sensor which is a decreasing function with the light intensity. The

controller sends a message if the light output falls below a set-point value. The experimental ADC values of high-brightness, medium-brightness and low-brightness are 2311, 2636 and 2837, respectively. Based on these values N_LLTH = 2500 is chosen, therefore, if light output falls below the set point value, a variable lo_lt_flx has been set to 1 and a a corresponding message of lumen degradation has been sent to the remote monitoring station.

5.4 Extraction of administrator command from the SMS

The controller reads the administrator command from the received text-message (SMS) which is being sent by the central controlling station. The extraction process of administrator command from the SMS has been discussed in this section and the corresponding algorithm is realized in State4. The serial data communication technique has been used for reading the SMS from the GSM module which is discussed in Section 5.6. The flowchart of the algorithm structure of state4 has been shown in Fig. 5. 5.

In this flowchart, State4 has been sub-divided into three phases based on the different functions of each phase. The primary function of each phase is given below.

Phase 0: Health check of the GSM module.

Phase 1: Read stored SMS from the GSM module.

Phase 2: Delete SMS from the GSM module.

In phase0 of state4, the health check of GSM module has been done. The flowchart of phase 0 is shown in Fig. 5.6.

The AT (i.e., attention) commands are the instructions which is used to control the GSM-module. The "AT" or "at" or “aT” or “At” prefix must be set at the beginning of each command line. To terminate a command line it is mandatory to enter a carriage return <CR> character. AT commands have the format of "AT <x> <n>", or "AT&<x> <n>", where "<x>"is the Command, and "<n>"is/are the argument(s) for that command. Commands are usually followed by a response that includes "<CR><LF><response><CR><LF>" where CR and LF represent carriage return and line feed, respectively. AT commands required for state 4 are given in Table 5.4 [2].

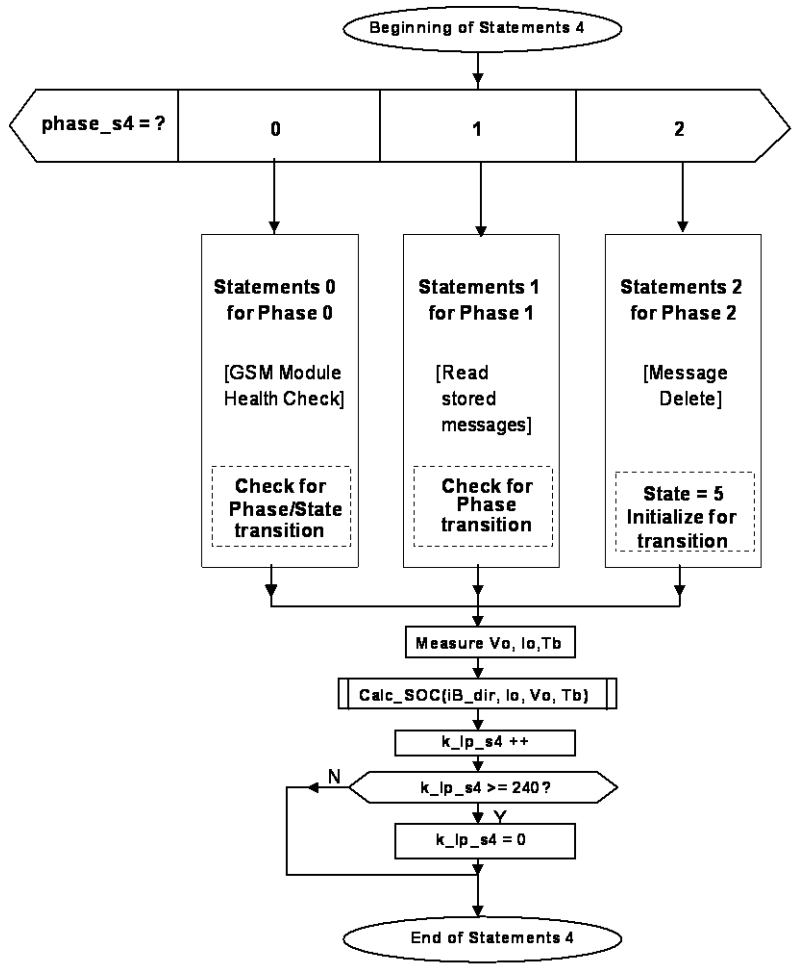

Fig. 5. 5. Flowchart for the program structure of state 4

Table 5.4. AT commands required for state 4

AT command	Description
AT	Check health of GSM module. The reply is "OK"
AT+CMGR= n	Read the SMS message from slot n.
AT+CMGD =1,4	Delete all messages from preferred message storage including unread messages.

The health of the GSM module has been checked by sending a command called "AT". If the reply comes from the GSM module is "OK" then the algorithm goes to the next phase. Otherwise, the algorithm goes to state5 for lighting.

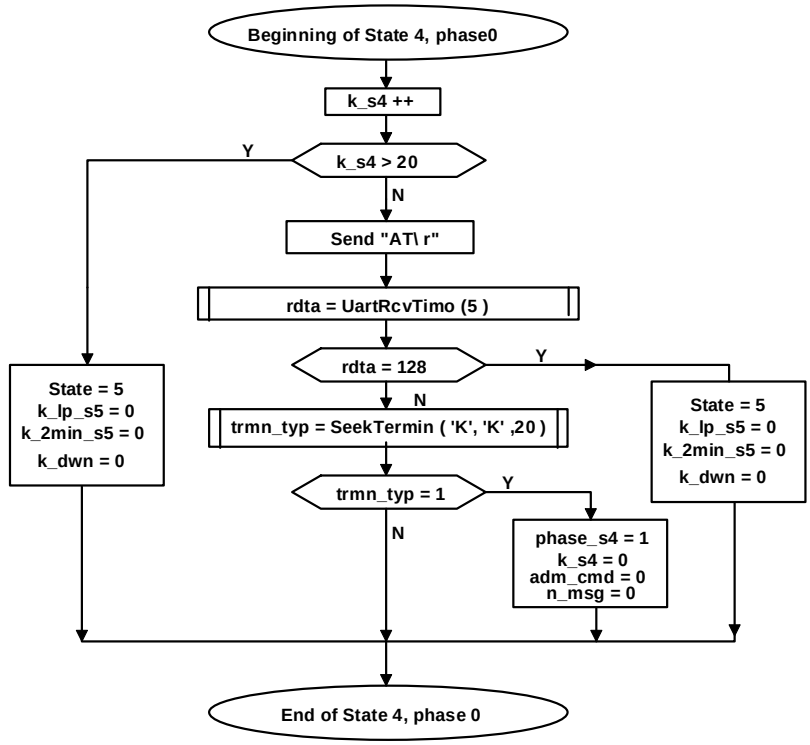

Fig. 5.6 Flowchart for the health checking of GSM module

Short descriptions of the functions for state4 are given below.

UartRcvTimo (n): This function is used to receive ASCII character with a timeout parameter of n * 1000 uS.

SeekTermin (prefc1, prefc2, max_tr): This function is used to receive incoming serial stream until either of the supplied characters 'prefc1' or 'prefc2' comes. It also returns with a 1 if 'prefc1' is encountered first or with a 2 if 'prefc2' is encountered. If neither is encountered within a maximum trails 'max_tr', a 0 is returned.

SkipChar (mychar, n): This function skips the given character, 'mychar' n times from an incoming serial stream.

FormStrng (mystr, a, maxsiz): This function is used to form an array 'mystr' by receiving a serial stream until the supplied character 'a' comes or the string length exceeds a maximum size 'maxsiz'. The formed string is terminated with a null.

In phase1 of state4, the message has been read from the SIM card to extract the administrator command. The flowchart of phase 1 is shown in Fig. 5.7. The AT command for reading a message (AT+CMGR) is used to receive an incoming serial stream of data. This

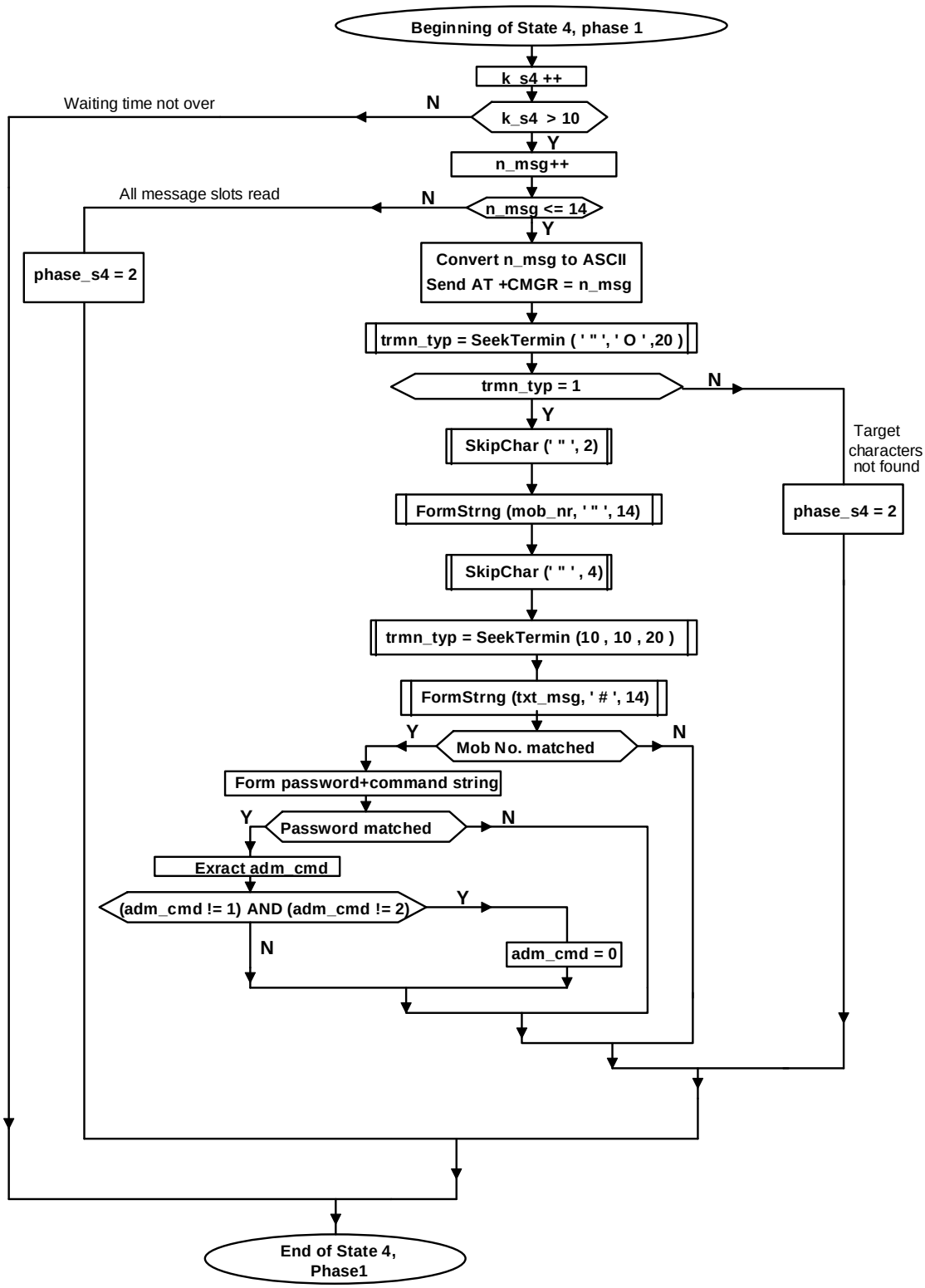

Fig. 5.7. Flowchart for extraction of administrator command from the SMS

stream contains sender information (such as mobile number, date and time stamping of received SMS etc.) and the text message. The algorithm compares the sender mobile number with pre-assigned mobile number, if the mobile numbers are matched, the controller extracts

the text message. Otherwise, the text message is ignored. The text message contains the password and the administrator command. The algorithm extracts the administrator command if the password is matched with the pre-assigned administrator password. This administrator command has been used to set different parameter of the OLS. The controller reads the maximum number of 14 SMS. Then all the received message of a day becomes deleted from the memory of the SIM card. The flowchart to delete the stored SMS from the GSM module is shown in Fig. 5.8. To start the algorithm, different values of run-time variables are needed to be initialized for state4. The initial value of runtime variables for state4 are given in Table 5.5.

Table 5.5. Initialization of run time variables for state 4

Variables	Value
Phase_s4	0
K_lp_S4	0
Phase_s4	0
adm_cmd	0
n_msg	0

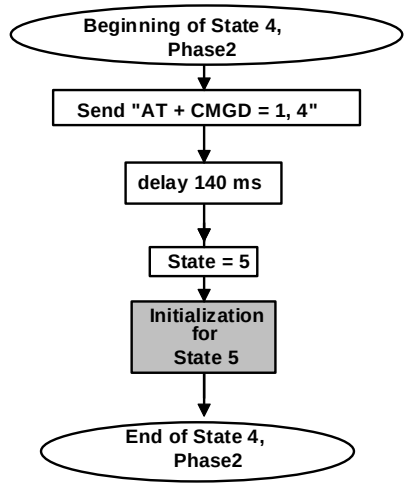

Fig. 5.8. Flowchart to delete the stored SMS from the GSM module

5.5 Sending the system status through SMS

The controller sends the status of the OLS through text-message (SMS) to the central monitoring station. The sending process of an SMS has been discussed in this section and the corresponding algorithm is realized in State0. In this realization, State0 has been sub-divided

into four phases based on the different functions of each phase. The primary function of each phase is given below.

Phase 0: Health check of the GSM module.

Phase 1: Network registration

Phase 2: Sending of message

Phase 4: Wait for dawn

Health check of the GSM module is done at phase0 of state1. The process of health check has already been discussed in Section 5.4 and the corresponding flowchart is shown in Fig. 5.10. To start the algorithm, different values of run-time variables and user defined constant are needed to be initialized for state0. Initialization of the run time variables and the user-defined constant for state0 are given in Table 5.6 and Table 5.7, respectively. AT commands required for state0 are given in Table 5.8. The flowchart of the algorithm structure of state 0 has been shown in Fig. 5.9.

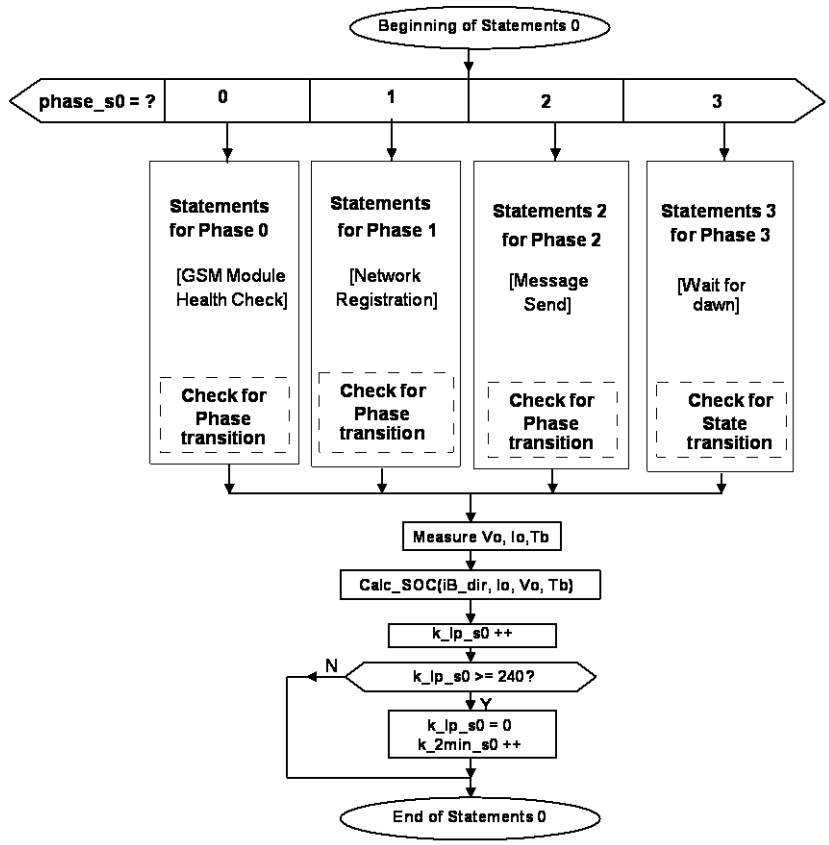

Fig. 5.9. Flowchart for the program structure of state 0

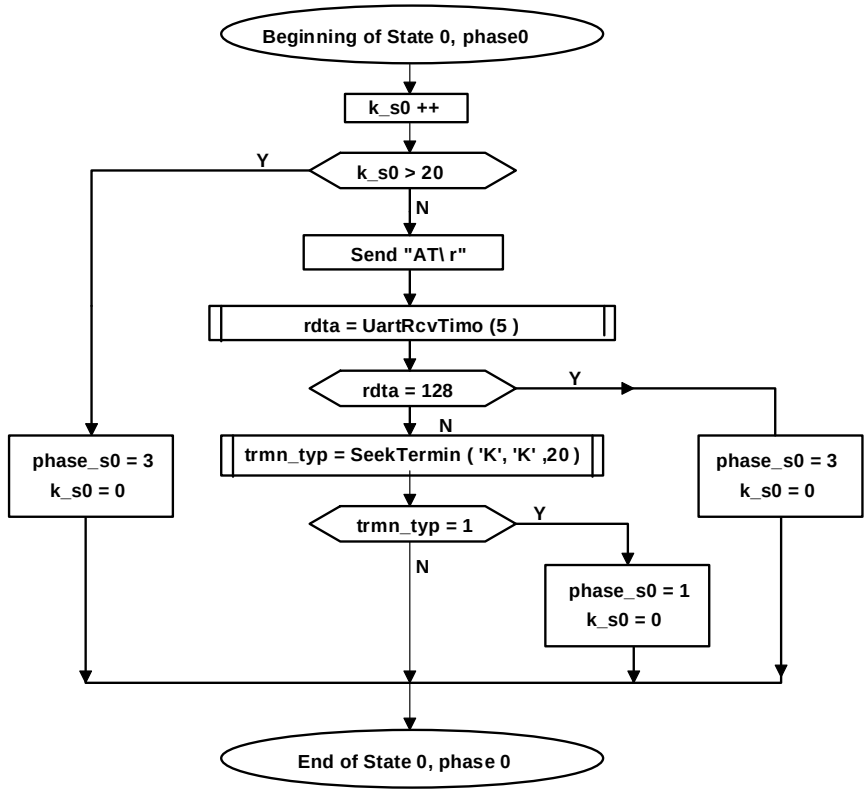

Fig. 5.10. Flowchart for the module health check

Table 5.6. User define constant for state 0

Constants	Value
VIO_DIFF	5.0

Table 5.7. Initialization of run time variables for state 0

Variables	Value
k_lp_s0	0
k_2min_s0	0
Phase_s0	0
k_s0	0

Table 5.8. AT commands required for state 0

AT command	Description
AT	Check health of GSM module. The reply is “OK”
AT+CREG?	Network registration
AT + CMGF = 1	Select SMS format as a text mode
AT + CMGS =“AdmMobNr”	Send SMS to the specified mobile number

Phase1 of state0 checks the network registration (by sending 'AT+CREG?' command) and in response 1 is received, if the SIM is registered in the home network. Then a command 'AT+CMGF = 1' has been sent to select SMS format as a text mode. The flowchart of phase1 for network registration is shown in Fig. 5.11.

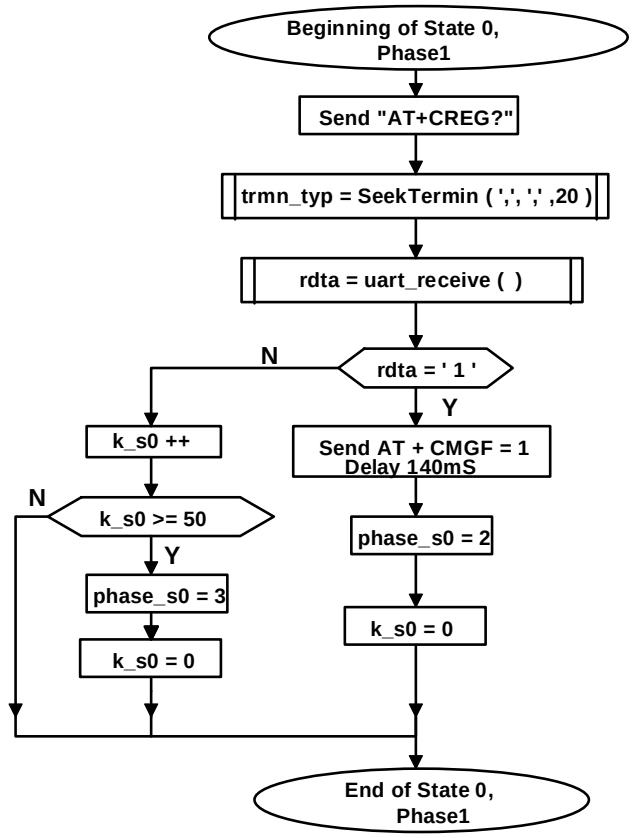

Fig. 5.11. Flowchart for the network registration

Phase2 of state0 sends the text message in accordance with the system-status. The controller sends the identity code of OLS, SOC of the battery and the status of OLS in form of a text message to the remote monitoring station. The identity code is used to locate the installation place of the OLS. The SOC of the battery is estimated for each of the OLS which has already been discussed in chapter 3. Different types of system-status are generated at the specified state which is shown in the flowchart of the respective state. In the respective flowchart, the system status is indicated by a variable named sys_stts. The flowchart and the text message for different status have been shown in Fig. 5. 12. Different conditions of the

system-status along with the text message are also given in Table 5.9. The message has been sent as a series of strings through USART communication technique.

In this realization, the OLS may be spuriously turned on due to cloudy condition as light is being automatically controlled based on the ambient light level. In this situation, an additional message regarding the spurious turn-on has been sent to the remote monitoring station. This is implemented by comparing the time-span of low-light condition with a predefined time, TTS and the corresponding logic has been shown in flowchart of Fig. 5.2. In this flowchart, a variable named SuprTrnOn has been used to assign the condition of turn-on. The additional text message with the condition for spurious turn-on is shown in Table 5.10.

Table 5.9. Different conditions and generated messages

Condition 1	Condition2	Message
sys_stts = 0	lo_lt_flx = 0	System healthy
	lo_lt_flx = 1	High lumen degradation
sys_stts = 1	---	Incomplete charging
sys_stts = 2	((hi_rib)||(hrtg = 4)) = 1	Battery needs replacement No lighting
	((hi_rib)||(hrtg = 4)) = 0	Low battery voltage Light turned off
sys_stts = 3	---	Low level lighting
sys_stts = 4	---	Followed admin command

Table 5.10. Additional message

Condition	Message
spur_ trn_on = 1	Spurious turn on
spur_ trn_on = 0	<None>

In phase3 of state0, the program waits for sufficient insolation at which the battery can be charged. The flowchart for detection of sufficient insolation has been shown in Fig. 5.13. The sufficient insolation level has been detected by measuring the input-output voltage difference Vio_diff, i.e., difference between the battery voltage and open-circuit voltage of the PV module. The state transits from 0 to 1, if Vio_diff increases beyond a pre-defined value of VIO_DIFF. In this case, VIO_DIFF has been set to 5 volt. To confirm the sufficient insolation, the algorithm detects the voltage difference 10times, i.e, the variable k_s0 should be equal to 10 for state transition which is shown in the flowchart of Fig. 5.13.

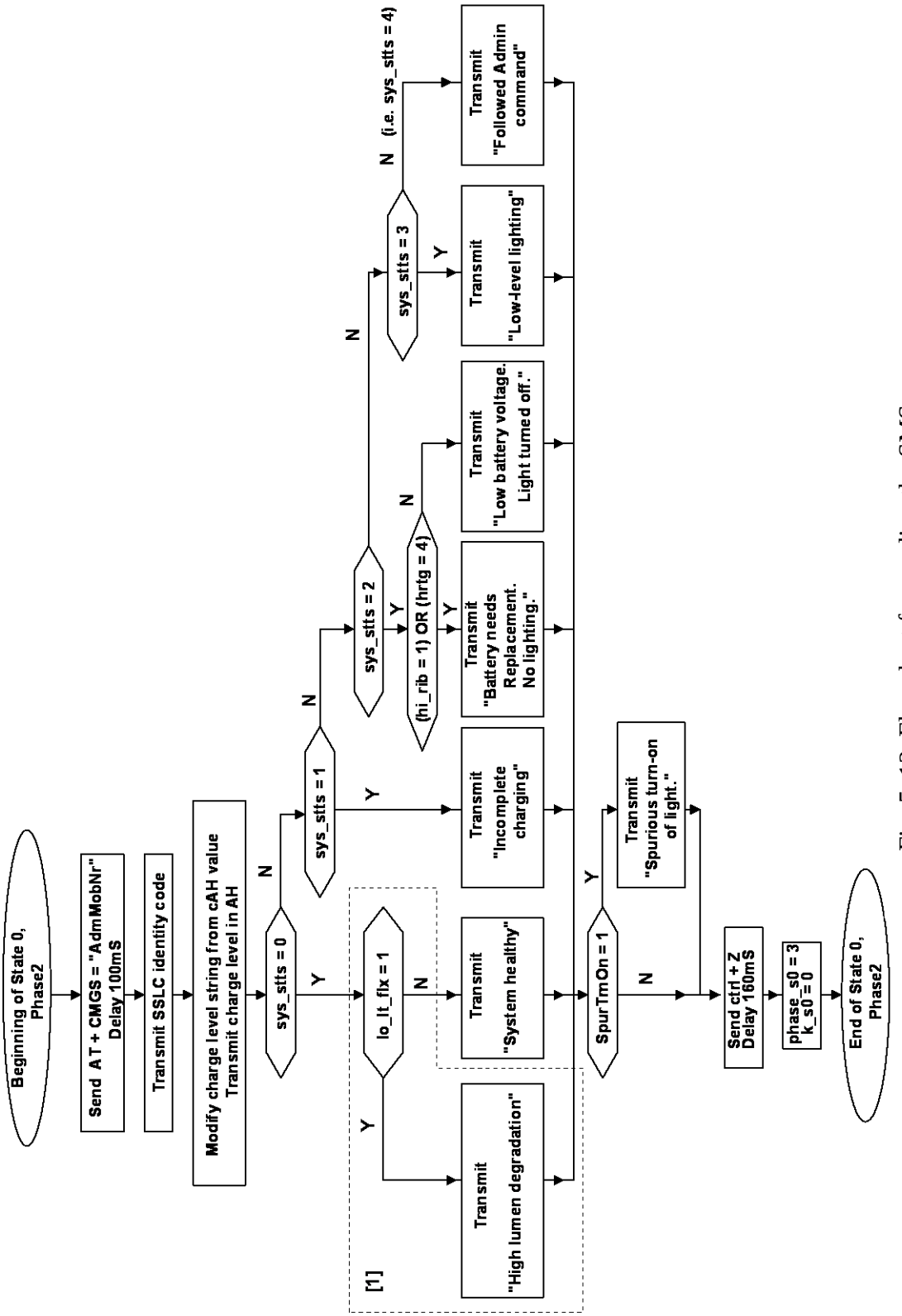

Fig. 5. 12. Flowchart for sending the SMS

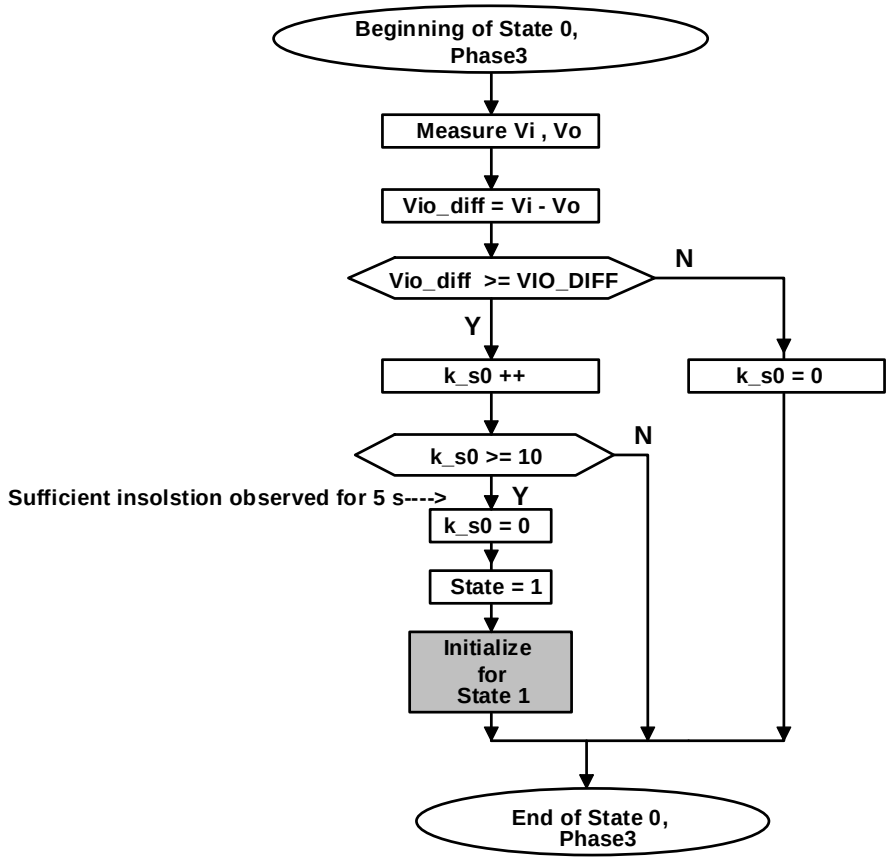

Fig. 5.13. Flowchart to wait for sufficient insolation for battery charging

5.6 Hardware implementation for GSM communication

In the present implementation, serial data communication technique has been used for transferring data between the MCU (ATmega32A) [3] and GSM module (SIM800)[4]. Both the chips have built-in USART (universal synchronous-asynchronous receiver-transmitter) communication technique. The USART of the MCU has to be initialized before any communication can take place. The initialization process normally consists of setting the baud rate, setting frame format and enabling the transmitter or the receiver depending on the usage. The MCU transfers or receives data serially at different baud rate (in bits per second, bps) which is programmable. For a given clock frequency, the value loaded into USART baud rate register (UBRR) decides the baud rate. For asynchronous normal mode, the value of UBRR can be calculated as

$$\text{UBRR} = \frac{F_{CPU}}{16BAUD} - 1 \qquad (5.2)$$

where BAUD is the baud rate (in bits per second, bps).

5.6.1 **Short description of GSM module**

A GSM module is a wireless modem which works with a wireless GSM network. Like a GSM mobile phone, the GSM module also requires a SIM card to receive or transmit data. The GSM module has a SIM card holder through which the SIM card can be inserted. Commercially available GSM modules are SIM300, SIM900 and SIM800. Among them SIM800 has been used in this implementation as it is chipper than SIM900. SIM800 is a quad-band GSM/GPRS module that works on frequencies GSM 850MHz, EGSM 900MHz, DCS 1800MHz and PCS 1900MHz [4]. The power supply (3.4V ~ 4.4V) required by the SIM800 is obtained from a switch-mode buck-regulator fed from the 12V battery.

5.6.2 **MCU and GSM-module interface**

In serial communication, the TXD and RXD pins of SIM 800 are connected to RXD and TXD pins of ATmega32A, respectively. The circuit diagram for MCU and GSM module (SIM800) interface is shown in

Fig. 5.14. Most of the MCU has a USART voltage level of 5Volt. USART voltage for the GSM module is 3.3Volt. Therefore, a logic level converter is needed in between the MCU and GSM module to match the voltage levels of TXD_OUT and RXD_IN pins. In this case, TXD_OUT of MCU is connected to RXD_IN pin of SIM800 through a voltage level converting circuit as received voltage at module side must be 3.3Volt. On the other hand, TXD_OUT of SIM800 is directly connected to RXD_IN pin of the MCU as the MCU can accept 3.3Volt level.

The logic-level converter (5V-3.3V) consisting of resistor R1, R2, R3, a transistor Q1 and a zener diode D1. The value of R1, R2 and R3 are chosen to 1KΩ, 47KΩ and 4.7KΩ, respectively. Voltage rating of D1 is chosen 3.3V as the required voltage at RXD_IN of SIM800 is of 3.3V. A voltage regulator circuit consisting of R1 and D1 is used to provide a constant voltage of 3.3V at node A. For logic output 1, at TXD_OUT pin of the MCU, 5V is present, hence, transistor Q1 is in cut-off due to the reverse bias of base-emitter junction. Therefore, 3.3V has been fed to the RXD_IN pin of SIM800 through R3. Corresponding to logic output 0, 0 volt is present at TXD_OUT pin of the MCU, hence, transistor Q1 operates in saturation region as base-emitter junction is forward biased. Therefore, 0 volt is fed to the RXD_IN pin of SIM800.

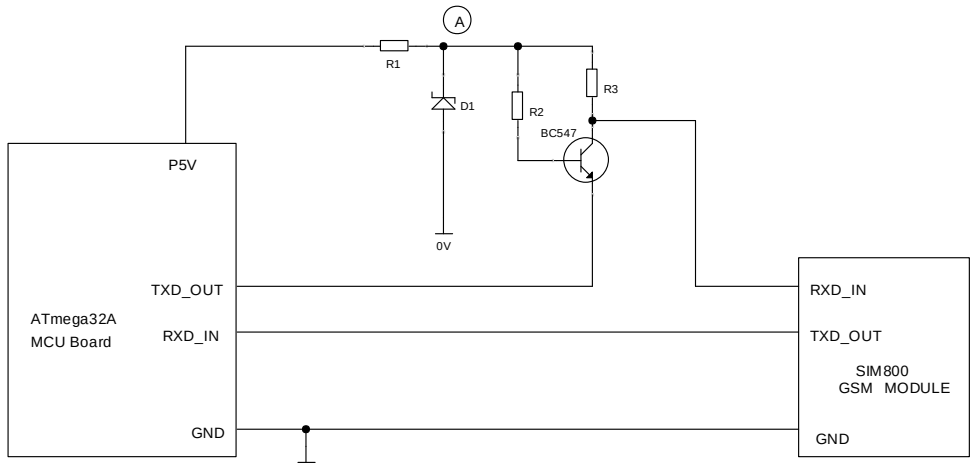

Fig. 5.14 . MCU and GSM module (SIM800) interface

5.7 Modification for tunable-CCT LED lighting system over fixed-CCT light

The modification required for the TCOLS over FCOLS has been discussed in this section. Modification is not needed in state1, state2 and state3 as exactly same charging algorithm is used for TCOLS and FCOLS. The modifications in state 0, state4 and state 5 are discussed below.

In TCOLS, the CCT and illuminance can be independently controlled which is discussed in Chapter4. Therefore, any value of CCT and illuminance can be set from the remote place. In the present realization, 20 numbers of administrator command is used to set the CCT and illuminance. To extract the administrator command from the text message, the content of block [1] of Fig. 5.7 has been modified (i.e., the decoding procedure), so that it can read 20 numbers of administrative command. The administrator command with the corresponding set points of CCT and illuminance have been given in Table.5.11. In this table, CCT and Illuminance are indicated by T_C and E, respectively. If more combination of CCT and illuminance is necessary in an application the program can be suitabilly modified. This might necessitate change in administrator command and decoding procedure. To set the CCT and illuminance with respect to the administrator command, the content of rectugular block [1] of Fig. 5.2 is modified accordingly. In this modification, the algorithm for dutycycle generation with respect to set CCT and illuminance has been added. This algoithm has already been discussed in Chapter4 with its operating principle and the corresponding flowchart has been

shown in Fig.4.5 In absence of administrator command, the brightness for high, medium and low have been set to 120lx, 60lx and 30lx, respectively and the CCT has been set to 6000K. The flowchart of Fig. 5.2 is therefore modified accordingly.

In this implementation, for TCOLS, the light-flux sensor has been ignored due to the unavailability of ADC channel. Therefore, block [1] of Fig. 5.3 and block [1] of Fig. 5. 12 are omitted from the algorithm as it is not necessary for the TCOLS.

Table 5.11. Administrator command with the corresponding CCT and illuminance set points for TCOLS

Administrator command	Action
00	Turn off the LED luminaire
01	Set T_c = 2500K and E = 120lx
02	Set T_c = 4000K and E = 120lx
03	Set T_c = 6000K and E = 120lx
04	Set T_c = 9000K and E = 120lx
05	Set T_c = 12500K and E = 120lx
06	Set T_c = 2500K and E = 90lx
07	Set T_c = 4000K and E = 90lx
08	Set T_c = 6000K and E = 90lx
09	Set T_c = 9000K and E = 90lx
10	Set T_c = 12500K and E = 90lx
11	Set T_c = 2500K and E = 60lx
12	Set T_c = 4000K and E = 60lx
13	Set T_c = 6000K and E = 60lx
14	Set T_c = 9000K and E = 60lx
15	Set T_c = 12500K and E = 60lx
16	Set T_c = 2500K and E = 30lx
17	Set T_c = 4000K and E = 30lx
18	Set T_c = 6000K and E = 30lx
19	Set T_c = 9000K and E = 30lx
20	Set T_c = 12500K and E = 30lx

5.8 Conclusion

This chapter has discussed the algorithms for monitoring and control of the OLS by using the GSM-SMS technology. It is a low-cost system as the SMS can reach to all locations at a very affordable price. In this realization, a low-cost mobile handset with message storage capabilities is used as a user interfacing device in the central monitoring station. Also the mobile handset is most convenient for the general user. One of the adventage of GSM

network is its high security, so the information transmitted or received through this network cannot be monitored by an eavesdropper.

The OLS sends the relevant information regarding the different electrical and physical parameters to the central monitoring station. The central station stores the information in the memory of the mobile handset for data analysis in the future. In turn, after analyzing the data, the OLS can be controlled from the remote station. It is demonstrated that the OLS can also operate automatically (based on the pre-programmed schedule) without any remote comment or physical intervantion. The software modification needed for TCOLS over FCOLS has also been discussed in this chapter. In this realization, we have controlled a low-power RBW LED luminaire from a remote place. This does not invalidate the generalized design concepts developed here.

References

[1] 1361™-2014 IEEE-SA-Standards-Board, "IEEE Guide for Selecting, Charging, Testing, and Evaluating Lead-Acid Batteries Used in Stand-Alone Photovoltaic (PV) Systems," 2014.

[2] "SIM800 Series AT Command Manual," 2015. [Online]. Available: https://www.elecrow.com/wiki/images/2/20/SIM800_Series_AT_Command_Manual_V1.09.pdf. [Accessed: 25-Apr-2019].

[3] "ATmega32A - 8-bit AVR Microcontrollers." [Online]. Available: https://www.microchip.com/wwwproducts/en/ATmega32A. [Accessed: 14-Mar-2019].

[4] "SIM800_Hardware Design_V1.09." [Online]. Available: http://mt-system.ru/sites/default/files/documents/sim800_hardware_design_v1.09.pdf. [Accessed: 25-Apr-2019].

Chapter 6
Scope of Future Research and Conclusion

Introduction

This research study has explored various aspects of modern solar-powered LED lighting systems that may be used for outdoor applications. In the last few decades, researchers have laid great emphasis on judicious use of sustainable energy to reduce the carbon footprint (i.e., reduction in the emission of greenhouse gases). The use of solar powered LED lighting systems is a very appropriate and decisive step in achieving the goal. Although switching to solar power and LED lighting definitely requires a high amount of capital investment, it can be justified when reduction of carbon footprint is the primary issue. It is an accepted fact that developing countries, especially those who are not fully grid connected, have energy deficiencies that can effectively be met by use of solar energy.

Major achievements

In this study, two remote control and monitoring based, 'smart', energy-efficient, long-life, low-cost and low-maintenance solar-powered outdoor lighting systems (OLSs) have been developed, implemented and successfully tested. This systems run automatically with minimal manual intervention. Moreover, they can send information related to management and maintenance of the system to the central monitoring station through a GSM-SMS technology. Such information can be sent on a periodic, say hourly, daily or weekly basis. After analyzing the received information, the central station can also control some parameters of the remote lighting system through the same network. Additionally, on receiving the information, the state-of-health and nature of the fault of the system can be predicted from the remote central station. Necessary maintenance strategy and procedure can then be decided centrally.

Two separate OLS have been developed depending on the application area. The FCOLS can be used for single colour outdoor lighting applications such as streets, pathways, parking lots, industrial yards, security areas, etc. The TCOLS can be used for colour-tunable outdoor

lighting applications such as residential non-living areas, public buildings and structures, gardens, parks, etc. The second kind of dynamic LED lighting system can also be used for indoor applications as tunable-colour light has a great impact on human psychology and biology (e.g., human centric lighting, daylight harvesting, mood lighting etc.).

To implement the tunable-CCT light, the average forward voltages of active LEDs are measured at runtime and the luminous parameters (e.g., xy chromaticity coordinates, peak illuminance) of the LEDs are estimated by using a simple algorithm. The method of estimation of parameters, which does not need direct measurement of LED junction temperature, demonstrates the capability of operation of the system over a wide ambient temperature range.

The multi-mode charger developed in this study can maximize the battery life and minimize the charging time for VRLA battery. Based on an MPPT battery charging scheme, the battery is charged at a fast possible rate under variable insolation and temperature conditions. The MPPT scheme uses a novel Perturb and Observe (P&O) technique.

The state-of-health (SOH) of the OLS has also been predicted by using three different schemes. First one is by measuring the open-circuit voltage of the battery after a given time. Second one is by measuring the internal resistance of the battery. Third one is by measuring the light output of the luminaire. The SOC of battery has also been estimated which can be used to predict the SOH from the remote central station.

The methodology and implementation approaches used in this work is quite simple, straightforward, and do not require any complicated algorithm or costly component or costly tools. The hardware of the whole outdoor lighting system has been implemented by using readily available components including a low-cost microcontroller. The developed algorithm is experimentally validated by this hardware. The control algorithm is developed using C programming language. The necessary compiler and the associated tools are available as freeware . This has reduced the software development cost to a large extent. If any changes in the control strategy and algorithms are necessary for a specific application, the programs can be easily modified.

Most of the commercially available solar-powered outdoor lighting systems in this country commonly use automatic dusk-to-dawn control and few have dimming facilities.

They do not provide facilities like MPPT-based control of battery charging, battery state-of-charge estimation, production of different CCTs of white light, remote health monitoring and control. The systems developed in this study have incorporated all the advanced technological features mentioned above.

Limitations of the present work

Despite the achievement of some encouraging outcomes and results, the system has some limitations. The limitations of the developed technologies are the following:

- Independent CCT and illuminance control have been implemented by using an open-loop system. Therefore, colour shift due to long-term aging of the LEDs is a limitation of this study. To mitigate this issue, a feedback of the output variables becomes essential. The use of additional sensors and hardware would then make the system too complex and expensive and some of the simplicities of our proposed method are then lost.

- In CCT control technique, the selection of white LED is an important factor: high-CRI white LEDs should be chosen as the primary source in the blending process to get high CRI throughout the CCT range. The chromaticity of the white LED also should be as close as possible to the planckian locus to improve the D_{uv} metric.

- The PWM-dimmable LED driver which drives the RBW LED string is not highly efficient as it operates in linear mode during on time of the LED.

Scope of future work

While many encouraging results that help towards better understanding of solar-powered outdoor lighting systems have been obtained during course of this investigation, the work herein can further be extended in the future, based on the following approaches:

- The values of the D_{uv} and CRI (for the CCT range of 2500K to 6500K) of the developed tunable-CCT light source, may be improved by replacement of the red LED string by a red-green composite LED source.

- For simplicity, the MPPT-based charge controller has been implemented by using a single-switch DC-DC buck converter. This converter may be replaced by a synchronous

buck converter to increase the efficiency of the charger. However, the consequent increase in the complexity and cost of the converter should be kept in mind.

- To get higher efficiency the linear LED driver in the tunable-CCT system should be replaced by a switch-mode LED driver.
- A mobile application may be developed for better visibility and analysis of the data.
- The tunable-CCT light source may be installed in the outdoor to record and analyze the visual performance data such as dark adaption, color discrimination, fog penetration etc., of the developed system.

Conclusion

In order to bring home the point that outdoor lighting systems can be smart in many respects with a judicious choice of existing technologies, the present author has described the development of two such systems in this treatise. The entire process of conceptualization, preliminary design, hardware and software selection, system integration and performance evaluation through testing has been described in necessary detail. A conscientious effort has been made so that the procedure, instead of being 'end-product' specific, remains as general as possible. With the availability of a new component, a new software paradigm or a new programming language the core of the development methodology will remain undisturbed. Only a few superficial changes will keep the key concepts as relevant as they are at the present point of time.